A Study of OER Intermediates on the Surface of $SrTiO_3$ and TiO_2 Catalysts through Time-Resolved Optical Spectroscopy and of Vibrational Modes in $SrTiO_3$ through Stimulated Raman Spectroscopy

by

Michael Paolino

B.S., Appalachian State University, 2016

M.S., Appalachian State University, 2018

A thesis submitted to the Faculty of the Graduate School
of the University of Colorado in partial fulfillment of the
requirements for the degree of
Doctor of Philosophy
Department of Physics
2025

Committee Members:
Associate Professor Tanja Cuk, Chair
Professor Dmitry Reznik
Professor Dan Dessau
Professor Markus Raschke
Professor David Jonas
Assistant Professor Andres Montoya-Castillo

Paolino, Michael (Ph.D., Physics)

A Study of OER Intermediates on the Surface of $SrTiO_3$ and TiO_2 Catalysts through Time-Resolved Optical Spectroscopy and of Vibrational Modes in $SrTiO_3$ through Stimulated Raman Spectroscopy

Thesis directed by Associate Professor Tanja Cuk

Hydrogen is an energy dense fuel that produces no carbon emissions when its energy is released in a combustion reaction. Water splitting in an electrochemical cell is an effective and potentially carbon neutral method of producing hydrogen. However, a high overpotential for the oxygen evolution (OER) portion of the reaction limits the efficiency of this process, making the process economically unfeasible. Catalysis presents the possibility of improving reaction efficiency by lowering the overpotential. Designing such catalysts demands thorough knowledge of the OER intermediates through which the catalytic process is understood. The work outlined in this thesis aims to further the knowledge of OER catalysis through studies of reaction intermediates on titanium-oxide catalysts and studying the properties of the titanium-oxides themselves. This studied described within this document use time-resolved optical spectroscopy to study OER intermediates on the surface of TiO_2 and $SrTiO_3$, and uses femtosecond stimulated Raman spectroscopy to study the bulk vibrational properties of $SrTiO_3$.

The first set of intermediates formed during OER on 0.1% n-doped $SrTiO_3$, denoted Ti-OH*, are investigated on multiple time-scales. The shorter time-scale investigation reveals emissive optical spectra of a pH dependent population of Ti-OH* which forms on the ps scale. The relationship between the shifting equilibrium population and pH reveals a Langmuir Isotherm with a half-rise at pH 11.7, corresponding to a free energy change of -0.14 eV associated with the formation of Ti-OH*. The long time scale investigation allows for direct observation of the metastability of emissive Ti-OH* population through a μs scale optical signal. The ps populations are preserved across the metastable region such that the pH dependence of the population reveals an isotherm through which the onset of pH dependence for the intermediate population is extracted at pH 11.3. This work shows through these distinctive pH values, that surface acidity i.e. pK_a for the first reaction intermediate describes a point when the favored site for OER shifts from OH^* to O^{*-}. This work shows that proton transfer from the $SrTiO_3$ surface prior to photo-excitation is important for stabilizing a particular population of OER intermediates.

Intermediates of OER on the surface of titanium-oxides have been described as being stabilized through Ti-O bond distortions which form hole-polarons. First principles calculations have identified electronic states within the material band-gap, assignments of specific polaron configurations to experimental spectra have been difficult due to broad optical transitions. This work compares excited state absorption (ESA) across two different titanium oxides ($SrTiO_3$ and TiO_2) during OER. Using a principle component analysis, ESA at early time scales are isolated from broadband, time-dependent optical spectra. Density functional theory (DFT) and time-dependent DFT calculations are used to predict energies of stable hole polarons within the material bandgap, and the optical dipoles which couple these states to those in the valance band and result in bright transitions. Comparison of experimental spectra and calculations are used to assign specific hole-polaron configurations to ESA across $SrTiO_3$ and TiO_2.

Spontaneous Raman spectroscopy has been used to study bulk vibrational modes of $SrTiO_3$ for decades. Group theory analysis shows that first order Raman transitions in cubic $SrTiO_3$ are inactive, meaning that observed peak are due to second order Raman transitions involving overtone and combination phonon modes. Femtosecond Stimulated Raman spectroscopy (FSRS) is a technique which provides a much high cross-section for Raman transitions, enabling stronger signal-to-noise ratios for vibrational measurements. The magnitude of the Raman peaks generated by FSRS experiments carries a linear dependence on the Raman pump intensity for first-order experiments. FSRS has yet to used as a tool for analysis of the vibrational structure of $SrTiO_3$, and no models exist to predict the Raman gain dependence on pump intensity for second order peaks. This work presents a FSRS spectrum collected on $SrTiO_3$ and shows a linear dependence of Raman gain on pump intensity. A semi-classical approach to model second-order FSRS is introduced as a

part of ongoing work which might predict this linear behavior and provide further evidence that these spectra are indeed second order.

Dedication

This thesis is dedicated to the people who are most important in my life. I will attempt to establish my gratitude with the tools provided by the English language.

Firstly, I must thank my wife Molly for leaving the comfort and familiarity of our North Carolina mountain town and undertaking the move to Colorado with me. Molly's support, patience and encouragement were instrumental in the maintaining of my sanity as I progressed through this painstaking process.

Thank you, mom, for always encouraging me to think independently, and to figure things out for myself.

Thank you, dad, for sparking my interest in science, teaching me the importance of critical thinking, and the importance of not taking myself too seriously.

Thank you, Nick, for never failing to make me laugh, for all the long conversations about music, and the absurdities of life and the world in which we live.

Thank you, David, for having an impact on my life that I will likely never be able to articulate. Knowing you helped me understand the importance of friendship and what it means to care about people in a non-judgmental way. Even though you did not live to see me complete this project, I know you were and are proud of me.

"You don't always get what you go after, but you do get what you wouldn't have got if you hadn't gone after what you didn't get" -Blaze Foley, the Duct Tape Messiah

"Don't let 'em take who you are boy, and don't try to be who you ain't, and don't let me catch you in Kendale with a bucket of wealthy man's paint" -Jason Isbell

Acknowledgements

At this time, I must give proper credit to those who made this thesis a possibility. First and foremost, I must thank my advisor Dr. Tanja Cuk for giving me the opportunity to do the work that is described within. Tanja's guidance, encouragement, and leadership in general were as good as any graduate researcher could hope for, and I consider it a privilege to have done research under Tanja's direction. I must also thank Ilya Vinogradov for his amazing mentoring as a post-doc when I first started working in Tanja's lab. Ilya's guidance was instrumental in the process of learning the skills in optics, spectroscopy, and programming that I needed to succeed as a researcher. I must also thank my fellow researchers, Suryansh Singh, Hanna Lyle, Casey Boyd and who contributed lots of effort to many of these projects. I also extend my warmest thanks to my theory collaborators Shay McBride and Geoffroy Hautier; working with a theory team was a true privilege and it enabled new understanding that would not have otherwise been possible. I certainly must not forget to thank the US Department of Energy and CEDARs for providing the funding which enabled me to complete this work. I would also like to thank my titular advisor Dmitry Reznik, and the rest of my thesis committee: Dan Dessau, Markus Raschke, David Jonas, and Andres Montoya-Castillo for reading this thesis and offering invaluable advice as I advanced to candidacy.

Contents

Chapter

Appendix

Tables

Table

Figures

Figure

Chapter 1

Introduction

Combating anthropogenic climate change is critical to the future of human society. Energy sources that produce little to no greenhouse gas emissions must be implemented to limit the effects of global warming. Several energy sources that do not produce direct greenhouse gas emissions such as solar, wind, and nuclear have been explored over the past several decades in various capacities. However, energy infrastructure is currently set up to accommodate fossil fuel energy production, which can be easily scaled up and down on a daily basis as energy demands change over a 24 hour cycle. Solar and wind energy production are subject to nature, and nuclear energy output cannot be easily turned up or down. Therefore, the implementation of such energy sources on a significant scale requires the development of large-scale energy storage. One method of storing energy is in the form of fuels, such as hydrogen, an energy-dense fuel that produces only water as a byproduct when its stored energy is released.

Hydrogen fuel has been manufactured for decades, but is commonly produced by reacting methane with water. This process, called steam reforming is highly carbon intensive; for every kg of H_2 produced by this process, 7 kg of CO_2 are emitted into the atmosphere [1]. Molecular hydrogen H_2 can also be produced through electrolysis of water in an electrochemical cell:

$$2H_2O \rightarrow 2O_2 + 2H_2. \tag{1.1}$$

The only emissions associated with producing hydrogen by electrolysis are from the energy used to drive the reaction. Thus, carbon neutral energy can be stored as hydrogen fuel without directly producing any carbon emissions. However, the cost of producing hydrogen through OER far exceeds that of steam forming. Therefore, making electrolysis as efficient as possible has the potential to reduce the cost of hydrogen production and thereby make it a more viable option for clean energy storage.

Water electrolysis is performed in an electrochemical cell, which consists of an anode and cathode, connected by a voltage source, submerged in an ionic solution as shown in Figure 1.1. In such a cell, H_2 and O_2 are produced by 2 separate 1/2 reactions shown in Equation 1.2 and 1.3.

$$2H_2O \rightarrow 2O_2 + 4e^- + 4H^+ \tag{1.2}$$

$$2H^+ + 2e^- \rightarrow H_2 \tag{1.3}$$

In the cell, O_2 is formed by oxidation at the cell anode through the oxygen evolution reaction (OER), and H_2 is formed at the cathode via the hydrogen evolution reaction (HER) [2]. Although these reactions occur in parallel, OER is the major bottleneck for the overall electrolysis of water

Figure 1.1: Water splitting in an electrochemical cell. Formation of 0_2 occurs at the cell anode (n-$SrTiO_3$) and H_2 forms at the cathode (Pt). The anode and cathode are connected by a voltage source that maintains a constant electric potential across the cell (0 V for most of our experiments). Submerging the cell components into a conducting solution of varying pH completes the electrochemical circuit.

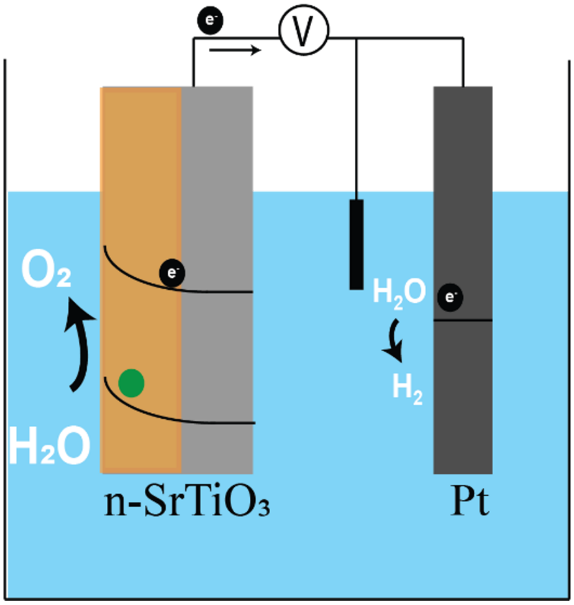

since it produces the protons and electrons which are reactants in HER. Therefore, improvement of water splitting efficiency depends on the increased efficiency of OER. OER catalysis is thus the focus of this work.

The oxygen evolution reaction (OER), involves the production of O_2 from water, along with the transfer of 4 protons (H^+) and 4 electrons (e^-) [3]. The reaction $H_2 + O_2 \rightarrow H_2O$ is spontaneous and exergonic under standard conditions, and thus OER, the reverse reaction, is non-spontaneous and endergonic. Therefore, external energy must be supplied for OER to proceed. Due in part to a free energy barrier, the energy required for OER to proceed will exceed the amount of accessible energy in the product H_2. Catalysts can improve the energy efficiency of reactions such as OER by lowering the free energy barrier, thereby reducing the excess energy that must be supplied to drive the reaction to completion.

Chemical reactions subject to catalysis are often described by a set of metastable chemical intermediates that reorganize reactants into products. Common theoretical descriptors for such intermediates are thermodynamic quantities, such as the free energy change ΔG associated with the formation of each intermediate species [4]. In this work, the catalysts of interest are transition metal oxides (TMOs), which serve as the anode in the electrochemical cell in which the reaction is performed. In such a system, OER occurs at the TMO surface, which acts as a catalyst by providing sites for O-O bond formation. When OER occurs in this environment, it is modeled as proceeding with four reaction steps, each consisting of 1 proton and 1 electron transfer [3]. Each charge transfer occurs along with a chemical transformation involving the formation and/or breaking of chemical bonds, giving rise to metastable chemical intermediates. Figure 1.2a shows the 4 reaction steps of OER. The metastable intermediates are shown on the product side of each reaction step, along with the transferred proton and electron.

Figure 1.2.b shows the free energy change ΔG for each step of OER, as calculated in [2], and plotted against a generalized reaction coordinate. The ΔG for each reaction step is dependent on the potential bias across the TMO electrode. At a bias of 0 V, all ΔGs are positive, meaning that all reaction steps are uphill. When a bias of 1.23 V, the redox potential of water is applied, there

Figure 1.2: The four steps of OER, highlighting reactants and products a), and highlighting free energy changes ΔG b). Each step is defined by a proton and electron transfer along with metastable species as products. ΔG for each step is dependent on the catalyst used and the applied potential across the cell. The step with the highest ΔG determines the overpotential needed for OER to proceed.

a.

$$\Delta \mathbf{G_1} \quad \mathrm{M-OH_2} \rightarrow \mathrm{M-OH^*} + e^- + H^+$$

$$\Delta \mathbf{G_2} \quad \mathrm{M-OH^*} \rightarrow \mathrm{M-O^*} + e^- + H^+$$

$$\Delta \mathbf{G_3} \quad \mathrm{M-O^*} + \mathrm{H_2O} \rightarrow \mathrm{M-O-OH^*} + e^- + H^+$$

$$\Delta \mathbf{G_4} \quad \mathrm{M-O-OH^*} \rightarrow \mathrm{O_2} + H^+ + e^- + \mathrm{M-}$$

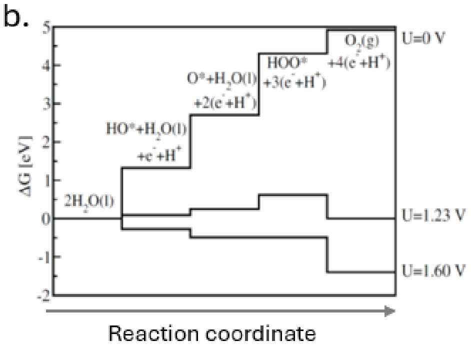

is still a free energy barrier that must be overcome. An overpotential, 1.6 V in total, is required for the reaction to proceed spontaneously. The reaction step with the highest free energy change determines the magnitude of this overpotential.

The magnitude of the free energy change of each reaction step is a function of the catalyst on which the reaction occurs. Given that the reaction step with the highest free energy change determines the necessary overpotential, an ideal catalyst is one in which the ΔG for each reaction step is the same. In such a system, a potential could be applied such that ΔG would equal zero for all steps, yielding a flat line in Figure 1.2b. In such an ideal system, all the energy that goes into maintaining the electric potential would go into the products of the water splitting reaction 1.1. Development of such catalysts requires understanding of OER intermediate steps from the perspective of thermodynamic and kinetic values. Such quantities, along with chemical forms of OER intermediates have been explored through theory, but experimental characterization of OER catalysts has most often been done through cumulative product evolution [5]. An example of this is monitoring the oxidative current through the electrochemical cell in which the reaction occurs (Figure 4.5). This work explores the OER catalytic cycle in a time-resolved fashion, thereby relating a time axis to the reaction coordinate along which the metastable intermediates are formed and decay. Such a scheme allows for resolution of the OER intermediates individually, and provides a direct connection to theory. Metastable intermediates of the OER catalytic cycle will correspond to local minima along a potential energy surface (PES).

Simplified models of the catalytic cycle and the PES for OER is shown in Figure 1.3. Figure 1.3a shows the OER catalytic cycle beginning from a water molecule bound to an arbitrary metal atom M. All reaction steps are represented by a curved gray arrow and consist of 1 proton and 1 electron transfer; the input of 2 water molecules during the cycle is shown. Each intermediate gives rise to the next in sequential order with a product O_2 molecule released in the final step, returning the site to its initial configuration. OER represented as a plot of electronic potential energy as a function of a generalized reaction coordinate is shown in Figure 1.3b. Each energy minimum corresponds to a meta-stable intermediate of OER. These energy minima are such that they allow for the existence of states whose lifetimes can range from microseconds to seconds, but are not deep enough to yield stable chemical forms. The diagram also demonstrates the sequential nature of the reaction cycle, in that one intermediate gives rise to the next. Because of this causal

Figure 1.3: OER shown as a catalytic cycle a) and in terms of a sequence of reactions along a potential energy surface b). The fact that the steps of OER occur in such a sequence enables the analogy of a time axis to the reaction coordinate. Establishing a clear time zero for the beginning of the reaction enables resolution of all reaction steps.

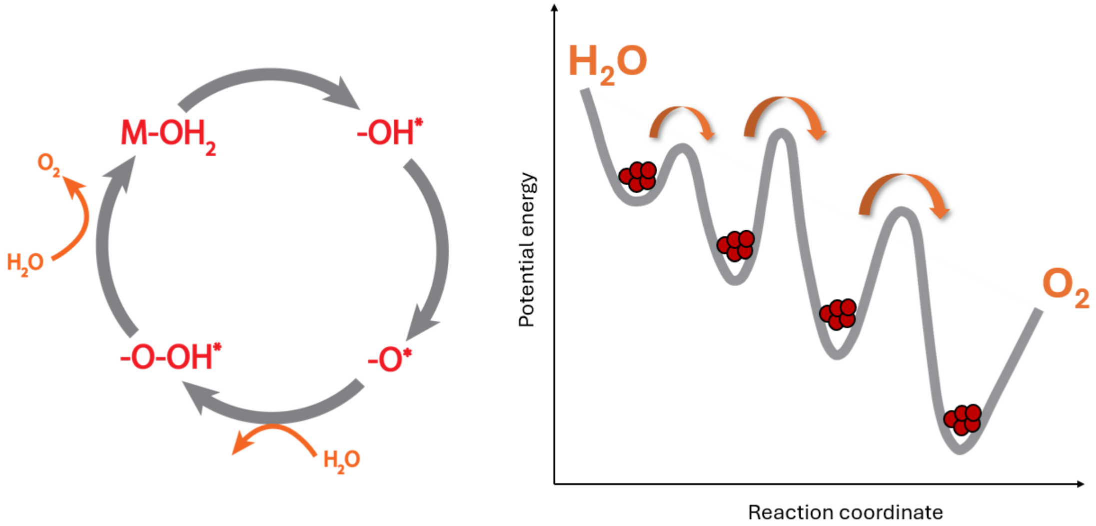

relationship between reaction intermediates, the reaction coordinate is equivalent to a time axis. Time resolution of such a catalytic cycle therefore allows direct tracking of the reaction progress, including formation and decay of OER intermediates.

Previous studies have attempted to isolate reaction intermediates by halting reactions through light, potential, or changing reactant flows [6]. A spectroscopic scheme in which reaction intermediates could be temporally resolved would extend knowledge obtained in these previous studies by providing kinetic and thermodynamic information necessary for fine tuning catalyst properties. To achieve the desired time resolution for such a catalytic cycle three critical considerations are necessary:

(1) The reaction must be initiated from a well-defined time zero such that all the subsequent reactions steps occur spontaneously (downhill). The reaction would thus proceed with the subsequent formation of chemical intermediates with their own potential energy minima. A time axis corresponding to the well-defined time zero should be representative of the reaction progress along its potential energy surface. Such a trigger would need to be on the ultra-fast time scale to resolve ps scale intermediate formation.

(2) The spectroscopic probe would need to be sufficiently time-resolved, allowing for resolution of sequential kinetics. The probe should target a broad set of intermediates, independent of their geometry, whose formation leads to kinetic events.

(3) The spectroscopic probe should be surface sensitive, and have the capability of probing energies relevant to the newly formed intermediates. Such a signal must not be convoluted with signals from the material bulk.

Triggering of OER at a distinct time point is achieved through ultrafast excitation and charge separation at the TMO/electrolyte interface, and thus enables a distinct time point from which the reaction progress can be tracked. Ultrafast excitation and charge separation promotes the system to an excited state surface from which all subsequent reaction steps are downhill (Figure 1.3b). The ultrafast trigger has a timescale of 400 fs, enabling resolution of ps scale formation of intermediates. The electronic spectrum of a broad set of OER intermediates, independent of a particular geometry, is collected through a reflective probe. The broad spectrum of the probe allows for interrogation of intermediates within a wide range of energies. The time evolution of the reflected probe spectrum is achieved by varying the time delay between the pump and probe as they arrive at the TMO surface. This provides the time axis which corresponds to the reaction coordinate along an excited-state potential energy surface (PES). The reflection configuration for the probe allows for the surface sensitivity necessary to monitor OER.

The optical spectroscopy used to resolve OER intermediates results from the formation of intermediates whose energies are in the TMO bandgap. This provides a spectroscopic signature that is unique to the intermediates and can tracked as a function of time. These states are described as hole polarons [7–9]. A hole polaron is a quasi-particle description of an electron vacancy and a local distortion of the atomic lattice in the form of equilibrium bond lengths and atomic positions. Electron vacancies can be equivalently described as “holes” which are generated by the charge separation provided by the ultrafast pump. Localization of photo-generated holes gives rise to polaron states. Polarons can form at a static defect site within an atomic lattice [10], or as a free polaron resulting from fluctuations in the electronic environment within the solid [11]. The “defect” that provides a site for polaron formation at the TMO/electrolyte interface is the interruption of the repeated lattice by the surface itself. The chosen TMOs for OER catalysis in this work are $SrTiO_3$ and TiO_2, which are n-doped with Neobium. Therefore, the interface consists of titanium and oxygen sites at the TMO surface and a hydration layer formed from water molecules in the electrolyte. This hydration layer consists of hydrated sites $Ti\text{-}OH_2$ and hydroxylated sites $Ti\text{-}OH^-$ [12]. The $Ti\text{-}OH^-$ “defect” site will serve as a favorable trapping site for delocalized holes [8]. Localization or trapping of these photo-generated holes at surface $Ti\text{-}OH^-$ sites will result in local bond distortions. These distortions disrupt the energy continuum of the semiconductor’s conduction band, yielding new polaron states with lowered energies, that will thus lie within the semiconductor bandgap. Observation of the time evolution of such intermediates is achieved through an optical

Figure 1.4: a) Band diagram showing pump excitation, simplifed polaron states, and optical transitions stimulated by the white light probe. Ultrafast bandgap excitation with a UV pump that serves to initiate OER is represented by the purple arrow. Stimulated emissive (SE) contributions to the spectrum are represented by the two blue arrows. Electrons in the conduction band can transfer to hole polaron states within the bandgap (light blue) or to empty states within the valence band (dark blue). The signal we observe as a band-to-band emissive signal could result from ground state bleach, which would have the same spectral signature as emission due to the way spectra are calculated. Excited State Absorptive (ESA) transitions are due to valence band electrons transitioning into hole-polaron states within the bandgap (red arrow). b) Potential energy surface with Raman active vibrational levels. Raman pump (green arrow) and Raman probe (red arrow) initiating a change in vibrational level associated with the emission of a photon of energy ω.

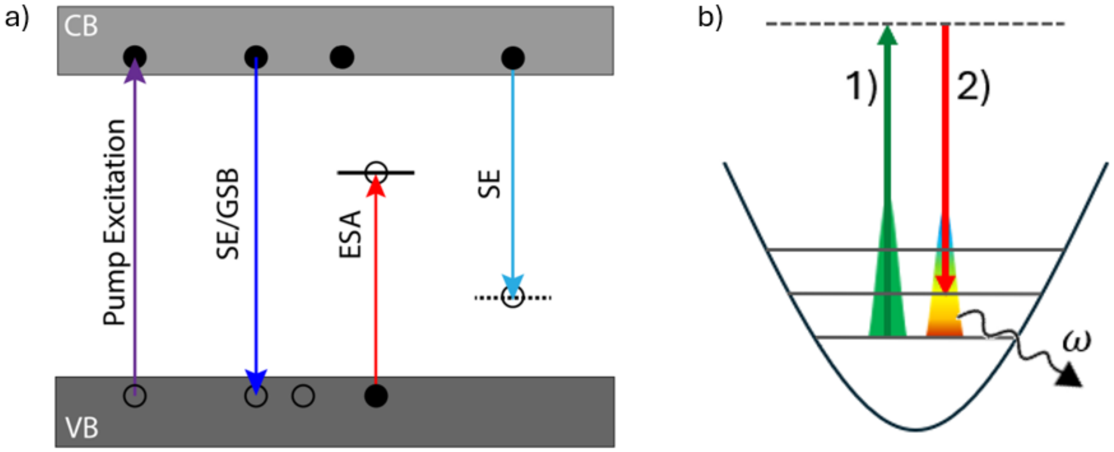

probe that can stimulate transitions between midgap states and the semiconductor valence and conduction bands. Bandgap excitation and spectrally active transitions associated with newly formed polaron states are shown in Figure 1.4a.

Bandgap excitation is represented by the leftmost purple arrow, with the transitions contributing to the optical spectroscopy represented by the blue and red arrows. Emissive signatures are due to electrons in the conduction band transitioning to midgap states or to the valance band. Spectra evaluated as band to band transitions could possibly arise from ground state bleach, which is spectrally identical based on our definitions. Absorptive transitions arise from valence band electrons transitioning to midgap states. Note that this is a simplified representation, and optical spectra will result from many different states whose energies overlap, resulting in a broad signal on the energy axis.

Oxygen evolution on n-doped semiconductor catalysts is a model system for time resolved studies since it involves multi- electron and proton transfer steps, chemical bond formation events, and is highly selective for O_2 formation. The chosen n-doped transition metal oxides $SrTiO_3$ and TiO_2 are ideal semiconductors for such studies. Both are d0 compounds such that their valence bands are comprised of oxygen 2p bonding orbitals and the conduction bands are made of 3d anti-bonding orbitals, which are essentially empty. Therefore, the electron transfers come from O 2p orbitals rather than Ti 3d orbitals which exhibit complex electron-electron repulsions. Ellipsometry measurements show no ground state absorption prior to the bandgap in either compound. Therefore newly formed intermediates whose energies are below that of the bandgap can be viewed with our optical probe without interference from ground state signals. Finally, reduction-oxidation reactions at potentials prior to OER are not prominent in either compound.

The projects investigating OER on titanium oxide catalysts that will described in this dissertation are as follows:

(1) A study of the formation of OER intermediates on an $SrTiO_3$ surface using time-resolved optical spectroscopy

(2) A study of the metastability and decay of OER intermediates on an $SrTiO_3$ surface using time-resolved optical spectroscopy

(3) Spectral assignments of excited state absorptive spectra on TiO_2 and $SrTiO_3$.

(4) A study of the bulk vibrational structure of $SrTiO_3$ through femtosecond stimulated Raman spectroscopy.

These projects can be divided into several classifications. The first 3 projects focus on OER intermediates on the oxide surface, and utilize time-resolved pump-probe optical spectroscopy. Of these three projects, the first two utilize the emissive portion of the optical spectra to track pH dependent OER intermediate population dynamics. The third project focuses the excited state absorption and makes molecular assignments to these transitions across 2 different oxides. The fourth project is focused on bulk properties of $SrTiO_3$ and utilizes stimulated Raman spectroscopy.

The first three projects contained in this work specifically target the first reaction intermediate, designated by Ti-OH* or Ti-O^{*-}. These should be thought of as the result of a water-bound titanium site subject to partial or full deprotonoation, plus the transfer of one electron. The star is a common designator to indicate a radical species or an active chemical site; for the purposes of this work, it should be thought of as the designator of a metastable OER intermediate. In most cases, OER intermediates will be described by Ti-OH* as a general designator, without claiming knowledge of their specific molecular structure. Optically active electronic transitions, shown in Figure 1.4a, are used to detect and study these Ti-OH* intermediates.

In the first two studies included in this dissertation, the emissive portion of time-resolved optical spectra are used to study population dynamics of Ti-OH*. Ti-OH* can be defined thermodynamically by the free energy change $\Delta G_1(OH^*)$ associated with its formation. Using scaling relationships described in [13], $\Delta G_1(OH^*)$ can be used as a predictive descriptor for OER activity on a TMO surface. Additionally, understanding of the thermodynamics of individual OER steps is vital to tailoring catalysts for optimized efficiency. Prior theoretical understanding of such thermodynamic properties of reactive surfaces has been compared to activity measurements using electrochemical current, which does not directly target thermodynamic descriptors, such as $\Delta G_1(OH^*)$. A free energy change is directly related to quantities such as an equilibrium constant K or surface acidity pK_a of the excited state surface. Changing the conditions in which OER occurs, such as pH, can open up new reaction pathways, giving rise to the formation of intermediates with different chemical identities. One can thus express an equilibrium condition between the two possible intermediates. A pK_a for such an equilibrium will describe the pH at which the concentration of each intermediate is equal (see Section 2.3). For this specific reaction, a surface pK_a describes the dissociation of the second proton from a surface bound water molecule, and thereby describes the transition from an intermediate Ti-OH* to Ti-O^{*-}. Understanding how OER is affected by changes in pH, and relating these changes to a pK_a is vital to understanding catalysis of this reaction, and is the focus of the second project highlighted in this thesis. OER intermediates are tracked spectroscopically out to ms timescales as a function of pH and an isotherm relating pH to the magnitude of an optical signal are used to assign a surface pK_a. The first study in this dissertation uses the pH dependent emissive optical signature to study population dynamics of OER during the ps formation of Ti-OH*, and to extract information about constants such as K and $\Delta G_1(OH^*)$ (Chapter 6). The second study continues this work on pH dependence, focusing on the metastable and decaying region of Ti-OH* populations. In this work, particular focus is given to the onset of the pH dependent population dynamics (Chapter 7).

The third study described focuses on the absorptive portion of the time-resolved optical spectrum (Figure 1.4a). In addition to their free energies, Ti-OH* intermediates are defined by their molecular and electronic configurations. From the perspective of electronic structure, hole polarons have been used to describe the states responsible for absorptive signature observed in different titanium oxides. This study compares the experimental absorptive spectrum across $SrTiO_3$ and TiO_2 to DFT and TD-DFT calculations. The comparisons are used to assign molecular configurations to the hole polarons responsible for these optical signatures (Chapter 8).

In the final work in this thesis, the focus is directed away from optical spectra, and toward vibrational transitions active in the $SrTiO_3$ bulk (Figure 1.4b). Using femtosecond stimulated Raman spectroscopy, the spectra of bulk phonon modes within the crystal are studied. Former studies have assigned spontaneous Raman peaks to sum and difference combination bands of phonon modes. This project uses stimulated Raman spectroscopy to confirm the energies of the Raman peaks, and support the combination band assignments through linear dependence of the Raman gain on Raman pump energy. (Chapter 9)

Chapter 2

Transition Metal Oxides

Oxygen evolution occurs at the interface of a transition metal oxide (TMO) and an electrolyte solution. Understanding the interaction between water in solution and the sample is at the core of understanding OER catalysis. Such interactions can be approached from the perspective of the hydration layer at the sample surface, and from the changing energetics at the solid-liquid interface. Properties of the hydration layer have been studied using ambient pressure x-ray photoelectron spectroscopy (AP-XPS) (Section 2.1). The structure of the hydration layer has important consequences for the formation of OER intermediates in the form of hole polarons. The polaron model for OER intermediates and its important consequences for optical spectroscopy are discussed in Section 2.2. A property often invoked to explain the hydration layer in terms of proton transfers from the surface is the surface pK_a, which is a logarithmic expression of an acid dissociation constant. This quantity is invoked to describe the acidity of the hydrated TMO surface. The general definition of pK_a is derived in Section 2.3. To model the surface coverage of OER intermediates as a function of pH, a Langmuir Isotherm model is invoked. This model serves to describe the surface in terms of hole trapping upon electron transfer. A derivation of this model for our specific system is presented in Section 2.4. This chapter will outline these properties of the interface and how they relate to our understanding of OER through this project.

2.1 Surface Hydration

The surfaces explored in this study are $SrTiO_3$ and the 100 facet of rutile TiO_2. The $SrTiO_3$ is a cubic perovskite structure with a TiO_2 surface exposed, thus both crystals present a TiO_2 surface to the electrolyte. The composition of the first hydration layer at this surface is a descriptor of the surface acidity of the TMO [14], i.e. it's ability to dissociate water at equilibrium. Dissociation of the first hydration layer is a common theoretical descriptor used to differentiate catalytic activity for OER on different TMO surfaces [3]. This is due to the fact that OER involves the transfer of 4 protons, and that proton transfer from a hydrated site provides a low potential energy minimum for polaron formation (Section 2.2). The primary tool for assessing the hydration layer of TMOs has been ambient pressure X-ray photoelectron spectroscopy AP-XPS [15]; this technique has been used to characterize the hydration layer of n-doped $SrTiO_3$ (Figure 2.1). The hydration layers on TMO surfaces can consist of complete hydroxylation [16–18] (Figure 2.1d), complete water absorption [19] (Figure 2.1c), or a combination of the two [20–22] (Figure 2.1e).

Figure 2.1: AP-XPS data on a) 0.1% and b) 0.7% n-doped $SrTiO_3$, and representation of the $SrTiO_3$ surface with c) full hydration, d) full hydroxylation, and e) partial hydration and hydroxylation.

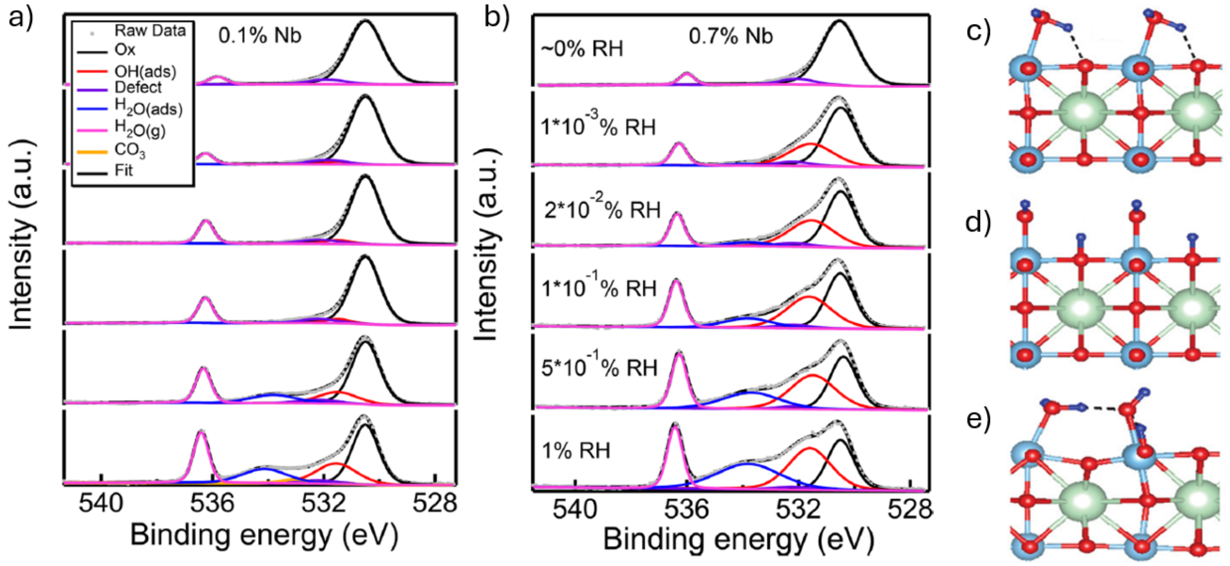

The ability of a TMO surface to dissociate water can be thought of, on a site-by-site basis, as the sum of the reaction free energy of the metal site to lose a proton and the reaction free energy of a neighboring oxygen site to accept the proton. Each site, i.e. metal and oxygen, can be assigned a pK_a, for which K_a is the equilibrium constant for proton release. The difference in pK_a of the metal and oxygen sites describes water dissociation in the absence of surface defects [14]. The hydration layer can depend on the bonding environment, particularly on the metal-oxygen bonds within the TMO; hydroxylation of 110 terminated TiO_2 occurs primarily at defect sites [19]. Additionally, the geometry associated with the TMO surface effects water dissociation; $SrTiO_3$ is TiO_2 terminated and exhibits partial water dissociation, rather than defect specific hydroxylation [21, 23]. Changes to the electronic structure of the TMO, such as an increase in delocalized charge carriers through n-doping will have effects on surface hydration as well. Water dissociation on 0.1% and 0.7% n-doped $SrTiO_3$ has been investigated through AP-XPS with varying humidity [12]. This study showed that surface hydroxylation is a factor of 9 greater for 0.7% doping at low relative humidity, and a factor of 2 greater at 1% relative humidity. For 0.1% doped $SrTiO_3$ which is of particular interest in this body of work, first hydration layer was found to consist of a 50/50 mix of hydrated sites (Ti-OH_2) and hydroxylated sites (Ti-OH^-) at neutral pH. An increase in pH will increase the amount of TMO surface hydroxylation and will thereby affect the chemical reactivity of the metal oxide surface [14], as will be described in the upcoming sections.

2.2 Electronic Structure

The bulk of this work utilizes optical spectroscopy to interrogate OER intermediates Ti-OH^*, providing information on their electronic energies. For this strategy to be effective, the electronic structure of Ti-OH^* must not be convoluted with that of the bare TMO catalyst itself. Incidentally, the electronic structure of Ti-OH^* is such that it's energies lie in the semiconductor bandgap; electronic transitions associated with these states are observable through optical spectroscopy. The formation of midgap states is initiated by charge separation induced by the above bandgap excitation provided by the UV pump. Delocalized charge carriers, specifically holes, will localize on sites at the TMO interface as a means of minimizing their potential energy (and increasing kinetic energy) as they become more confined. At the TMO interface, a local polarization traps a carrier through the distortion of neighboring chemical bonds. This distortion, along with the trapped carrier itself is termed a polaron. Confined or trapped carriers can be localized to a single chemical bond distance or more diffusely across several bond lengths. The characteristic bond distortions of hole polarons disrupt the continuum of states in the TMO valence band, resulting in electronic states in the bandgap. Transitions associated with these states provide the optical spectroscopy through which Ti-OH* is studied in this work. This section will describe the electronic structure responsible for this spectroscopic signal.

2.2.1 1-D Atomic Chain Model

An understanding of polaron formation in a solid can be motivated by beginning with a 1-D atomic chain tight-binding model. Starting with the atomic model for hydrogen, we can see that as the electron becomes less spatially bound by the nuclear potential energy, the electronic levels rise less steeply as the electron's kinetic energy lowers with decreasing confinement as shown in Figure 2.2a. Introducing another H-atom, giving rise to H_2, we can see how the electrons lower their potential energy by localizing between the 2 nuclei (Figure 2.2b). As more H-atoms are added to the chain, the tight-binding approximation can be made, in which the distance between neighboring atoms is defined by the potential energy minimum. Orbitals hybridize across similar bonds and degenerate electronic levels form across the chain (Figure 2.2c). Electrons delocalize across the degenerate energy levels, thus lowering their kinetic energy. In this model, a polaron is the occupation of quantum mechanical levels that cannot be described fully by a homogeneous chain. These can occur as bound or free polarons. Bound polarons occur at lattice defect sites that trap charge carriers. Less-bound or free polarons occur without the presence of a defect and are a result of fluctuations in the electronic environment that changes the potential energy surface (PES) [10, 24]. For either case, as a charge carrier interacts with a defect or fluctuation, a new potential minimum is created within the lattice, and a unique bond length compared to the rest of the lattice

Figure 2.2: Potential energy surfaces of atomic hydrogen a), molecular hydrogen b), a 1-D atomic chain of hydrogen atoms c), a chain of hydrogen atoms along with a polaron, showing changes in bond length and potential energy minimum at the polaron site d).

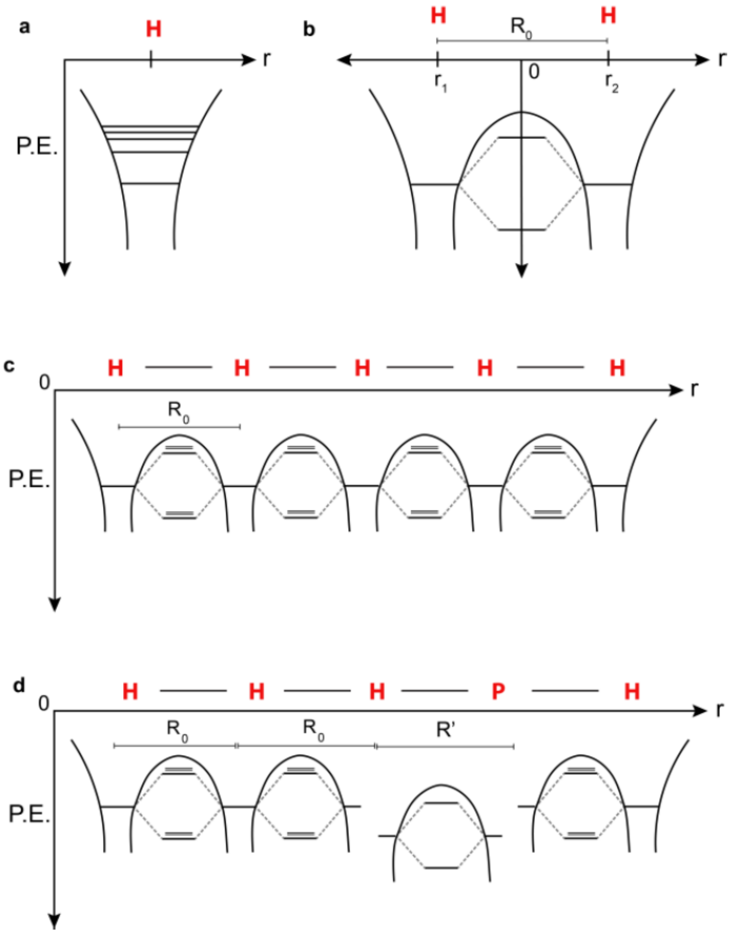

is formed Figure 2.2d shows a new bond length R' and new potential energy minimum at the site of a polaron P. For charge trapping to occur, it must be associated with a lower potential energy minimum, although bond lengths can expand or contract depending on the local polarization. The new potential energy minimum forms a local box around the trapped charge, localizing the charge carrier. Another way to think of this is a breaking of the degeneracy of the energy levels across the chain by the polaron, resulting in less hybridization and increased localization (higher kinetic energy) of the carrier.

Figure 2.3: Surface termination for a generic metal-oxide with full hydroxylation a), hydration with a hydroxylation defect b), and a top down view of partial hydroxylation on a $SrTiO_3$ surface c).

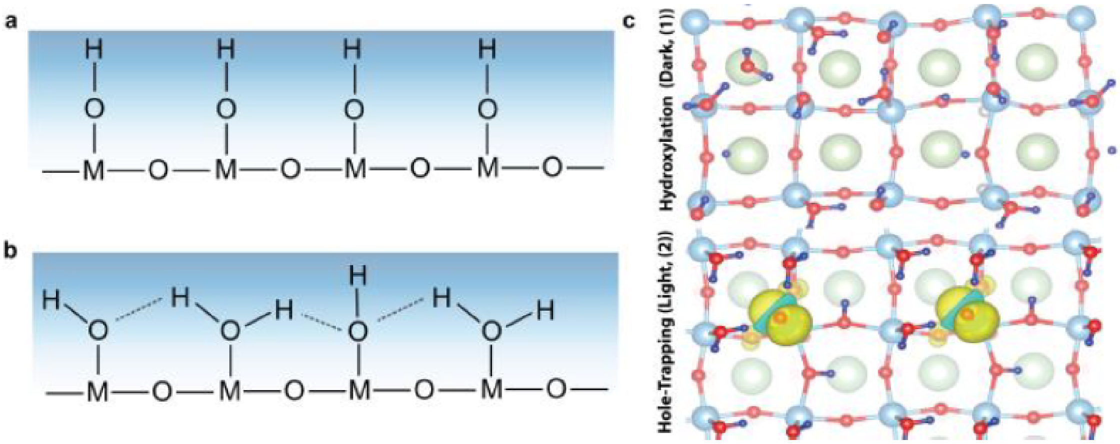

2.2.2 Polarons in a 3D TMO

The 1-D atomic chain model model with a single atomic defect is a simplification of the reality of a 3-D TMO. At the oxide/electrolyte interface, where the catalytic reaction occurs, many cites can contribute to polaron formation, and some will be more active than others. The defect which contributes to polaron formation itself on a TMO is the disruption of the repeated lattice by the surface itself. For both of the TMO species of interest in this study, TiO_2 and $SrTiO_3$, the surface is dominantly TiO_2 terminated [12]. Upon exposure to the aqueous electrolyte, titanium sites will become terminated with water and hydroxyl groups. Figure 2.3 shows a generic metal oxide surface terminated with full hydroxylation 2.3a or hydration with a hydroxyl defect 2.3b. The heterogeneous nature of the surface termination can further differentiate the active sites for catalysis. As determined in [12] (see section 2.1), a 50/50 mix of hydroxylated and hydrated titanium cites is favored for a 0.1% n-doped $SrTiO_3$ surface. Such a surface has been calculated [21, 25] and is shown in figure 2.3c. Although the surface itself provides the defect for polaron formation, the polaron's potential energy surface is defined by the surface termination: trapping a hole at a hydroxylated site $Ti\text{-}OH^-$ will have a lower potential than trapping at a $Ti\text{-}OH_2$ site [8].

Hole polaron OER intermediates are detected through spectral signatures defined by their electronic energies. The reaction in which a hole carrier is trapped at the surface of a general TMO at a Ti-OH$^-$ defect is

$$Ti - OH^- + h^+ \rightarrow Ti - OH^* \rightarrow (Ti - O^*, H^+). \tag{2.1}$$

The reactant hole h$^+$ is photogenerated by above band gap excitation and exists in the valence band. The Ti-OH$^-$ is an electron dense surface site with that has energy overlap with the continuum of energies in the valence band [8]. Hole trapping at Ti-OH$^-$ can also be associated with the release of H$^+$, leading to Ti-OH*. However, since it is difficult to track such proton transfers spectroscopically, the notation is kept generic. Equation 2.1 represents the stabilization of a delocalized hole which is facilitated by the distortion of Ti-O bond lengths, at the TMO/electrolyte interface, resulting in new potential energy minima that are located in the semiconductor band gap. These states provide new spectroscopic transitions that are observable through optical spectroscopy, allowing for polaron detection.

Intermediates of OER are detected spectroscopically via a broadband visible white light probe which spans the visible region of the electromagnetic spectrum. The probe generates a spectroscopic signal through stimulated absorption and emission associated with the polaron states within the TMO bandgap. A potential energy surface modeling the electronic ground and excited states, along with the hole-polaron state in a TMO is shown if Figure 2.4a. Potential energy surfaces are shown as a function of the Ti-O bond length, which can either stretch or shrink with polaron formation. Charge separation through bandgap excitation is shown as the purple arrow, indicating a transition from the ground state to an electronic excited state.

A curve crossing between the excited state and the hole polaron state facilitates energy minimum that facilitates the hole trapping reaction 2.1. Emissive and absorptive transitions, that contribute to the observed optical spectrum are shown as blue and red arrows respectively. In the emissive transition, a conduction band electron occupies the electron vacancy on the polaron site, at the distorted reaction coordinate $R_{polaron}$. The lattice then relaxes to the potential energy minimum of the ground state through non-radiative processes. For the absorptive transition, it is a valance band electron that occupies the vacancy at $R_{polaron}$, after which the lattice relaxes to a

Figure 2.4: Simplified potential energy surfaces a), simplified bandgap diagram b), and characteristic absorption and emission spectra of n-doped $SrTiO_3$ c). The potential energy surface diagram a) highlights the electronic transitions responsible for our optical signal. The bandgap excitation is shown in yellow, absorption is shown in red, and emission is shown in blue. This diagram shows the final state of the system after the relevant optical transition. The bandgap diagram b) shows emissive and absorptive transitions, highlighting the midgap states that provide the optical spectroscopy.

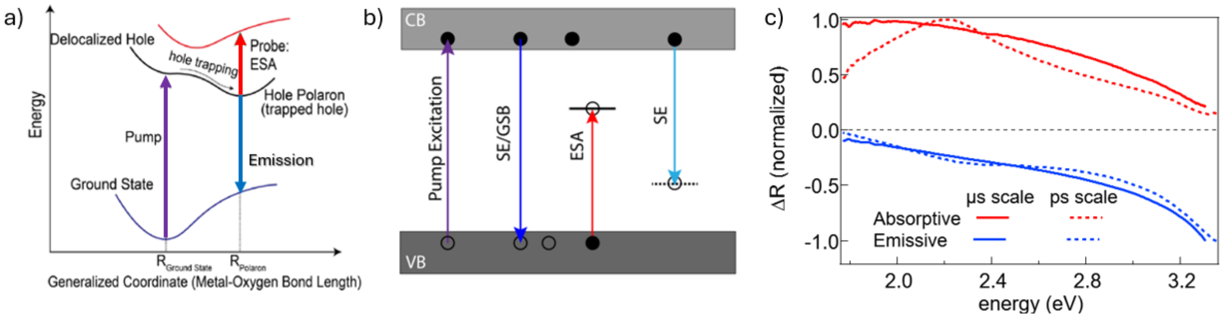

potential energy minimum in the charge-separated excited state. These transitions are represented in a simplified version of the band diagram is shown in Figure 2.4b. Here, absorptive and emissive transitions are shown from the perspective of electrons. Characteristic absorptive and emissive spectra from $SrTiO_3$ are shown in 2.4c. Both are broad transitions due in part to the involvement of Franck-Condon vibrational broadening. Intermediates described more generally as M-OH* can take a variety of configurations with different energies, resulting in broad spectra. Surface heterogeneity will result in both different molecular configurations and the electronic nature of the polaron states. Surface M-OH* species have been shown to interconvert on picosecond time scales [8,26]. Intraband transitions and changes to the refractive index upon photoexcitation could contribute to spectral broadening. Emission near the band-edge could be associated with occupation of a rising density of at the conduction band edge through dopant or refractive index changes.

The materials of interest are $SrTiO_3$ and rutile TiO_2, whose bandgaps are 3.25 eV (381 nm) and 3.15 eV (394 nm) respectively. These can be deduced from the sharp rise in the imaginary part of the refractive index shown in Figure 2.5. The white light probe, represented by the gray box in Figure 2.5, ranges from 1.8 eV to 3.3 eV (375 nm - 700 nm), allowing for the observation

Figure 2.5: Ellipsometry Data for a) $SrTiO_3$ and b) TiO_2. The real n (black curve) and imaginary k (red curve) part of the refractive index are extracted from these measurements. Dispersion of light through a medium is described by n, where light absorption is described by k, which is more relevant for these studies. Wavelengths of the UV pump and broadband probe are indicated by the blue arrow and gray box respectively. The UV pump is well above the bandgap for both semiconductors (indicated by the sharp rise in k). The broadband probe is below the bandgap for both oxides, where there is little to no ground state absorption, allowing for clear resolution of OER spectra.

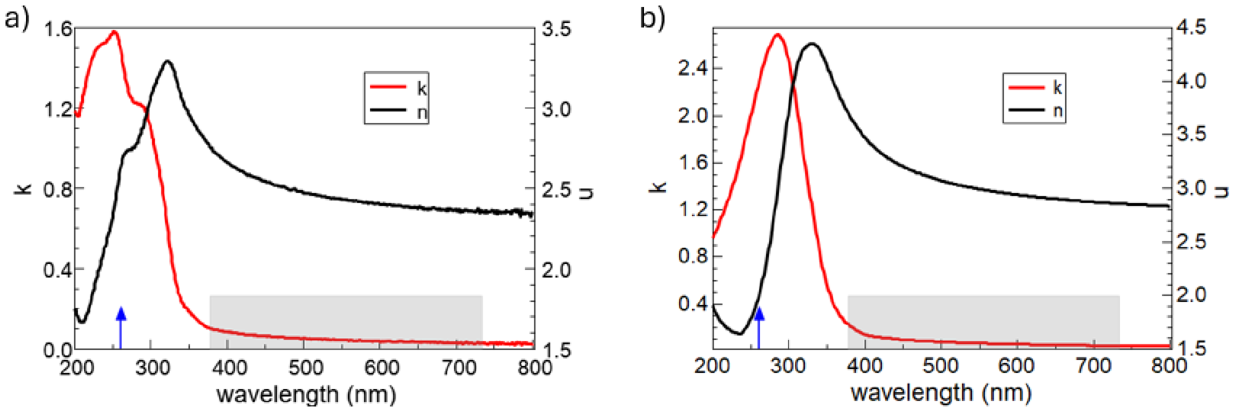

of mid-gap to near band edge transitions. This region is free from ground absorptions, indicated by the small value of k, in the spectral region corresponding to the probe. A lack of ground state absorption in the probe region allows for clear observation of optical signal associated with OER intermediates formed upon pump excitation. The excitation pump is in the UV region at 4.66 eV (266 nm), which is well above the bandgap for both $SrTiO_3$ and rutile TiO_2. The pump energy is indicated in Figure 2.5 by the blue arrow in both plots.

2.3 Hole Trapping and pK_a

The first step of OER at the TMO interface is defined by the transfer of one proton and one electron. The first proton transfer can be understood as the hydroxylation of a metal site as the TMO first comes into contact with the electrolyte. Dissociation of water molecules bound to metal sites on the TMO surface amounts to a the transfer of a proton from the hydration layer to the electrolyte bulk. This process occurs in the dark, without any external energy input.

The first electron transfer only occurs once energy has been supplied to the TMO surface via ultrafast excitation by an ultraviolet pump pulse (266 nm). The UV pump induces charge separation within the TMO through above bandgap excitation: valence band electrons are excited into the conduction band leaving behind delocalized valence band holes. These holes find energy minima through localization onto Ti-OH$^-$ sites at the TMO surface, yielding Ti-OH*. These bound reactive intermediates lead to O-O bond formation prior to the release of O_2. The concept of pK_a is used to model the data presented in Chapters 6 and 7, and is derived below.

The amount of oxygen evolved from OER is dependent on the pH of the electrolyte. This can be modeled by defining a single site model for OER, beginning with a hydrated titanium site, Ti-OH_2. These hydrated surface sites are in equilibrium with hydroxylated titania sites Ti-OH$^-$, as described by

$$Ti - OH_2 + OH^- \leftrightarrow Ti - OH^- + H_2O. \tag{2.2}$$

This equilibrium is shifted to the product side with increasing pH, making the formation of Ti-OH$^-$ at the TMO electrolyte interface more favorable. This can be viewed from the perspective of the energy required to transfer a proton into solution or from chemical considerations via Le Chatelier's principle. From an energetics perspective, increasing pH lowers the energy needed to transfer a proton to solution by -59 mV/pH, making proton transfer more favorable at higher pH [27]. This will discussed in detail in Chapter 4. Chemical considerations describe the relationship between reactants and products as an equilibrium. The equilibrium, associated with a proton transfer into solution, can be quantified in the form of an equilibrium constant K_{OH^-}:

$$K_{OH^-} = \frac{[Ti - OH^-]}{[Ti - OH_2][OH^-]}. \tag{2.3}$$

This equilibrium constant describes how the concentration of products will change in response to changing reactant concentration; this is Le Chatelier's principle. Increasing the pH of the electrolyte (increasing [OH$^-$]) will thus push the equilibrium of the reaction in equation 2.2 to the product side, increasing the number of hydroxylated surface sites ([Ti-OH$^-$]). This equilibrium can be written explicitly as a proton transfer by adding the auto-ionization of water:

$$\begin{aligned} Ti-OH_2+OH^- &\leftrightarrow Ti-OH^-+H_2O \\ +H_2O &\leftrightarrow H^++OH^- \\ Ti-OH_2 &\leftrightarrow Ti-OH^-+H^+. \end{aligned} \tag{2.4}$$

Equation 2.2 thus takes the form of the dissociation of a weak acid, whose equilibrium constant K_a is referred to as the acid dissociation constant and can be written as:

$$K_a = \frac{[Ti-OH^-][H^+]}{[Ti-OH_2]}. \tag{2.5}$$

Acid dissociation reactions are often quantified by their pKa, which is defined as the negative base 10 logarithm of equation 2.5:

$$-\log K_a = pKa = -\log\frac{[Ti-OH^-]}{[Ti-OH_2]} - \log\,[H^+]. \tag{2.6}$$

Using the definition of pH, we can write this as

$$pH - pKa = \log\frac{[Ti-OH^-]}{[Ti-OH_2]} \tag{2.7}$$

which is the Henderson-Hasselbach equation. From equation 2.7 we can see that when the pH is equal to the pK_a, the number of hydroxylated sites is equal to the number of hydrated sites. It is in this sense that the pK_a quantifies the behavior of the TMO surface with respect to pH.

Pump excitation initiates the first electron transfer of OER and is represented by

$$Ti-OH^- + h^+ \rightarrow Ti-OH^*, \tag{2.8}$$

from the perspective of a photogenerated hole h$^+$. This reaction can be written explicitly as an electron transfer in the form: $Ti-OH^- \rightarrow Ti-OH^* + e^-$. Note that this reaction is written with a one-sided arrow indicating that it is an irreversible reaction rather than an equilibrium condition. A reaction constant K_{OH^*} can still be expressed, in terms of equation2.8 in the same fashion as an equilibrium constant:

$$K_{OH^*} = \frac{[Ti-OH^*]}{[Ti-OH^-][h^+]}. \tag{2.9}$$

The number of photogenerated holes h^+ is a constant controlled experimentally by maintaining a constant laser fluence of 0.04 mJ/cm2. Therefore, K_{OH^*} shows that as the number of hydroxylated sites increases, so do the number of OER intermediates Ti-OH*.

2.4 Langmuir Isotherm Model

OER intermediates described can be thought of as adsorbates on the TMO surface. The concentration of Ti-OH* is directly related to the Ti-OH$^-$ concentration as shown by K_{OH^*}. Since the Ti-OH$^-$ surface concentration is dependent on the solution pH, we can define an isotherm for the OER intermediate concentration as a function of pH. A model invoked to describe the ps-scale behavior of OER intermediate formation on the TMO surface is that of a Langmuir Isotherm. This model, used in Chapter 6 relates adsorption onto a surface to the concentration of adsorbate in the liquid phase. Using this model, it is shown that the adsorption isotherm for hydroxylated surface sites is related to the coverage of a meta-stable intermediate.

The pH of the electrolyte solution is tuned experimentally to shift the equilibrium shown in equation 2.4. Since the equilibrium is shifted using NaOH, it is convenient to use a pOH scale, describing OH$^-$ concentration to construct the model. We begin by defining units for the equilibrium constants K_{OH^-} and K_{OH^*}, shown in equations 2.2 and 2.8 respectively. Both [Ti-OH$^-$] and [Ti-OH$_2$] have units of surface coverage and OH$^-$ is in units of M, therefore K_{OH^-} has units of M^{-1}. In reaction 2.8, [Ti-OH$^-$], [h^+], and [Ti-OH*] all have units of surface coverage, giving K_{OH^*} units of number density.

Several assumptions are made in the Langmuir reaction isotherm model. First, the surface (TMO) contains a finite number of sites that can accommodate an adsorbate; second, all surface sites are either occupied by an adsorbate or are unoccupied; third, there are no preferential sites; fourth, for each concentration of adsorbate in solution, an equilibrium is reached. These conditions are met by the isotherm described by the equilibrium condition shown in equation 2.2. Water adsorbed sites, Ti-OH$_2$ are treated as unoccupied sites, since they are the reactant in equation 2.2; similarly, Ti-OH$^-$ are treated as occupied by OH$^-$. As the surface comes into equilibrium with the electrolyte for a given OH$^-$ concentration, unoccupied and occupied cites will exchange up to a limit imposed by a finite surface site density S_0. Given the second assumption of the Langmuir Isotherm model, we can express S_0 as a limiting equation:

$$S_0 = [Ti - OH^-] + [Ti - OH_2]. \tag{2.10}$$

Defining a surface coverage θ_{OH^-}, and use the limiting condition S_0 to relate coverage to K_{OH^-} gives

$$\theta_{OH^-} = \frac{[Ti - OH^-]}{S_0} = \frac{K_{OH^-}[OH^-]}{1 + K_{OH^-}[OH^-]}, \tag{2.11}$$

which is the standard form of a Langmuir Isotherm.

To apply the equilibrium assumption of the Langmuir Isotherm to the hole trapping reaction which yields the meta-stable product Ti-OH*, a few considerations are necessary. The following model treats reactions 2.2 and 2.8 as separate isotherms which are then combined. This is justified in part by the fact that the Ti-OH* coverage yields a sigmoidal dependence on [OH$^-$] [28]. Thus the product of the dark equilibrium, Ti-OH$^-$ independently tunes Ti-OH*. For reaction 2.8, [Ti-OH$^-$] is treated as the reactant concentration in an adsorption isotherm, and h$^+$ are treated as the unoccupied sites. The total hole density $h_0{}^+$ provides a limiting equation

$$h_0^+ = [h^+] + [Ti - OH^*] \tag{2.12}$$

where h$^+$ are delocalized holes, and Ti-OH* are trapped holes. A surface coverage θ_{OH^*} is again defined and related to K_{OH^*} using the limiting equation 2.12:

$$\theta_{OH^*} = \frac{[Ti_O H^*]}{h^+} = \frac{K_{OH^*}[Ti - OH^-]}{1 + K_{OH^*}[Ti - OH^-]} \tag{2.13}$$

which is the isotherm for reaction 2.8. To combine both isotherms, we must write equation 2.13 as a function of aqueous [OH$^-$]. We can relate [Ti-OH$^-$] to [OH$^-$] using equation 2.3, which results in

$$\theta_{OH^*} = \frac{K_{OH^*} S_0 K_{OH^-}[OH^-]}{1 + K_{OH^-}[OH^-] + K_{OH^*} S_0 K_{OH^-}[OH^-]} = \frac{K_{OH^*} S_0 K_{OH^-}[OH^-]}{1 + K_{OH^-}[OH^-](1 + K_{OH^*} S_0)}. \tag{2.14}$$

This can be further simplified by recognizing that $S_0 \sim 2 \times 10^{15} cm^{-2}$ and for an exergonic reaction $K_O H^* >> 1$. Therefore, given that $K_O H^* S_0 >> 1$ we have

$$\theta_{OH^*} = \frac{K_{OH^*} S_0 K_{OH^-} [OH^-]}{1 + K_{OH^*} S_0 K_{OH^-} [OH^-]} = \frac{K_{eff}}{1 + K_{eff}} \tag{2.15}$$

which is Langmuir Isotherm with a single equilibrium constant K_{eff}. This serves as a model for Ti-OH* formation on SrTiO$_3$ surface as a function of pH.

2.5 Free Energies of First and Second Proton Transfer from Hydrated Surface

The first reactive intermediate of OER formed on a SrTiO$_3$ surface is defined by a proton transfer in the dark, followed by an electron transfer upon photoexcitation. Such proton transfers originate from the water molecules bound to titania atoms at the oxide/electrolyte interface. The first proton transfer from the hydrated surface into solution is described by the equilibrium condition

$$Ti - OH_2 + OH^- \leftrightarrow Ti - OH^- + H_2O, \tag{2.16}$$

which is assumed to be dominant at lower pH, (pH prior to the hydrated surface pK_a). As pH increases, a new pathway opens, providing more sites for surface hole trapping and OER intermediate formation. The pH at which this pathway becomes accessible is quantified by the surface pK_a and is demonstrated through the pH dependent emissive signal. This new pathway is the result of newly created sites for hole trapping due to the second proton transfer from the hydrated surface defined by:

$$Ti - OH^- + OH^- \leftrightarrow Ti - O^{2-} + H_2O. \tag{2.17}$$

Reactions 2.16 and 2.17, coupled with the electron transfer, serve to model the formation of OER intermediates defined by Ti-OH* and Ti-O^{*-}. The subsequent electron transfers that occur upon photoexcitation are described as:

$$Ti - OH^- \rightarrow Ti - OH^* + e^- \tag{2.18}$$

and

$$Ti - O^{2-} \rightarrow Ti - O^{*-} + e^{-}. \tag{2.19}$$

We can combine the proton and electron transfers into a single step, representing both charge transfers as an equilibrium condition. To do this, Equations 2.16 and 2.18 along with 2.17 and 2.19 are combined. The resulting equilibrium conditions, along with the associated free energies, are as follows:

$$Ti - OH_2 \leftrightarrow Ti - OH^{*} + H^{+} + e^{-} \quad \Delta(G_{OH^{*}}) \tag{2.20}$$

$$Ti - OH^{-} \leftrightarrow Ti - O^{*-} + H^{+} + e^{-} \quad \Delta(G_{O^{*-}}) \tag{2.21}$$

The reaction describing the equilibrium of products on the excited state surface can be written as

$$Ti - OH^{*} \leftrightarrow Ti - O^{*-} + H^{+} \quad \Delta(G_{OH^{*}/O^{*-}}). \tag{2.22}$$

The free energy of Reaction 2.21, $G_{O^{*-}}$, can be related to that of Reactions 2.20 and 2.22 by summing them:

$$Ti - OH_2 + Ti - OH^{*} \quad \leftrightarrow \quad Ti - OH^{*} + 2H^{+} + e^{-} + Ti - O^{*-} \tag{2.23}$$

$$= Ti - OH_2 \quad \leftrightarrow \quad 2H^{+} + e^{-} + Ti - O^{*-} \tag{2.24}$$

Using the auto-ionization of water ($H_2O \leftrightarrow OH^{-} + H^{+}$), we can write

$$Ti - OH^{-} + H^{+} \quad \leftrightarrow \quad 2H^{+} + e^{-} + Ti - OH^{*} \tag{2.25}$$

$$= Ti - OH^{-} \quad \leftrightarrow \quad Ti - OH^{*} + H^{+} + e^{-} \tag{2.26}$$

which is Equation 2.21. Therefore,

$$\Delta G_{O^{*}-} = \Delta G_{OH^{*}} + \Delta G_{OH^{*}/O^{*}-}, \tag{2.27}$$

which is a relationship that will be used to discuss the results of Chapter 7.

Chapter 3

Transient Setup

Chapter 2 introduced a polaron description of OER intermediates at a TMO/electrolyte interface, 2 models that describe proton and electron transfers at this interface, and relationships between free energies associated with proton transfers. In this chapter, the process of hole trapping as it relates to proton and electron transfers will be described (Section 3.1). The methods of data collection utilized in this work are also described. Time-resolved pump-probe optical spectroscopy, used in the studies described in Chapters 6, 8, and 7, is described in Section 3.2. Data sets collected using this technique are described and shown in Section 3.2.1, and the phonon removal process used in data processing is described in Section 3.2.5. Femtosecond stimulated Raman spectroscopy (FSRS), the technique used in the study in Chapter 9 will described in Section 3.3. Finally, the layout of the experiment will be discussed and shown in Section 3.4.

3.1 Interface and Hole Trapping

The interface between an n-doped semiconductor and a conducting medium, (titanium oxide and electrolyte solution) forms a device called a Schottky diode, which is described in Section 4.1. The Schottky Diode has important consequences for hole trapping and intermediate formation upon photo-excitation. The rapidly changing potential represented by bent valence and conduction bands near the interface is representative of the built-in electric field which facilitates charge separation. When bandgap excitation occurs within the depletion region, electrons are shuttled to the back of the sample and holes to the front. In an OC configuration, this results in a potential across the

TMO which counteracts the built-in electric field, and works to flatten the bands. The result in this case is fast charge recombination, limiting the number of photo-generated holes that will localize at the TMO interface and contribute to OER intermediates. In CC geometry, the rear of the sample is held at a constant (0 V) potential, preserving the built-in field. In this case, a far more significant number of holes are able to localize at the TMO surface, giving rise to OER intermediates.

The first step of OER is defined by the transfer of a proton and an electron, each of which can be considered as separate phenomena under the experimental conditions. Each of these steps are represented in the diagrams in Figure3.1. The equilibrium condition associated with proton transfer is shown in the chemical equation in Figure 3.1a. This proton transfer occurs in the dark as the TMO surface equilibrates with the electrolyte. As pH is increased, proton transfers from the hydrated surface into the electrolyte bulk become more favorable, increasing the number of hydroxylated

Figure 3.1: Diagram showing the interface of the TMO and electrolyte. Conduction and valence band bending near the interface, in closed circuit conditions at a 0V bias is shown. The open-circuit position of the bands under photo-excitation is represented in gray lines. a) Shows the interface in dark equilibrium with the electrolyte, represented as a diagram and by an equilibrium chemical equation. b) Shows the interface upon pump excitation. The pump energy is above that of the TMO bandgap, and thus promotes electrons to the conduction band, leaving behind delocalized valence band holes.

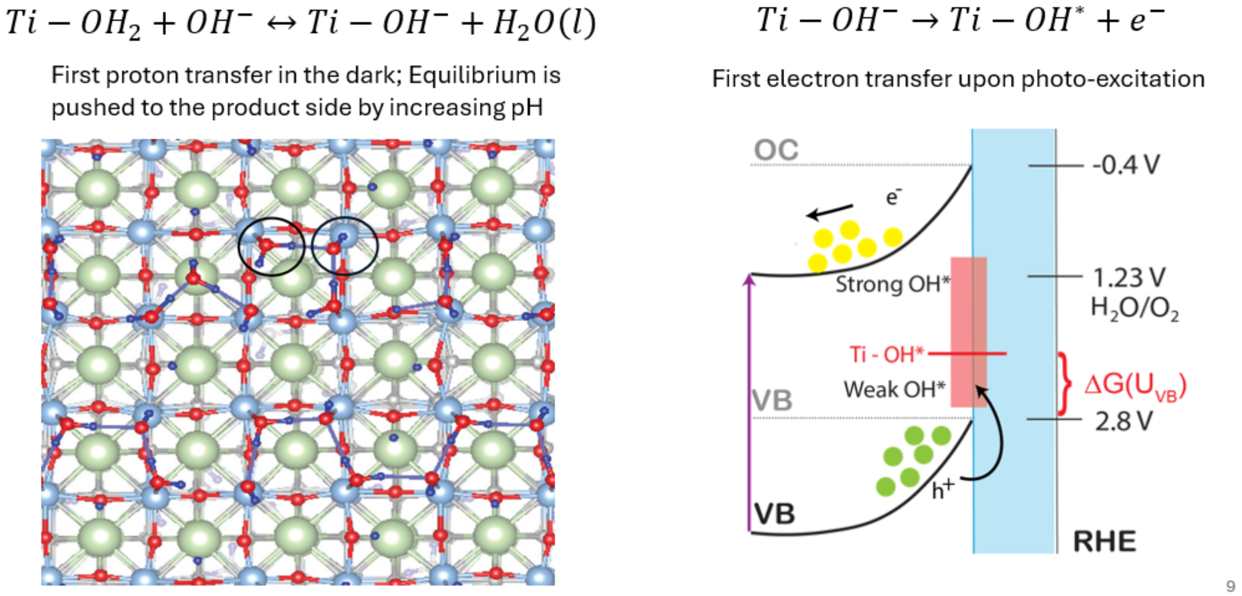

$Ti - OH_2 + OH^- \leftrightarrow Ti - OH^- + H_2O(l)$

First proton transfer in the dark; Equilibrium is pushed to the product side by increasing pH

$Ti - OH^- \rightarrow Ti - OH^* + e^-$

First electron transfer upon photo-excitation sites Ti-OH$^-$ at the TMO surface. This can be understood via Le Chatelier's principle and the equilibrium condition in Figure3.1a, or as a change in the free energy of a proton transfer to solution ΔG_{OH^-} of -59mV/pH. A cartoon of the surface calculated by molecular dynamics simulations [21] is also shown in Figure 3.1a with a hydrated and hydroxylated cite circled. Figure3.1b shows the interface upon photoexcitation. Electron transfer only occurs upon photoexcitation in which the UV pump promotes electrons into the conduction band, leaving behind delocalized valence band holes. In CC conditions, delocalized holes can be described as finding a potential minimum or "rolling uphill" from the perspective of potential shown on in the diagram, and ultimately being trapped at surface sites. Similarly, electrons will "roll downhill" to the rear of the sample. In OC conditions, charge recombination dominates the pathway for delocalized holes, reducing the amount of OER intermediates formed. The trapping of holes is described by the chemical equation in Figure 3.1b with h^+ representing delocalized holes and Ti-OH* representing an active site for the OER, i.e. a trapped hole. Although the proton and electron transfer can be completely separated in time for the physical reaction, they are related through the Ti-OH$^-$ species. Modulating pH changes the amount of Ti-OH$^-$ at the surface, which acts as a more effective hole trapping site than Ti-OH$_2$. Therefore, as the equilibrium in Figure 3.1a moves toward the product side, more OER intermediates can form, meaning that formation of Ti-OH* carries a pH dependence. this relationship, along with associated energetics is detailed in Section2.3 and 2.4. This pH dependence is a critical part of several studies that will be outlined within.

3.2 Pump-Probe Optical Spectroscopy

The OER catalytic cycle is resolved in the time domain by initiating the reaction from a clear time 0 using ultrafast excitation via an above bandgap (3.25 eV $SrTiO_3$, 3.15 eV TiO_2) pump. The reactive surface is then probed with a broadband white probe at a known delay after the well-established time zero. This technique, in which a system is placed into an excited state by one laser pulse, and is then probed by a second laser pulse is termed pump-probe spectroscopy. The pulse sequence used in this technique is represented in Figure3.2. The 266 nm pump pulse is normally

Figure 3.2: Diagram of the pulse sequence used in pump-probe spectroscopy. The pump pulse is 266 nm, and white light pulse is broadband white light ranging from 375-750 nm. The probe operates at twice the rate of the pump, enabling comparison of probe reflectivity with and without pump excitation. The data from this spectroscopy that is analyzed is the difference in reflected spectra during pump on and off shots.

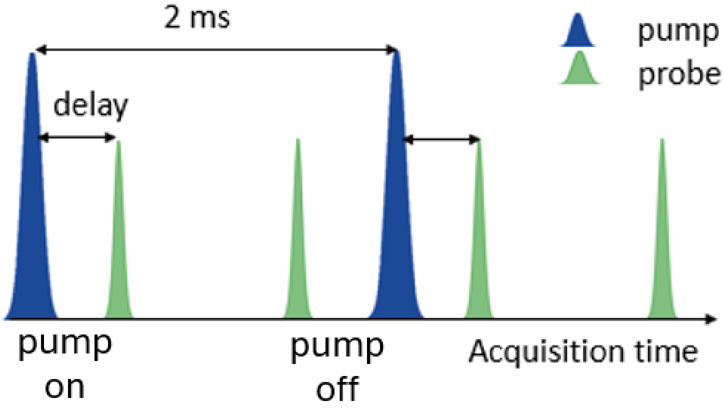

incident on the sample, and the white light probe, spanning the visible region of the spectrum is incident on the sample in reflection geometry. The pump operates at a repetition rate of 500 Hz, with the probe operating at 1 kHz. The probe operating at twice the pump rate means that we can define 2 types of probe pulses: a “pump off” shot, and a “pump on” shot. The base 10 logarithmic difference between on the on and off shots produces the spectrum of interest at a given time delay,

$$\Delta mOD = -\log\left(\frac{on}{off}\right) \tag{3.1}$$

giving a spectrum in units of mOD. This means that the spectrum of interest represents the change in reflectance due to the pump excitation. The spectrum is the result of new emissive and absorptive transitions related to newly formed OER intermediates whose energies lie in the TMO bandgap. (See Section 2.2.) Experimental time resolution is achieved by varying the delay between the pump and probe, such that the pump-probe delay corresponds to an experimental time axis.

3.2.1 Optical Spectra of $SrTiO_3$

Transient reflectance spectra at the ps - ns time scale for the full range of pH are shown in Figure 3.3 for closed circuit A and open circuit B conditions. Electrolyte solutions of NaOH

Figure 3.3: pH-dependence of transient optical spectra for (A) phosphate-buffered solutions at 0 V and (B) unbuffered solutions at open-circuit (OC).

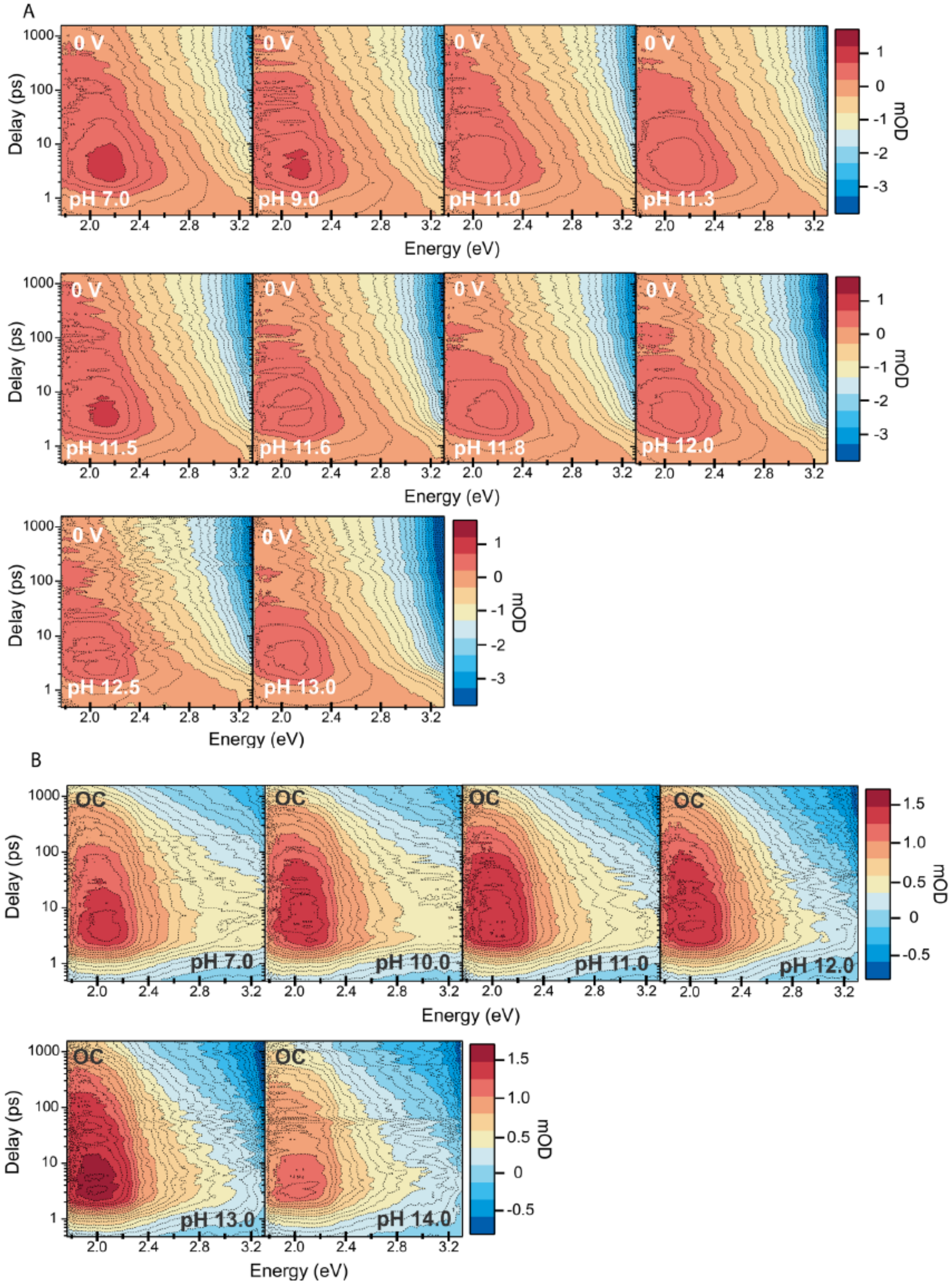

were buffered with phosphate while maintaining a constant Na^+ concentration. The optical maps in Figure 3.3 reveal a pH dependent emissive component (blue) with a relatively pH-independent absorptive component (red) in 0 V conditions, and although signal strength is smaller, a similar trend is observed in OC. The emissive signal is representative of the population of hole-trapped surface species, which grows larger with increasing delay and transition energy. As pH increases, a more basic surface allows for a higher concentration of hole-trapping sites, resulting in a stronger emissive signal.

3.2.2 Spectra of 0.5% n-doped STO and TiO_2 at 0° and 90°

Figure 3.4: Spectroscopic details: a) Contours of pH 7, 0.5% Nb-STO and TiO_2 (100) in open and closed-circuit conditions. b) Cartoon of pump-probe geometry with sample rotated 0° and 90°. Contours of pH 7, OC data collected in these configurations also shown.

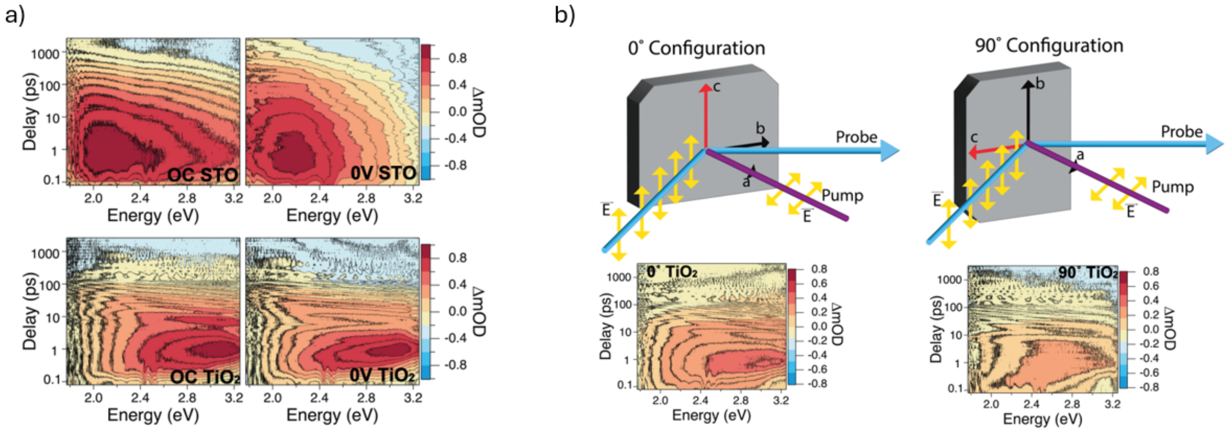

Contours of pH 7, 0.5% Nb-$SrTiO_3$ and Nb-TiO_2 in open (OC) and closed circuit (CC) conditions are shown in Figure 3.4b. For the $SrTiO_3$ data, the ESA's maximum is in the same energy range in both OC and CC conditions. There is slightly less absorption at higher energies in the CC contour due to an increase in emission. Thus, the ESAs in STO appear to be quite similar. An analogous trend is observed in the TiO_2 contours. The dominant ESA in TiO_2 reaches its' maximum in the same energy and time range under CC and OC conditions. Since the ESA in STO and TiO_2 exhibits very similar behavior in OC and CC conditions, our focus on OC datasets was justifiable.

Cartoons of the experimental geometry in different orientations of the sample in the experimental setup are shown in Figure 3.4c. Contour plots taken in these configurations are also shown. In the 0° configuration, the notches are oriented onto the top side of the single crystal and the extraordinary, c axis is pointed vertically. This enables the probe pulses' electric field to be parallel to the extraordinary crystal axis, as seen in 3.4c. In the 90° configuration, the entire crystal is rotated 90° (relative to the 0° configuration) and the extraordinary axis lies along the horizontal axis. As shown in 3.4c, this causes the probe's electric field to become perpendicular to the extraordinary axis. Datasets taken in the 0° and 90° configurations exhibit differences in intensity. The contours shown in 3.4c were collected within 24 hours of each other to limit external variations in the experiment that could influence the resulting TR spectra. Clear differences in intensity are observed between the two datasets. This suggests that the polarization of the probe relative to the extraordinary crystal axis influences the resulting TR spectra. Consequently, all of the other datasets presented hereinafter were collected in the 0° configuration.

3.2.3 Raw TiO_2 TR Data (Chapter 8)

Figure 3.5: Raw transient spectra of TiO_2 at different delay times: a) Evolution of transient absorption spectra from 1 ps to 100 ps. b) Normalized to 1 to emphasize the change in spectral shape.

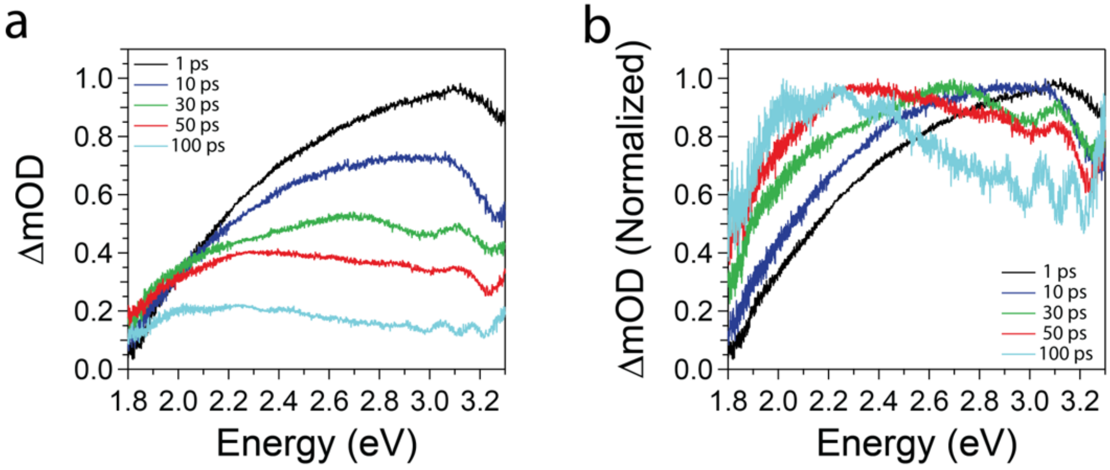

Figure 3.5 shows raw spectral slices of a 0.5% Nb-TiO2 (100) dataset at various time delays. Time slices at 1, 10, 30, 50, and 100 ps were obtained by averaging the spectra collected between 0.8-1.2, 8-12, 28-32, 48-52, and 98-102 ps, respectively. Unnormalized time slices show that the excited state absorption clearly decreases in intensity over time. Normalizing those time slices illustrates the change in spectral shape over time. One can see that the lower energy excited state absorption slowly grows in and eventually overtakes the higher energy absorption between 50 and 100 ps.

Figure 3.6: Contour plots of TiO_2 datasets: Additional raw TiO_2 spectra that were used to obtain the averaged SVD spectrum. The first column contour plots are the same as in Figure 8.4a of the main manuscript.

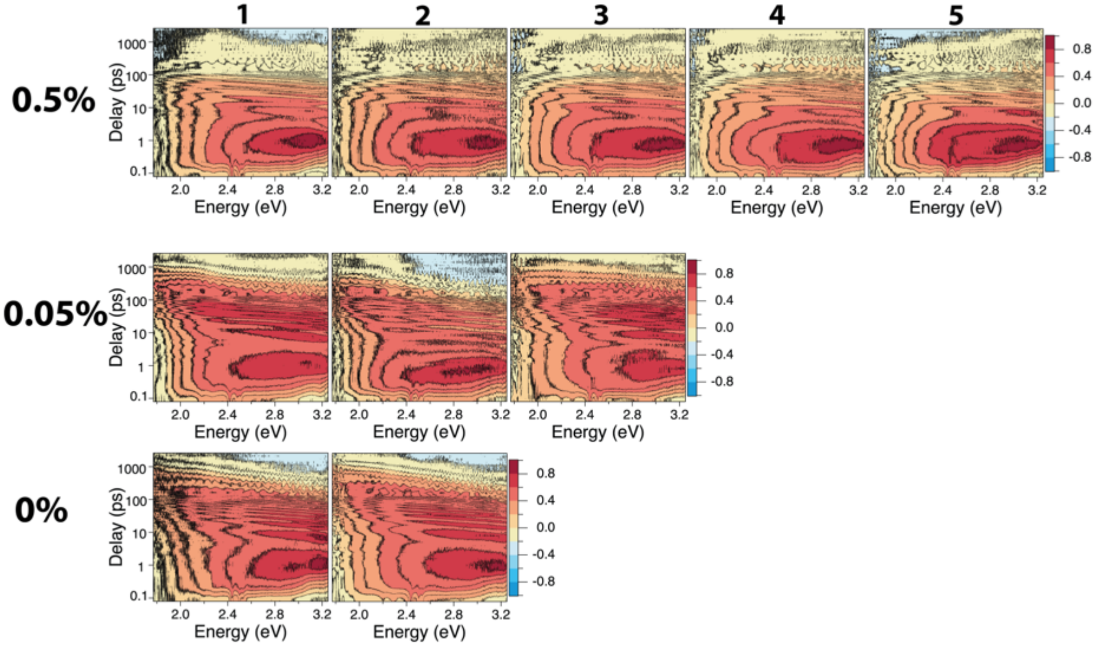

The normalized datasets used to obtain the final, averaged, constrained first component TiO_2 spectrum are shown in Figure 3.6. Contours shown in the first column are identical to the ones shown in Figure 8.4a of the main manuscript. All of the additional datasets were taken to ensure that the results were reproducible and that there was enough data to accurately extract the two constrained SVD components.

3.2.4 Raw $SrTiO_3$ TR Data (Chapter 8)

Figure 3.7: Raw transient spectra of $SrTiO_3$ at different delay times: a) Evolution of transient absorption spectra from 1 ps to 100 ps. b) Spectra normalized to 1 to emphasize the change in shape.

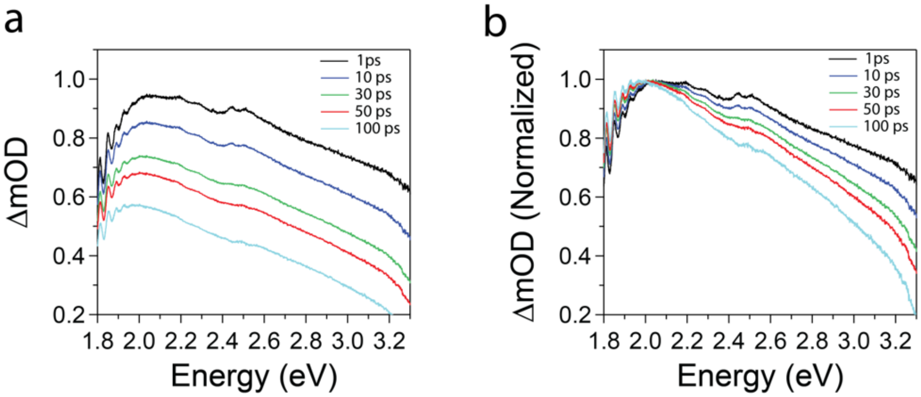

Figure 3.8: Contour plots of $SrTiO_3$ datasets: Raw $SrTiO_3$ datasets at 0.5% Nb doping (1st row), 0.1% Nb doping (2nd row) and undoped $SrTiO_3$ (3rd row).

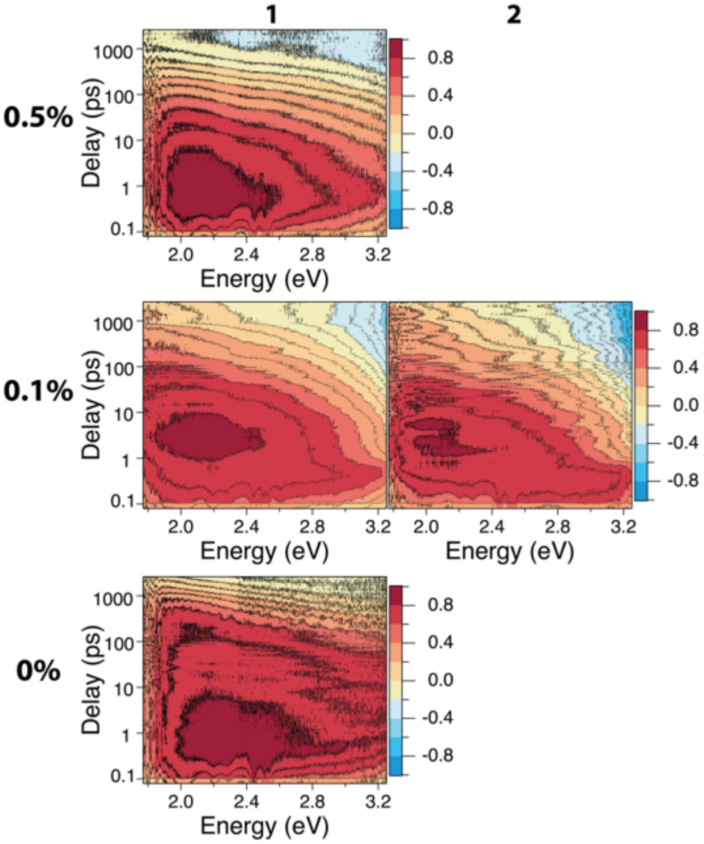

$SrTiO_3$ timeslices are shown in Figure 3.7. Here a maximum intensity is observed at around 1 ps with a maximum at around 2 eV. The signal then decays on the order of picoseconds. In contrast to TiO_2 the shape of the absorptive spectrum does not seem to change over time as can be seen by looking at the normalized timeslices. No second absorptive peak is visible.

Raw, OC pH 7 datasets of Nb-$SrTiO_3$ at 0.5%, 0.1%, and 0% niobium content are shown in Figure B.2. The 0.5% and 0.1% datasets have some emission at longer times, and at higher energies. No such emission is present in the 0% dataset. The lower energy absorptive peak is present in all doping contents though.

3.2.5 Acoustic Phonon Removal

Closed-circuit transient reflectance data collected in the method described in Section 3.2 contains an oscillatory component caused by probe scattering from coherent longitudinal acoustic phonons (CLAPs) [29]. Though these oscillations impact the data, they are not directly related to the optical transitions being studied in this work. Therefore, the oscillations can be removed without changing any of the conclusions presented within. Additionally, these oscillations must be removed so that data can be decomposed into two components using SVD (Section 5.1). Phonon removal consists of fitting oscillations present in the data to a model, and subtracting the fit from the data.

The model, based on probe scattering from CLAPs initiated by the pump pulse is a function of probe wavelength λ, and pump-probe delay t, is given by:

$$\Delta R_{phonon}(\lambda, t) = c_1 A(\lambda) e^{-c_2 t/\xi(\lambda)} \sin\left(\Omega(\lambda)(t + \delta t - t_c(\lambda)) + \phi_0\right) \tag{3.2}$$

$A(\lambda)$ is the phonon scattering amplitude and is related to the acoustic pulse shape and the elasto-optic effect. $\xi(\lambda)$ is the phonon damping coefficient, and is assumed to be proportional to the probe penetration depth (Equation 4.3). c_1 and c_2 are scaling factors for the amplitude and damping respectively, and are free parameters of the fit. $t_c(\lambda)$ is the wavelngth-dependent time-zero that is related to the chirp (group velocity dispersion) of the broadband probe. δt and ϕ_0 are free parameters extracted from the fit: δt accounts for errors in time-zero determination and ϕ_0 adds an additional wavelength independent phase for phonon oscillations. The phonon angular frequency $\Omega(\lambda)$, is defined by Brillouin zone phase matching condition [30] which is defined by

$$\Omega(\lambda) = \frac{4\pi\nu \cdot n(\lambda)}{\lambda}\sqrt{1 - \frac{\sin^2\theta}{n(\lambda)}} \tag{3.3}$$

for the geometry relevant to the experiments described within. The acoustic velocity ν was left as a free parameter of the fit and closely match the literature value for $SrTiO_3$ of 7.9 nm/ps [31–33]. The remaining parameters were fixed: θ is the incidence angle of the probe with respect to the sample cell (45°) and $n(\lambda)$ is the wavelength dependent index of refraction of n-$SrTiO_3$, as measured by ellipsometry [34].

To ensure that phonon removal does not remove effects due to electronic states, the absoprtive and emissive signal contributions are removed by subtracting off the first 2 SVD components (Section 5.1) from the data. Next, the subrange of 25 to 700 ps and 375-700 nm is selected to avoid spectral artifacts at the edge of the data matrix. An example data matrix for a pH 13 data set is shown in Figure 3.9A. The five-parameter fit $(c_1, c_2, \nu, \delta t, \phi_0)$ is performed using the Multistart/lsqnonlin solver from MATLAB's global optimization toolbox. A best fit data matrix

Figure 3.9: a) Raw data after removing first two SVD components. b) Fit for ΔR_{phonon}. c) Residuals from the fit. We speculate that the residual ¿100 ps oscillations are caused by CLAPs propagating in water. Data shown is for the 460 nm grating position of pH 13/phosphate.

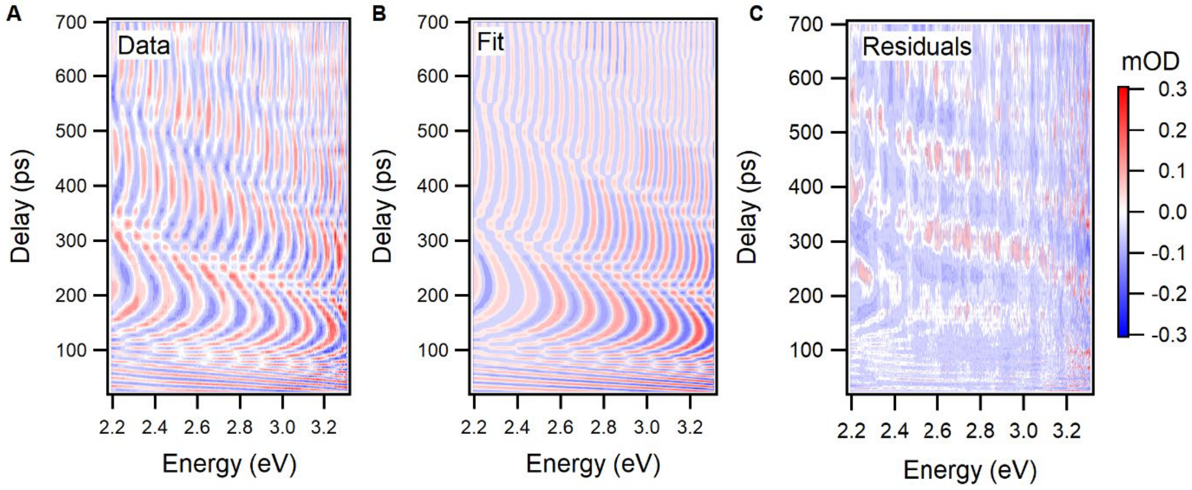

is shown in Figure 3.9B, along with residuals in Figure 3.9C. The subtraction procedure contains additional steps to account for the probe's chirp and convolution with the pump-probe domain instrument response function $g(t)$, which is assumed to be a Gaussian with a FWHM of 1.4 ps:

$$\Delta R_{removed}(\lambda, t) = \Delta R_{raw}(\lambda, t) \cdot (\theta(t - t_c(\lambda) + \delta t) \otimes g(t)) \tag{3.4}$$

where $\theta(t-t_c(\lambda))$ is the Heaviside step function. This procedure was repeated for every raw spectral map ΔR_{raw}. All phonon removed spectral maps $\Delta R_{removed}(\lambda, t)$ were chirp corrected (Supplemetal ref 11) and averaged to yield the spectral maps shown in Figure 6.1.

3.3 Femtosecond Stimulated Raman Spectroscopy

3.3.1 Technique Theory and Overview

Femtosecond stimulated Raman spectroscopy (FSRS) is also employed to provide supplemental information to electronic energies of OER intermediates. Similar species that form as OER intermediates may have similar electronic energies with respect to the valance and conduction band edges while having different geometries. Geometrically different species will possess different vibrational modes that may be active in IR or Raman spectroscopies. Subsurface vibrations have been assigned to a Ti-O* intermediate on $SrTiO_3$ using attenuated total reflectance infrared spectroscopy (AT-IR). Species with different geometries that do not possess vibrational modes associated with a change in dipole moment will not be IR active. However, these species may have modes (or linear combinations of modes) that change the polarizability of the oscillator and will thus be Raman active.

Spontaneous Raman scattering is an ineleastic photon scattering process in which a small number of incident photons either gain or loose energy to a vibrational mode in the scattering molecule. This phenomenon is utilized in Raman spectroscopy, in which the vibrational modes of a molecule or solid are probed. The spontaneous Raman effect is modeled by the absorption of a photon with energy ω_i, followed by the emission (or rather scattering) of a photon of energy ω_s, leaving the scatterer in a new vibrational state. The vibrational energy change during the scattering process is defined by $\omega_{vib} = \omega_i - \omega_s$. Some drawbacks of this technique include the small number of photons that undergo Raman scattering. Additionally, the scattering of photons is is not a coherent process, making collection of a high percentage of Raman scattered photons difficult. Thus, high laser fluence interacting with a large number of scatterers is necessary to produce a quality spontaneous Raman signal.

FSRS provides the ability to both amplify the Raman signal and allows for the probing of vibrational modes in an electronic excited state. In this technique, the interaction of a ps-scale, narrow bandwidth Raman pulse and a femtosecond broadband probe leads to the appearance of sharp spectral gain features on top of the probe envelope as shown in Figure 3.10a [35]. This is the result of a coherence between of Raman pulse with frequency ω_p and the probe at frequency ω_s as they propagate through a medium with vibrational mode with frequency $\omega_{vib} = \omega_p - \omega_s$.
The resulting amplification of the probe beam at ω_s is termed the Raman gain. The frequency shift ω_{vib} is typically plotted on a wavenumber axis and is equivalent to a spontaneous Raman spectrum in terms of frequency distribution. The Raman gain carries an exponential dependence

Figure 3.10: Profile of the pulses associated with FSRS in the wavelength a) and time domaine b). a) The spectrally narrow Raman pulse transfers energy to the spectrally broad probe be at resonances associated with Raman active vibrational modes. The Raman Gain is extracted by taking the logarithmic difference of the probe spectrum with I and without I_0 the Raman pulse: Raman Gain(mOD) $= log(I/I_0)$. b) The actinic pump is narrow in the time domaine and provides electronic excitation, prompting the formation of OER intermediates. After time Δt the ps scale Raman pulse and the fs scale Raman pulse are overlapped in space and time, and interrogate the vibrational modes of the newly formed species.

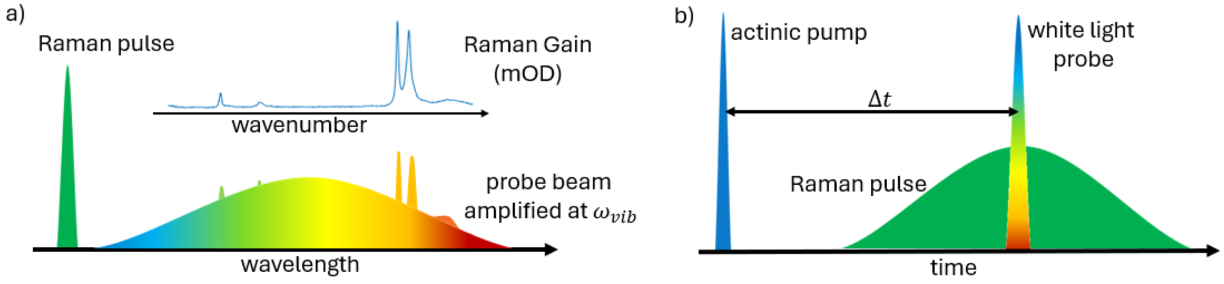

on the intensity of the Raman pulse I_{pu} in units of (photons/cm^2/s)

$$\text{Raman Gain} = \frac{I}{I_0} = e^{a\sigma_R c I_{pu} z} \tag{3.5}$$

where I is the reflected white light intensity with the Raman pulse, I_0 is the reflected white light probe without the Raman pulse, a is a constant with units of cm^{2}s, σ_R is the Raman scattering cross section, c is the sample concentration, and z is the pathlength. Due to the exponential dependence on I_{pu}, the Raman Gain is often expressed in units of mOD by taking the log of Equation3.5 such that

$$\text{Raman Gain (mOD)} = log(\frac{I}{I_0}) = a\sigma_R c I_{pu} z \propto I_{pu}. \tag{3.6}$$

There are several advantages of this technique over spontaneous Raman. One advantage is the high photon yield for stimulated Raman, indicated by the cross-section σ_R. This term exceeds the cross-section for spontaneous Raman by a factor of 10^7. A second advantage is the coherence of the photons associated with Raman gain. Since the Raman signal is carried on the probe envelope, directing the reflected probe beam into a spectrometer means that nearly all photons associated with Raman modes are collected. Finally, an actinic pump can be incorporated with this technique, which allows for probing vibrational modes of an electronic excited state, and time resolution of the Raman signal. Figure 3.10b shows the actinic pump in the time domain with a delay δt before bringing in the Raman pulse and probe.

The actinic pump is a femtosecond scale pulse that promotes the system under investigation into an electronic excited state, after which the system is interrogated by the Raman pulse and probe combination as shown in Figure 3.10b. For the studies being showcased here, the electronic excitation is identical to that described in pump-probe spectroscopy. The pump promotes the system into an excited state from which OER intermediate formation is spontaneous, providing a time 0 point for observing the catalytic cycle. The new Raman active vibrational modes associated with OER intermediates can then probed in a time resolved fashion by varying the delay between the actinic pump and the Raman pulse and probe. The actinic pump in this scheme is a 266 nm above bandgap pump, the Raman pulse is a 400 nm ps pulse, and the white light probe is a fs scale broadband pulse spanning 395 - 460 nm.

The existence of three pulses within this spectroscopy provides several different data collections schemes consisting of different pulse combinations. The possible combinations of both pumps are outlined in table B.1 below. The on and off shots for each pulse train are represented by 1's and 0's respectively, and collectively define different configurations defined by 1,2,3,4. Evaluating the logarithmic difference between different configurations produces different "analysis schemes". For example, ground state Raman is the difference in reflectance with and without the Raman pump, with the Actinic pump off for both shots; therefore, ground state Raman is defined by $\log \frac{config4}{config2}$. Similarly, one could analyze transient reflectance, which is the difference in reflectivity with and without the actinic pump, with the Raman pump off for both shots, and is evaluated as $\log \frac{config3}{config2}$. Excited state Raman could be analyzed as $\log \frac{config1}{config3}$.

Table 3.1: Configuration possibilities of the 3 FSRS pulses: the white light probe, the Raman pulse, the actinic pump. Configuration possibilities should be read vertically down the numeric columns. A 1 indicates that the pulse is on, while a 0 indicates the pulse is off. The different configurations are numbered as indicated in the bottom row.

Probe	1 1 1 1
Raman Pulse	1 0 0 1
Actinc Pump	1 0 1 0
Configuration	1 2 3 4

3.3.2 FSRS Spectra

Ground state spectra ($\log \frac{config4}{config2}$), collected from the bulk of n-$SrTiO_3$ in air are shown in Figure 3.11. To examine the dependence of Raman Gain on Raman Pump intensity described in Equation 3.3.1, spectra were collected for several different Raman Pump energies I_{pu}. Along with the expected increase in the height of the Raman peaks, a negative background signal also is present and grows with increasing I_{pu}. The source of the background is not fully understood, and is not investigated in this work.

Figure 3.11: FSRS Spectra Collected at Different Raman Pulse Energies. Spectra are plotted as Raman Gain against the Raman shift with respect to the Raman Pump energy in units of wavenumber. Three example spectra shown are collected at different Raman pump energies. The height of the Raman peak can be seen to increase with higher Raman Pump energy. This is expected since the Raman Gain is linear with Raman Pump intensity according to Equation 3.3.1. The Raman spectra collected by this method come with a strong negative background that increase with Raman Pump intensity. The source of this background is not fully understood.

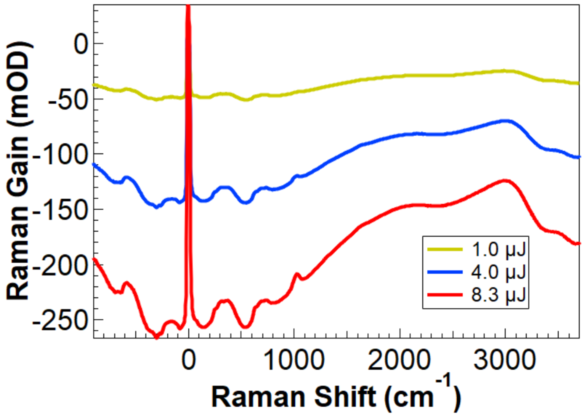

3.4 Physical Layout

Spectroscopy experiments are custom-designed and built on a standard optical table. Optical components and beam paths will vary between experiments, and are described within this section, and are shown in Figure 3.12. A regenerative Ti:Sapphire laser system (Coherent Legend, Coherent Inc., Santa Clara, CA) which outputs laser pulses centered around 800 nm, with a temporal length of approximately 150 fs, at a repetition rate of 1 kHz, is used to produce the white light probe, the Raman pulse, and the 266 nm pump for measurements in the time scale of ps - ns. When doing spectroscopy in the 0-4 ns time range, fundamental pulses from the laser system are then split into 2 separate pathways using a beamsplitter (BS1) Figure 3.12a & b. The reflected section of the pulse from BS1 passes through an optical chopper which is synchronized to block every other pulse, resulting in a beam with a repetition rate of 500 Hz. This beam is then passed through a mechanical delay stage (MTM250CC1) which provides the pump-probe delay for ultra-fast time scale measurements. The chopped and delayed beam is then passed through an Eksma Optics Femtokit (FK-800-200-M) which provides third harmonic generation, producing the 266 nm pulse

Figure 3.12: Diagram of spectroscopic setup for ultrafast TR a), long-time TR b), and FSRS experiments c). Key optical components and beam pathways are shown.

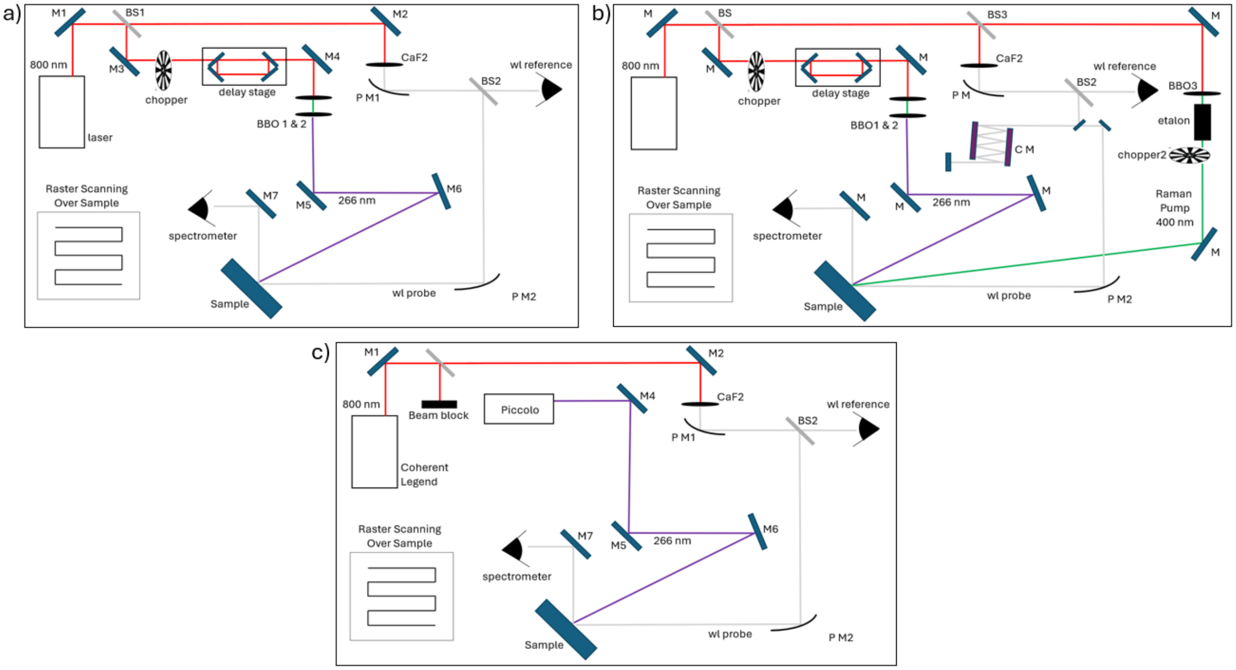

for pump excitation.

For time scales of 4 ns out to 500 microseconds, an Nd:YVO$_4$ Innolas SpitLight Piccolo, electronically triggered laser system is used for bandgap excitation (Figure 3.12c). The electronic triggering of this laser system allows for generation of delays out to hundreds of microseconds. This time scale is necessary for observation of the entire kinetic cycle of the first OER intermediate, and is not possible to achieve using a mechanical delay stage within laboratory space. The Piccolo produces pulses on the ns timescale and therefore cannot resolve the formation of the intermediates, which occurs on the ps timescale. Both laser systems are thus necessary to spectroscopically resolve the intermediates from growth to decay. The Piccolo produces a fundamental pulse at 1064 nm, then generates and separates high harmonics within the laser system. The Piccolo is triggered with a time-variable electronic pulse, therefore the delay stage and high harmonic generation optics are not needed, and the output from this laser is simply directed to the sample surface. Synchronizing this pulse with the master clock within the Coherent laser system poses an interesting problem, which will be detailed, along with its solution in Section 5.2.

The portion of the 800 nm beam which passes through BS1 is used to generate the white light continuum used to probe the dynamics initiated by the pump pulse. This beam is focused and directed through a CaF_2 crystal. Through a $\chi^{(3)}$ nonlinear process, a supercontinuum of visible light (375 – 750 nm for TR measurements) is generated. The visible probe beam is divided into two pathways by BS2 (Figure 3.12). The reflected probe beam is directed to the sample surface such that its reflection from the sample can be directed into the analysis spectrometer/camera (Princeton Instruments). The transmitted probe beam is directed into a referencing camera (Ultrafast Systems) which monitors the probe beam for shot-to-shot fluctuations that could potentially impact the data. The referencing system performs a noise rejection algorithm based on the stability of the white light probe [36, 37].

Figure 3.13: Laser pulse trains associated with FSRS experiments, and the relevant chopper signals. When the chopper signal is high, the chopper is in a position to block the main laser pulse. The kHz laser pulse is used to generate both the actinic pump and Raman pulse trains. Every other pulse from the initial laser pulse train, shown at the top of the diagram, is blocked by chopper 1 to produce the pulse train for the actinic pump. For the Raman pulses, every other pair of pulses is blocked by chopper 2, producing the the pulse train shown at the bottom of the diagram. the white light pulse train is the same as that of the laser.

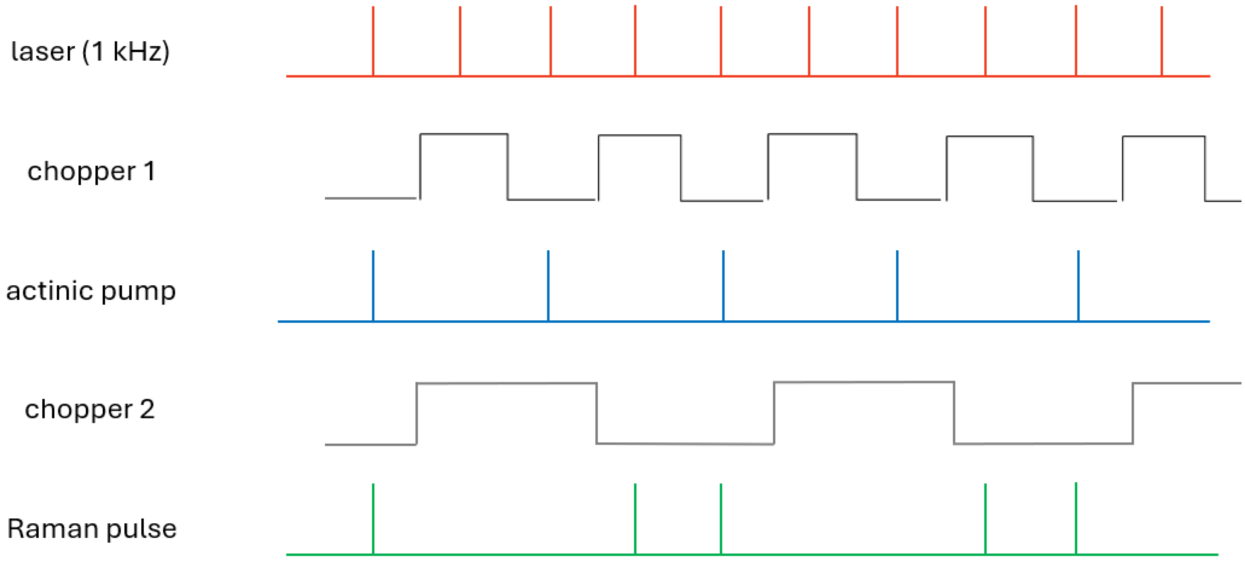

When performing FSRS experiments, a modification is necessary to reduce group velocity dispersion (GVD) within the white light probe. For the stimulated Raman effect to occur across the entire spectrum carried by the white light, probe wavelengths of interest must arrive at the sample simultaneously. The water in the sample cell introduces a positive GVD to the light pulse, which cannot be avoided. To prevent long wavelength light from arriving first, a negative GVD is introduced to the white light pulses. This is achieved through a pair of chirp mirrors, labeled C M in Figure 3.12b. The GVD introduced by this multi-bounce mirror system is sufficient to counteract the dispersion introduced by the water.

FSRS experiments also require a Raman pump to establish the fundamental line to which all measured transition energies are defined. This pump beam is established by splitting the 800 nm fundamental at BS3 just before the CaF_2 window that generates the white light continuum as shown in Figure 3.12b. The transmitted beam through BS3 is doubled using a BBO crystal, yielding a 400 nm beam. The doubled light is then passed through an etalon which spectrally narrows the 400 nm pulse and stretches out the pulse duration to the ps scale. The output from the etalon is chopped such that every other pair of pulses is blocked as shown in Figure 3.13. Chopping is done in this fashion to allow for all possible combinations of the actinic and Raman pumps. The chopping sequence for the actinic pump is also shown in Figure 3.13, along with the chopper synchronization responsible for producing these pulse trains.

Chapter 4

Electrochemistry

The formation of OER intermediates depends on the electronic properties of the interface of titanium oxide catalyst and electrolyte, where the reaction occurs. This chapter will continue the discussion of this interface with a focus on electronic circuit models and how different conditions effect the formation of OER intermediates and our ability to detect them. The properties of the Schottky diode formed at the interface are of key importance and are described in some detail in Section 4.1. The water splitting reaction occurs within a custom-designed electrochemical cell. The properties of this cell, and measurements used to characterize them are described in Section 4.2. A semi-quantitative way to monitor OER during experiments is through the oxidative photocurrent through the cell. Measurements of this current through $SrTiO_3$ samples of different doping densities are shown in Section 4.3. Section 4.4 briefly describes surface degradation of $SrTiO_3$ samples undergoing photo excitation in closed circuit, and Section 4.5 describes information on the source of the samples and the preparation procedure.

4.1 Bandgap and Interface

The TMO/electrolyte interface is a Schottky diode which forms naturally when an n-type semiconductor comes into electrical contact with an electrolyte. At an aqueous interface for which ions on the surface or in the liquid cannot be oxidized or reduced, the O_2/H_2O oxidation-reduction reaction of water levels the chemical potential of electrons in the TMO with that of the reactants in the electrolyte:

$$\begin{aligned} O_2 + 4H_3O^+ + 4e^- &\rightarrow 6H_2O \qquad\qquad 0.815V \\ +2H_2 + 4H_2O &\rightarrow 4H_3O^+ + 4e^- \qquad 0.414V \\ O_2 + 2H_2 &\rightarrow 2H_2O. \qquad\qquad 1.23V \end{aligned} \tag{4.1}$$

By summing the potential of the reduction and oxidation steps, we get the overall redox potential of water, 1.23 V. Diagrams of the interface in open-circuit OC and closed-circuit CC conditions are shown in Figure 4.1.

The redox of water, shown in equation 4.1, levels the chemical potential through charge transfer from TMO to electrolyte. Dopant electrons within the semiconductor conduction band are provided by Neobium Nd, which replaces Ti in the lattice without disrupting the lattice structure [38, 39]. Leveling of the chemical potential results in a region at the TMO surface that is lacking in electron density provided by the Nb doping; this positively charged area is referred to as the depletion region and has width W. The effective positive charge in the depletion region, defined as N_dW where N_d is the doping density, results in a built in electric field within the TMO, causing bending of the conduction and valence bands at the electrolyte interface. The device that results from these phenomena, pictured in Figure 4.1 is termed a Schottky diode. Excitation of a Schottky diode with a laser pulse whose energy is above that of the semiconductor's bandgap will provide efficient charge separation, provided the penetration depth d of the pulse is less than the depletion width W.

The open-circuit (OC) condition shown in Figure 4.1a is a Schottky diode that is not connected to a complete electrochemical circuit. Potentials associated with this system in OC, shown in Figure 4.1a are often described on the reversible hydrogen electrode (RHE) scale. The RHE scale is a purely theoretical reference for potential that is independent of pH. It is often convenient to use the RHE scale, since all potentials on this scale will be relative to that of water oxidation, 1.23 V, regardless of the electrolyte pH. For $SrTiO_3$, the TMO depicted in Figure 4.1a, at vacuum conditions, the conduction band potential U_{CB} is -0.4 V vs. RHE, and the valence band U_{VB} is

Figure 4.1: Diagram showing the interface of a TMO (SrTiO$_3$ and electrolyte in open circuit (OC) conditions on an RHE scale a), and in closed circuit (CC) conditions on an Ag/AgCl scale b). In a) the open-circuit potential of the conduction band under photoexcitation $U_{app,OC}$ is represented as a dotted line. V_{SC} refers to the voltage drop across the semiconductor diode, which can be measured as open circuit photovoltage V_{OC}. The potentials of the valence U_{VB} and conduction U_{CB} bands at the edge of the Helmholtz layer on the RHE scale are -0.4 V and 2.8 V. The voltage drop across the Helmholtz layer is labeled as $V_{H,\ OUT}$. Finally, the redox potential of water U_{redox}, as defined by the RHE scale is 1.23 V and is equal to the chemical potential that has equilibrated across the interface, and is shown as a dashed line. In b), the TMO/electrolyte interface is shown for a closed-circuit (CC) geometry, with the electrolyte at pH 13. On the Ag/AgCl scale, U_{CB} is -1.4 V and U_{VB} is 1.8 V. U_{redox} sits slightly below the Fermi level in the TMO, indicating that the Schottky diode formed by the interface is forward biased.

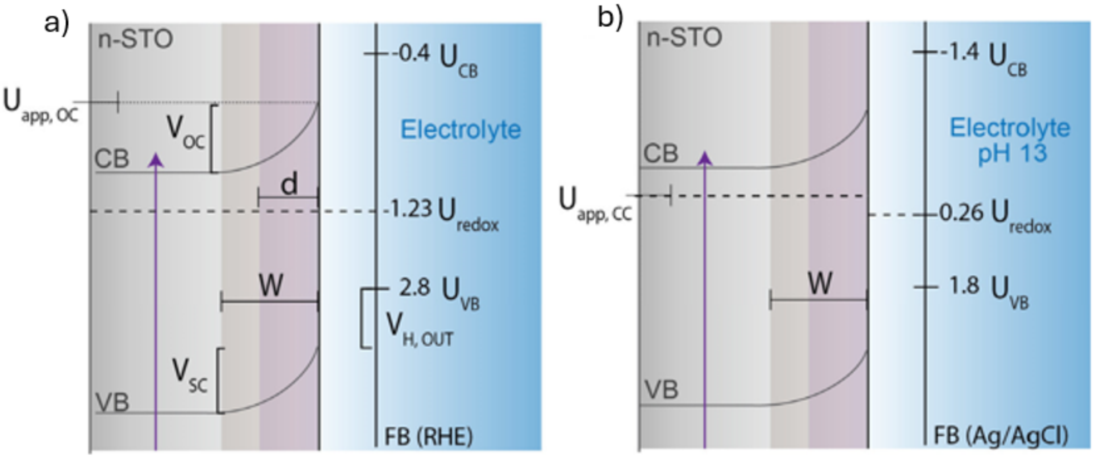

at 2.8 V vs. RHE. These potentials are described at the edge of the Helmholtz layer, designated by the vertical line separating the light blue from the blue region of the electrolyte, and are thus higher than at the edge of the TMO. The Helmholtz layer is comprised of ions absorbed on the TMO surface and in solution, as well as surface dipoles which screen the charge in the depletion layer; this will be further described in Section 4.2. This potential drop across the Helmholtz layer is designated $V_{H,OUT}$. Under experimental conditions, potential is measured against an Ag/AgCl reference electrode. The pH dependence of the redox potential for water (U_{redox} = -59mV/pH) will be reflected in potential measurements against Ag/AgCl. For a diode in OC conditions, the floating potential at the rear of the sample will equilibrate to U_{redox}. Photoexcitation of sufficient fluence, typically done with a UV laser pulse, will counteract the built-in electric field and flatten the valence and conduction bands. The potential at the rear of the electrode in OC conditions is

given by $U_{app,OC}$, and represented by a dotted line in Figure 4.1a.

The closed circuit (CC) condition, for a pH 13 electrolyte, depicted in Figure 4.1b, is one in which the diode is part of a complete electrochemical circuit. In this configuration, the rear of the sample is held at a constant potential $U_{app,CC}$; for most experiments described here, this potential is 0 V. Important results of $U_{app,CC}$ being held constant are 1) U_{redox} will be slightly above that of the Fermi level, meaning that the diode is slightly forward biased in CC, 2) during photoexcitation, $U_{app,CC}$ will be unchanged, preserving the built in electric field and the shape of the bands. The potentials shown on the CC diagram are defined in reference to Ag/AgCl, which is the reference electrode used in experiments. Using Ag/AgCl as a reference means that U_{redox} will move by -59mV/pH. As U_{redox} moves with pH, so will U_{CB} and U_{VB}.

The Schottky diode interface has important consequences for spectroscopic studies of OER. Initiation of OER through UV pump excitation is reliant on effective charge separation, which is facilitated by the built in electric field at TMO surface. Therefore, efficient charge separation relies on bandgap excitation occurring in the region of the built-in electric field, i.e. within the depletion width W. This means that the penetration depth of the UV pump d should be less than W. The depletion layer width is defined by:

$$W = \sqrt{\frac{2\epsilon\epsilon_0}{e_0 N_d}|V_{sc} - \frac{k_B T}{e_0}|} \tag{4.2}$$

where $N_d, \epsilon, \epsilon_0, e_0, k_B, T$, and V_{sc} represent the doping density, the dielectric constant of the semiconductor, the vacuum permittivity, the electronic charge, the Boltzmann constant, the absolute temperature, and the potential difference across the diode in the semiconductor. In the absence of an applied voltage, V_{sc} is simply the built-in voltage at the TMO surface due to the built-in electric field. This represents the potential barrier that must be overcome to flatten the bands, thereby countering the built-in electric field and can be measured through open-circuit photovoltage, which will be described later in this chapter. For 0.1% n-doped $SrTiO_3$, $N_d = 8 \times 10^{18} cm^{-3}$ and $V_{SC} = 0.85V$. Therefore at room temperature, $W \sim 25$ nm. The penetration depth of the UV pump d can be approximated by

$$d = \frac{\lambda}{4\pi k} \tag{4.3}$$

where λ is the excitation wavelength, and k is the imaginary part of the refractive index of the TMO. This gives a penetration depth of $d \sim 17$ nm for $SrTiO_3$ pumped with a 266 nm pulse, thus providing excitation within the depletion layer, and in turn effective charge separation.

4.2 Electrochemical Cell and Measurements

In the electrochemical cell used in our experiments, only the front surface of the TMO is exposed to the electrolyte. A diagram of the electrochemical cell with a TMO sample is shown in Figure 4.2. Laser beam paths representing the UV pump and optical probe are shown as purple and green lines respectively. The pump-probe spectroscopic technique represented by these lines is described in Section 3.2. The sides and rear of the sample are insulated from the electrolyte through procedure that will be detailed in Section 4.5. The sample cell was machined from electrically

Figure 4.2: Diagram of the electrochemical cell in which data is collected. The pump and probe pulses are shown incident on the sample surface, the pump being normally incident and the probe incident at at 45°. The reference electrode is Ag/AgCl and the counter electrode is a platinum wire; both are submerged in the electrolyte to make a complete circuit. The working electrode is in electrical contact with the rear of the sample and is insulated from the electrolyte.

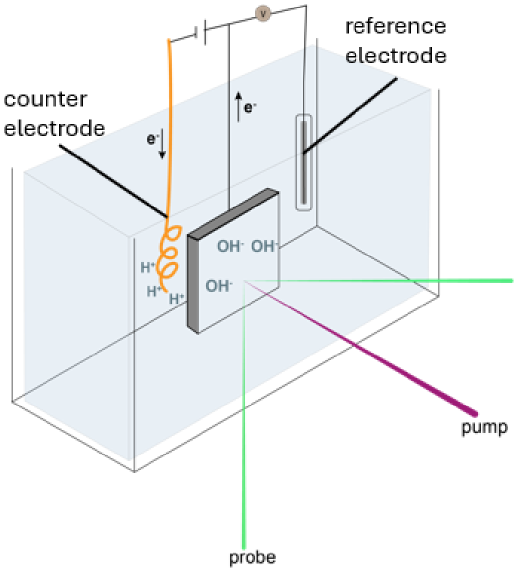

insulating material, is open to air at the top, and has windows at the front and back, which can be sealed with calcium fluoride glass covers such that light can pass through. The cell is designed so that minimal space exists between the TMO surface and the CaF_2 window. This serves to minimize the group velocity dispersion of the white light pulse as it passes through the electrolyte. For experiments conducted in closed-circuit geometry, the TMO surface is the working electrode (anode) in the electrochemical circuit. A platinum wire serves as the counter electrode (cathode) is the circuit, with potential measured with respect to an Ag/AgCl reference electrode. The potential across the electrochemical circuit is controlled by a CHI Instruments 650E potentiostat via a copper electrode connected to the back side of the TMO. In most CC experiments, the rear of the sample is held at a potential of 0 V.

Several techniques are available for measuring electrical and optical properties of the semicon-

Figure 4.3: Photoelectrochemical properties of n-doped $SrTiO_3$. a) Cyclic-voltammogram in the dark and under light excitation. b) Ellisometry data showing the real and imaginary parts of the n-$SrTiO_3$ refractive index. Quantum efficiency of as a function of wavelength is also shown. c) Open-circuit photovoltage as a function of laser fluence for 0.1% and 0.7% n-doped samples. d) Mott-Schottky plots for 0.1% and 0.7% dopings.

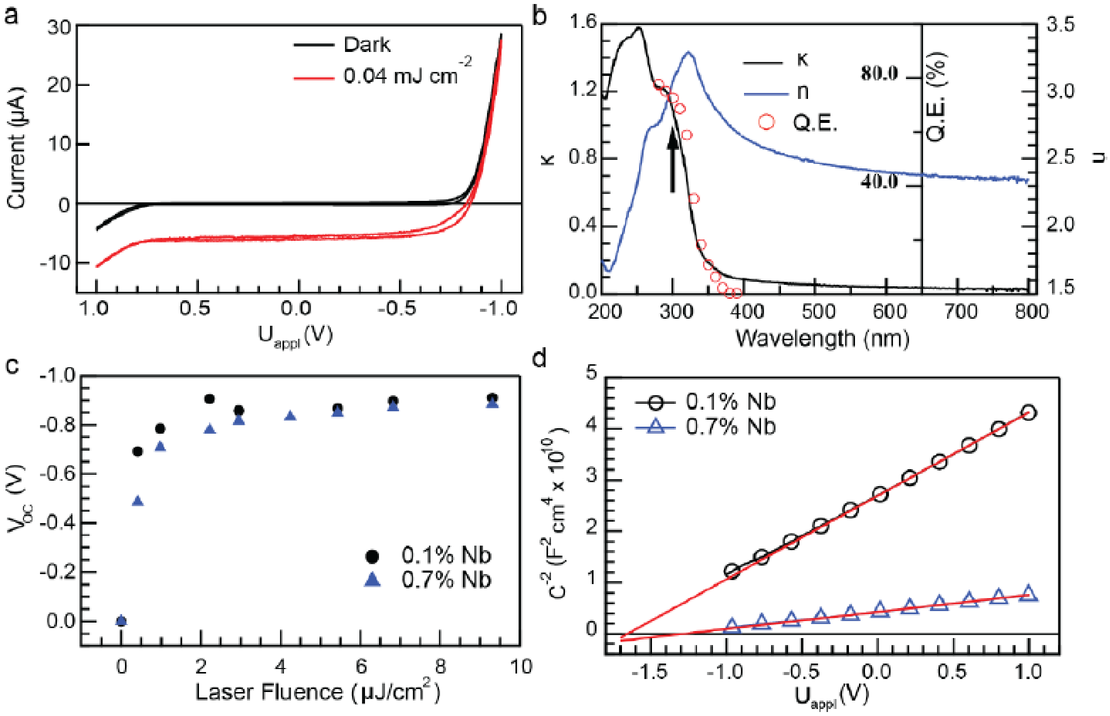

ductor/electrolyte interface. Figure 4.3 showcases measurement results of several such techniques including cyclic voltammetry 4.3a, ellipsometry 4.3b, open-circuit photovoltage 4.3c, and impedence vs potential 4.3d. Cyclic voltammetry (CV) involves monitoring current through the TMO while scanning the electric potential across the diode. Results of a CV measurement collected on 0.1% n-doped $SrTiO_3$ are shown in Figure 4.3a with above bandgap excitation using a laser fluence of 0.04 mJ/cm^2 (light-on measurement, red curve), and in the dark (black curve). The red curve clearly shows current due to photoexcitation, even at zero potential. This is a result of efficient charge separation by the pump within the depletion region. Both dark and light-on curves show typical diode behavior; current will be essentially independent of potential until a certain breakdown voltage is reached, after which current flows virtually resistance free. For cathodic voltages more negative than -0.085 V, the built in electric field that separates electron-hole pairs has decreased in width such that photocurrent no longer evolves. For anodic potentials, the depletion width is at a maximum, and therefore current is independent of potential.

Ellipsometry data, collected on n-doped $SrTiO_3$, shows the real n, and imaginary k parts of the refractive index, and is plotted in Figure 4.3b. Since k corresponds to light absorption, it is of more interest for this study. From the plot, we see that at higher wavelengths there is minimal light absorption across the visible region. Then, absorption increases dramatically as we approach the $SrTiO_3$ bandgap at 3.25 eV. The quantum efficiency Q.E. of charge separation is also included in the plot Figure 4.3b. Q.E. is defined as the ratio of photo-induced charges to the number of photons absorbed, and closely follows k. To determine quantum efficiency, we first determine the number of incident photons P. This is calculated using the laser fluence F, repetition rate of the laser R, the laser spot size A, the photon energy E, and a factor accounting for losses of pump energy at the sample cover glass L

$$P = \frac{F \cdot R \cdot A \cdot L}{E}. \tag{4.4}$$

Next, the number of free charges is calculated using the difference between the current under photoexcitation I_L and in the dark I_D, divided by the electron charge e

$$N = \frac{I_L - I_D}{e}. \tag{4.5}$$

Q.E. is calculated as

$$Q.E. = \frac{N}{P} \cdot 100, \tag{4.6}$$

and is often expressed as a percentage. For the experimental parameters in this study, Q.E. is calculated as 70% or more. This high quantum efficiency is due to $d < W$ as described in Section 4.1.

Open-circuit photo-voltage measurements on 0.1% and 0.7% n-doped $SrTiO_3$ as a function of laser fluence are shown in Figure 4.3c. These measurements are of the change in voltage across the TMO in open circuit after photoexcitation, driving electrons to the back of the sample and holes to the front. This voltage saturates with respect to pump fluence at -0.85 V as shown in in Figure 4.3c, close to the onset of anodic photocurrent in Figure 4.3a. Once sufficient laser fluence has been applied to separate enough charge to flatten the bands, increasing laser fluence will no longer increase charge separation. This measurement reflects the voltage that must be applied to counteract the built in electric field and flatten the bands; i.e. it is a measurement of V_{SC} in Figure4.1a.

Figure 4.3d shows Mott-Schottky plots for n-$SrTiO_3$ at 0.1% and 0.7% doping. These plots show inverse capacitance squared C^{-2} as a function of applied potential U_{app}. This is plot is derived through impedance-potential measurements. Total capacitance of the system will be due to capacitance of the semiconductor, and the capacitance of the Helmholtz layer. Electrical impedance has an inverse linear relationship with capacitance and the frequency of the current through the system. Since the capacitance of the semiconductor itself is expected to depend on U_{app}, both the applied potential and the frequency of the alternating current are varied. Each potential bias at which this measurement is performed yields a data point in Figure 4.3d. The relationship between C^{-2} and U_{app} is described by the Mott-Schottky equation

$$\frac{1}{C^2} = \frac{1}{C_H^2}[1 + \frac{2C_H^2}{q\epsilon N_d}(U_{app} - U_{FB} - \frac{kT}{q})] \tag{4.7}$$

which is derived by de Gryse [40]. Equation 4.7 relates the total capacitance of the system to U_{FB}. This capacitance is also a function of the doping density N_d, the applied potential U_{app}, and the capacitance of the Helmholtz layer C_H. The Helmholtz layer is a model [27] that describes the electric double layer (EDL) by treating the electric field screening the electrode as arising from 2 parallel plates of charge: one being the charge on the electrode, the other being the charge of ions in the electrolyte. The potential distribution across the Helmholtz layer is often considered as 2 separate layers. The inner Helmholtz later consisting of ions adsorbed directly on the TMO surface (H^+, OH^-) [27]. The outer layer is comprised of free ions (OH^-, SO_4^-, PO_4^-) and oriented dipoles at the interface which screen the positive charge in the depletion region of the TMO. Equation 4.7 treats the Helmholtz layer as a single capacitance C_H. To model the data in Figure 4.3d, one assumes $C_H = 20\mu F/cm^2$ [34], and N_d can be extracted from the slope of the linear fit, with U_{FB} extracted from the intercept.

Cyclic voltammetry and open-circuit photo-voltage measurements are also performed as a function of pH. These measurements provide understanding of how U_{redox} and V_{OC} change with the changing hydration layer as Ti-OH^- dipoles increase in population with growing pH. Cyclic voltammetry data on n-$SrTiO_3$ at pH 7 and 13 is shown in Figure 4.4a. At pH 13, the cathodic current has an onset that is more cathodic (negative) than at pH 7, indicating a change in U_{redox} with pH. In Figure 4.4b, the cathodic current onset along with open-circuit photo-voltage data are plotted against integer pH steps between pH 7 and 13. From this data we see V_{OC} (black dots) change with a slope of -45mV/pH, with U_{redox} (gray dots) following closely. On high quality TiO_2 surfaces, a value of -59mV/pH is found for the movement of the flatband potential [41], the potential at which there is no depletion layer across the semiconductor U_{FB}. For such high quality surfaces, U_{redox} is expected to scale with U_{FB} because the surface deprotonates via full proton transfers to solution [27, 38]. This change in potential with pH reflects the change in free energy cost for transferring a proton from the surface into solution, as described by the equilibrium condition 2.2.

Figure 4.4: Dark and light-on CV data at pH 7 and 13 (a). Open-circuit photo-voltage and CV current onset voltage collected at integer steps from pH 7 to 13 (b).

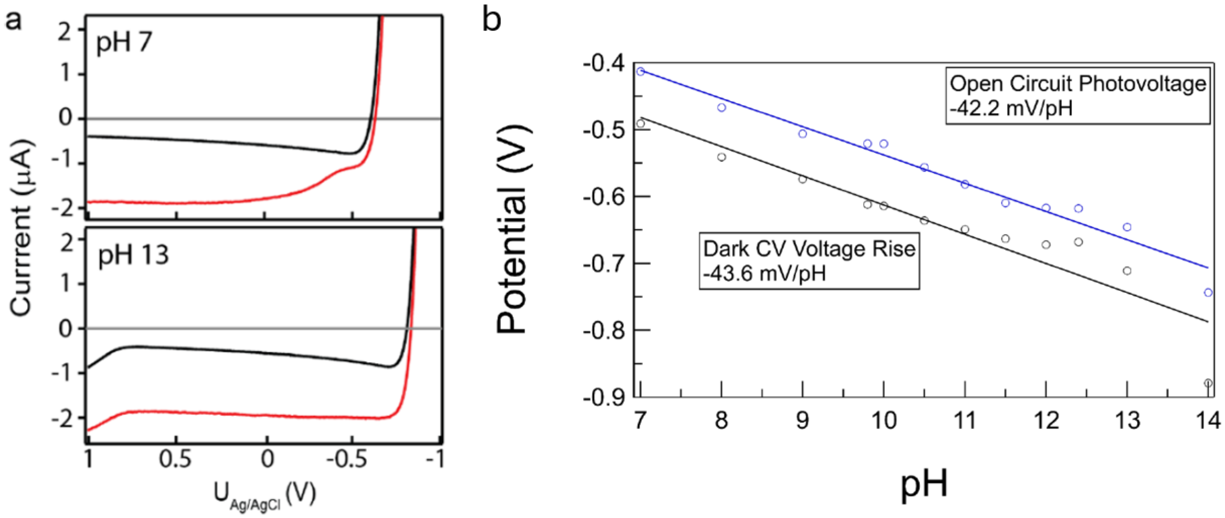

4.3 Steady-state photocurrent

Photocurrent through the electrochemical cell is monitored during transient reflectance measurements. The current is averaged over several repeats (Figure 4.5A) as a function of acquisition time and is then plotted as a function of time delay (Figure 4.5C). The stability of the current during data collection is reflected by a standard deviation of the current for each pH condition of 0.01 μA or 0.05%.

Photocurrent and quantum efficiency (Q.E.) are plotted against pH for an unbuffered electrolyte solution Figure 4.5B and for phosphate buffered solutions at several different doping densities of $SrTiO_3$ Figure 4.5D. Steady state current in phosphate buffered solutions possess a sigmoidal dependence on pH, leading to a 9.8% change between pH 7 and 13. The most likely origin of this is that under certain conditions the O_2 evolution recalls the pH-dependent surface coverage of Ti-OH* as will be developed in Chapter 6. This effect is limited to $\sim$ 10% and the unbuffered solutions do not exhibit such a clear pH dependence.

Figure 4.5: A) Raw current; B) average current and its standard deviation vs pump-probe delay; C) average current/Q.E. vs pH in phosphate-buffered and sulfate-unbuffered conditions, D) average current/Q.E. vs sodium ion concentration in two unbuffered pH conditions in Na_2SO_4. The phosphate buffered data is shown for all three STO samples: 0.1%, 0.5%, and 0.7% Nb doping.

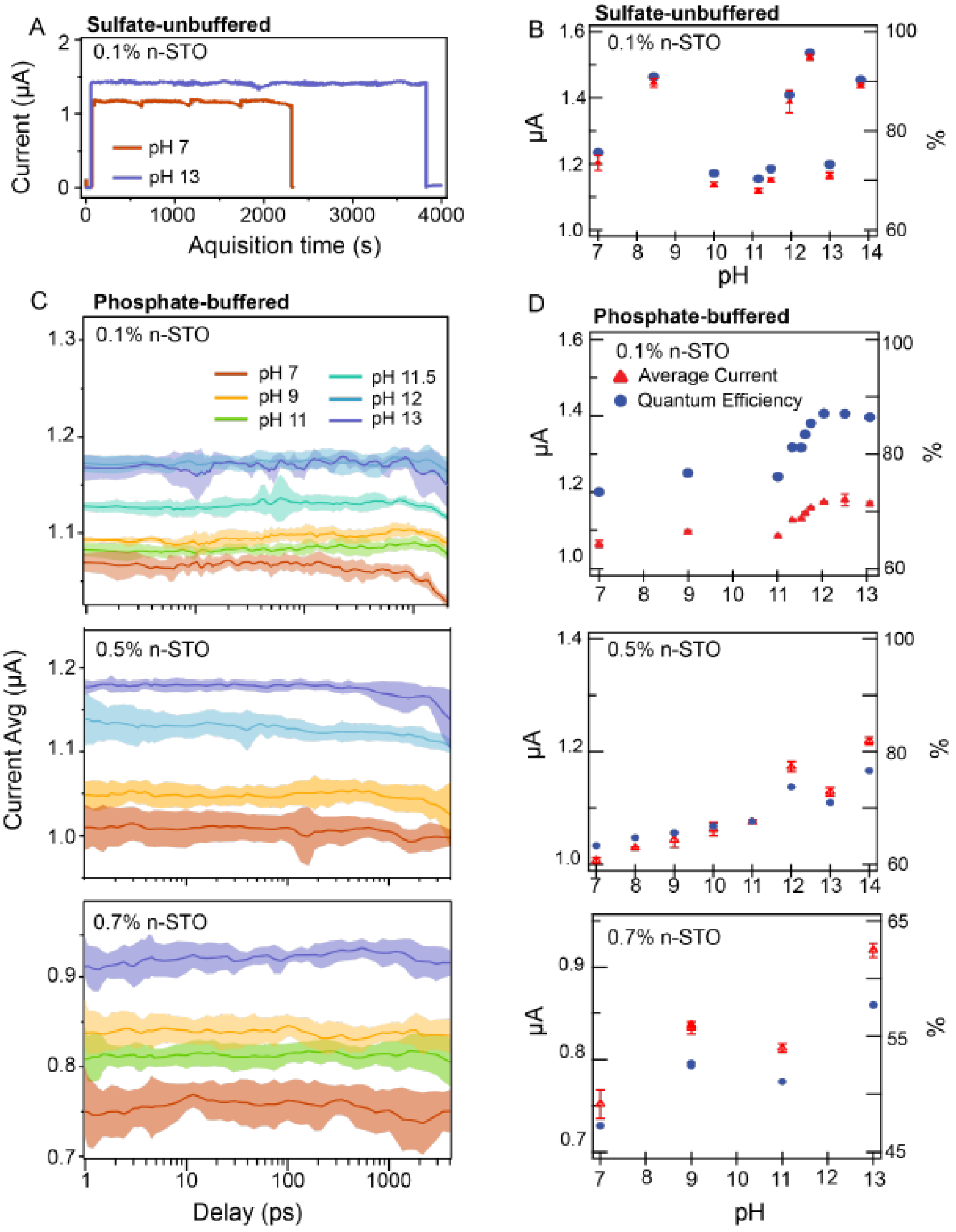

4.4 Sample Surface Degradation

When OER is driven by pump excitation, chemical changes occur on the sample surface at the site of optical pumping [42]. The chemical changes on the surface (surface degradation)

Figure 4.6: Changes in reflectivity with acquisition time a) and transient kinetics at 400 nm with delay b) due to surface restructuring. Collecting data on a single spot for 90 seconds at a time (red trace) results in a decreased reflectivity of the surface a), and an increase in the magnitude of the transient signal b) due to surface restructuring. Scanning across the sample surface at continuous speeds of 7, 14, and 28 μm/s (green, purple, and blue curves) minimizes changes on sample reflectivity a), and at sufficient speed, eliminates changes in transient data shown by the convergence of the curves in b), as we approach 28 μm/s. The static scan data collected at 90 s/spot agrees with the converged continuous scan data each time collection moves to a new spot on the sample.

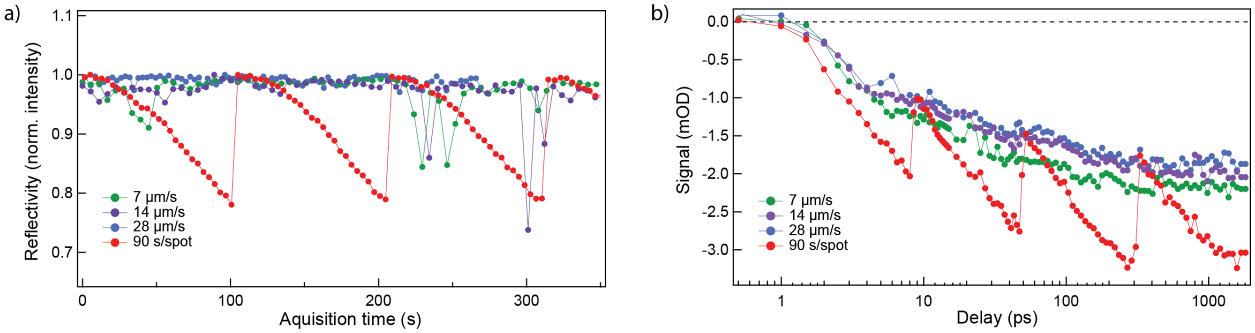

are evident through changes in reflectivity of the broadband probe, as well as changes in the pump/probe spectrum. Experiments have been carried out to determine how long a single point on the sample surface can be exposed to an above bandgap pump in closed circuit before such changes are evident [28]. Key results of these experiments, shown in Figure 4.6 demonstrate that the sample can be pumped at 0.04 mJ/cm^2 for at least 5 seconds, which is the standard fluence and time for which a single spot is pumped, before degradation effects contribute to the signal.

Figure 4.6 shows the sample reflectivity as a function of acquisition time (Figure 4.6a), and the transient signal at 400 nm as a function of pump-probe delay Figure (4.6b) when the sample is pumped at a single spot for 90 seconds (red trace) vs. when the pump is continuously scanned across the sample. These traces demonstrate how surface restructuring affects our data. By increasing scan speed across the sample, the transient data converge to a common trace, which is tracked by the static scan at each new spot. This indicates that restructuring effects can be avoided by collecting each delay at a new spot on the sample surface. To achieve this, the sample itself is mounted onto a translation stage controlled by ThorLabs APT precision actuators. Each data point consists of 5000 probe pulses (2500 averaged pump on/off pairs) and corresponds to a specific pump-probe delay. After each data point is collected, the pump is blocked by a shutter until the sample stage has moved to the proper location for collection of the next data point. Movement of the sample stage is done in a raster scanning motion as shown in the diagram in Figure 3.12.

4.5 TMO Samples

TMO samples are obtained from Crystek Crystals Corporation and Shinkosha crystals. Both $SrTiO_3$ and TiO_2 crystals are 10mm x 10mm x 0.5mm and are polished on one side. The polished side of the sample is reflective and is thus the side on which data is collected. The unpolished surface on the rear of the sample is hardwired to the electrochemical circuit. To achieve this a copper wire is attached to the rear face of the TMO with epoxy. A gallium-indium eutectic is used to ensure a robust electrical connection between the copper wire and the sample. The rear and sides of the sample are sealed with epoxy to keep all surfaces of the sample dry except for the polished front, where data is collected. An insulating coating of liquid electrical tape is then applied to the outside of the dry epoxy and the wire to prevent any unwanted electrical contact between the electrolyte and rear of the sample or the wire. The insulated sample is then mounted in a custom designed sample cell in which the polished sample surface is in electrical contact with the electrolyte and the reference and counter electrodes.

Chapter 5

Technical TR

This chapter will cover several of the technical aspects of the experimental setup and data analysis procedure that are critical to acheiving the results discussed within this document. Section 5.1 is dedicated to a data analysis technique called singular value decomposition (SVD), which is instrumental in reaching the results in Chapter 6, 7, and 8. Successful data collection requires that the experiment recognizes specific laser pulse combinations. A description of how this is achieved is in Section 5.2. Several different laser systems and signal delay generators are used in the experiment, which all contain clocks that do not operate on consistent time bases. The experiment is thus set up to operate on a common clock from the main laser seed; this is described in Section 5.3.

5.1 Singular Value Decomposition

Analysis of time resolved optical spectra in a quantitative way is not a straightforward process. Spectral features are generally broad and result from different molecular processes, which will have different time sales. In order to isolate these processes and study their spectral and kinetic properties on their own, a technique called constrained singular value decomposition (SVD) is employed. This technique is a critical data analysis tool that is used in the studies described in Chapters 6, 7, and 8 of this thesis. It is therefore described in detail as a vehicle for principle component analysis.

Singular Value Decomposition (SVD) analysis is the factorization of any matrix M into the form $U \cdot S \cdot V^T$, where U and V are square unitary matrices and S is rectangular diagonal. The diagonal entries of S are referred to as the singular values of the decomposition. SVD of a dispersed time resolved spectrum can be thought of as the sum spectral components, multiplied by their associated kinetic components, and weighted by their corresponding singular values. Stating this mathematically, the dispersed TR spectra, with frequency along the columns and time delays along the rows can be decomposed as follows:

$$\boldsymbol{M}^{(pH)} = \boldsymbol{U}^{(pH)} \cdot \boldsymbol{S}^{(pH)} \cdot (\boldsymbol{V}^{(pH)})^T = \sum_k s_k^{pH} \boldsymbol{U}_k^{(pH)} (\boldsymbol{V}_k^{(pH)})^T. \tag{5.1}$$

Here the columns of $\boldsymbol{U}^{(pH)}$ and $\boldsymbol{V}^{(pH)}$, designated by $\boldsymbol{U}_k$ and $\boldsymbol{V}_k$ represent the 1D spectral and kinetic components of the decomposition at the reaction condition designated by (pH) (The pH will be the reaction condition varied through several of these studies, but this will not always be the case).

SVD is unique in rank 1 decompositions in that it is required that square matrices $\boldsymbol{U}^{(pH)}$ and $\boldsymbol{V}^{(pH)}$ form an orthonormal basis, as indicated by the right most expression in Equation 5.1, and that the spectral and kinetic components are ordered by decreasing singular value. Since the singular values serve as component weights, only spectral and kinetic components with large

Figure 5.1: Singular values s_k from the SVD of a pH dependent data set collected at a ps-ns time scale. a), along with their spectral b) and kinetic c) components. Singular values are plotted as a function of index k and are thus in descending order. The first two singular values from all data sets are far greater than those that follow, indicating that the data can be well represented by the first two SVD components.

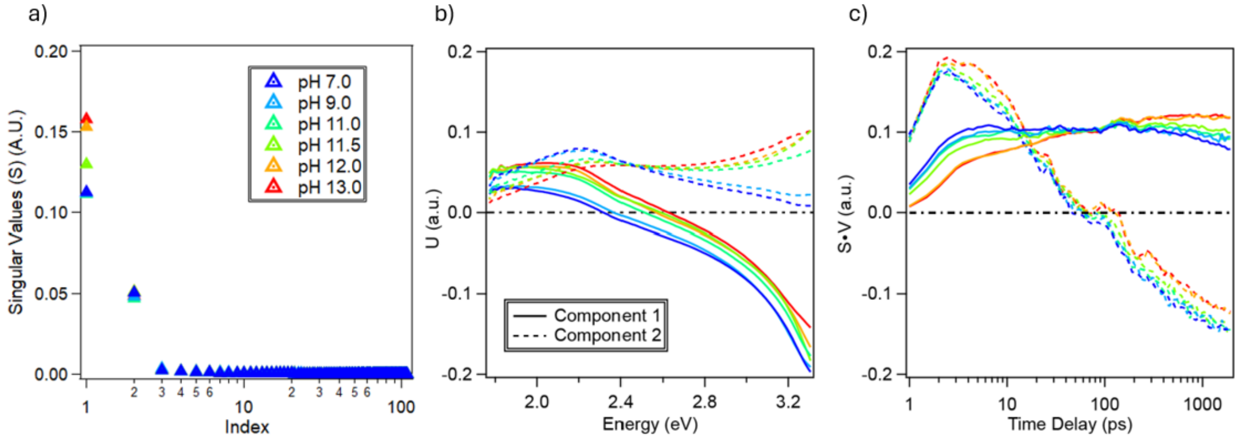

singular values will contribute significantly to the time resolved spectrum from which they were derived. Singular values from a pH dependent TR data set plotted as a function of index k are shown in Figure 5.1a. Plotting the singular values in this way allows for determination of the number of singular values needed to represent the data set thoroughly. From the plot in Figure 5.1a, it is evident that this particular data set is well represented by the first 2 SVD spectral and kinetic components shown in Figure 5.1b and 5.1c. This means that the sum in Equation 5.1 can be truncated at $k = 2$ while still preserving all key information contained in that original data sets:

$$\boldsymbol{M}^{(pH)} = \boldsymbol{U}^{(pH)} \cdot \boldsymbol{S}^{(pH)} \cdot (\boldsymbol{V}^{(pH)})^T \approx \sum_{k}^{2} s_k^{pH} \boldsymbol{U}_k^{(pH)} (\boldsymbol{V}_k^{(pH)})^T. \tag{5.2}$$

To demonstrate that data from this set can be thoroughly represented by the first 2 SVD components, an example is shown below in Figure 5.2.

In general, the spectral components obtained from SVD of the dispersed TR spectra do not yet correspond to spectra of any given species. Ideally, if an entire dataset can be described by different kinetics of the same species as a function of the reaction condition (e.g. pH), the two dominant spectral SVD components from one reaction condition can be transformed from

Figure 5.2: Data showing time-resolved spectra of pH 13 data a), and pH 13 data reconstructed from its first two SVD components b). The reconstructed data shows all the keys features of the original data set, indicating that the first two components contain all the key information from the original data set.

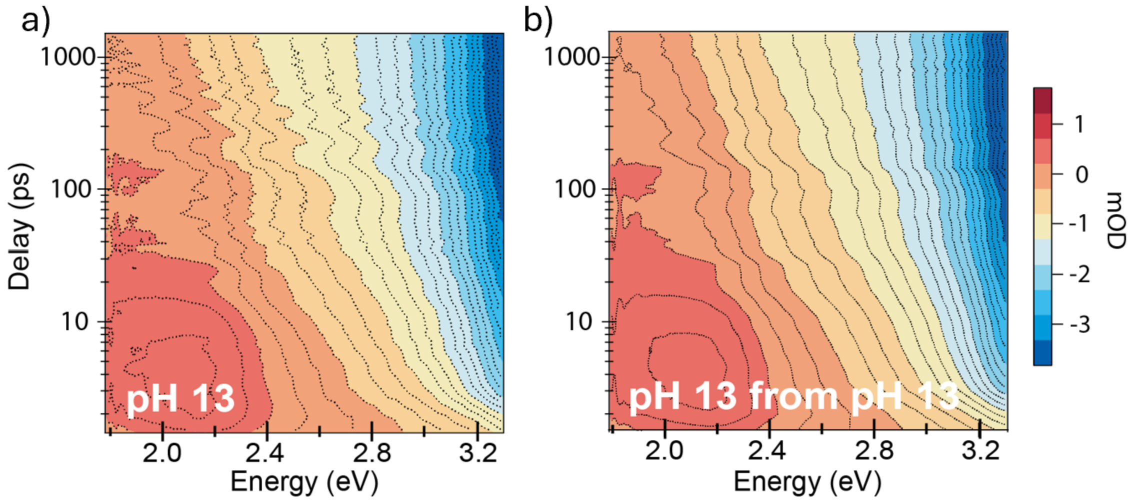

another one using a rotational transformation matrix, when appropriate reflections are taken into consideration. In this scenario, the rotation matrix can be obtained by employing a pseudoinverse, as shown in Equation 6.4:

$$\boldsymbol{R_{ij}} = (\boldsymbol{U}_{1,2}^{(pHi)})^T \boldsymbol{U}_{1,2}^{(pHj)} \approx \begin{bmatrix} \cos\theta_{ij} & -\sin\theta_{ij} \\ \sin\theta_{ij} & \cos\theta_{ij} \end{bmatrix} \tag{5.3}$$

Here, θ_{ij} represents the angle of rotation between the pair of spectral bases in the two-dimensional subspace. In practice, minor deviations in R_{ij} from being a pure rotational matrix can be attributed to noise and systematic errors between the TR spectra.

The SVD components as they are have no physical significance, i. e. they do not represent spectra from any specific population. However, the SVD decomposition itself is non-unique, meaning it can be be represented using a different spectral basis. The orthonormal pairs of spectral and kinetic basis vectors obtained from SVD span a two-dimensional subspace on which the spectrally relevant basis vectors lie. Linear combinations of SVD component vectors can thus be used to produce a physically relevant spectral basis. If different reaction conditions can be described by different kinetics, while maintaining common spectral components, these spectral components are the basis spectra for the data set, and the populations which contribute to each basis spectrum are described by the kinetics. Establishing a spectrally relevant basis is known as constraining and results in the constrained SVD for the data set. The constraining operation is performed by inserting a matrix $\boldsymbol{X}$ and it's inverse $\boldsymbol{X}^{-1}$ into the SVD product:

$$\begin{aligned} \boldsymbol{M}^{(n)} &= \boldsymbol{U}^{(n)} \cdot \boldsymbol{S}^{(n)} \cdot (\boldsymbol{V}^{(n)})^T \\ &= \boldsymbol{U}^{(n)} \cdot \boldsymbol{X}^{(n)} \cdot (\boldsymbol{X}^{(n)})^{-1} \cdot \boldsymbol{S}^{(n)} \cdot (\boldsymbol{V}^{(n)})^T \\ &= \boldsymbol{U}^{(t)} \cdot (\boldsymbol{V}^{(t)})^T \end{aligned} \tag{5.4}$$

where $\boldsymbol{U}^{(t)} = \boldsymbol{U}^{(n)} \cdot \boldsymbol{X}^{(n)}$ are the constrained spectra and $(\boldsymbol{V}^{(t)})^T = (\boldsymbol{X}^{(n)})^{-1} \cdot \boldsymbol{S}^{(n)} \cdot (\boldsymbol{V}^{(n)})^T$ are the constrained kinetics for the n^{th} data set. The constraining matrix is defined as

$$\boldsymbol{X} = \begin{pmatrix} a(n) & \alpha(n) \cdot b(n) \\ \beta(n) \cdot a(n) & b(n) \end{pmatrix} \tag{5.5}$$

such that

$$a(n)^2 + a(n)^2 = b(n)^2 + b(n)^2\alpha(n)^2 = 1. \tag{5.6}$$

In Equation 5.5, $a(n)$ and $b(n)$ are normalization factors defined by the condition in Equation 5.6. The parameters $\alpha(n)$ and $\beta(n)$ are determined by manual tuning during the constraining process.

The process of tuning the constraining parameters $\alpha(n)$ and $\beta(n)$ is a feedback loop designed to generate an appropriate spectral basis. An appropriate spectral basis in one that is physically relevant, and allows the kinetics to describe the changing population of a spectrally active species that is characterized by the spectral basis. In several of our data sets, this means choosing one spectral component to be completely absorptive (positive), and one to be completely emissive (negative). This is not the case for all data sets; the key defining limitation is that the kinetics be completely positive such that they describe the population of the species contributing to their associated spectra. In the example shown in Figure 5.3 below, the spectra are being constrained to be strictly absorptive/emissive. The data demonstrates how the spectral traces change as $\alpha(n)$ and $\beta(n)$ are tuned. This process is performed at each reaction condition in the given data set, and the resulting spectra are averaged to generate the basis used to represent the data set in constrained SVD analysis.

Spectral bases for all data sets are normalized such that changes in populations (reflected in signal magnitude) are accurately described by changes in the kinetics. This change can take the form

Figure 5.3: Examples of generating a spectral basis by tuning parameters α and β for pH 7 and 13 data sets. In this example, the goal is to create a basis such that one spectral component is entirely absorptive, the other entirely emissive. This process is done for all data points (which in this case correspond to pH), to achieve a similar spectrum for each data point. The resulting spectra are averaged, then used as the basis to represent the data in constrained SVD analysis.

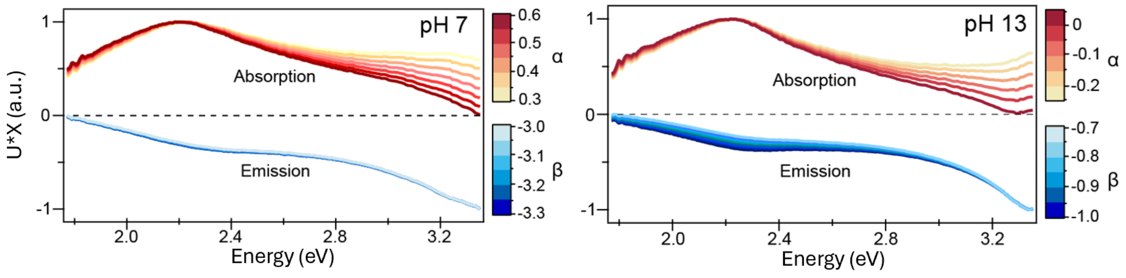

of different kinetic behavior at different reaction conditions, or a change in the overall magnitude of the kinetic signature. Constrained SVD in this sense is a principle component analysis, the principle components being the basis spectra, whose dependence on time and reaction conditions are contained within their associated kinetics.

5.2 Synchronization of Cameras with Laser Pulse Combinations

Collecting time-resolved pump-probe spectra or FSRS spectra requires the synchronization of the data collection and referencing cameras with the arrival of specific light pulse combinations. The camera used in these experiments is a Princeton Instruments Pixis, which is set up for external triggering during data acquisition. The experimental software is set up such that for each data point, the automation program requests a specific number of frames from the camera, which are provided when the camera receives a trigger signal. This provides synchronization with the 1 kHz pulse train from the main laser, but misses a critical part of the synchronization. For transient reflectance measurements, every other 'shot' from the kHz pulse train is a 'pump on' shot, the rest being 'pump off' shots. Without a way for the data collection program to recognize 'on' vs. 'off' shots, each collected set of frames will produce data sets with a random sign flip at each delay. The problem becomes more complicated when FSRS experiments are being conducted; Table B.1 shows that there are 4 unique pulse combinations that must be distinguished for successful data processing to be consistent for each data point. More specifically, there must be a way for the software to designate a 'shot 1' from the laser pulse sequence, based on the signals associated with the experimental timing. Without this distinction, each data point in a FSRS experiment would begin on a random pulse combination shown in Table B.1 and data analysis would be unmanageable. Therefore successful implementation is needed for ease of data analysis for the projects in Chapters 6, 7, and 8, and is absolutely necessary for analysis of data in Chapter 9. This method must not only be reliable, but should be easily transferrable between TR and FSRS data collection schemes.

The signal which possesses a distinctive feature with regard to which laser pulse should be designated 'shot 1' is the optical chopper signal output. The optical choppers are triggered with a signal that corresponds to the master clock signal of the experiment (ultimate source of this signal is the main laser system). The set frequency of the optical choppers (500 Hz for TR pump, 250 Hz for Raman pulse) is calculated from this main trigger signal. The phase of each optical chopper is tuned such that the pulses meant to blocked are blocked completely, and those meant to pass through are done so undisturbed. The controllers for the optical choppers have an output waveform which indicates the phase and frequency of the choppers themselves. The rising edge of this waveform is the signal that is used to determine 'shot 1' for both series of pulses (TR and FSRS). This, along with several other signals are used as inputs to an Arduino program that controls the trigger input to the data collection camera. These signals, the Arduino program and corresponding pseudo-code can be found in Appendix A.

5.3 Longtime Laser Timing and Synchronization

5.3.1 Timing Jitter in Main Laser

The fundamental pulse from our laser system is an 800 nm fs scale pulse, which is amplified by a Coherent Legend chirped-pulse amplifier. The seed for this amplifier is produced by a laser termed the 'Vitesse', which operates at 80 MHz. A signal delay generator (SDG) that is part of the OEM laser system, uses an internal clock to operate the amplifier q-switch. The programming of this SDG is such that it will choose a seed pulse to trigger the q-switch based on maintaining an output frequency as close to 1 kHz as possible, based on its own internal clock. Since the SDG clock does not exactly agree with the time-base of the 80 MHz Vitesse, some phase and frequency jitter is introduced by this process. When all pulses relevant to a given experiment are derived from the same amplifier output, this is not a problem, since the relevant delay between such pulses is established independently of this frequency jitter. However, this does pose a problem when creating pump-probe delays using a separate electronically triggered laser system as an optical pump. Long-timescale data is collected using an electronically triggered laser system that is separate from the main Coherent laser system. This is necessary for the work presented in Chapter 7 since μs scale time delays cannot be achieved with a mechanical delay stage inside a typical laboratory.

A positive pump-probe delay is defined as the pump arriving at the sample before the probe. However, the pump must be triggered from a signal originating from the main Coherent laser system; this means that in order to establish a positive pump-probe delay, we must define the delay with respect to previous pulse from the main laser system as shown in Figure 5.4. Timing jitter will thus result in incorrect pump-probe delays as shown in Figure 5.4. The intended pump-probe delay in the example shown in Figure 5.4 is 200 μs. To achieve this delay, an 800 μs delay must be programmed into the longtime laser, since the delay is defined with respect to the previous 1 kHz pulse. The timing jitter will regularly result in inaccurate delays as the Coherent SDG selects different seed pulses to time the q-switching. The example in Figure 5.4 presents a situation that results in a higher than desired pump-probe delay.

Figure 5.4: Frequency and phase jitter in the fundamental laser system. This timing jitter results from the laser SDG selecting 80 MHz seed pulses based on q-switch operation as to 1 kHz as possible based on its own clock frequency. This is important because triggering for the longtime laser is such that the pump-probe-delay is defined based on the pulse prior to the "on" shot in the kHz cycle. In the example below, a programmed delay of 800 μs results in a pump-probe delay of 200 μs. The timing jitter will produce occasional pulse sequences that result in an inaccurate pump-probe delay. The example below shows a pump-probe delay that is greater than the expected 200 μs.

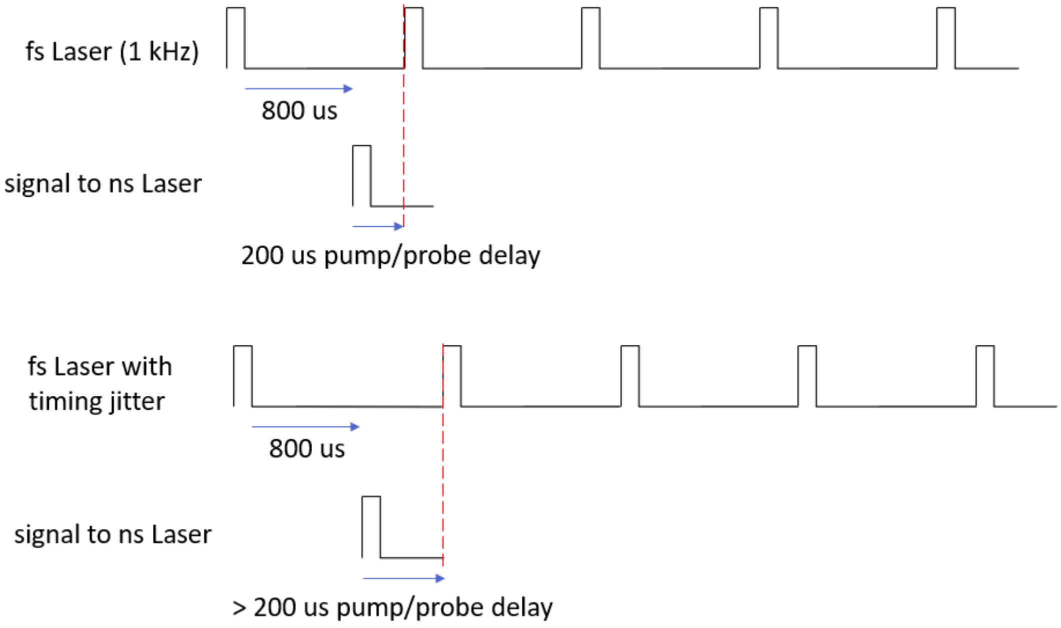

To overcome this problem, the timing of q-switch is done with an external trigger that is generated from the 80 MHz timing signal from the seed laser. Using a Stanford Research Systems DG645 Digital Delay Generator (SRSDG645) to divide the 80 MHz signal down to 1 kHz. The resulting pulse train is used as an external q-switch trigger to our laser system, and becomes the time base for the entire experiment. This eliminates the timing jitter, and produces reliable pump-probe delays for the longtime scale laser.

5.3.2 Electronic Trigger Using an External Delay Generator

A pulse width of 1 μs is required to trigger the output of the longtime laser used to collect data presented in Chapter 7. This trigger is supplied using an SRSDG645 delay generator, which has a time base directly synchronized to the q-switch trigger. One feature of the SRSDG645 is that all output signals must be resolved by the time the next trigger pulse arrives; if not, then this trigger pulse will be ignored. This means that for any pump-probe delays less than 1 μs, the pump trigger will interfere with the master clock signal for the experiment.

Figure 5.5: Relevant pulse trains for triggering of the longtime UV pump laser. A master clock signal is directed into SRSDG546 #2, which is programmed to produce delays for the longtime laser. Pulse width for the trigger to the longtime laser is 500 μs, and all delays are based on 1 ms, ensuring that every other trigger pulse is ignored while the outputs are resolved. The programmed delay is equal to the desired pump-probe delay subtracted from 1 ms.

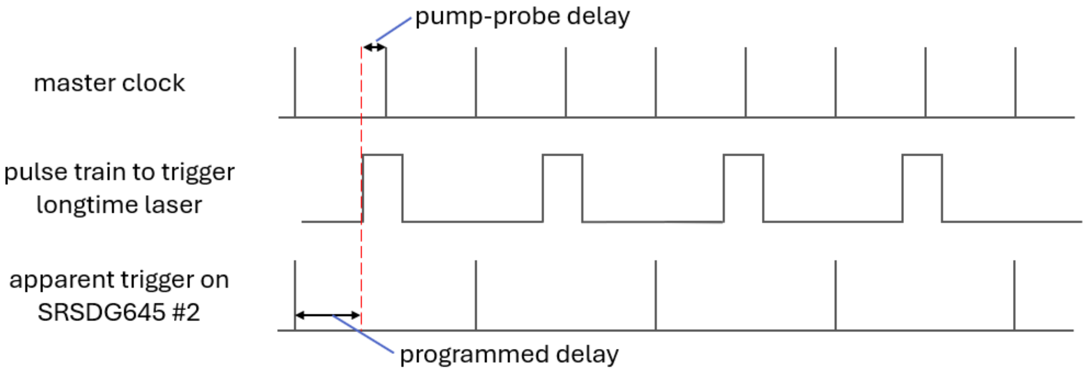

The solution to this problem is introducing a second SRSDG645 to provide the trigger for the longtime laser. The master clock signal from the first SRSDG645 is fed into the second, from which pump-probe delays are generated and sent to the longtime laser. The SRSDG645 will ignore any trigger that occurs before all outputs are resolved; this feature is used to divide the kHz signal down to 500 Hz, the desired repetition rate for the optical pump. Then, delays are based on an offset of 1 ms, and the pulse width of the trigger is 500 μs, which corresponds to the delay range for longtime measurements, so that every other trigger pulse to the second SRSDG645 is ignored, resulting in a 500 Hz pulse train to trigger the longtime laser. Pulse width is a preset parameter within the SRSDG546, and the delays are sent to the SRSDG546 via RS-232 from the LabVIEW automation program. The relevant pulse trains for this configuration are shown in Figure 5.5.

Chapter 6

Free energy difference to create the M-OH* intermediate of the oxygen evolution reaction by time-resolved optical spectroscopy

6.1 Original Publication

This work has been previously published as Vinogradov, I., Singh, S., Paolino, M. et al. Free energy difference to create the M-OH* intermediate of the oxygen evolution reaction by time-resolved optical spectroscopy

6.2 Introduction

Catalytic reactions are described by a set of metastable intermediate chemical forms that reorganize reactants into products [4]. Yet, the activity of material surfaces for catalysis has been differentiated largely by their cumulative product evolution, with a primary example being the steady-state current in electrochemical measurements [5]. Given several underlying and separate reaction steps, multiple mechanistic models could explain the same outcome [43–45]. Thus, there exists a need for experiments to access the individual reaction steps [44, 45]. To do so through the free energy differences (ΔG) between intermediates would directly underpin the theory [2] and would provide thermodynamic quantities by which to tailor the material and its environment for desired functionality [46].

One of the most important and studied reactions in this context is the electrochemically driven oxygen evolution reaction (OER) on transition-metal oxide surfaces [6, 47]. The M-OH* intermediate, created upon the first electron and proton transfer from water, is expected to initiate the formation of the first chemical bond of O_2 (O–O), with corresponding free energy differences $\Delta G_1(OH^*)$ and $\Delta G_3(O-O)$ [2,48]. With scaling relationships [3], $\Delta G_1(OH^*)$ becomes a predictive theoretical descriptor of OER activity: when $\Delta G_1(OH^*)$ is large, forming M-OH* is rate limiting, and when it is small, forming the O–O bond is rate limiting. However, to date, these thermodynamic and calculated limitations on O_2 evolution have been compared against experiment using the electrochemical current, which is inherently kinetic.

A series of time-resolved studies of photo-electrochemically driven OERs have isolated the spectral and kinetic signatures of the hole-trapping M-OH* intermediate, including titanium oxyls (Ti-O$^{\bullet-}$ terminal and Ti-O$^{\bullet+}$-Ti in-plane) [49, 50], the cobalt oxo (Co=O) [51] and the iron oxo (Fe=O) [52]. The M-OH* notation is generic for all these intermediates, with H^+ either bound to the oxygen site or having transferred to a nearby one [8, 53]. While vibrational spectroscopies determine these detailed bonding geometries [54, 55], optical spectroscopy [49, 56] revealed easily trackable electronic levels created in the middle of the semiconducting bandgap that target the total population of M-OH*. Using these mid-gap levels, ultrafast optical studies of $SrTiO_3$ (STO) followed the picosecond formation of the Ti-OH* population from delocalized valence band (VB) holes [49] and its subsequent, microsecond decay towards the next reaction step [57].

While such time-resolved studies structurally identified transient surface intermediates and provided insight into their role in the catalytic cycle, comparatively little experimental information exists on their energetics. The difficulty lies in finding a methodology that both isolates the reaction steps and captures their thermodynamic properties [58,59]. In photo-electrochemistry, light excites the reaction instantaneously from a surface prepared by the dark equilibrium with the electrolyte. Therefore, the first proton and electron transfer can be well separated in time, with the proton transfer occurring in the dark and the electron transfer occurring only upon photo-excitation of VB holes:

$$Ti - OH_2 + OH^-(aq) \leftrightarrow Ti - OH^- + H_2O(l) \tag{6.1}$$

$$Ti - OH^- + h^+ \rightarrow Ti - OH^* \tag{6.2}$$

In reaction 6.2, h^+ represents a hole. Using the self-ionization of H_2O into OH^- and H^+, reaction 6.1 can be written with a product H^+ instead. Both reactions equivalently describe the acidity of a water-absorbed Ti site. If one adds an electron at the chemical potential of the delocalized hole to each side of reaction 6.2, the hole-trapping reaction is equivalent to an electron transfer out of the electrode, such that the two reactions net to $Ti\text{-}OH_2 \rightarrow Ti\text{-}OH^* + H^+ + e^-$ where e^- represents an electron.

The first reaction is an explicit equilibrium defined by the free energy difference for surface hydroxylation, ΔG_{OH^-}, or equivalently, the pK_a of $Ti\text{–}OH_2$. The second reaction forms a metastable species, where $\Delta G_{OH^*}(U_{VB})$ is the free energy difference between a hole at the VB edge potential (U_{VB}) and a trapped hole, $Ti\text{-}OH^*$. U_{VB} is utilized since the photo-excited holes are presumed to thermalize to the VB edge before transfer given the inefficiency of hot-hole transfer from bulk semiconductor crystals [60, 61]. By being separable, the surface hydroxylation prior to light excitation can shift the reaction equilibria, which allows our work to identify $\Delta G_1(OH^*)$ by time-resolved optical spectra. In particular, the sigmoidal pH dependence of the picosecond $Ti\text{-}OH^*$ population generates a Langmuir isotherm of a metastable intermediate on the photo-driven surface. For surfaces in which the hydroxylation can be modulated in an accessible pH range, the work closes a vital missing gap between the observation of the kinetics and structure of catalytic intermediates and experimental determination of the energetics of elementary steps. The results show how reaction kinetics, inherent in experimental investigations, can begin to be analyzed with respect to measured, rather than largely theoretical, free energy differences.

6.3 Transient optical spectra of the electrochemical interface

Figure 6.1 shows the primary pH-dependent optical spectra from which we draw our conclusions. The transient data are taken under steady-state conditions of photo-electrochemical O_2

evolution using pulsed (150 fs, 500 Hz) bandgap (266 nm, 4.66 eV) excitation of n-doped STO (n-STO; 0.1%, 0.5% and 0.7% Nb STO) described previously and in detail in Sections 4.1,4.2, and 4.3. Here, the surface is probed by a broad-band optical pulse (375–700 nm, 1.7–3.3 eV). While there is a high quantum efficiency of charge separation (∼75%), side reactions do affect the sample surface. Therefore, to obtain the high-quality kinetic data, we employ a continuous scanning method (Figure 4.6). At a photo-excitation density of 0.04 mJ cm^{-2}, one maintains a constant steady-state current to within 0.5% in a single measurement (Figure 4.5), which corresponds to

Figure 6.1: a), Cartoon of energy level alignments at closed circuit (0 V versus SCE) and at open circuit (OC) on the RHE scale (pH 0) at the solid-electrolyte (white-light blue) interface. The purple block indicates the redox level of M-OH* intermediates for different oxygen binding strengths. The grey open circles represent VB holes. b), Volcano plot of OER theoretical analysis, for which the minimum potential needed to drive the reaction spontaneously is depicted as a function of $\Delta G_1(OH^*)$; strong and weak oxygen-binding branches are denoted. c), Cartoon of the optical transitions induced by Ti-OH* intermediates, leading to emission (blue arrow) and absorption (red arrow). The dashed purple level corresponds to the redox level for creating Ti-OH*, also depicted in a). The absorptive and emissive transitions are vertical ones, which involve states in the CB and VB, respectively, that are at the reaction coordinate of the distorted Ti-O bonds in Ti-OH*; the difference in the blue and red lines reflects that these are separate potential energy surfaces. d), normalized emission and absorption derived by a constrained, singular value decomposition of the optical spectra in e). The black arrow corresponds to the STO bandgap. e), Transient optical spectra of the absorption (red) and emission (blue) in the visible regime for select pH at closed circuit. From the raw data, the acoustic phonon oscillations have been removed (Figure 3.9). The colour scale is the optical density of the measured change in reflectivity (mOD or 10^{-3} OD), positive for absorption and negative for emission. f), Transient optical spectra at open circuit (OC) for pH 7 and pH 13 on the same mOD scale as the closed circuit data.

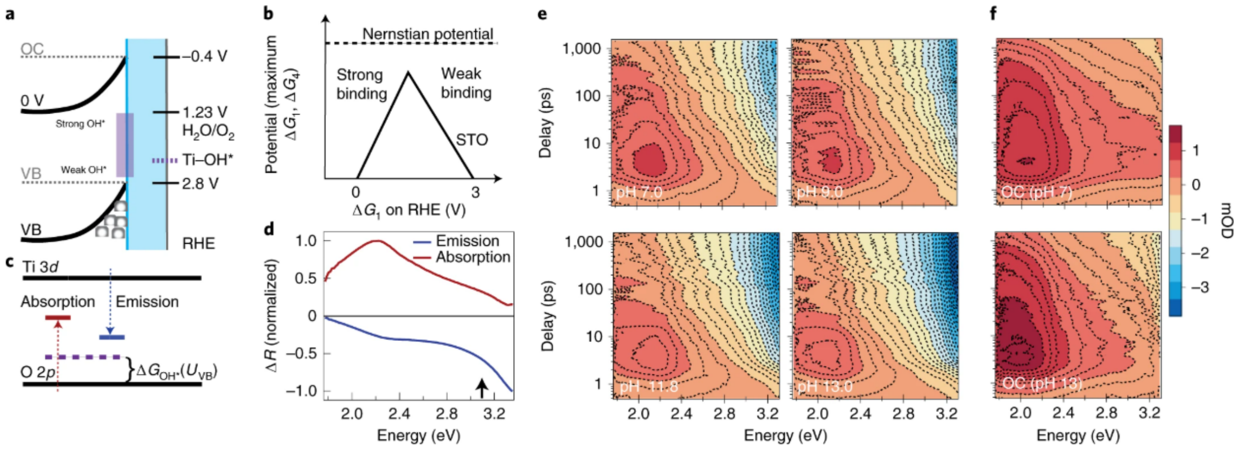

a turnover frequency of ~1 O_2 per site per second of the illuminated area. The cartoon (Fig. 6.1a) shows the level alignment of the valence and conduction bands of STO with the Nernstian potential of water oxidation on the reversible hydrogen electrode (RHE) scale. The primary data are taken with a constant 0 V versus saturated calomel electrode (SCE) applied to the back of the electrode. A constant 0 V versus SCE is chosen to maintain the same potential drop across the part of the electric double layer that involves free ions in the electrolyte (phosphate, sulfate, OH^-, H^+), such that reaction 6.1 can be considered fairly independently of salt concentration (Section 4.1). With this electrochemical configuration, the Schottky barrier will necessarily increase with pH due to the interfacial Ti-OH^- dipole [27] (Sections 4.1 and4.2). Data taken at open circuit aid in the assignment of spectral components and in the interpretation of the pH dependence. Finally, 0.1% Nb and 0.7% Nb STO were characterized for hydroxylation at near neutral conditions by ambient pressure X-ray photoelectron spectroscopy [12] (Section 2.1).

Upon excitation, a delocalized hole in the valence band can relax to create Ti-OH^*. When a hole traps to an oxygen site, the Ti-O distances distort and mid-gap levels form, as described in detail for TiO_2 [8,53] and for STO [49,62,63]. These mid-gap levels are relatable to $\Delta G_1(OH^*)$ by the $\Delta G_{OH^*}(U_{VB})$ of reaction 6.2:

$$\Delta G_1(OH^*) = VB + \Delta G_{OH^*}(U_{VB}). \tag{6.3}$$

The redox level (RHE) corresponding to $\Delta G_1(OH^*)$ for STO is shown schematically in Fig. 6.1a (purple dotted line). The pH dependence of reaction 6.1 is that of the RHE scale (-59 mV per pH unit), which results from a cathodically increasing VB edge due to the interfacial dipole [27]. With equation 6.3, $\Delta G_1(OH^*)$ for different materials can also be placed within the bandgap of STO (purple block, Fig. 6.1a), rising within the gap and lower on the RHE scale for stronger oxygen binding within M-OH^* (volcano plot, Fig. 6.1b).

Emissive optical transitions in the visible regime (blue arrow, Fig. 6.1c, blue emission, Fig. 6.1d) result from conduction band (CB) electrons transitioning to the newly created Ti-OH^* at the distorted reaction coordinate (blue line, Fig. 6.1c). Photoluminescence of STO samples routinely assigns the spontaneous emission peak between 2.4 eV and 2.8 eV to localized holes [62, 64, 65]. The recent transient optical spectroscopy during OER characterized the stimulated emissive optical dipole transitions [49] by a 1.3 ps kinetic growth, which also occurred in the vibrational spectroscopy identifying the titanium oxyl (Ti-O$^-$) [50]. Here, the broad-band probe records this emission in time for lightly doped Nb 0.1% STO as a function of pH (Fig. 6.1e). From these optical spectra, acoustic phonon oscillations have been subtracted out (Section 3.2.5). The emission (blue) appears clearly during in situ OER and increases with higher pH (Figure 6.1e and Figure 3.3) but is independent of salt concentration (Figure B.1); at open circuit conditions for which electrons can more easily recombine with Ti-OH*, the emission is much less pronounced but has the same trend with pH (Figure 6.1f and Figure 3.3) and salt (Figure B.1). Moreover, the emission appears dominantly as a ∼2 ps kinetic growth after the initial excitation, as expected for an exoergic $\Delta G_{OH^*}(U_{VB})$, with the timescale assigned previously [49].

Alongside this emissive transition, an absorptive transition (red arrow, Fig. 6.1c, red absorption, Fig. 6.1d) also exists. We find the absorption to be less sensitive to the Ti-OH* population: the absorption appears most prominently at open circuit, exhibits decay kinetics and is not substantially modulated by surface conditions (pH). An absorptive transition in the visible regime could arise from VB electrons promoted to an excited potential energy surface (red line, Fig. 6.1c) for which the Ti-O distortion is maintained and a VB hole is left behind, as proposed for titania [8] and other transition-metal oxides [10, 66]. A red-shifted absorption to the emission has been attributed to the intermediate population in iron oxide [56] but to the VB hole population in a variety of oxides [34, 67, 68]. Since the proposed absorptive transition is modulated by the VB density of states for hole occupation, a function of both trapped and VB holes, one might expect the kinetics to exhibit a complex interplay of the two populations. By contrast, the CB electron density of states responsible for the emissive transition is independent of the trapped hole population. The anticipated optical transitions are further discussed in Figure 2.4.

6.4 Principle component analysis of the optical spectra

The spectra shown in Fig. 6.1d are the result of a principal component analysis constrained [69, 70] to have a pure emissive component and an absorptive one. We first show how two predominant spectral components exist in common for the full dataset. Singular value decomposition [71] (SVD; Section 5.1) directly yields two dominant components for each reaction condition. If these are common to the dataset, one should be able to reconstruct one reaction condition's optical spectra from a linear combination of the principle components of another, or

$$M^{(pH13)} \approx (U_{1,2}^{(pH7)} \cdot R^{-1}) \cdot S_{1,2}^{(pH13)} \cdot (V_{1,2}^{(pH13)}). \tag{6.4}$$

$M^{(pH13)}$ is a matrix of the spectral-kinetic data at pH 13. The columns of $U_{1,2}^{(pH)}$ and $V_{1,2}^{(pH)}$ are orthonormal and represent the SVD spectra and kinetics, respectively; T denotes transpose. $S_{1,2}^{(pH13)}$ is a diagonal matrix that defines the singular values of the two components. The linear combination matrix is $R = (U_{1,2}^{(pH13)})U_{1,2}^{(pH7)}$. If a common two-component basis exists, R will be a rotation matrix (accounting for reflections).

We show the similarity between the pH 13 dataset reconstructed from its own two SVD components in Fig. 6.2a and the pH 7 SVD components in Fig. 6.2b. The rotation matrix can be calculated for any pair of reaction conditions within a dataset with small error bars. This rotation analysis shows a sigmoidal pH dependence already encoded in the 0.1% Nb STO data by a common basis set without constraints (Fig. 6.2c) and quantifies little dependence of the spectral components on the salt concentration (Fig. 6.2d). It also shows little pH dependence for highly doped (0.5%, 0.7% Nb) STO (Fig. 6.2c).

6.5 Modulating the Ti-OH* equilibrium by pH

While the above establishes that a clear and quantifiable trend in pH exists, it does not in itself assign a spectral component to the Ti-OH* population and its origin from reaction 6.2 photo-excitation (Fig. 6.3a). The undoped STO surface is understood to partially dissociate H_2O at neutral conditions [23, 25, 72], such that approximately half the titania sites are water

Figure 6.2: a) Reconstruction of the pH 13 spectrum from its first two SVD components. b) Reconstruction of the spectrum in a from the spectral SVD components of the pH 7 transient optical spectra. c) Rotation angle analysis for the phosphate-buffered pH dataset showing a sigmoidal trend across pH in 0.1% Nb STO. The angle is given relative to the pH 7 data in solid lines and relative to the pH 13 dataset in dotted lines. Data are shown for all three STO samples (0.1%, 0.5% and 0.7% Nb). d) Rotation angle analysis for the dataset showing little trend with salt concentration for pH 7 (red) and pH 13 (blue) in a) Na_2SO_4/NaOH solution. In both pH 7 and pH 13, the reference spectral components are from the corresponding 100 mM [Na^+] spectral map. For c) and d), error bars indicate the standard deviation of the four angles in the rotation matrix R, which measures how orthogonal the transformation is between the reference and final spectral components.

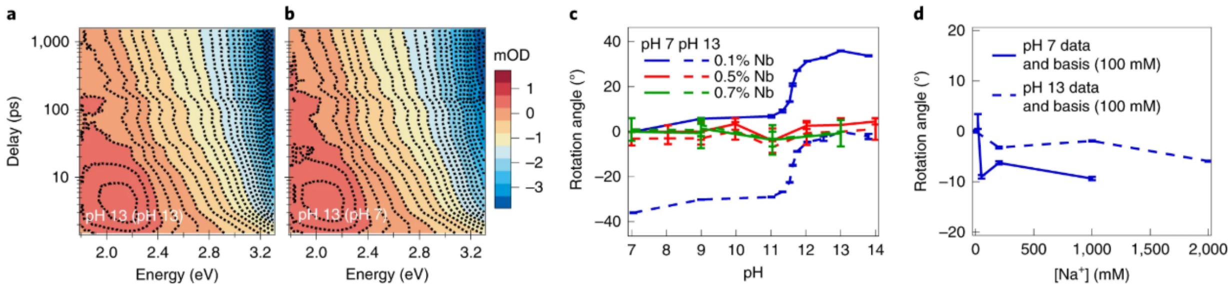

absorbed and half hydroxylated. The lightly doped 0.1% Nb STO surface exhibits a similar ratio of hydroxylation to water absorption by ambient pressure X-ray photoelectron spectroscopy (Section 2.1). Since they are separated by Ti-OH_2 groups, the isolated Ti-OH^- are well positioned to trap holes quickly (reaction 6.2). Further, given the above dichotomy between the emission and absorption, a constrained SVD analysis identifies the rising components of the Ti-OH^* population using

$$M \approx (U_{1,2} \cdot X) \cdot (X^{-1} S_{1,2} (V_{1,2})^T). \tag{6.5}$$

Here, X is a new matrix that describes the projection of the raw SVD components $U_{1,2}$ onto purely emissive (1) and absorptive (2) spectral components. The procedure is outlined in Section 5.1. The emissive spectrum (Fig. 6.1d) increases with shorter wavelengths, which may be related to the probe stimulating electrons closer to the surface. The absorptive spectrum has a peak near ∼2 eV, as identified in a number of other oxides [8, 10, 66].

Figure 6.3b shows the constrained kinetics associated with emission, $(X^{-1} S_{1,2} (V_{1,2})^T)_1$, for each pH at 0 V versus SCE. While the kinetics exhibit consistent growth rates across pH, the kinetics

Figure 6.3: a) Cartoon of the 0.1% Nb STO surface in the dark and upon light excitation, reflecting the two separable proton and electron transfer steps. Red atoms are O, blue atoms are Ti and green atoms are Sr. The Ti-OH- are denoted by black circles, and the orbital of hole trapping on Ti-OH* is yellow. b) Weighted, emissive growth kinetics $(X^{-1}S_{1,2}(V_{1,2})^T)_1$ on an mOD scale as a function of pH (colored diamonds) fit with two rising exponentials (black solid and dotted lines). c) The same as a, but for the weighted, absorptive decay kinetics $(X^{-1}S_{1,2}(V_{1,2})^T)_2$ d) The time constants of the two rising exponentials for the emissive kinetics as a function of pH. e) The populations (A_1, A_2) defined by the two time constants, normalized by the integrated absorption (A_n/Abs), as a function of pH; and the integrated absorptive signal (Abs) as a function of pH. Bottom left:, A_1/Abs is compared for the three n-STO samples, 0.1%, 0.5% and 0.7% Nb, taken on a new optical set-up (Figures B.2,B.3,B.4). These analyses are for data taken at 0 V versus SCE. Bottom right: A_1/Abs is shown for 0.1% Nb STO under OC conditions with sulfate buffer.

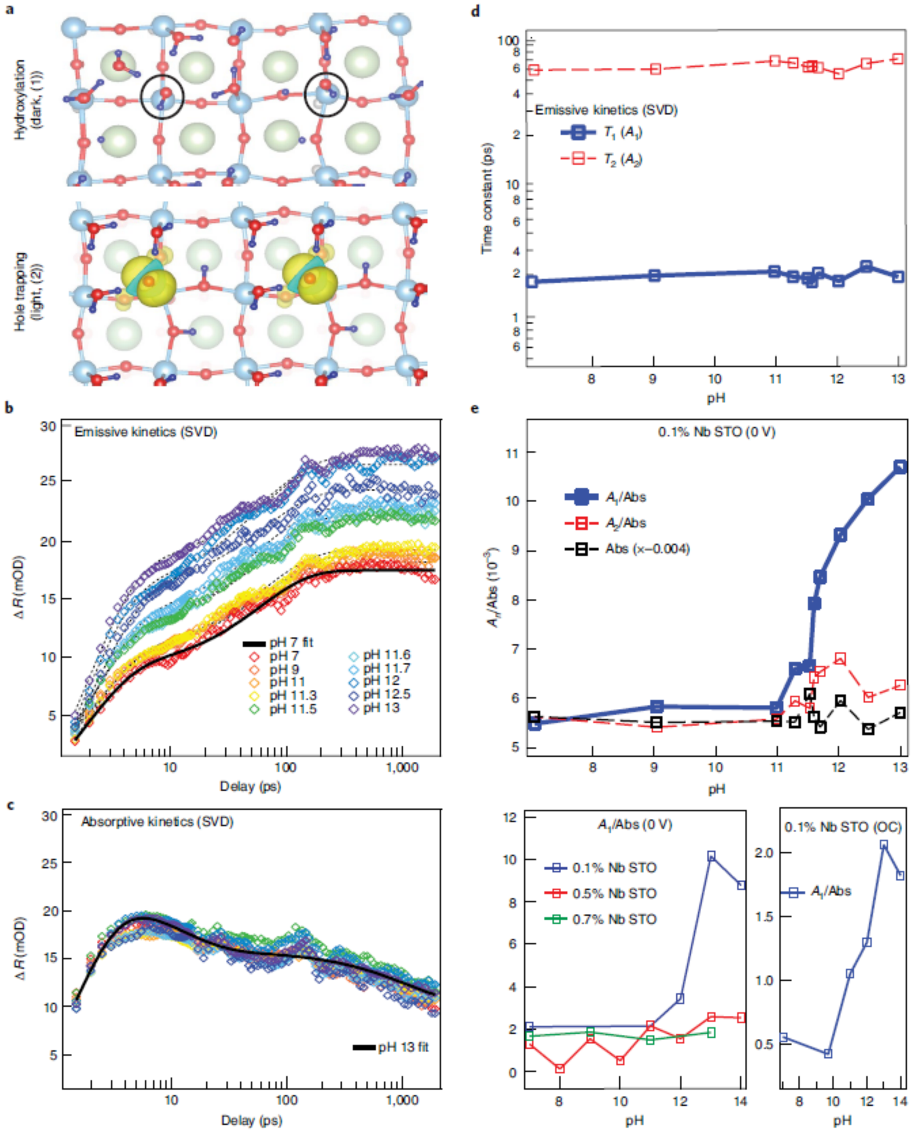

associated with absorption, $(X^{-1}S_{1,2}(V_{1,2})^T)_2$, exhibit decay kinetics and show little change with pH (Fig. 6.3c). Fitting the emissive curve with two rising exponentials defines the two timescales ($\tau_1 \approx 2$ ps and $\tau_2 \approx 60$ ps) shown in Fig. 6.3d. Since the time-integrated absorption is independent of pH, we can use it to normalize the emission for fluctuations in pump–probe overlap. In Fig. 6.3e, we show the normalized emissive response as a function of pH and for different experimental conditions. For 0.1% Nb STO, the amplitude of the fast, 2 ps rise (A_1) has a clear sigmoidal dependence on pH centered at 11.7. However, the same analysis of 0.5% and 0.7% Nb STO shows little pH dependence, reflecting the rotation analysis (Fig. 6.2c); the highly doped STO optical data is shown (Figure B.2) and analyzed further (Figures B.3 and B.4) in Section B.2. For 0.1% Nb STO, the amplitude of the 60 ps rise (A_2) is also fairly pH independent. While in this analysis A_1 and A_2 both report on the Ti-OH* population, since A_2 occurs later, A_2 represents either a time evolution of the 2 ps Ti-OH* population or a separate population of Ti-OH* arising from a different source. While the pH dependence shown in Figs. 6.1 and 6.3 is taken with a phosphate-buffered solution that allows for finer steps in pH, a sigmoidal pH dependence also occurs for A_1 with a sulfate solution (Figure B.5). Importantly, the same methodology extracts a sigmoidal pH dependence from the open-circuit data (Fig. 6.3e and Figure B.6) for which no surface degradation exists and photo-excitation flattens the Schottky barrier; this independently isolates the effect as coming from the interfacial hydroxylation.

These results establish a sigmoidal pH dependence for the 2 ps component of Ti-OH* creation from VB holes, which reflects a reaction isotherm and the two reaction steps proposed above. The fast timescale for the A_1 population aids in separating reaction 6.1 from 6.2, since any re-equilibration with OH$^-$ in solution should occur at substantially longer timescales [73, 74]. It also suggests that the hole transfer occurs without a simultaneous full proton transfer to solution. This is similarly anticipated by ab initio molecular dynamics simulations on titania [8,53]. The absence of a clear H/D kinetic isotope effect (Figure B.7) substantiates the lack of free H^+ as a product [75,76].

The two separable reactions are also supported by investigating a similar sample, but one for which the surface is expected to be hydroxylated already under neutral conditions. The 0.7% Nb

STO indeed exhibits a much higher hydroxylation than 0.1% Nb STO by ambient pressure X-ray photoelectron spectroscopy, with a factor of 2–3 increase at high relative humidity (Section 2.1); the more-electron-dense, in-plane, lattice oxygen sites could promote H_2O dissociation [77]. Since the optical spectra for both 0.5% and 0.7% Nb STO also do not exhibit a resolvable pH dependence, the results reflect a dark equilibrium that cannot be pushed by pH in basic conditions. In contrast to the more isolated, defect Ti-OH$^-$ sites in lightly doped STO, a fully hydroxylated surface in highly doped STO could reflect a two-dimensional network for hole trapping.

6.6 A Langmuir Isotherm with an effective equilibrium constant

The free energies of the relevant steps are depicted within the full photo-driven OER reaction in Figure 6.4a. Reaction 6.1 is described by the chemical potential of Ti-OH$^-$ relative to Ti-OH$_2$ along the same free energy surface in the dark (solid black lines). However, reaction 6.2 involves a crossing of two distinct surfaces, where the light pulse (yellow arrow) first creates the hole on the oxidized surface at the reaction coordinate defined by the reduced VB but then quickly transfers to the surface for which the trapped hole, Ti-OH*, is a minimum.

We now turn to the description of the sigmoidal pH dependence using a Langmuir-type reaction isotherm, albeit for a meta-stable intermediate population. The model and its application is developed in detail in Section 2.4. In a Langmuir isotherm, the sigmoidal rise of the product, an adsorbed surface species, with respect to a tunable reactant concentration reflects the equilibrium constant of the reaction. The saturation in the sigmoid reflects a limiting equation that restricts occupied and unoccupied sites to exchange with each other up to a maximum coverage [78]. For the simple adsorption isotherm of reaction 6.1, Ti-OH$^-$ exchanges with Ti-OH$_2$, the tunable reactant is OH$^-$ and the limiting equation is $S_0 = [Ti - OH^-] + [Ti - OH_2]$; S_0 is the total surface site density. However, reaction 6.2 involves an exchange between delocalized and trapped holes and is tuned by the surface hydroxylation, Ti-OH$^-$. The limiting equation compatible with a Langmuir isotherm is $h_0^+ = [h^+] + [Ti - OH^*]$; h_0^+ represents the total hole density excited by a single laser pulse, which is kept constant at 2% of the surface site density. In this model, Ti-OH$^-$ independently

Figure 6.4: a) Free energy diagram of Ti-OH$^-$ adsorption and Ti-OH* creation in the context of the full reaction scheme. Photo-excitation (yellow arrow) separates the diagram into the dark, equilibrated and oxidized free energy surfaces. The black dotted line represents the excited hole in the VB, while the yellow solid line represents the pathway to O_2 for a photo-excited hole. The ΔG for each reaction step per site in OER is shown in the standard state, with the ones relevant to the experiment highlighted in red. The time constant (2 ps) for Ti-OH* creation from the VB hole highlighted in this work is shown by the blue arrow; the dotted blue arrow (on the scale of 10 μs) denotes the downhill reaction kinetics for O-O bond formation, as suggested by previous work [57]. The full, multi-site reaction scheme suggested by this diagram is stated to the left. b) The A_1/Abs component (blue triangles) of 0.1% Nb STO in Fig. 6.3e at 0 V versus SCE, where the pH 7 contribution has been subtracted and the pH 14 contribution is normalized to 1. The data points have been fit to the Langmuir isotherm described by equations 6.6 and 6.7 in the text, with coverage $\theta = [Ti - HO^*]/[h_0^+]$ and $K_{eff} = 153 \pm 32 M^{-1}$. The inset shows the agreement on a logarithmic scale with the characteristic sigmoidal behavior of an isotherm.

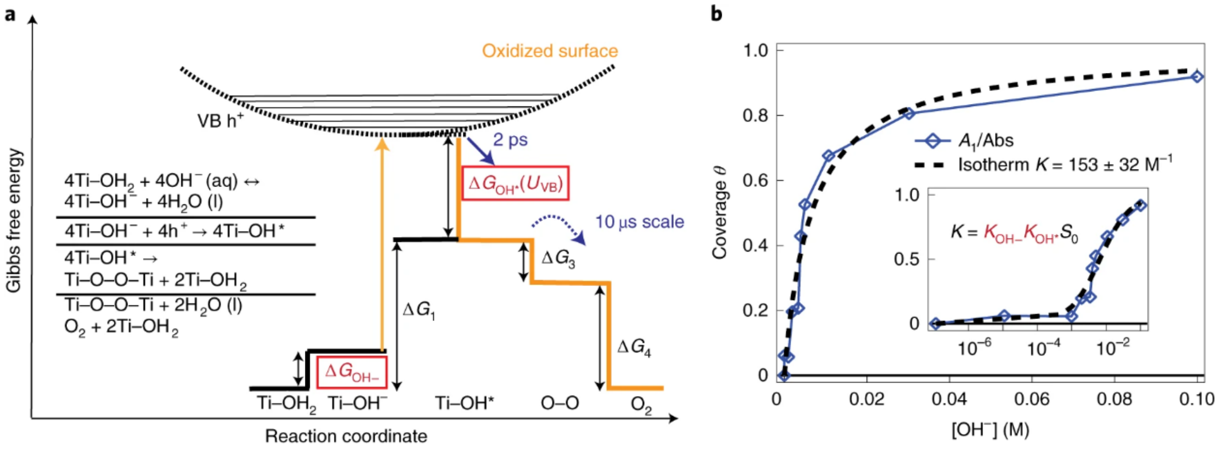

modulates the isotherm for Ti-OH* coverage, since Ti-OH$^-$ does not re-equilibrate with OH$^-$ on the picosecond timescale. Therefore, the isotherm of reaction 6.2 can be written in terms of [OH$^-$] by using [Ti-OH$^-$] established in the dark, leading to the following net isotherm for the coverage θ:

$$\theta = \frac{[Ti - OH^*]}{h_0^+} = \frac{K_{eff}[OH^-]}{1 + K_{eff}[OH^-]} \tag{6.6}$$

$$K_{eff} = K_{OH^-} K_{OH^*} S_0 \tag{6.7}$$

Here K_{eff} is the effective equilibrium constant of both reactions. where $K_{OH^-} = [Ti - OH^-]/[Ti - OH_2][OH^-]$ and $K_{OH^*} = [M - OH^*]/[M - OH^-][h^+]$. The $[OH^-]$ is in units of M^{-1}, while the rest of the reactants $([Ti - OH^-], [Ti - OH_2], [h^+])$ carry a real number density (for example cm^{-2}). Therefore, K_{eff} carries a total unit of M^{-1}. The sigmoidal dependence of the extracted coverage is well described by an isotherm with a fitting constant of $K_{eff} = 153 \pm 32M^{-1}$ reflecting the pH = 11.7 half-rise. A K_{eff} within this error was obtained also for data through pH 14 (Figure B.8); that the isotherm saturates is also apparent in the rotation analysis (Fig. 6.2c). It is important to note that this K_{eff} is in the context of a continually downhill catalytic cycle for which a meta-stable population is being isolated, rather than a reaction that reaches completion.

We now estimate the anticipated value of K_{eff} from theoretical calculations. In theoretical calculations, each VB hole is tied to a Ti-OH$^-$ surface site and does not appear as a separate concentration [8]. Therefore, obtaining a theoretical equilibrium constant, K_{eff}, requires dividing K_{eff} by $[h_0^+]$, which represents the degeneracy of the VB hole states upon photo-excitation. Multiple surface sites, each with their own protonation within the hydration layer, could be the source of the dark reaction (reaction 6.1), which leads to a range of relevant pK_a. For a spontaneous $\Delta G_{OH^*}(U_{VB})$, the pK_a should be larger than the pH of the isotherm's half-rise; the higher the pK_a, the more spontaneous the $\Delta G_{OH^*}(U_{VB})$. An upper bound pK_a of 16, associated with the creation of an oxide anion, yields a $\Delta G_{OH^*}(U_{VB})$ = -0.14 eV for the observed $K_{eff} \approx 150M^{-1}$ and a hole density ($[h_0^+]/S_0$) of 2%.

We now obtain the electrochemically driven redox level for the first proton and electron transfer of OER. Using equation 6.3, with a calculated $\Delta G_{OH^*}(U_{VB})$ = -0.14 eV consistent with the isotherm and a 2.8 V VB versus RHE for STO [27], $\Delta G_1(OH^*)$ = 2.66 V versus RHE in the standard state, which places STO comfortably on the weak-binding branch of the usual volcano plots (Fig. 6.1b) [3,48]. In applying equation 6.3, $\Delta G_{OH^*}(U_{VB})$ is a constant across the pH range. Further insight into the weak binding derives from how much $\Delta G_{OH^*}(U_{VB})$ leads to a sigmoidal half-rise close to the $\mathrm{pK_a}$ of Ti-OH$_2$: it occurs at pH 11.7 rather than at 8 [79]. An increasingly more exoergic $\Delta G_{OH^*}(U_{VB})$ would be needed to move the half-rise towards 8. The weak binding and the downhill pathway towards O-O bond formation observed previously [57] support the full multi-site reaction mechanism of Fig. 6.4a, where the first electron transfer creates four Ti-OH* intermediates from four H_2O molecules, and then subsequent thermo-chemical reaction steps form

O_2 and release two H_2O molecules.

6.7 Conclusions

This work discovers a methodology for obtaining equilibrium constants of meta-stable surface intermediates of a driven catalytic reaction using Langmuir isotherms and time-resolved optical spectra of the intermediate population. In particular, we constructed an effective equilibrium constant that defines the reactive Ti-OH* population during water oxidation to O_2. It is in the range of 10^2 due primarily to the combination of an endoergic ΔG_{OH^-} for surface hydroxylation and an exoergic $\Delta G_{OH^*}(U_{VB})$ for VB hole trapping. In this regard, the work finds experimental evidence to categorize STO as an electro-catalyst whose energy efficiency is limited by creating rather than removing bound Ti-OH* intermediates, as predicted by theoretical calculations. More generally, the results demonstrate how time-resolved spectroscopic investigations of the water oxidation reaction can reveal the free energy differences of elementary reaction steps, uniquely establishing a necessary connection between thermodynamic and kinetic quantities that guide theory and experiment, respectively.

Chapter 7

Surface acidity of oxygen evolution intermediates by excited state optical spectroscopy

7.1 Original Publication

This work is currently under review through JACS as Paolino, M., Singh, S., Boyd, C., Lang, M., et al. Surface acidity of oxygen evolution intermediates by excited state optical spectroscopy

7.2 Introduction

Half of the water splitting reaction that creates an energy storing fuel in the form of H_2 is the oxygen evolution reaction (OER) that involves four electron and proton transfers per O_2. These are generally considered to occur as single and precisely proton coupled electron transfer (PCET) reactions for which the metal-oxygen bond defines the binding energies of reaction intermediates [2, 4, 48]. In principle, however, acidity of the catalytic site and its environment can change the energetics of electron transfer out of the metal-oxygen bond [80], which then defines different mechanistic regimes as a function of electrolyte pH. Such effects can be important to better understand the molecular and chemical mechanism of OER [3, 43].

The role of acidity for homogeneous OER has been the most well defined to date, providing mechanistic diagrams as a function of pH and electrode potential by electrochemical characterization of tailored synthetic molecules. For the most studied mononuclear Ruthenium catalyst [81,82], regimes of pH and electrode potential exist for which reaction intermediates are created by electron transfer uncoupled to the proton transfer, by coupled two-electron, two-proton transfers, and by single electron transfers coupled to two proton transfers [81]. Separations between the regimes of proton assisted electron transfer can be related to an acid dissociation constant or pK_a of the electron transfer reaction intermediates. The role of acidity for heterogeneous, electrochemical OER is becoming more well defined by electrochemical characterization of single-crystal epitaxial thin films. For RuO_2, the binding energies of the first two OER reaction intermediates of electron and proton transfer have been shown to depend on pH [83]. A challenge has been to quantify how acidity influences the stability of OER reaction intermediates on heterogeneous, semiconducting metal-oxide surfaces. For (photo)-electrochemical OER on TiO_2, pH dependencies have been observed on the populations and lifetimes of transient, photo-excited intermediates [84–86]. However, the dependencies have not been quantified precisely enough across the range of relevant timescales to associate them with an equilibrium descriptor of the intermediates.

There are several reasons to anticipate that the reaction intermediates and their binding energies do depend on the acidity and protonation environment of the semiconducting catalyst surfaces. Firstly, for noble metal TiO_2, the electron transfers out of the water species and into the electrode—or, equivalently, a valence band edge hole transfer out of the electrode—have been associated with hole-polarons for which distortions of neighboring Ti-O bonds localize charge onto surface oxygens [8,57,68]. Having such local charge directly implies that surface acidity would play a role in the stability of PCET reaction intermediates. For example, the hole-polaron configurations are calculated to be uniquely stable for hole-trapping on water species that have already been singly or doubly deprotonated. Further, O-H bond dissociation energies in PCET reactions are calculated to be significantly modified by the presence of hole and electron polarons [53, 87]. Secondly, the early transition metal-oxides are associated with a non-uniform hydration layer by both calculation and experiment; water dissociation leads to a heterogeneous distribution of adsorbed water species, hydroxyl groups, and fully deprotonated surface oxygens [23, 79, 88, 89]. Each set of sites could influence the OER mechanism by allowing for differently protonated reaction intermediates, each with their unique binding energies, upon single electron and proton transfers. Finally, recent experimental work has identified pH 12 as distinctive for both hematite and strontium titanate; for hematite [21], the interpretation is that the formation of the iron oxo (Fe=O) by electron transfer depends on the protonation of the surrounding solvent.

For strontium titanate, a scenario for which the proton configurations of the ground and excited state surface dictate the electron transfers has been recently advanced by experiments using an ultrafast and visible broad-band probe of photo-excited (0.1% Nb) $SrTiO_3$ (STO). The excited state emission that forms within an ultrafast time scale of electron transfer (< 2 ps) exhibits an isotherm with pH whose half-rise occurs at pH=11.823. However, identifying this pH dependence with an acid dissociation constant (pK_a) implies that an equilibrium is reached on the excited state surface. Here, we show that the pH-dependence originating at ultrafast time scales is preserved through microseconds. Furthermore, the decay of the excited state populations to the subsequent reaction steps depends on a similar pK_a. The formation and decay kinetics are defined by two time constants each (1 ps, 60 ps and 20 μs, 100 μs), with the 1 ps, 10 μs populations exhibiting the pH-dependence with an onset of pH=11.8, pH=11.3 respectively. The metastable emission has components at the band edge and below it. Assigning the excited state spectra in the visible region to theoretically calculated optical dipoles of hole-polarons is a challenge and a part of ongoing work [90] Here, we separate out the short-lived excited state absorption to focus on the long-lived and pH-modulated emission.

The finding of a sharp pH dependence for intermediate populations metastable from ultrafast time scales on a heterogeneous metal-oxide undergoing OER identifies a surface pK_a that has so far characterized proton-assisted electron transfer on molecular catalysts. A mechanism based on how the formation free energy differs between the $OH^{\bullet}$ and $O^{\bullet -}$ reaction intermediates is proposed, whereby intermediates of $OH^{\bullet}$ formed from water occur for pH prior to the pK_a and $O^{\bullet -}$ formed from hydroxyl groups for pH beyond the pK_a. Given that the hydration layer involves complex networks of hydrogen bonding at the solid-liquid interface [28], these entities represent chemical rather than geometrical configurations for which the proton in $OH^{\bullet}$ is thought of local not to a site but to the hydration layer. More generally, the work shows that excited state optical spectroscopy of heterogeneous metal-oxide surfaces, predominantly associated with electron transfer, is also quite sensitive to the protonation of meta-stable intermediates.

7.3 Experimental Methods

Electrochemistry. 0.08% Nb-doped STO by weight (henceforth referred to as 0.1%) STO single crystals with the (100)-facet exposed to the electrolyte were obtained from MTI corporation. The thickness of the crystals was 0.5 mm and the exposed side was polished (Ra<5Å). The rear face of the STO crystal is brought into electrical contact with a copper wire via a Gallium-Indium eutectic (Sigma-Aldrich, St. Louis, MO). The sample and wire are then covered with epoxy, followed by an insulating layer of liquid electrical tape, leaving the polished surface exposed. The sample is then mounted in a custom designed cell which holds the sample steady and accommodates an electrolyte solution along with a reference and counter electrode. The pH of the electrolyte solution is varied between 7 and 14 during experiments. Solutions below pH 14 were prepared using a phosphate buffer; the pH 14 solution was a 1 M solution of NaOH. An Ag/AgCl (3M KCl) electrode was used as a reference and a Pt wire served as a counter electrode (cathode). The potential was kept at 0V throughout all experiments and was controlled by a CHI650E Potentiostat (CH Instruments, Austin, TX) via the copper wire at the rear of the STO sample (anode). Sweeping this potential, while monitoring current through the sample amounts to a cyclic voltammetry measurement (Figure 4.3a). This serves to clean the sample surface of contaminants and confirms a good electrical connection at the rear of the sample. Electrical current through the sample is monitored during data collection. This current is used to calculate quantum efficiency of charge separation as shown in Figure 4.5.

Pump-Probe Spectroscopy. The OER catalytic cycle is time resolved using a pump-probe spectroscopy. The pump provides above bandgap excitation, placing the $SrTiO_3$ in an electronically excited state from which subsequent reaction steps are downhill. The system is then probed by a white light continuum pulse which interrogates the newly formed OER intermediates on the $SrTiO_3$ surface through a change in reflectivity after pump excitation. The probe beam is derived from a regeneratively amplified Ti:Sapphire laser system (Coherent Legend, Coherent Inc., SantaClara, CA) which produces pulses with a center wavelength of 800 nm and pulse length of ca. 150 fs at a repetition rate of 1 kHz. Part of the amplifier output is directed into a CaF_2 crystal to generate a white light continuum spanning from ca. 375 nm-730 nm. The probe beam was directed onto the sample in a ca. 45° angle, which translates to a 32° angle of incidence on the sample itself after refraction through the cover glass and electrolyte (Figure 4.2). Two different pump sources are used to fully resolve the dynamics of our signal. Early time dynamics (short-time data, ps – ns scale) are resolved using a fast (~500 fs) pump pulse generated from the third harmonic of the Coherent Legend output, with delays generated via a mechanical stage. Longtime dynamics (long-time data, ns – μs scale) were studied using the 266 nm fourth harmonic output of an Innolas SpitLight Piccolo. The delay between the pump (Piccolo) and probe beams was adjusted using a digital delay generator (SRSDG645, MenloPark, CA) where only every second trigger signal was used, resulting in a repetition rate of 500 Hz for the pump pulses. Raster scanning of the pump and probe across the sample surface are employed to prevent surface reconstruction from effecting the data. Information on these scanning methods and potential effects on data are shown in Figure 4.6.

7.4 Results

7.4.1 Absorptive and emissive populations from transient reflectance

An ultrafast and visible broadband probe of the (0.1% Nb) STO/electrolyte interface tracks the excited state absorption, stimulated emission, and band-edge emission during OER (Figure 7.1). Due to the well-defined Schottky barrier (Figure 7.1a), this interface was previously shown to have a high photon-to-current quantum efficiency (>70%) in a 3-electrode configuration with above bandgap and ultrafast excitation (266 nm, 400 fs) and 0 V vs. Ag/AgCl on the STO working electrode (Figure 4.5) [7]. The change in reflectivity is defined as ΔR = -log(R_{on}/R_{off}) where R_{on} and R_{off} are the measured intensities of the broadband reflected light with and without the pump excitation; in reflectivity, the pump-probe signals arise from a depth d $\sim \lambda/4\pi n$ [91] where n is

Figure 7.1: Excited state optical spectra at the STO/aqueous interface. a) Schematic of the Schottky barrier at the 0.1 % Nb STO/aqueous interface with 0 V vs. Ag/AgCl applied to the back of the electrode. Above band gap photoexcitation (pump: 266 nm) leads to spontaneous OER probed by an ultrafast, broadband visible pulse (probe: 375-730 nm). b) Energy level diagrams depicting emissive and absorptive transitions that contribute to the spectra in the visible range after bandgap excitation. The bulk hole polaron state is shown as a dashed line. The corresponding transition is outside of our experimental range. c) Normalized characteristic emissive and absorptive spectra from constrained SVD analysis at both pico- and micro-second time-scales. d) Langmuir isotherm derived from picosecond emissive population as a function of pH, suggesting a quasi-equilibrium constant for the excited state surface. Coverage $\Theta = [Ti - O^-]/h_0^+$ where Ti-O$^{\bullet -}$ denotes a particular chemical configuration of trapped hole and h_0^+ the total hole population. Adapted with permission from [28]. Inset is a schematic of surface protonation at low (<10) and high (>12) pH prior to photoexcitation.

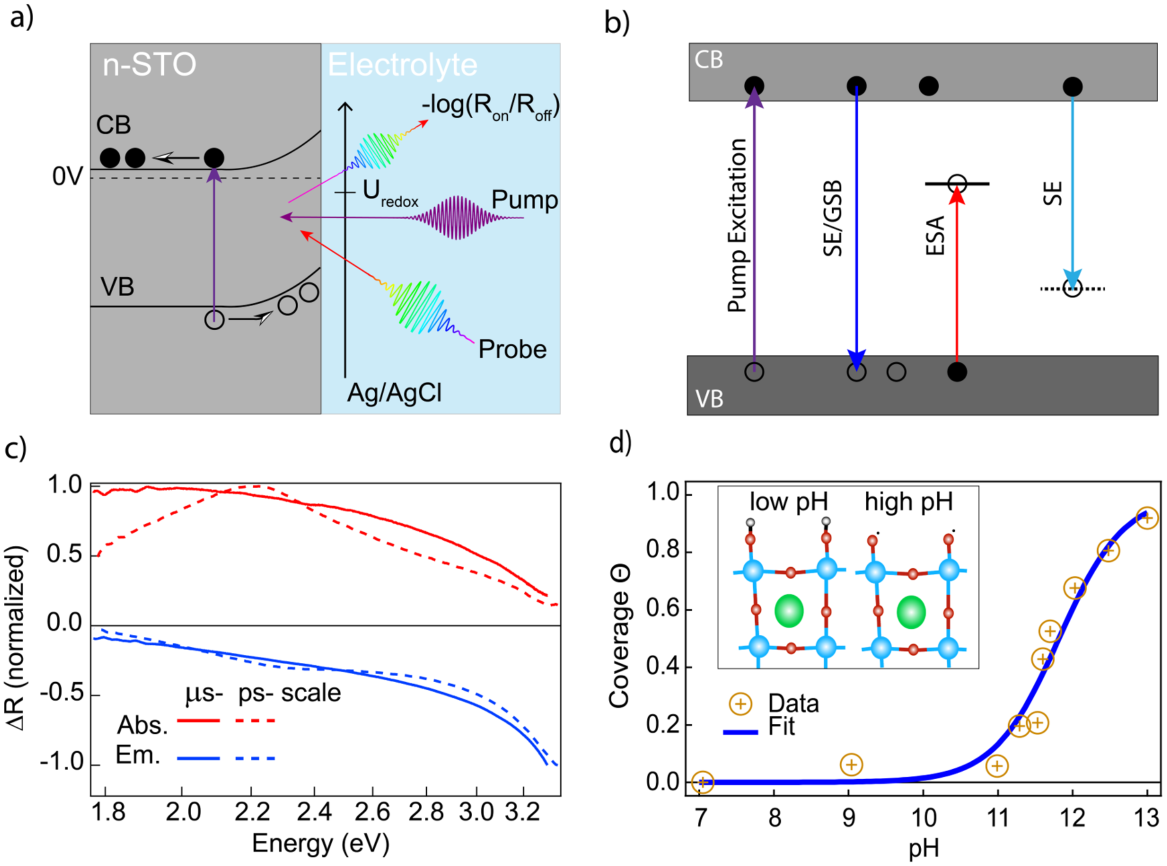

the real part of the refractive index and for the wavelengths λ probed d is 10-20 nm. Due to the high quantum efficiency during OER, a Schottky barrier of ~25 nm [7] and the surface sensitivity of reflectance, the pump-induced changes are associated with delocalized and trapped holes. The pump penetration depth d, and the Schottky barrier W are shown in the diagram in Figure 4.1. Further, trapped electrons associated with occupied mid-gap states are not anticipated in Nb-doped STO due to the shallow Nb donor states [38] and the lack of a propensity to trap electrons in the form of Ti(III) in STO [92]. Emissive and absorptive signals arise due to excitations of electrons from the conduction and valence bands respectively to either unoccupied mid-gap states arising at a distorted reaction coordinate or band edge states at the equilibrium reaction coordinate (Figure 7.1b). If the excited state is due dominantly to a change in absorptivity (rather than a change in the real part of the polarization), a positive ΔR corresponds to an excited state absorption (ESA, red) and a negative ΔR signifies a ground state bleach (GSB, blue) or a stimulated emission (SE, blue). Transient spectra can be decomposed into characteristic absorptive and emissive spectra [19] (Figure 7.1c), allowing for separate analysis of their contributions to the data. Both contain spectral weight well below the band gap (3.2 eV) for which there is little ground state absorption; Figure 2.5a shows the real and imaginary refractive indices for STO.

In this manuscript, data are taken during OER to focus on the population dynamics of long-lived hole polaron states. In particular, the focus will be on a long range of metastability between the picosecond and microsecond timescales found for the emissive component. Spectrally, the below band-gap emission is associated with bulk hole-polarons, stable in STO; a prominent spontaneous emission peak near 2.5 eV is seen in photoluminescence which theoretical calculations have assigned to bulk hole-polarons [93,94] (Figure 7.1b). In our data, a near band edge emission is present, which is also seen in some photoluminescence studies through the band edge [62,64] (Figure 7.1c). There could be multiple origins of the near-band-edge emission that arise from either excited state populations of the ground state electronic levels or changes in the conduction and valence band states due to photoexcitation. The most usual assignment is a ground state bleach of the electronic levels due to electron, hole occupation of the valence, conduction bands respectively. However, the population dynamics associated with this excited state configuration are that of electron-hole recombination. For STO, recombination dynamics measured by a near band edge pump excitation (to highlight bulk, delocalized carriers) exhibits a $\sim$60 ns lifetime and can be modeled by band-to-band auger recombination processes as a function of photocarrier intensity [95]. The metastability over a wide range of time-scales encompassing the nanosecond regime suggests that this near-band-edge emission originates from new stable states. Further, the emissive component of the data, inclusive of the mid-gap and near-band edge regions, consistently tracks a similar metastable population modulated by circuit conditions [7] (open, closed) and electrolyte [19] (pH), which also suggests that it probes long-lived hole states whose population is subject to external conditions.

One of the unique properties of the metastable emission is that it describes an intermediate population with a sharp pH dependence between 11 and 12. The pH-dependent population arises from the ultrafast emissive growth. This was shown in a recent manuscript [19] using a principal component analysis [65] whose emissive and absorptive spectrum for the < 1 ns range is reproduced in Figure 7.1c, alongside that of the spectra for the microsecond data reported here. The pH-dependence of the picosecond emissive population is shown in Figure 7.1d (baseline corrected using pH 7). The dependence saturates at higher pH and is therefore modeled with a surface-limited Langmuir isotherm as a function of pH or [OH$^-$]. Its half rise of pH 11.8 corresponds to an equilibrium constant of $K = 153$. Since this isotherm is for the excited state surface formed within a couple picoseconds, it is a composite of the ground-state equilibrium of the surface with the bulk electrolyte prior to photoexcitation and the metastable equilibrium upon photoexcitation. Cartooned in the inset of Figure 7.1d are changes to the protonation of the hydration layer with pH prior to excitation that we come back to in the discussion.

7.4.2 Ultrafast formation, metastability, and decay of pH-dependent emission

Transient spectra of the n-doped STO/electrolyte interface, showing the entire lifetime of the emissive population, were collected at pH values ranging from 7 to 14. To view the dynamics of these transient spectra over their entire lifetime, data must be collected on two separate time scales. Ultra-fast dynamics at the early time scale (short-time) are resolved using finely spaced delays in the range of 0 ns - 4 ns. The remainder of the dynamics (long-time) are captured using delays in the range of 1 ns – 500 μs. Time-resolved spectra were achieved by concatenation of short- and

Figure 7.2: Time-energy contour plots of absorptive and emissive signals for pH 7-14. Contour plots of concatenated data reconstructed from the first 2 SVD components for each pH data point. Each pH point shows time-dependent absorptive (red) and emissive (orange-blue) optical transitions. The green line highlights the zero-contour line. The absorptive signature fully develops within ~1 ps and decays within ~100 ps. The emissive signature grows more slowly (~ 100 ps) and remains metastable through the microsecond scale and fully decays only by ~ 100 μs. The magnitude of the absorptive signature is not sensitive to pH, whereas the emissive signature increases markedly past pH 11

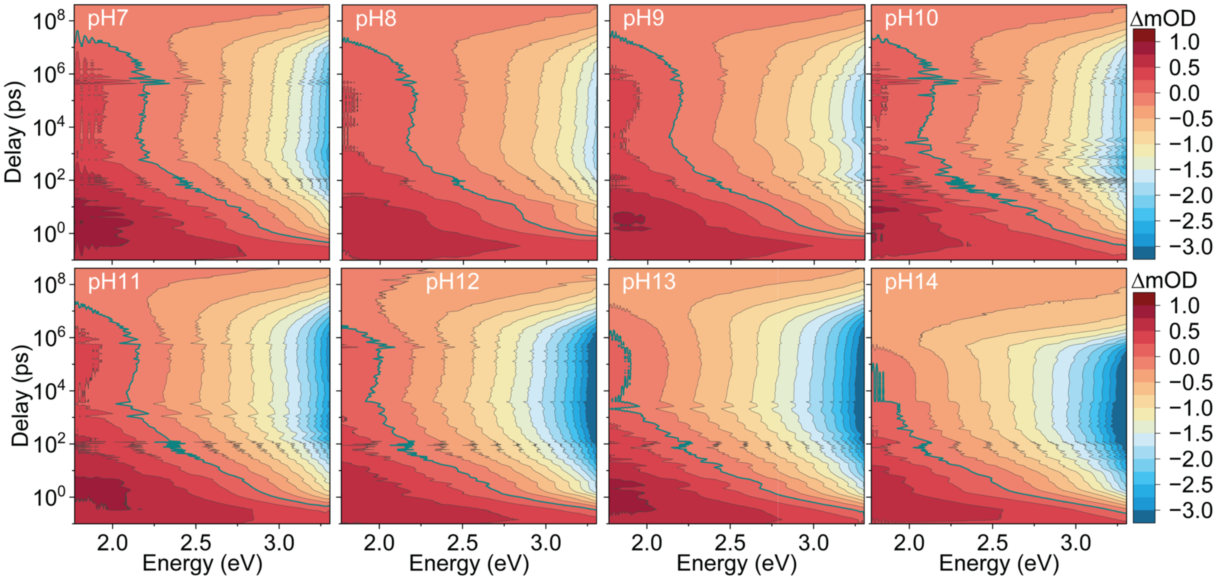

long-time scale data sets, using the short-time scale transient spectra Figure C.1 as a benchmark.

The resulting concatenated transient spectra shown in Figure 7.2 are achieved by a linear scaling of the longtime data, calculated by a comparison of spectra from short- and long-time scale data Figure C.2 at common delays. A comparison of spectra at the point of concatenation is used to establish a common zero crossing point Figure C.4. Scaling factors, which minimize the difference between spectra for each common delay Figure C.4 are then used to determine a single scaling factor for the longtime data, at each pH point.

The resulting contour plots allow for the rise, metastability, and decay of the absorptive (positive OD, pink-red) and emissive (negative OD, orange-blue) signals to be viewed simultaneously (Figure 7.2). The absorptive contribution occurs for the lower energy range of the broadband probe, decays after 100's of ps and does not show a distinctive pH dependence. The emissive contribution occurs in the high energy region of the broadband probe and shows a distinct pH dependence. This emissive signal develops with-in the first ~100 ps, remains metastable on the nanosecond scale, and ultimately decays on the microsecond scale. The pH dependence is reflected in the overall magnitude of the emissive signal. Between pH 7 and 10 there is little dependence on the emission. Beginning near pH 11, the emissive contribution increases as shown by the higher energy range of the transient spectrum (2.8 – 3.2 eV) and by a changing zero contour line (green) as the emission increasingly reduces the overlapping absorption. The microsecond kinetics also display a dependence on pH; the emissive signal at pH 14 decays to zero faster.

For a more quantitative analysis of the emissive population dynamics, constrained singular value decomposition (SVD) analysis is performed on the concatenated data (Figures D.1- D.3). SVD analysis reveals two dominant spectral components that represent the transient data, as indicated by the relative magnitude of singular values (Figure D.1). These spectral components can be constrained such that there is one purely absorptive and one purely emissive spectral component representing poles of the imaginary refractive index in the optical spectroscopy (Figure D.2). Constraining the spectra amounts to choosing a basis and is achieved by manually tuning parameters which shift the spectra at each pH (Figure 5.3). Kinetics have a positive sign by convention and represent the relative magnitudes of the corresponding emissive and absorptive populations at each pH. When the different pH conditions are represented with common spectral components, the corresponding kinetic components confirm that the absorptive portion of the spectrum is fairly pH independent, and that the bulk of the pH dependence is carried by the emissive population dynamics (Figure D.3). The common emissive and absorptive spectra across the full time and pH range of the concatenated data are shown in Figure 7.1c.

Figure 7.3a shows the pH-dependent emissive kinetics for the concatenated data set; these kinetics are normalized to the integrated absorption at each pH to account for changes in fluence and pump-probe overlap during data collection. To quantify the pH dependence, the emissive SVD

Figure 7.3: Emissive population dynamics from picoseconds to microseconds and its pH dependence. a) SVD kinetics (circled dots) and fits of concatenated data (solid lines). Kinetics were normalized by integrating the corresponding absorptive kinetics for each pH point, then fit with a 4-exponential function. Regions are shaded to highlight the rise, metastability, and de-cay of the emissive populations. b) Exponential time constants obtained from the fits. The rising portion of the signal is defined by 2 distinct time constants (grey circles τ_1 black circles τ_2), and the decaying portion is defined by 2 distinct time constants (light blue circles τ_3 dark blue circles τ_4). c) Amplitudes of the fast (grey circles, A_1) and slow (black circles, A_2) rising components, representative of their relative populations. The fast rise emissive population carries a pH dependence with an onset between pH 11 and 12. Included is the pH dependence reproduced from the previously published ultrafast data (dark yellow crosses, A_1, Ref) shown also in Figure 7.1c; adapted with permission from [28]. d) Amplitudes of the fast (light blue circles, A_3) and slow (dark blue circles, A_4) decaying components, representative of their relative populations. The fast-decaying population carries a pH dependence with an onset past pH 11.

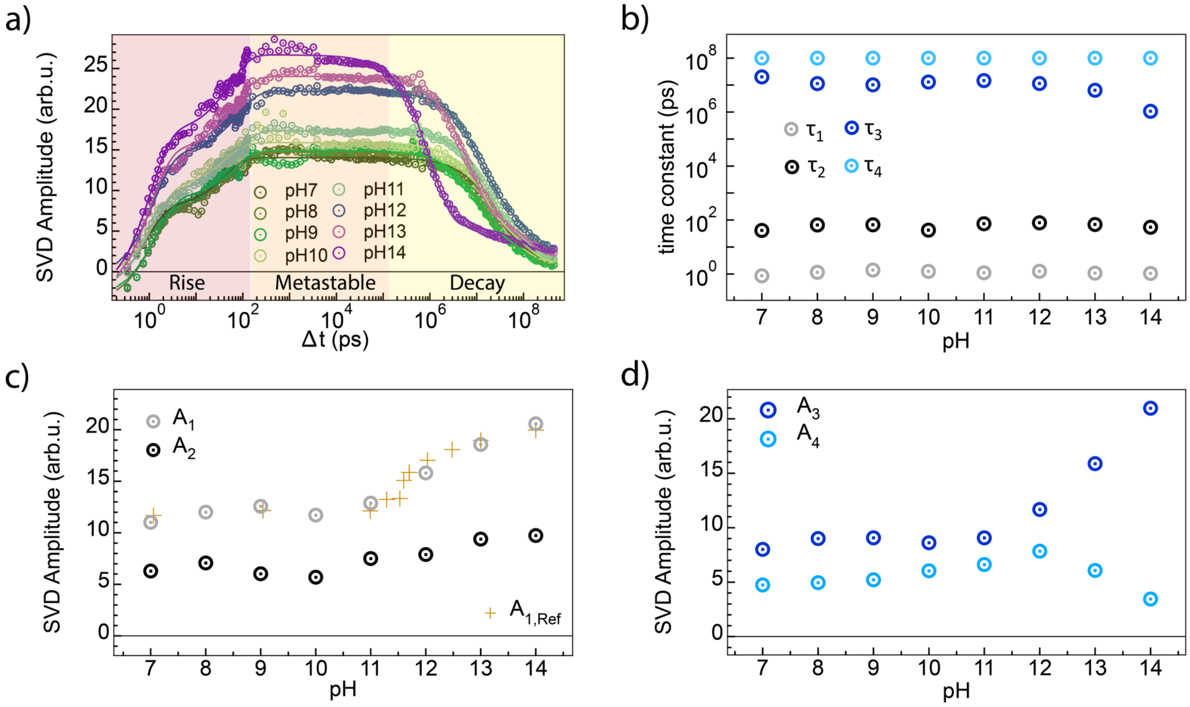

kinetics are fit with a 4-exponential function:

$$S(t) = A_1 \cdot [1 - \exp -t/\tau_1] + A_2 \cdot [1 - \exp -t/\tau_2] + A_3 \cdot \exp t/\tau_3 + A_3 \cdot \exp t/\tau_3 + C. \tag{7.1}$$

This model contains two rising exponentials, two decaying exponentials, and a constant offset accounting for background fluctuations in the data and any pump-probe signals beyond the time-window. For all pH conditions, four distinct time constants τ_n (Figure 7.3b) with corresponding amplitudes A_n (Figure 7.3c, 7.3d), were obtained. For the two rising exponentials, the fit results reveal a fast ($\tau_1 \approx 1ps$), and a slow ($\tau_2 \approx 60ps$) rising time constant, both of which are constant across all measured pH. The corresponding amplitudes represent the relative populations of fast A_1, and a slow A_2 growing emissive species. The pH dependence on the growth amplitudes is carried by the fast ($1ps$) growth amplitude A_1 (gray circles, Figure 7.3c) while the slow ($60ps$) growth amplitude A_2 remains relatively constant across pH (black circles, Figure 7.3c). We note that A_1 used for the Langmuir isotherm in the previous work was collected with six pH points between pH 11 and 12, while the data here are sparser, with a point at each pH [19]; these are plotted along with this concatenated data (yellow crosses, Figure 7.3c).

The microsecond decay is fit by a fast ($\tau_2 \approx 1\mu s$) and a slow ($\tau_4 \approx 1\mu s$) decay constant. The results are shown in Table E.2. The decay constants τ_3 and τ_3 decrease towards higher pH (Figure 7.3b). The bulk of the pH dependence for the microsecond decay lies in the fast decay amplitude A_3 and onsets after pH 11 (Figure 7.3d). The slow decay amplitude A_4 remains relatively constant across pH. Altogether, several characteristics of the population dynamics extracted from the SVD kinetics are preserved from the picosecond rise to the microsecond decay: 1) Both regions are defined by two distinct time constants, one fast and one slow, across all pH. 2) The pH dependence of the emissive populations in both regions are carried by the populations associated with the faster time constant. 3) The pH dependence has a distinct onset after pH 11.

SVD emissive kinetics were also fit with a different version of a 4-exponential function that explicitly assumes only 2 populations: A_1 and A_2. The assumption is that A_1 and A_3, along with A_2 and A_4 are the same populations. These fits resulted in similar results to those displayed in Figure 7.3 suggesting also that the population with the fast, slow growth is connected to that of the fast, slow decay respectively. Details of this fitting are shown in Figure E.1, and we return to the two different fitting procedures in the discussion.

7.4.3 Excited state pK_a by the metastable emissive population

We now focus on quantifying the pH dependence of the microsecond emission. The fitting of concatenated data with a single equation means that the behavior of the kinetics in the short-time region have an influence over the fit parameters in the long-time region (A_3 and A_4). Data concatenation itself also scales the long-time data, which can impact the fit results. By focusing on the microsecond regime, we can also collect finally spaced pH points which are needed to quantify the onset beyond pH 11.

Data collection at the long-time scale requires the use of an electronically triggered laser system. Though this laser system is excellent at producing pulses at irregular intervals (varying delays), it does suffer from energy and Poynting instabilities. Short-term instabilities can be easily accounted for, but long-term instabilities (hours to days) are more challenging to correct. We have addressed this problem in two different ways: 1) Collecting multiple repeats (≥ 4) of long-time data for each pH point, which are then averaged, 2) Collecting long-time data sets consisting of all pH points in a single day, while controlling for beam size and power between each data set (see Figures E.2 and E.3).

The results for the kinetic traces using the averaged data at each pH, which is the focus of quantifying the pH dependence, are shown in Figure 7.4a. Since the absorption has almost completely decayed by the beginning of the long-time scale (1 ns), the dynamics of the transient spectrum in this region can be described in whole by the emission. SVD analysis of the long-time spectra (Figure D.4) reveals one significant principal component whose spectrum is nearly all emissive. This allows for direct analysis of the long-time data through the raw kinetics of the transient spectrum at a single wavelength in the emissive region, 400 nm (3.1 eV) plotted in Figure 7.4a for each pH. The 3.1 eV long-time kinetic traces are fit by:

$$S(t) = A_3 \cdot \exp t/\tau_3 + A_3 \cdot \exp t/\tau_3 + C \tag{7.2}$$

The resulting curve fits are plotted on the kinetic traces of Figure 7.4a. The decay time constants τ_n, and the extracted amplitudes A_n are plotted in Figures 7.4b and 7.4c as a function of pH.

Figure 7.4: Quantifying microsecond emissive population dynamics as a function of pH. a) Time traces at 3.1 eV (circles) at various pH and corresponding fits (lines) of averaged long-time data using equation (2). b) Microsecond exponential decay time constants obtained from the fits (dark blue circles τ_3, light blue circles τ_4). c) Amplitude of microsecond populations from the fits (dark blue circles A_3, light blue circles A_4). d) Amplitude of the fast-decaying population (A_3) of the averaged data shown in a). The pH-dependence is fit by equation (3), a constant and linear rising function. The estimated error (shaded red) is shown with respect to the fit (red line) as described in the text. The onset (pH0) is found to be at ca. pH 11.3. Black crosses (A_3^{Ref}) are the amplitudes of the fast-decaying component when the data is not averaged while controlling for beam power and stability as described in the text.

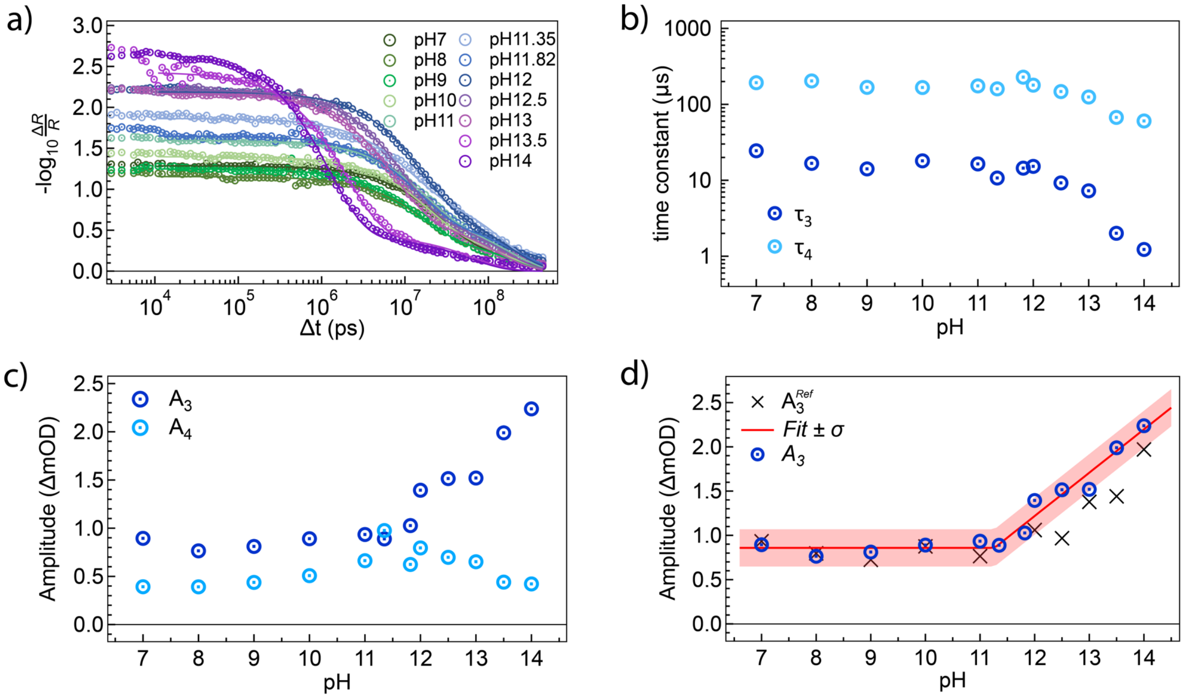

Consistent with concatenated data, the 2-exponential fit reveals two distinct time constants, one fast ($\tau_3 = 20\mu s$) and one slow ($\tau_4 = 100\mu s$) across all measured pH. As observed with the concatenated data, there is little to no population pH dependence prior to pH 11, and the pH dependence that onsets after pH 11 is carried by the fast decay population A_3. The long-time data, when viewed independently, also carries a clear pH dependence on τ_3 and reveals a pH dependence on τ_4. Figure 7.4b shows that past pH 12, τ_3 and τ_4 constants decrease.

The pH dependence carried by population A_3 is quantified in Figure 7.4d. A piecewise linear function, constant for pH<pH0 with a linear increase for pH>pH0, was chosen to establish a pH onset (pH0):

$$A_3(pH, pH_0, A_0, m) = A_0 \cdot \theta(-pH + pH_0) + (m \cdot (pH - pH_0) + A_0) \cdot (pH - pH_0) \tag{7.3}$$

It is important to establish an uncertainty in this model beyond that of the fit itself. To achieve this, Equation 7.2 was fitted to the kinetics at 3.1 eV for each repeat of the long-time data set at each pH. The resulting A_3 populations at each pH are then averaged, and a standard deviation for each pH is calculated. The averages are plotted as blue circles in Figure 7.4d and fit by Equation 7.3; the fit is shown as the red line. The uncertainty in the fit for A_3 vs pH (red shaded area in Figure 7.4d) is taken to be the standard deviation of the data with respect to the fit to Equation 3. The standard deviation of ca. 0.21 mOD reported here is the average standard deviation across all pH points (Figure E.3 and Table E.1). The fit yields an onset pH of ca. 11.3 and a rise of ca. 0.49 mOD/pH. The black crosses in Figure 7.4d represent fast decay amplitudes from the dataset collected in a single day with rigid control over beam size and power between each pH point. This method of data collection serves to minimize longtime variance at the expense of signal-to-noise due to a smaller data set. The points follow the same trend as the highly averaged data, confirming that the trend is independent of longer-term laser instability.

7.5 Discussion

The pH dependence observed for the transient populations on $SrTiO_3$ during OER associates a fast picosecond rise to a microsecond decay, with a long range of meta-stability in between. Further, the pH dependence is quantified to be between 11-12 using a Langmuir isotherm for the $1ps$ population (pH=11.8) and a linear onset for the $20\mu s$ population (pH=11.3). These results, the similar and quantifiable pH onset in very different time regimes along with the region of meta-stability, suggests that an acid equilibrium dissociation constant (pK_a) exists for intermediate populations of OER in this pH range.

Such a pK_a for intermediates species of OER has often been observed for molecular, homogeneous catalysts, categorizing regimes electron and proton transfer as a function of pH and potential in Pourbaix diagrams. An example is the 2.9 pK_a of the one-electron transfer intermediate $[\mathrm{Ru(III)\text{-}OH_2}]^{3+}$ for the mononuclear Ru catalyst [81]. Using electrochemical voltammetry, breaks in the Nernstian dependence of -59 mV/pH and regions of pH independence are associated with a pK_a for the intermediate. For wide band gap semiconductors, surface protonation modulated by the electrolyte pH has been well documented by how the band edge potentials move with circa -59 mV/pH [96]. However, since the band potentials are measured rather than the potential of an intermediate species, the Nernstian dependence represents an average of electron and proton transfers across many sites. Figure 4.4 shows the Nernstian dependence for Nb-doped $SrTiO_3$ with a somewhat smaller slope (-45 mV/pH). There is a leveling off at higher pH that could be associated with a pK_a but it is not pronounced.

Here we advance an interpretation of the results based on a pK_a of the transient, intermediate species isolated by photoexcitation and the emissive spectra. The closest analogy is pulse radiolysis that initiates reactions with high energy pulses from an accelerator, isolates populations spectrally, and quantifies their pH dependence to regularly assign pK_a's to intermediate species of electron transfer, especially in aqueous solutions [27, 97–99]. In this interpretation, the extracted emissive population counts the total number of one-electron intermediates or equivalently, hole-polarons [100]. As discussed at the beginning of the results section, the excited state emission is associated with hole-polaron states. The similarity in the emissive spectra at picosecond and microsecond time scales (Figure 7.1c) and the meta-stable kinetics (Figure 7.3a) suggest that a trapped population is counted independently of its geometric configuration or protonation. The single electron transfer required for one-electron intermediates is justified by: 1) the picosecond time scale of the ultrafast pH dependence, 2) the relatively low fluence used in the experiments (0.04 $\mathrm{mJ/cm^2}$) equivalent to 2% of surface sites [2, 7]) a saturation in the emissive signal with higher fluence corresponding to an equivalent of 5% of surface sites [7].

One way to understand an increase in the emissive population after pH 11 is that an additional driving force for hole-trapping becomes relevant at pH $>$ the pK_a of the intermediate. This is an underlying as-sumption for the Langmuir isotherm model in the prior manuscript [19]. Here, only a difference in free energy for intermediate formation between the hydroxyl (Ti-OH$^{\bullet}$) and oxyl (Ti-O$^{\bullet-}$) radicals is invoked without attempting to model the detailed isotherm(s) of Figure 7.3 and 7.4. The Ti-OH$^{\bullet}$ is presumed to occur from initially hydroxylated sites, while Ti-O$^{\bullet-}$ is presumed to occur from fully deprotonated sites; given the simplified nature of the reactions and a heterogeneous hydration layer, the protonation of the intermediate only refers to whether a proton has left to the bulk electrolyte. In other words, Ti-OH$^{\bullet}$ could occur in many different configurations, with the proton in the dangling configuration or bound to neighboring surface sites either directly or by H-bonds. We use the following reactions for Ti-OH$^{\bullet}$ and Ti-O$^{\bullet-}$:

$$Ti - OH_2 \leftrightarrow Ti - OH^{\bullet} + H^{+} + e^{-} \quad with \quad \Delta G_{OH^{\bullet}}(U_{VB}) \tag{7.4}$$

$$Ti - OH^{-} \leftrightarrow Ti - O^{\bullet-} + H^{+} + e^{-} \quad with \quad \Delta G_{O^{\bullet-}}(U_{VB}) \tag{7.5}$$

In the above, the reactant VB hole is written as a product electron transfer from the surface species into the VB; this presumes that the reaction occurs with a free energy difference defined by the VB edge (U_{VB}). To write $G_{OH^{\bullet}}(U_{VB})$ as a function of $G_{O^{\bullet-}}(U_{VB})$, the following reaction is used for the products on the excited state surface:

$$Ti - OH^{\bullet} \rightarrow Ti - O^{\bullet-} + H^{+} \quad with \quad \Delta G_{O^{\bullet-}/OH^{\bullet}} \tag{7.6}$$

As shown in Section 2.5, one can then write the formation free energy of reaction 7.5 in terms of the formation free energies of 7.4 and 7.6:

$$\Delta G_{O^{\bullet}-} = \Delta G_{OH^{\bullet}} + \Delta G_{O^{\bullet-}/OH^{\bullet}} \tag{7.7}$$

Equation 7.7 is derived by first summing Reaction 7.4 and 7.5 and then replacing Ti-OH$_2$ by Ti-OH$^-$+ H$^+$. With this re-casting, Ti-O$^{\bullet-}$ formation from valence band holes requires an additional, proton-related formation free energy compared to Ti-OH$^{\bullet}$ formation. In the data, the emission is constant prior to pH 11, which this interpretation suggests is due to Reaction 7.4 being spontaneous and reaching completion (of the product side) already for pH between 7 and 11. The increase in emission is then ascribed to Reaction 7.5 becoming spontaneous only after pH 11, given the additional free energy for proton transfer required by $\Delta G_{O^{\bullet-}/OH^{\bullet}}$ (Reaction 7.6).

Some of the assumptions that go into this interpretation can be justified by calculated and experimentally measured pK_a values. First, the deprotonation of an adsorbed water site (Ti-OH_2) to create a hydroxylated one (Ti-OH^-) has a calculated pKa 7-9 [88], albeit for a rutile TiO_2 structure. With this pK_a for Ti-OH^-, Ti-$OH^{\bullet-}$ formation by Reaction 7.4 would reach completion already in the near-neutral region. We note that in the prior manuscript for the ultrafast data [19], only Reaction 7.4 was invoked. Given the range of the relevant pK_a for titanium oxide and that the data do not show a change near neutral pH, it is Reaction 7.5 which is likely more appropriate. Reaction 7.6 has been measured by pulse radiolysis to have a pK_a of 11.839, which is very close to what is obtained for the ultrafast isotherm and in the range of the onset of the microsecond isotherm. For this pK_a, the additional free energy needed for proton transfer at pH=0, $\Delta G_{O^{\bullet-}/OH^{\bullet}}$, is ~0.68 eV. Since the electron transfer events in the pulse radiolysis experiments arise from exciting bulk water, to make a connection between them and the STO electrode assumes that the Ti sites are spectators in the reaction. That Ti is a spectator is also suggested by the noble metal configuration of Ti(IV) and the neutral pH range for deprotonation of a water absorbed site.

In addition to the thermodynamic reasoning given above, a full kinetic modeling of the mechanism that patterns the time-dependent emission is desired. There are several difficulties in defining this kinetic modeling, which would yield time-dependent coverages of Ti-$OH^{\bullet}$ and Ti-$O^{\bullet-}$. The first is that the protonation of the surface hydration layer prior to excitation is understood to differentiate the coverages (Figure 7.1d), rather than a proton transfer on the excited state surface. The sample equilibrates with the bulk electrolyte prior to photoexcitation and the initial formation of the intermediates is ultrafast. Further, we did not observe an H/D isotope effect on the formation of the emissive signal which would be anticipated for a population that strongly depends on proton transfer occurring on the excited state surface [19]. While metal-oxides have been quantified for their hydration layer at near neutral conditions by ambient pressure XPS, doing so as a function of pH has proved challenging experimentally [23,39,101,102]. Thus, the starting conditions required for the kinetic model are not well-defined. Second, the data shows bi-exponential rises and decays, which means that in principle four populations are tracked. While modeling using only two populations can fit the data, such that the pH-dependence of one population is connected from ultrafast to microsecond time scales, this constraint is hard to justify without other experimental or theoretical input. Most of the pH dependence might be carried by a single population, but exchanges with the less pH-dependent population in the region of metastability would significantly change kinetic models. Evidence of this exchange is in the decay time constants, which both exhibit a pH dependence when four populations are tracked (Figure 7.4b) while the rising time constants are largely pH-independent. The exchange is especially relevant in the case that the pH dependence is truly linear for the 20 μs population (Figure 7.4d), while it saturates for the 1 ps population (Figure 7.3c). Finally, the band-gap emission is not specific to a surface hole-polaron configuration, such that the spectra themselves cannot differentiate between the protonation of different intermediate populations.

7.6 Conclusions

Three regimes of a picosecond rise, nanosecond metastability, and microsecond decay are observed for the dynamics of an excited optical emission that is prominent when the $SrTiO_3$/aqueous interface is undergoing efficient, photo-driven oxygen evolution catalysis. While previous work has associated the mid-gap and near band-gap transitions with trapped holes on oxygen sites, or equivalently one-electron intermediates of the reaction, one missing and defining feature for such an assignment is the nanosecond metastability isolated here that connects ultrafast electron transfer processes with microsecond time-scales associated with chemical bonding. Together with the meta-stability, the distinctive pH dependence of the emission now established across the full time-range—with a half-rise at pH 11.8 for the 1 ps population and an onset at pH 11.3 for the 20 μs population—identifies an acid dissociation constant as being relevant to the type of intermediate created on the excited state surface. Given previously calculated and measured pK_a's for oxygen radicals and titanium oxide surfaces, an interpretation is advanced whereby intermediates of Ti-

$OH^{\bullet}$ formed from water occur for pH prior to the pK_a and Ti-$O^{\bullet-}$ formed from hydroxyl groups for pH beyond the pK_a. The finding of a pK_a for intermediate populations that has so far characterized proton-assisted electron transfer for homogeneous, mononuclear catalysts is unique for a heterogeneous metal-oxide, and advances our understanding of the electron and proton transfers that occur to generate oxygen evolution intermediates.

Chapter 8

Assigning Surface Hole Polaron Configurations of Titanium Oxide Materials to Excited-State Optical Absorptions

8.1 Original Publication

This work has been previously published as Boyd, C., McBride, S., Paolino, M. et al. Assigning Surface Hole Polaron Configurations of Titanium Oxide Materials to Excited-State Optical Absorptions

8.2 Introduction

For transition metal oxides, delocalized charge has a propensity to trap on a set of sites, creating a polaron-an entity for which the charge is trapped through the polarization induced by distortions in the local metal-oxide bonds (Figure 8.1a) [10, 103]. Since the charge localizes within a distorted, molecular environment, the polaron is central to how electrochemical transformations occur [104]. A prime example is water splitting at heterogeneous metal-oxide surfaces for which the application of an electrochemical potential or illumination evolves O_2 and H_2. By localizing positive charge to a set of molecular sites at the surface, hole polarons can initiate the breaking apart of water and formation of O_2. Beyond photoelectrochemistry, electron and hole polarons are also relevant to photovoltaic processes [105], long-range phase transformations [106] (e.g., metal-to-insulator), and electronic transport [107], and generically as trapped states in semiconductors.

The family of titanium oxides and their photoelectrochemistry has been a focus within the field of water splitting [89, 108–110]. According to the first-principles computations, delocalized

Figure 8.1: What are hole polarons: hole polarons in connection with optical transitions. a) Marcus diagram of ground state, excited state produced by pump pulse, and hole polaron potential energy surfaces. b) Band diagram with hole polaron midgap states that can be measured as an excited state absorption. c) Ground-state perovskite $SrTiO_3$ (001) and rutile TiO_2 (100) surfaces with orientation of pump and probe polarization relative to the surface. d) Three-dimensional representations of $SrTiO_3$ lateral, $SrTiO_3$ terminal, TiO_2 bridge, and TiO_2 terminal polarons. Electron density of trapped holes highlighted in yellow.

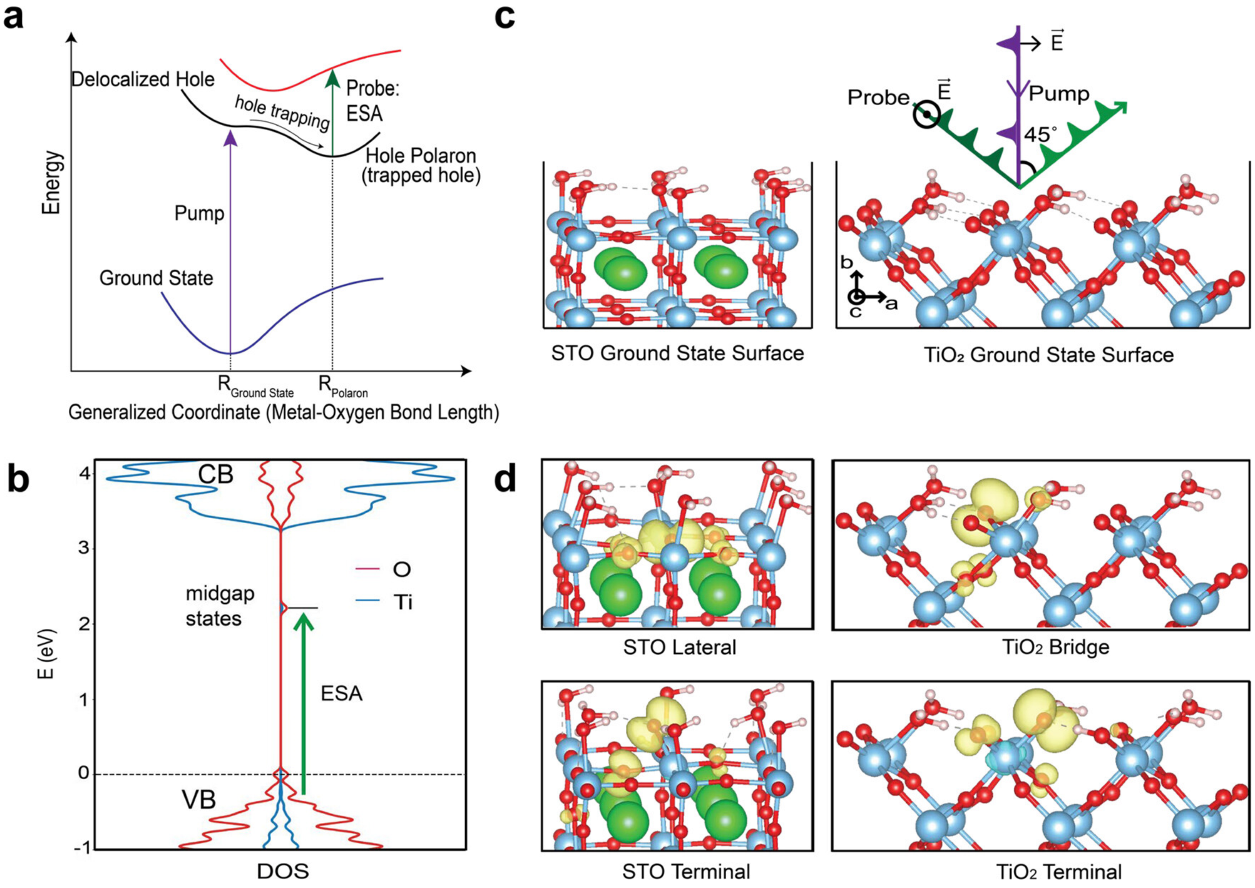

holes excited in the oxygen valence band localize on oxygen sites, resulting in the formation of hole polarons. These are stabilized by local Ti-O bond distortions, for both rutile [8, 9, 111, 112] and anatase [88, 113] TiO_2. Yet, a connection to an experimentally measured quantity has been challenging, especially on a surface. One of the most often invoked experimental signatures is an excited-state optical spectrum that occurs because the polarons create a state in the middle of a semiconductor bandgap [8, 10] For an empty hole polaron midgap state, an excited-state absorption (ESA) results when an electron from the valence band is promoted to the midgap state

(Figure 8.1b). Prominently, a hole polaron has been invoked to explain a visible ESA in the early transition metal oxides, including titanium oxides, [8] iron oxides [114–116], vanadium oxides [106], nickel oxides [116], and cobalt oxides [117]. More recently, X-ray absorption spectroscopy has tracked polaron formation by changes in the metal and oxygen edges consistent with theoretical calculations; prominent among these studies is an electron polaron in iron oxide [118–121].

Here, we enable an assignment of optical spectra to surface hole polaron configurations by considering a substantial shift in the otherwise broad visible spectrum between two different titanates: rutile TiO_2 (100) and perovskite $SrTiO_3$ (001) (Figure 8.1c). $SrTiO_3$ has a predominant TiO_2 surface crystal structure [94] for which a visible ESA has been more recently observed [28,49] and can be obtained in a single-crystal form alike to rutile TiO_2. Like the rest of the TiO_2 family, $SrTiO_3$ exhibits a high photoelectrochemical ($> 70\%$) efficiency for O_2 production [122]. On the experimental side, the excited-state absorptive spectra in the two titanium oxides are identified through a principal component analysis that extracts the spectra associated with ultrafast hole trapping. The ESA spectra are interpreted using first-principles computations. The energy levels of hole polarons localized to surface bridging and terminal oxygens (Figure 8.1d) are determined by hybrid density functional theory (DFT) and their optical absorption by time dependent DFT (TD-DFT). Overall, the red shift in the ESA by ~ 0.9 eV from rutile TiO_2 (100) (TiO_2) to perovskite $SrTiO_3$ (001) (STO) is rationalized by which optical dipoles are bright in the two materials and the initial states in the valence band from which they arise. The rationalization of the energy shift in the ESA between two titanium oxide materials via their different crystal structures paves the way for assigning hole polaron configurations and their associated dynamics in transition metal oxides, especially for oxygen evolution catalysis.

8.3 Methods

8.3.1 Experimental Procedures

For the transient reflectance experiment, pump and probe beams were derived from a regenerative Ti:Sapphire laser system (Coherent Legend, Coherent Inc., SantaClara, CA) which outputs fundamental laser pulses with a pulse length of ca. 150 fs and a wavelength centered at 800 nm at a repetition rate of 1 kHz. One part of the fundamental is guided into a CaF_2 for the generation of a white light continuum ranging from ca. 375 nm to 730 nm. The probe beam has an incident angle of ca. 45° onto the sample cell. Another portion of the fundamental is used to create UV pulses in a third harmonic generation set-up, resulting in a center wavelength of 266 nm. The photon energy in those pulses exceeds the band gap energies of TiO_2 and STO and is therefore sufficient for band gap excitation of both materials. To alternate between probing the sample in ground and excited state, the pump beam is guided through a chopper resulting in a 500 Hz repetition rate. The delay between pump and probe pulses was varied using the mechanical delay stage (MTM250CC1; Newport, Inc). For each delay a spectrum was recorded with the spectrometer ((Lightfield Pixis, Princeton Instruments). To cover a broad bandwidth the experiment was carried out at two different grating positions and merged in preprocessing. To correct chirp effects, a wavelength dependent t0 correction was done.

All purchased rutile TiO_2 (100) crystals were manufactured with the extraordinary axis, denoted as c-axis in Figure 8.1c, directed towards one side of the sample, easily identifiable by notches. The samples were mounted with the c-axis positioned vertical and the polarization of the probe pulses was set parallel to this axis, i.e., vertical. Conversely, the pump pulse polarization was horizontal, perpendicular to the extraordinary crystal axis.

Nb-doped $SrTiO_3$ and TiO_2 single crystals were obtained from MTI corporation and Crystech respectively. The side exposed to the probe is chemo-mechanically polished and the sample thickness is 0.5 mm. Samples were attached to custom made sample containers with liquid tape and placed in a home-built electrochemical cell. All experiments were carried out in unbuffered, sodium sulfate, pH 7 electrolyte. The electrolyte pH was measured before and after each experiment to ensure that the pH remained relatively constant during TR measurements.

Data was taken in either closed circuit (CC) or open circuit (OC) conditions. In closed circuit conditions, a potential is applied to the back of the sample. The front of the sample, an Ag/AgCl (3M KCl) electrode and a Pt wire served as the working, reference, and counter electrodes of the electrochemical cell, respectively. For CC, the potential was kept at 0 V throughout all experiments and was controlled by a CHI650E Potentiostat (CH Instruments, Austin, TX) via the copper wire at the back of the sample. For OC, the electrical circuit is disconnected from the back of the sample.

8.3.2 Theoretical Procedures

First-principles hybrid DFT polaron computations were performed in the CP2K package using the truncated PBE0 (α) functional with a cutoff radius of 6 angstroms [123–125]. We used α=0.15, which is the fraction of exact exchange determined to both reproduce the band gap and satisfy the generalized Koopmans' condition for electron and hole polarons in bulk STO and TiO_2 (Figure F.1). This value of α did not satisfy Koopmans' condition for all of the surface polarons (Figure F.2); where this was the case, we report the single-particle level of the occupied polaron state, which is near-constant with varied α. This method is adopted from the work of Chen et al. (2022) on defects in 2D materials [126]. Detailed parametrization of the hybrid functional is in Appendix F.1. Polarons were modeled using a four-layer slab with 16 active sites (4x4) in 15 angstroms of vacuum. Only the Γ-point of the Brillouin zone was sampled. We used the Gaussian plane wave method with Geodecker-Teter-Hutter pseudopotentials and primary basis sets of triple- or double-zeta quality with valence and polarization [127–129]. Hybrid computations were accelerated with the auxiliary density matrix method (ADMM). For the pristine bulk configuration, atomic positions and volume were relaxed until all ionic forces were under 0.01 eV/angstrom. Slabs and surface polarons were relaxed in fixed volume until all forces were under 0.01 eV/angstrom.

Surfaces were modeled with 1ML water coverage. Polaron configurations were determined by distorting the lattice around an oxygen atom, removing one electron, and allowing the atoms to relax in fixed volume until the forces on all atoms was less than 0.01 eV/angstrom.

Finite size corrections were applied to total energy and single-particle levels using the scheme of Falleta et. al. [130] The frequency-dependent dielectric constants were calculated with the PBE functional using density functional perturbation theory.

Linear-response (LR)-TDDFT was performed using the implementation in the CP2K package and solving the Casida equation [131, 132]. We used the hybrid functional in the kernel and computed the first 10 vertical excitations to a convergence of 10^{-7} eV.

8.4 Results

8.4.1 Absoprtive Components of TiO_2 and STO

Figure 8.2: Singular value decomposition (SVD) analysis: (a) contour plot of 0.5% Nb-TiO_2 (100) taken at 0.1 mJ/cm^2 in open-circuit, pH 7 conditions. Maximum intensity normalized to 1. (b) Contour plot of 0.5% Nb-STO taken at 0.04 mJ/cm^2 in open-circuit, pH 7 conditions. Maximum intensity normalized to 1. (c) Singular values for TiO_2 (open circles) and STO (filled circles) from the SVD analysis. (d) First (U_1) and second (U_2) spectral components of TiO_2 (red, purple) and STO (orange, blue) and (e) weighted first ($S_1 \cdot V_1$) and second kinetic components ($S_2 \cdot V_2$) for TiO_2 (red, purple) and STO (orange, blue).

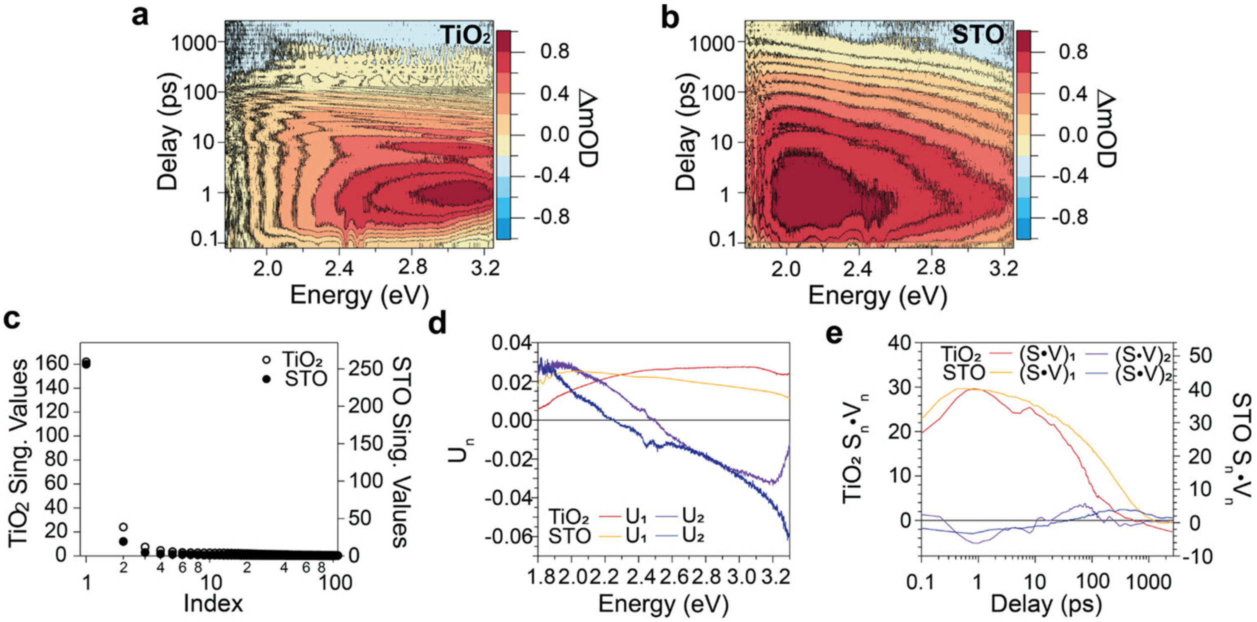

Normalized transient optical spectra of the 0.5% Nb-STO and 0.5% Nb- TiO_2 surfaces in pH 7, OC conditions are shown in Figure 8.2a and 8.2b, respectively. The color scale is the optical density of the measured change in reflectivity (10^{-3} OD = mOD). We define the change in reflectivity as ΔR = -log(R_{on}/R_{off}) where R_{on} and R_{off} are the measured intensities of the broadband reflected light with and without the pump excitation; in reflectivity, the pump-probe signals arise from a depth $d \sim \lambda/4\pi n$ [92], where n is the real part of the refractive index, and for the wavelengths λ, probed d is 10-20 nm. Note that ΔR is positive when $R_{on} < R_{off}$ and negative when $R_{on} > R_{off}$. In the case that the excited state is due dominantly to a change in absorptivity (rather than a change in the real part of the polarization), a positive ΔR corresponds to an excited-state absorption (ESA) and a negative ΔR signifies an emission. An ultrafast ESA with a fast rise and a decay on the picosecond scale is clearly present in both STO and TiO_2 below their respective band gaps (STO: 3.2 eV, TiO_2: 3 eV), for which there is little ground-state absorption; Figure 2.5 shows the real and imaginary refractive indices for TiO_2 and STO. That the ESA appears well below the band gaps in both systems suggests the appearance of midgap or trapped states. The ESA appears similarly for CC (0 V vs Ag/AgCl) and OC (floating potential on electrode) conditions (Figure 3.4a), for which the transient response of the electric field at the n-type semiconductor/electrolyte interface will differ. The ESA also appears in undoped samples for which there is no built-in electric field at the interface. Together, the findings suggest that the dominant ESA component results from an ultrafast trapping process at the TiO_2, STO/aqueous interface independently of the details of the electric field. To highlight the interface in the absence of stable electric fields, we focused on OC data sets. Additionally, the experiments are performed at neutral pH. For the rutile TiO_2 (100) samples that are uniaxial, the polarization of the probe beam is kept parallel to the extraordinary c-axis. Polarization can change the intensity of the signal especially for the uniaxial rutile TiO_2 samples (Figure 3.4b). The STO samples are isotropic.

While with rutile TiO_2 only the TiO_2 surface can be exposed, for $SrTiO_3$, SrO disorder of the thermodynamically preferred TiO_2 exists. For the as-is chemo-mechanically polished surfaces, this has been determined to be as much as 30% in ultrahigh vacuum [12,94], although it has been shown to decrease with exposure to water by ambient-pressure photoelectron spectroscopy [12]; we have not treated the samples to an HF or hydrothermal etch, which would minimize the SrO exposure, due to the fragility of this pure termination to different environments by noncontact atomic force microscopy [133] and the possibility of a reconstruction to an anatase-like phase within the very surface layers especially under electrochemical conditions [134]. On the other hand, there are positive correlations experimentally that identify hole-trapping on the TiO_2 termination of STO. The hole traps in the form of surface titanium oxyls were found to create a distinctive vibration below the STO surface in the range of Ti-O stretches both experimentally and theoretically [50]. Furthermore, in an aqueous environment, surface Sr is anticipated to dissolve and, for the electrochemical conditions used here, is measured to be dissolved significantly (with respect to Ti and O) by electron microscopy [42]. For these reasons, the dominant TiO_2 termination is the one considered for surface hole trapping.

As evident by the red maximum in the contour plots, the ESA for STO occurs at a lower energy than for TiO_2, which we now quantify by a series of principal component analyses. Specifically, singular value decomposition (SVD) [71, 135] extracts pairs of spectra and kinetics from our transient reflectance data. In SVD, a data matrix is factored into a rotation, followed by a scaling, and another rotation. The rotation matrices are denoted as U and V, and the scaling matrix is represented by S. The SVD equation is summarized in Equation 8.1:

$$Data = U \cdot S \cdot V^T \tag{8.1}$$

By applying SVD to a data set, one can obtain spectra and kinetics from the orthonormal basis vectors in the U and V matrices, respectively. We refer to these as our raw spectral (U_n) and kinetic (V_n) components. The diagonal elements of the S matrix are called the singular values, and they sort the SVD components in descending order of importance (see Figure 5.1). A plot of the singular values (Figure 8.2c) shows that there is one dominant component and a non-negligible secondary component in the TiO_2 and STO data sets. Figure 5.1 shows how considering only these first two components reduces the dimensionality of the SVD analysis to a planar subspace. The first two raw spectral and kinetic SVD components in STO and TiO_2 are shown in Figure 8.2d and 8.2e, respectively. The kinetic components are weighted by the singular values as defined by $S_n \cdot V_n$. While there is a dominant component in both materials, the second component is distinctly non-negligible and occurs on a similar time scale, overlapping with the first component. To address this overlap, a constrained SVD analysis is applied, which is detailed next.

The first component spectra resemble the dominant ESA present in the data sets. Kinetic traces for the first component also rise on the ultrafast < 1 ps time scale and decay on the 10-100 ps time scale. Unlike the kinetic trace of the first component, the second component's trace is negative for the earliest time range. If one interprets the spectra in terms of a change in absorptivity in the excited state, the negative sign represents an unphysical, negative population induced by the pump. Furthermore, the second component spectrum is smoothly and broadly absorptive and emissive, which does not resemble poles in the optical spectrum due to a change in absorptivity. While the raw SVD analysis points to a 2D planar subspace to describe the spectra (Figure 8.2c and Figure 5.1), any linear combination could represent the spectral and kinetic vectors of the optical system.

To assess linear combinations that could represent different absorptivity components of pump induced populations, we introduce a matrix identity $1 = (XX^{-1})$ into our SVD equation, where X is a square matrix with a dimension corresponding to the dominant components in the raw SVD analysis. The mathematical application of X to the SVD equation is known as constrained SVD [136, 137] and is given by

$$Data = U \cdot S \cdot V^T = U \cdot (X \cdot X^{-1}) \cdot S \cdot V^T = (U \cdot X) \cdot (X^{-1} \cdot S \cdot V^T) \tag{8.2}$$

Through Equation 8.2, $U_n^t = U_n \cdot X_n$ and $V_n^t = X_n^{-1} \cdot S_n \cdot V_n^T$ are defined as the constrained spectral and kinetic vectors. By varying the elements of X, one obtains new spectral vectors in U^t as linear combinations of the initial raw SVD basis vectors. Additional information about the X matrix and how it is used to constrain the raw SVD components is outlined in Equation 5.4 and Figure 5.3.

Since many possible combinations of constrained spectra can be constructed in this manner, it is important to find ways in which the raw data could constrain the solutions and lead to physically relevant optical spectra and population dynamics. One strategy is to investigate how the ESA spectrum in the raw data changes over time. The ESA spectra as a function of time delay is shown in Figure 3.5 for the TiO_2 data set. The spectra peak at higher energies between 1 and 5 ps and then slowly shift toward lower energies between 60 and 100 ps. The shift suggests two separate ESAs occurring on different time scales, such that time slices can then be used as reference spectra for the constrained spectral components. Reference spectra were taken at 3 ps, averaged over ± 2 ps, and at 80 ps, averaged over ± 20 ps. Reference spectra extracted from all TiO_2 data sets (shown in Figure 3.6) are shown in Figure D.5. The full analysis utilized many TiO_2 data sets and constrained all those data sets' SVD components to a single reference spectrum. Finding X such that our first and second components match this reference spectrum as closely as possible provides an initial solution. From this starting point, X is varied around this solution while the population dynamics are monitored for any unphysical zero crossings. The process of constraining and refining the first and second 0.5% Nb-TiO_2 spectral components shown in Figure 8.2d is outlined in detail in Figure D.6. The constrained SVD spectra for the entire data set and the reference spectrum chosen is shown in Figure D.7; all the spectra closely resemble the reference spectrum, especially for the dominant component.

Figure 8.3 shows the results of the constrained SVD analysis for TiO_2 (Figure 8.3a) and STO (Figure 8.3b). The first contour map of Figure 8.3a shows the raw, 0.5% Nb-TiO_2 (100) data set. The other two contour maps are reconstructed from the first two components $(U^t \cdot V^t)_{1,2}$, and the first component $(U^t \cdot V^t)_1$ of the SVD analysis. From the $(U^t \cdot V^t)_{1,2}$ contour map, the first two components alone represent the key features of the overall data set, showing that the 2D planar subspace is a complete description. The $(U^t \cdot V^t)_1$ contour map shows that the dominant absorptive peak captures most of the raw data but clearly misses the lower energy absorption between 60 and 100 ps. $(U^t \cdot V^t)_2$, depicted in Figure D.11a, shows a secondary absorptive peak in this time range.

Unlike with TiO_2, STO's components are constrained such that the first component is completely absorptive and the second is completely emissive. This is done in accordance with previous work by some of us on the ESA in STO [28]. Normalized time slices of STO (shown in Figure 3.7) also support this methodology, because only one ESA is present in the experimental window. An analogous large data set to TiO_2 was used for STO (see Figure 3.8). Constrained 0.5% Nb-STO absorptive and emissive spectra (with corresponding kinetics) obtained from several linear combinations of the raw SVD components are presented in Figure D.8. The constrained spectra and kinetics for the full STO data set are highlighted in Figure D.9.

Contours of the raw data, $(U^t \cdot V^t)_{1,2}$, and $(U^t \cdot V^t)_1$ for 0.5% Nb-STO are shown in Figure 8.3b. As with TiO_2, just two components are needed to represent the main features of the STO data set. A lower-energy ESA and a high energy emission are shown in $(U^t \cdot V^t)_1$ and $(U^t \cdot V^t)_2$ (shown in Figure 3.7b), respectively. Again, the dominant ESA component shown in $(U^t \cdot V^t)_1$ captures most

Figure 8.3: Constrained SVD analysis: Contours of data, the data reconstructed from the first two spectral and kinetic components $(U^t \cdot V^t)_{1,2}$, and the first constrained spectral and kinetic component $(U^t \cdot V^t)_1$, for a) TiO_2 and b) STO.

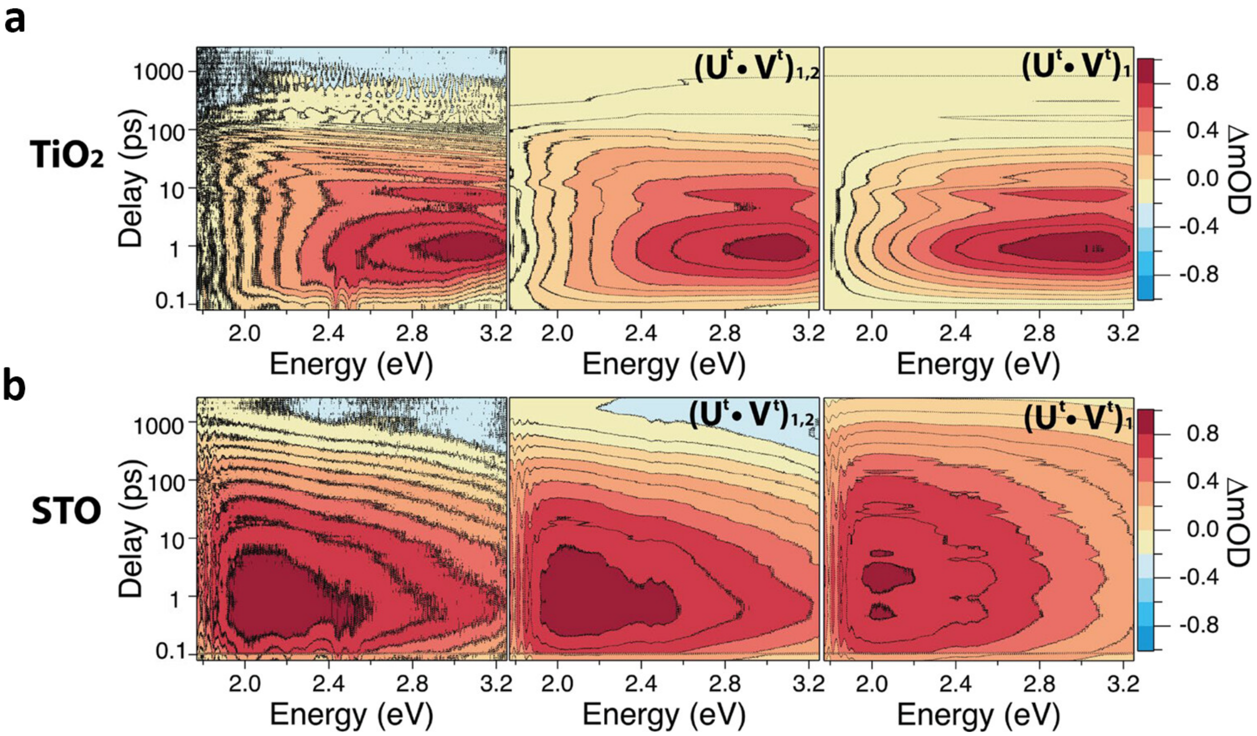

of the raw contour map. Note that the emissive signal present in OC pH 7 is quite small relative to the ESA. The sign change observed in $(U^t \cdot V^t)_2$ is an indication that the solution can be further optimized; this will be discussed in the next section. However, Figure 8.3a,b already illustrates that constrained SVD can be used to effectively isolate key spectra and kinetic components in the transient reflectance optical data.

8.4.2 Doping Modulation of Absorptive Components

In the previous section, the constrained SVD components for single TiO_2 and STO data sets were extracted. In a single data set, it is possible that a range of mathematical solutions fulfills our objective criteria for SVD basis components. To achieve a more accurate representation of the physical spectra, it can be beneficial to modulate parameters such that the same spectra are preserved, but with different spectral weights and kinetics. Finding a common solution that is valid for different external conditions restricts the analysis and can result in a more accurate description of the actual processes. Depending on the nature of the states underlying the optical signals, the appropriate external conditions can be unique to different materials. In the case of TiO_2, it was found that varying the Nb doping affects the population dynamics of the secondary absorptive component. In the case of STO, from a previous work [28], pH affects the population dynamics of the secondary emissive component.

In addition to the 0.5% Nb-TiO_2 (100) sample discussed above, time-resolved spectra were also taken for 0.05% Nb-TiO_2 (100) and undoped TiO_2 (100). Like in the 0.5% Nb sample, a dominant ESA peak in the range of 2.8 to 3.2 eV with a decay on the picosecond scale is observed. A secondary absorptive component with a decay on the ps-ns scale also appears. However, by examining the contour plots in Figure 8.4a, differences in the dynamics and weights of the different components become apparent. Compared to the 0.5% Nb sample, in the lower doped ones, the secondary component centered around 2 eV appears more pronounced and extends to longer times. The same constrained SVD procedure was applied to both the 0.05% Nb-doped and undoped samples. Within the accuracy of our experiment, the same spectral components were obtained across

Figure 8.4: Nb-doping dependence of TiO$_2$ and constrained SVD analysis: a) Contours of 0.5, 0.05, and 0% Nb-TiO2 (100) reconstructed from first two SVD spectral and kinetic components. Maximum normalized to 1. b) Constrained first ($U_1 \cdot X_1$, red) and second ($U_2 \cdot X_2$ purple) spectral SVD components for 0.5, 0.05, 0% Nb-TiO$_2$. c) Constrained SVD kinetics associated with the spectra shown in b).

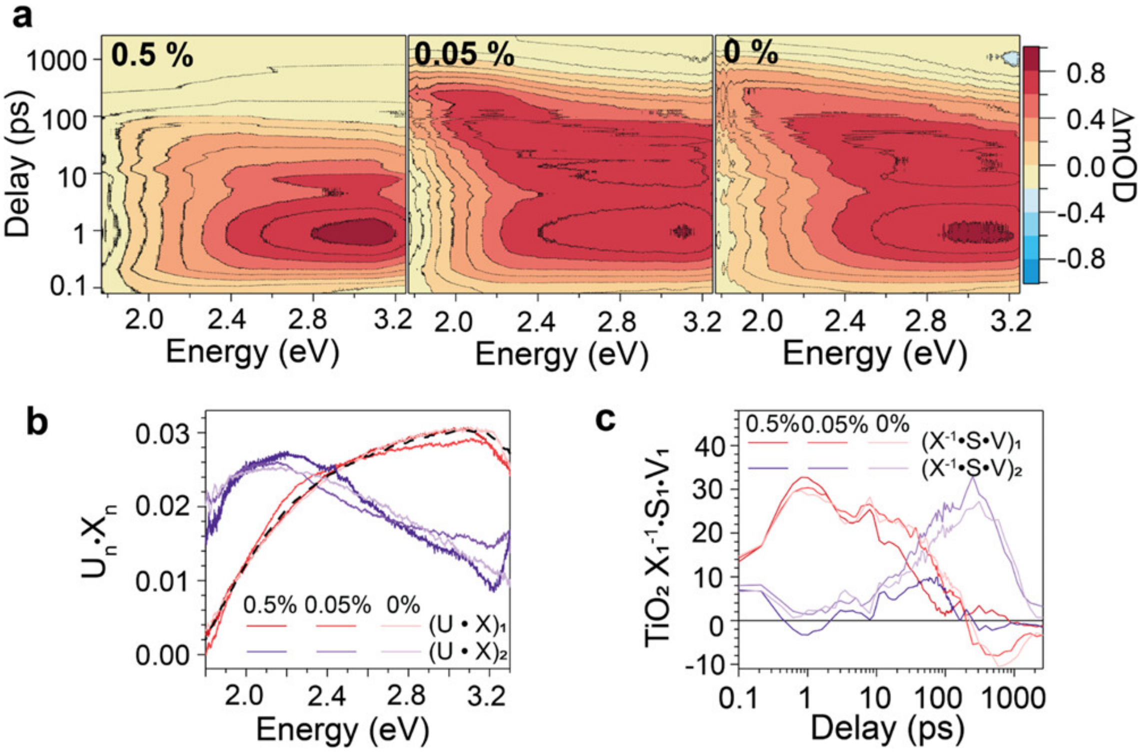

the different doping levels, as shown in Figure 8.4b. This corroborates the assumption that the general electronic states, transitions, and processes remain consistent. However, the second component shows a significant increase in population and lifetime (Figure 8.4c); the population increases roughly three times while the lifetime is extended by approximately a factor of 10. The consistency of the spectra alongside these changes in the secondary component allow for the unambiguous extraction of the first absorptive component. The analysis with which we compare to theory utilizes an averaged constrained spectrum derived from multiple data sets (dotted black line in Figure 8.4b obtained in Figure D.7).

For STO, a doping dependence does not allow for an accurate separation between the dominant absorptive and secondary emissive component (see Figure D.10). For the undoped sample, the second component is too weak to be extracted. In a previous work on 0.1% Nb-STO, [28] accurate separation of the dominant ESA component was achieved through pH-dependent data sets taken under OC and CC conditions. The spectrum shown in this previous work was obtained using a data set with varying pH and a phosphate buffer. To use analogous experimental conditions, a data set without phosphate buffer (shown in 3.3b) was used for this study. Increasing the pH from 7 to 14 increased the emission while keeping the absorption constant. Full details on the OC, pH-dependent constrained STO analysis are shown in Figures 3.3 and B.6. The variation in emission with pH is more significant for CC conditions (see Figures 3.3 and B.5). Consequently, the constrained, averaged ESA SVD spectrum obtained from the CC, pH-dependent data set of STO is used in comparison to theoretical calculations below.

In the last two sections, it was explained how spectra of specific components in our data can be extracted. It was shown that for both TiO_2 and STO, one absorptive component in the visible range is the dominant optical transition by the singular values of raw SVD. In both materials, a weaker second component is present in the data set, overlaying the first component. Due to the nature of the secondary component in each material, it was found that different approaches to constraining the raw SVD components were needed. Varying the doping of TiO_2 significantly modifies the population dynamics of the secondary absorptive component while preserving the spectrum of the dominant ESA. For STO, significantly modulating the emissive component with pH separates the dominant ESA from the emission. It is important to emphasize that the thorough analysis of the secondary component provided above is necessary to extract the dominant ESA component in STO and TiO_2.

While the population dynamics of the ESA in TiO_2 and STO are similar with a picosecond rise and nanosecond decay, the spectrum shifts in energy, which we quantify here. Just comparing the maxima of the two raw data sets (Figure 8.2a,b) yields an energy shift of 1.1 eV. The maximum of the dominant ESA component of the 0.5% Nb-doped samples of Figure 8.3 exhibits a red shift of 1 eV from TiO_2 to STO (Figure F.8a). The averaged constrained ESA STO spectrum and the averaged constrained ESA TiO_2 spectrum are shown in Figure F.8b. Analyses of these ESA spectra yield a redshift of 0.9 eV from TiO_2 (maximum at 3.1 eV) to STO (maximum at 2.2 eV). While explaining the broad optical spectrum is a much more extensive endeavor, this analysis provides an experimental benchmark for the significant energy shift.

8.4.3 DFT Calculations of Electronic Levels of TiO_2 and STO

First-principles DFT computations were performed to investigate the absorptive transitions between valence band states and localized midgap hole states at the perovskite STO (001) and rutile TiO_2 (100) surfaces. We model holes localized either in the bulk region of the slab or at the surface as Ti-OH$^{\bullet}$, O$^{\bullet-}$, or $Ti_2O^{\bullet-}$ radicals. Ti-OH$^{\bullet}$ and O$^{\bullet-}$ are terminal radicals to the surface referred to as OH$^{\bullet}$ and O$^{\bullet-}$; $Ti_2O^{\bullet-}$ are radicals parallel to the surface, referred to as lateral in STO and bridge in TiO_2. Figure 8.5 shows the spin density of holes for the different surface polarons: bridge $Ti_2O^{\bullet-}$ and terminal O$^{\bullet-}$ for TiO_2 and lateral $Ti_2O^{\bullet-}$ and terminal O$^{\bullet-}$ for STO. Holes did

Figure 8.5: Computed surface trapped holes in TiO_2 and STO. (a, b) Side view of structure and spin density of holes trapped on the surface of (a) rutile TiO_2 and (b) STO at bridge and terminal sites. The electronic density is shown as yellow isosurfaces at a spin density of 0.005. (c, d) Computed vertical electronic energy levels for trapped surface holes and bulk polarons in (c) rutile TiO_2 and (d) STO. Arrows indicate vertical transitions from VBM to hole states.

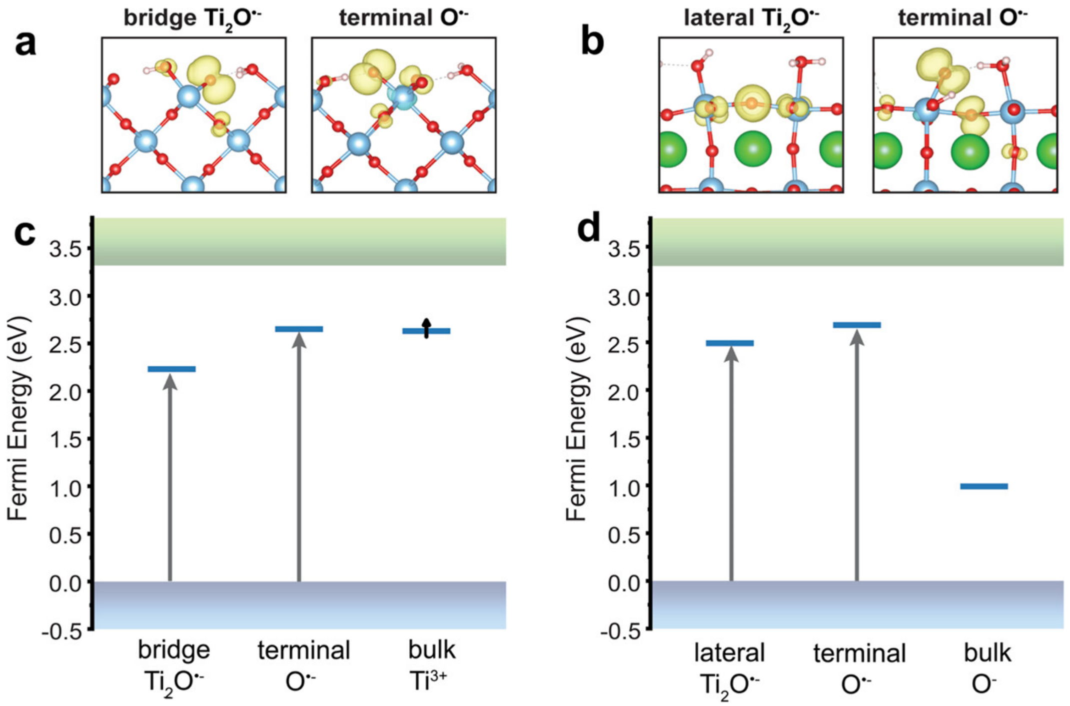

not trap on $OH^{\bullet}$ in either STO or TiO_2, preferring the adjacent lateral/bridge site. In STO, we find that the lowest energy configuration is an O 2p hole at a lateral $Ti_2O^{\bullet -}$ site, about 0.2 eV lower in energy than a hole trapped at the terminal $O^{\bullet -}$ site, in agreement with a previous work [49]. Conversely, on TiO_2, we find that holes most favorably localize at the terminal $O^{\bullet -}$, with a binding energy about 0.4 eV lower than at the bridge site. The surface hole polarons have large self-trapping energies, defined as the energy difference between the polaron state and a delocalized valence band hole, in the range of 300-900 meV. We thus expect holes to trap at the surface on the ultrafast time scale. Small-hole polarons form in the bulk in STO and not in TiO_2; these polarons have a small self-trapping energy ($\sim$ 70 meV) compared to the surface polarons [138].

Figure 8.5 also shows the midgap hole states created in the oxide band gap corresponding to the stable surface and bulk polarons. Surface hole polarons on STO and TiO_2 create midgap unoccupied hole states between 2.3 and 2.7 eV above the valence band edge. Computed binding energies and midgap levels are shown in Table F.1. The bulk hole polaron in rutile TiO_2 does not form, but we show as reference the electron polaron. For STO, the bulk polaron forms but in a very different energy range around 0.9 eV above the valence band edge.

8.4.4 TD-DFT Calculations of Optical Dipoles of Different Titanium Oxides

To further distinguish between surface polarons, time-dependent density functional theory (TD-DFT) was used to compute transition optical dipole from valence band states to the unoccupied hole state for each surface polaron. Figure 8.6 plots the oscillator strength computed with TD-DFT as they relate to the optical absorption. We show only the most stable polarons (STO lateral and TiO_2 terminal) for clarity. We expect the highest population of these polarons, and therefore the brightest signature. We also expect these polarons to be the brightest from theory. The optical dipole of the STO terminal and TiO_2 bridge polarons is shown in Figure F.3. The absorption by bulk polarons in both materials is expected to be much lower in energy than is detectable in experiment using a white-light probe in the visible range and is not included.

From TD-DFT, the STO lateral polaron has an absorption peak around 2.3 eV, and the

TiO_2 terminal polaron has an absorption peak around 3.0 eV. The STO optical transitions are red-shifted by 700 meV compared to TiO_2. We attribute this shift to three factors: (a) the energy difference between the polaron midgap levels, (b) the difference in exciton binding energy for STO and TiO_2, and (c) the difference in valence band density of states for TiO_2 and STO. The polaron midgap state is 2.5 eV for STO and 2.7 eV for TiO_2, a difference of 200 meV. Both STO and TiO_2 optical transitions are lower in energy than the electronic transitions from which they arise, which is consistent with the effects of exciton binding. Electron-hole interactions, which are included in TD-DFT, lower the energy of optical transitions compared to electronic transitions. The computed exciton binding energy is large in STO, around 300 meV, while in TiO_2, it is under 50 meV (Figure F.5). This 250 meV difference in exciton binding energies plays a significant role in the observed red shift. Finally, TiO_2 has low density of states close to the valence band edge, with higher density of states in the band below the valence band maximum (Figure F.5). The strongest absorption in TiO_2 arises from transitions originating $\sim$ 200 meV below the VBM to the hole polaron, as transitions directly from the VBM are weak (Figure F.6). A detailed analysis of the

Figure 8.6: Computed optical dipole of surface trapped holes. (a, b) Optical dipole of first 10 vertical excitations (black) from the valence band to trapped hole states at, respectively, TiO_2 terminal $O^{\bullet -}$ and STO lateral $Ti_2O^{\bullet -}$. Spectral line shape (red) is approximated with Gaussian broadening with fwhm = 800 meV. Dipole is reported for probe electric field parallel to the extraordinary axis in TiO_2 and averaged in the plane of the surface for STO.

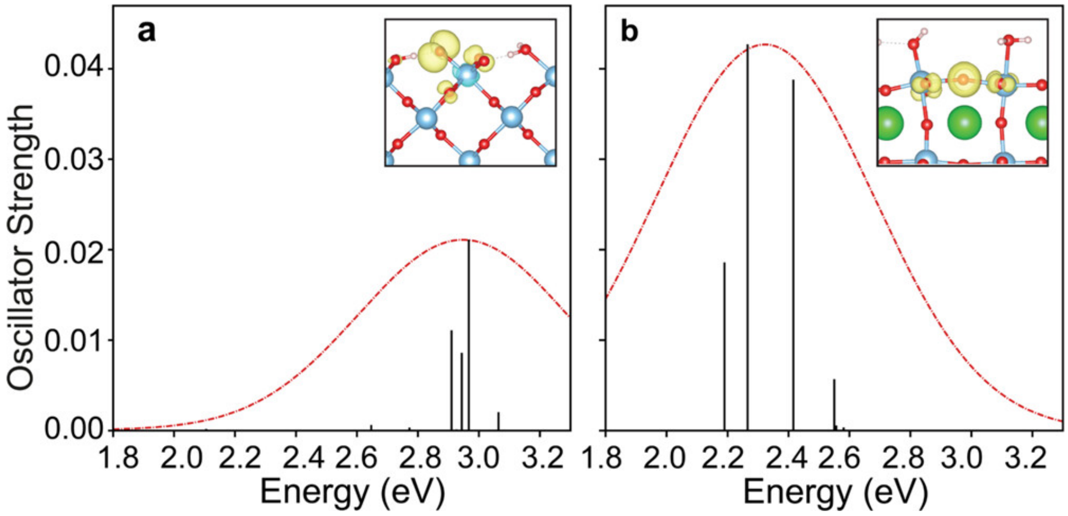

vertical transitions and the origin of the shift is provided in Section F.4. A 2.25 eV absorption in STO is close to the experimentally observed peak at 2.2 eV. In TiO_2, the experimentally observed 3.1 eV peak is associated with the terminal polaron seen theoretically at 2.95 eV.

8.5 Discussion

8.5.1 Comparing ESA to Calculated Optical Dipoles of Hole Polarons

Within the family of titanium oxides, theoretical calculations, while differing in detail, find unoccupied midgap levels for hole polarons with transitions from the valence band in the visible range of 2-3 eV and larger self-trapping energies for surface than for bulk hole polarons. The midgap states and self-trapping energies are consistent with the terminal and lattice (bridge, lateral) hole polarons we found for rutile TiO_2 (100) and perovskite STO. For example, previous work on the rutile TiO_2 (110) surface calculates midgap levels from the VB edge at 2.8 eV for the terminal and 2.4 eV for the bridge intermediate; formation free energies are 1 and 0.5 eV, respectively [8]. For anatase TiO_2, calculations show that surface hole polarons form states well above the VB edge and the terminal $O^{\bullet-}$ preferably forms at undercoordinated surface sites. [87] For STO, the bulk hole polaron with 2.5 eV visible emission from the conduction band to the midgap state and a smaller self-trapping energy has been the focus of photoluminescence studies [65] and DFT calculations [62]; the terminal and lateral hole polarons were investigated in more recent studies [49, 50] by some of us, but without a spectral assignment in the visible range.

Due to the complexity of first-principles calculations, they always rely on a series of assumptions that aim to best reflect the predominant factors involved in hole trapping at an aqueous interface of a transition metal oxide. First, the computational results directly depend on the DFT functional used. Here, we use a hybrid functional as required to localize the polaron and tune the amount of exact exchange by ensuring Koopmans' condition in the bulk. Excitonic effects are captured using TD-DFT. Our model also assumes only a specific coverage. Namely, the hole polarons are calculated from a hydrated surface for which deprotonated waters are the trapping sites.

This is justified as the experiments are conducted near neutral pH for which water dissociation can provide deprotonated water sites; such water dissociation is relevant experimentally to STO [12] and TiO_2 [139] to varying degrees. No vibrational effects are included in our model. We neglect the effect of the Nb doping on the vertical transitions, as these low-concentration shallow donors are not expected to significantly impact the electronic structure. Finally, we also neglect the effect of solvent and applied electric field as our slabs are computed in vacuum. Given these simplifications, a form of direct comparison between theory and experiment is critical for demonstrating the existence of surface hole polarons despite both suggesting that absorptions occur in the visible range.

On the experimental side, the complexity lies in the extraction of broad spectral bands from the time and energy contour plots. As described above, this involves a constrained singular value decomposition analysis that separates out time independent poles of spectral absorption and emission. Thus, an underlying assumption is that the excited-state spectra relate to populations that change the imaginary part of the dielectric function. Since the changes are probed in reflectance, the real part of the dielectric function could play a role. However, the spectral changes extend significantly below the band gap and any dispersive change of the real part due to electron and hole excitations would be confined to the near band gap region. Furthermore, we utilize external conditions (Nb doping for TiO_2 and pH for $SrTiO_3$) that change the population dynamics of the different components but not the shape of the dominant absorptive spectral component, which identifies it as an underlying pole in the optical spectroscopy. The analyses point to underlying mechanisms for how the populations in optical transitions change with external conditions, which has been suggested previously for the pH dependence [28], while their nature regarding Nb doping is left for future work. Finally, we utilize Nb doping experimentally to explore all the necessary conditions for the analysis. Low percentages of Nb doping in titanium oxides contribute largely delocalized electrons to the conduction band with negligible changes to the electronic structure due to the comparative size of Nb(V) and Ti(IV) [93], leading to shallow donor states; such low concentrations are challenging to include explicitly with doping in the computations. Furthermore, we do not expect shallow donors to affect absorptive transitions from the valence band to states in the middle of the gap and the dominant absorptive transition seen experimentally is not affected by Nb doping (see Figure 8.4).

Despite the assumptions within the theory and the experimental analyses, our model matches reasonably well the experimental spectra both in the absolute peak positions and in the relative shift between rutile TiO_2 and STO, as illustrated in Figure 8.7, which directly compares theory and experiment. Here, for a better comparison, the experimental and theoretical data are normalized to one. The experimental spectra are normalized with respect to their maximum. The theoretical stick spectra are normalized to the optical transition with highest intensity. The stick spectra are broadened with a Gaussian line shape and width of 800 meV to suggest what the theoretically predicted spectra might look like after broadening due to vibronic effects. The experimental data compared to the less probable hole polarons is shown in Figure F.7. The shallow maxima in the experimental data are found at 2.2 eV for STO and 3.1 eV for TiO_2. The theory predicts maxima at 2.25 and 2.95 eV for STO and TiO_2, respectively. The comparison shows how the transition optical dipole from the valence band, considering both the edge and deeper states in the valence band, being bright for certain configurations of hole polarons in TiO_2 (terminal $O^{\bullet -}$) and STO (lateral $Ti_2O^{\bullet -}$) can rationalize the shift in the ESA seen experimentally. The rationalization of the large shift in the broad spectra with the theoretical calculations also makes an alternative assignment for absorptions below the bandgap-lower cross-section intraband transitions within the conduction or valence band due to delocalized electrons and holes respectively-less viable.

However, the comparison does not yet describe the shallow maxima or the broad bandwidth of the optical spectra. To do so would require including the heterogeneity of the populations that arise from quite different self-trapping energies for each hole polaron configuration. Furthermore, it would require modeling of vibrational effects from the surfaces and the absorbates as well as from the solvent. On the other hand, the good match between experiment and theory despite the neglect of the electric field in the model aligns with the experimental observation that the ESA is not affected when the built-in electric field (e.g., Schottky barrier and Helmholtz layer [40]) is strongly

Figure 8.7: Comparison between calculated optical dipoles and excited-state absorption: Excited-state absorption from constrained SVD analysis of TiO_2 (red, left) and STO (orange, right) across a larger data set (solid lines) compared with calculated absorption intensities of the most stable hole polarons in TiO_2 (terminal) and STO (lateral). The theoretically calculated absorption intensities are normalized and shown as sticks. The dashed lines show theoretical absorption spectra obtained by Gaussian broadening of the single transitions with an FWHM of 800 meV.

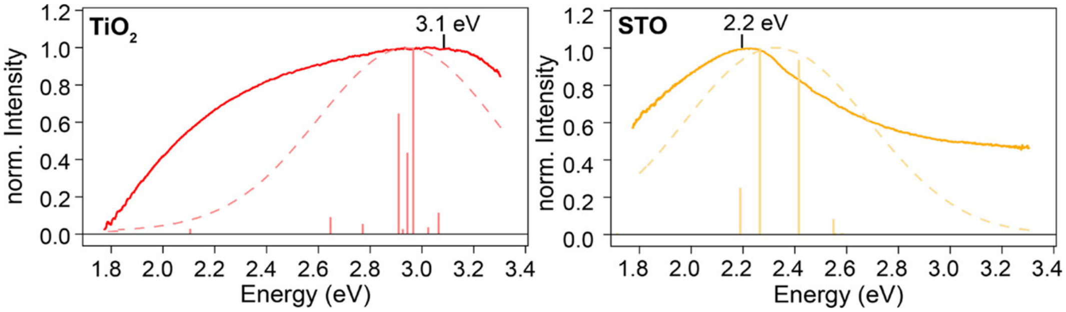

modulated across the aqueous interface, which includes n-doped and undoped crystals and open- and closed-circuit arrangements. Next to the spectral shapes, we note that the large, computed trapping energy for hole polaron on both TiO_2 and STO surfaces agrees with the substantial and fast (< 1 ps) trapping process observed experimentally.

The dominant ESA compared to the TD-DFT calculations exhibits a nanosecond decay in addition to the ultrafast rise. While interpreting such dynamics is beyond the scope of this work, we highlight that the decay dynamics could have various origins. Upon hole trapping, the population could evolve to an intermediate configuration facilitated by surface proton transfer characterized by separate optical dipole transition(s) from the band edges. Chemical exchange could occur between terminal and bridge/lateral hole polarons, facilitated by surface diffusion and proton transfer. Indeed, such surface dynamics have been suggested by first-principles molecular dynamics simulations [8, 9, 113, 140] and are particular to proton migration within the hydration layer [91, 140]. Alternatively, since not a single hole but a hole population is created by the pump pulse in the experiment, changes to the valence band states as the delocalized hole population becomes trapped could modify the optical transitions.

8.6 Conclusions

The different crystal structures of perovskite $SrTiO_3$ (001) and rutile TiO_2 (100) result in an energy shift of optical transitions associated with transient hole polarons, an important intermediate in the oxygen evolution reaction on titanium oxide materials. First-principles computations predict the formation of two distinct hole polaron configurations stable in both materials. For STO, the most stable hole polaron is lateral, and for TiO_2, it is terminal to the surface. While the location of the unoccupied midgap state relative to the valence band edge is calculated to be similar in the two cases (differing by 0.2 eV), the measured excited-state absorptions differ significantly by ~ 0.9 eV. This discrepancy is explained by computing optical absorption spectra with TD-DFT. The hole polaron configuration being bright for the most stable polarons in each material, the strong exciton binding energy of STO, and the high probability for transitions originating from deeper valence band states in TiO_2 rationalizes the shift seen experimentally. The agreement between experiment and theory assigns the lateral STO and terminal TiO_2 polarons to the dominant transition optical dipoles observed by the ultrafast excited-state absorption. To be able to fully model the broad optical spectra, vibronic effects and relative populations of different configurations based on self-trapping energies should be included. Differences in the polaron configurations could affect the reaction mechanism of OER, so a deeper understanding of how their relative populations describe the optical spectra would advance our understanding of water splitting catalysis.

Chapter 9

Analysis of Second Order Raman Modes in Bulk STO Crystal Using Femtosecond Stimulated Raman Spectroscopy

9.1 Introduction

The vibrational structure of single-crystal $SrTiO_3$ (STO), along with other cubic perovskites, has been studied through Raman spectroscopy for decades. The crystal structure of STO is one of high symmetry, belonging to the O_h point group [141]. The phonon modes originating within the Brillouin zone center (those which are first order) all have F_{1u} or F_{2u} symmetry which are Raman inactive for this point group. A common explanation for strong Raman peaks observed in STO is second-order assignment to the Raman peaks due to phonon overtones and combination bands [142]. Multiple phonons contributing to the spectra means that phonons can originate from anywhere in the Brillouin zone and satisfy energy and momentum conservation.

First-order Raman spectra have been described in STO and other cubic perovskites under a few special conditions. Studies have used external applied electric fields to break the symmetry associated with the forbidden modes, resulting in first order Raman spectra for $KTaO_3$ [143] in the cubic phase, and for $BaTiO_3$ [144] in the tetragonal phase. Thin films of STO have shown to possess first order Raman peaks up to room temperature that have been attributed to micropolar regions due to oxygen vacancies [145]. Several optical modes, inactive for first order Raman, have been shown to be active for hyper-Raman experiments [146,147]. Perovskites which possess a cubic structure have been shown to undergo a phase transition below a critical temperature [148, 149], resulting in Raman peaks that have been described as both first order [150] and second order

[142]. However, at room temperature, at atmospheric pressure, for bulk crystals in the absence of external electric fields, the Raman spectrum of STO is typically attributed to second order phonon contributions [142, 150–152].

Femtosecond stimulated Raman spectroscopy (FSRS) is a technique used to produce Raman spectra with a much higher signal to noise ratio than that of spontaneous Raman. It is a 2-pulse technique involving a spectrally narrow and temporally wide pump beam which defines the fundamental frequency (Rayliegh scattering frequency), and a broadband ps scale probe pulse. FSRS not only produces Raman active photons at a much higher yield than spontaneous Raman, but results in coherent photons carried by the probe envelope, which are much easier to collect [153] (see Section 9.2.1 for details). While FSRS has been used (often with incorporated time resolution) to probe biological and chemical reaction dynamics [35, 154], it has seldom been used on solid crystals, and no FSRS spectra for solid crystal STO have been reported. Theoretical descriptions of the FSRS phenomenon have been developed which predict the behavior of Raman peaks with respect to pump intensity [155, 156]. Additionally, semi-classical models have been used to explain the coupling between the fundamental Raman pulse and Raman active vibrations within the medium for first and second order phenomena [157] (see Section 9.4). Yet, no models that predict the relationship between pump energy and Raman peak intensity for second order FSRS spectra exist. In this work, we present the first FSRS spectra of bulk STO crystal and show that the Raman is linear with pump energy for the first 7 stokes peaks. Additionally, I will present the semiclassical approach to building a model for the relationship between second order FSRS peaks and pump intensity, the development of which is an ongoing effort.

9.2 Experimental

9.2.1 Technique

Femtosecond stimulated Raman spectroscopy is a two-pulse technique, capable of producing sharp spectral features corresponding to Raman active vibrational transitions. The pulses involved

Figure 9.1: Pulses responsible for the Stimulated Raman effect. Two pulses are overlapped in space and time on a Raman active medium to produce the effect. a) A narrow bandwidth Raman pump ω_p and a broadband probe ω_s stimulate vibrational transitions within the medium and result in Raman active transitions at $\omega_\nu = \omega_p - \omega_s$. The emitted photons ($\omega_s$) are carried by the probe envelope after interacting with the medium. b) The broadband probe is narrow in the time domain, while the Raman pulse is wide; this is necessary since the Raman pump must interact twice with the active medium to generate the effect. c) Diagram representing the vibrational energy level shift and photons associated with stimulated Raman.

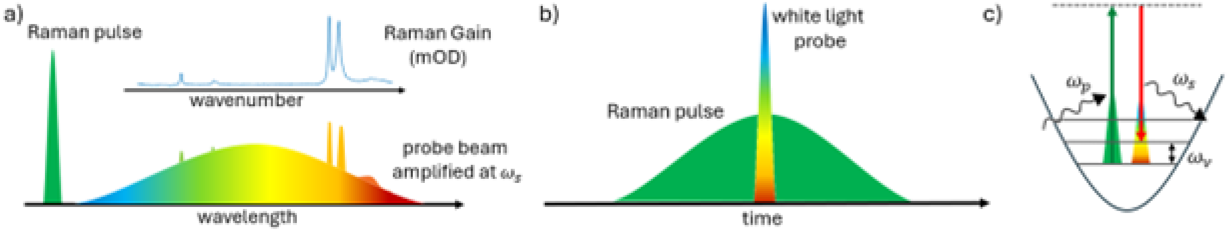

are a Raman pump pulse which is spectrally narrow and temporally broad and a broadband Raman probe pulse, which is temporally narrow (Figure 9.1a,b). The stimulated Raman effect occurs when these 2 pulses are overlapped in time and space on a Raman active medium. Stokes Raman transitions occur at frequency $\omega_\nu = \omega_p - \omega_s$ where ω_p is the Raman pump frequency and ω_s is the probe frequency (Figure 9.1c). Pump photons at frequency ω_p will exchange energy with the scattering medium via a change in vibrational energy corresponding to ω_ν, through the emission of a photon of energy ω_s. Stimulated Raman spectra are plotted as energy shift with respect to ω_p, in units of wavenumber. The peaks associated with the stimulated Raman process are the same as those which occur in spontaneous Raman scattering, with a fundamental Raman pulse at frequency ω_p [35, 154, 158].

Though the two techniques in principle provide the same vibrational information, stimulated Raman spectroscopy has several advantages over spontaneous Raman scattering. Firstly, stimulated Raman spectroscopy produces a strongly amplified signal compared to spontaneous Raman. This is evident through the differential scattering cross-section for stimulated Raman which is given by [153]:

$$\frac{d^2\sigma_{srs}}{d\Omega d\omega_s} = \frac{32\pi^2\hbar\omega_p\omega_s F(\omega_s)}{c^2 N}\,\mathrm{Im}(\chi_R^3) \tag{9.1}$$

The cross-section depends on the number of scatterers N, the imaginary part of the third order Raman susceptibility $\mathrm{Im}(\chi_R^3)$, and the spectral photon flux of the probe $F(\omega_s)$. To illustrate the degree to which the Raman signal is amplified by this technique, we turn to the ratio of the stimulated to spontaneous Raman differential scattering cross-sections [153]:

$$\frac{d^2\sigma_{srs}}{d^2\sigma_{spont}} = \frac{32\pi^3 c^2}{\omega_s^2} F(\omega_s) \tag{9.2}$$

For a typical probe photon flux of $10^{12} photons/cm^2/s/Hz$, the approximate ratio of SRS to spontaneous Raman is $\sim 10^7$, a quite significant improvement [153]. Secondly, the stimulated Raman effect results in the emission of coherent, self-phase matched photons. The interaction of the Raman pump and probe with the Raman active medium place the system in a vibrationally coherent state. As the coherence decays, the Raman pump interacts with the system a second time, resulting in the emission of a photon at frequency ω_s (Figure 9.1b). The FSRS emission is self-phase matched with the probe, resulting in emitted photons which are carried by the probe wave packet [35, 153, 158]. The Raman spectrum, commonly referred to as the Raman Gain, is extracted from the amplified probe after interaction with the sample of interest. This is performed by evaluating the logarithmic difference between the probe spectrum with (on) and without (off) the pump interaction :

$$RamanGain = -\log \frac{on}{off} = a \cdot \sigma_R I_{pu} z \tag{9.3}$$

Here, a is a constant with units of $cm^2 \cdot s$, σ_R is the integrated Raman scattering cross-section (calculated from Equation 9.1), c is the sample concentration, z is the sample pathlength, and I_{pu} is the intensity of the Raman pump pulse [158]. From Equation 9.3, we can see that the Raman Gain has a linear dependence on the Raman pump energy.

9.2.2 Methods

The pump and probe pulses used in FSRS experiments are generated from an amplified Ti:saphhire laser system (Coherent Legend, Coherent Inc. Santa Clara, California). The output of this system is a 3.8 W, 1 kHz pulse train centered around 800 nm, with pulses ~150 fs in duration.

A portion of this beam is directed into a CaF_2 window (Newlight Photonics) which generates white light continuum (wlc) pulses through a $\chi^{(3)}$ nonlinear process. Group velocity dispersion (GVD) in the wlc pulses is corrected by a pair of dispersion compensation mirrors (chirp mirrors) purchased from Thorlabs. Multiple passes of the wlc pulses through the chirped mirror pair compensate for the GVD inherent in the wlc pulse. The wlc wavelengths range from 375 – 500 nm after passing through the chirp mirror pair. After GVD compensation, and before interacting with the STO sample, a portion of the wlc beam is directed into an Ultrafast Systems referencing camera, which monitors fluctuations in the beam, and reduces noise in the data [36, 37]. The remainder of the 800 nm beam is directed into a beta-Barium Borate (BBO) crystal which generates the 400 nm Raman pump pulse through a $\chi^{(2)}$ nonlinear process. The crystal is mounted such that it can be easily rotated about the axis of beam propagation, allowing for easy adjustment of the pump intensity. The 400 nm pump beam is then passed through an etalon (Tec Optics) which produces a spectrally narrow time-asymmetric pulse with a $\sim$ps scale duration. An etalon is chosen as the tool for Raman pulse tuning since it has been shown to enhance the Raman signal by up to 2-fold [159] and is simple to align.

The two pulses are then focused and directed to the STO sample. The path of the wlc is focused using a parabolic mirror to prevent further GVD, and has a path that is essentially fixed. The sample of interest is aligned with the focus of the wlc using an X,Y,Z stage controlled with Thorlabs DC servo motor actuators. The pump beam is then adjusted in space and time to overlap with the wlc as both beams pass through the sample. After passing through the STO sample, the pump beam is absorbed by a beam block, and the wlc, now carrying the peaks corresponding to the Raman active transitions is directed into a Princeton Instruments Isoplane spectrometer. The beam is spatially dispersed using a grating with 1800 g/mm and a 500 nm blaze. The dispersed spectrum is then collected via a Princeton Instruments Pixis camera. Data acquisition is automated via a custom-designed LabVIEW program, which calls MATLAB scripts that perform data processing.

On and off Raman pump shots are created by blocking every other shot from the Raman pump, resulting in a pulse train with a 500 Hz frequency. This is performed with a New Focus optical chopper with adjustable frequency and phase. The chopper outputs a waveform that is monitored by our data analysis software and is used to define pump on and off shots for data analysis (Section 5.2). The STO sample is a 0.1% Neobium doped (n-doped) STO crystal with 2 sides finished to a polished surface. The STO crystal was made by MTI corporation and is held in a custom-designed sample holder that allows for transmission of the pump and probe beams.

9.3 Results

Figure 9.2: FSRS data plotted, and peaks compared to data from Nilsen et. al. a) Full-scale FSRS spectrum collected at high pump power and normalized such that the spectrum is positive. b) Data from Figure a) at a zoomed in scale with peaks labeled. c) Raman shift of peaks from this work compared to those collected by Nilsen et. al.. Assignments of observed peaks to combination and overtones and the associated phonon branches are shown along with calculated Raman shifts [142].

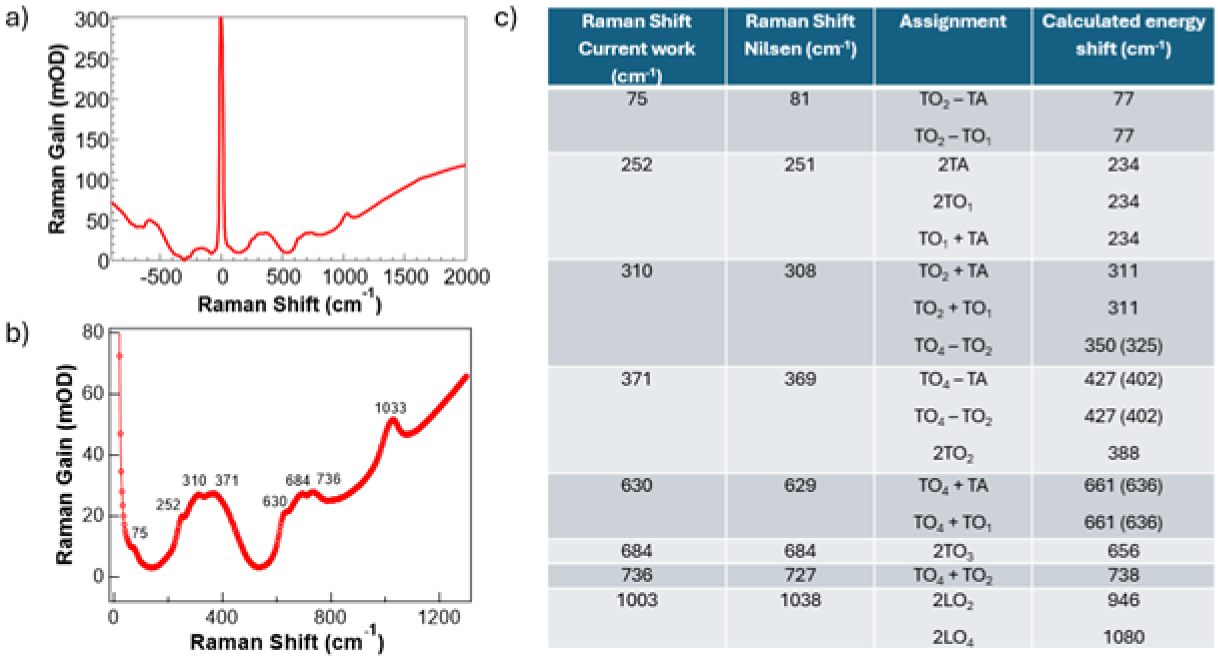

Raman Shift Current work (cm^{-1})	Raman Shift Nilsen (cm^{-1})	Assignment	Calculated energy shift (cm^{-1})
75	81	$\mathrm{TO}_2 - \mathrm{TA}$ $\mathrm{TO}_2 - \mathrm{TO}_1$	77 77
252	251	2TA $2\mathrm{TO}_1$ $\mathrm{TO}_1 + \mathrm{TA}$	234 234 234
310	308	$\mathrm{TO}_2 + \mathrm{TA}$ $\mathrm{TO}_2 + \mathrm{TO}_1$ $\mathrm{TO}_4 - \mathrm{TO}_2$	311 311 350 (325)
371	369	$\mathrm{TO}_4 - \mathrm{TA}$ $\mathrm{TO}_4 - \mathrm{TO}_2$ $2\mathrm{TO}_2$	427 (402) 427 (402) 388
630	629	$\mathrm{TO}_4 + \mathrm{TA}$ $\mathrm{TO}_4 + \mathrm{TO}_1$	661 (636) 661 (636)
684	684	$2\mathrm{TO}_3$	656
736	727	$\mathrm{TO}_4 + \mathrm{TO}_2$	738
1003	1038	$2\mathrm{LO}_2$ $2\mathrm{LO}_4$	946 1080

FSRS spectra on solid crystal STO have been collected in transmission geometry with varying pump energy. The collected spectrum at high pump energy is shown in Figure 9.2a,b. Figure9.2a shows the spectrum at a scale in which the stokes and anti-stokes peaks that could be well-resolved within the range of our broadband probe. Figure 9.2b shows the first few stokes peaks at a zoomed-in scale with the first 8 peaks labeled. These peaks agree well with previously collected spontaneous Raman spectra on solid crystal STO. Figure 9.2c shows the Raman shifts for the data displayed in figure 9.2b compared with those from Nilsen et. al. [142]. The phonon overtone and combination bands assigned to each Raman shift and the predicted energy shifts from said bands are also shown. Along with the expected Raman peaks, the spectrum contains a strong negative background on top of which the vibrational peaks are found. The spectrum shown in Figure 9.2b has been normalized to eliminate this background, allowing the focus to be on the Raman peaks.

Data sets were collected at several different Raman pump energies and the resulting spectra are shown in Figure 9.3a. The area of the FSRS peaks and the magnitude of the background

Figure 9.3: FSRS spectra collected at varying pump energies a), integrated peak areas for the first 2 clusters of overlapping peaks b),c) and the 1033 cm^{-1} peak plotted as a function of pump energy d). The peak areas are shown with a linear fit overlaid to highlight the linear dependence on pump energy.

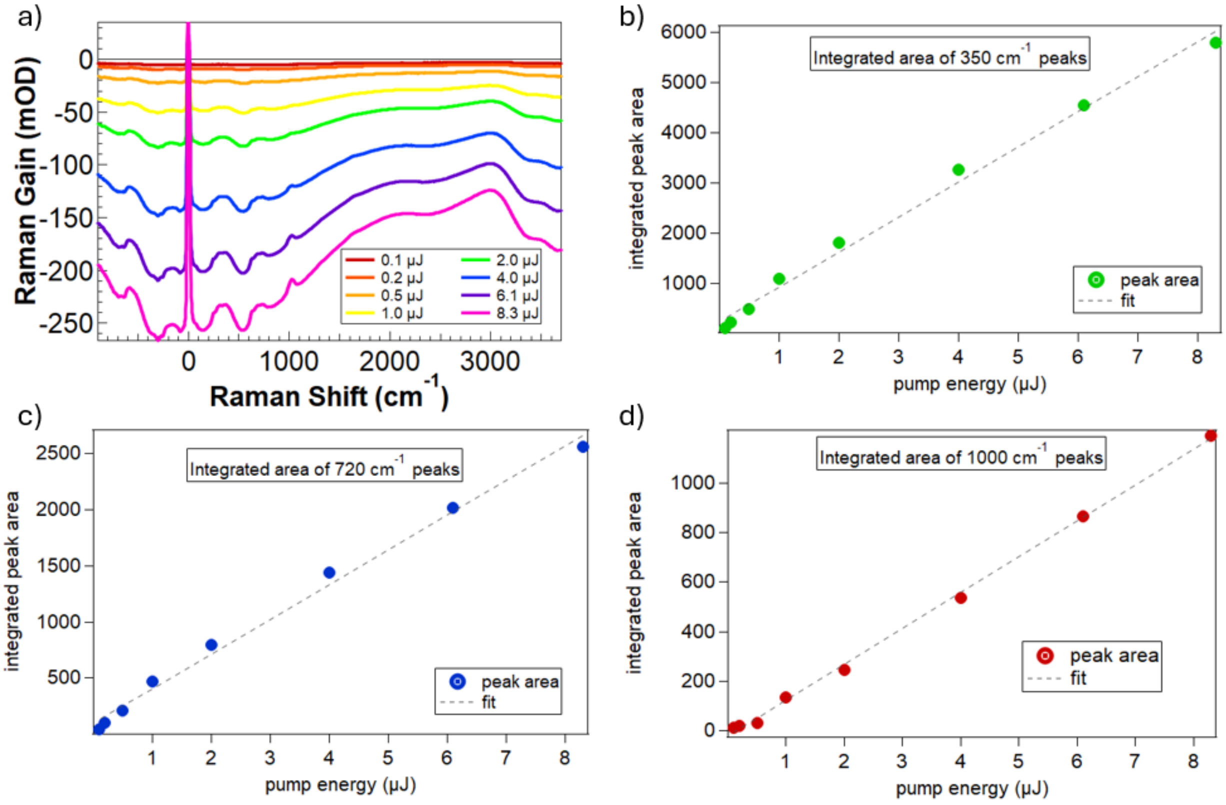

signal both increased with the intensity of the Raman pump. Since the shape and source of the background signal was not obvious, it was not trivial to remove and isolate the Raman peaks. Therefore, the integration of the Raman peaks was performed manually using a custom-written MATLAB script. For each peak, two points on the wavenumber axis are chosen to bracket the peak, and are used to define a straight line at the base of the peak. The integration is defined as the area under the peak and above the straight line. The same pair of bracketing points is used across all all pump energies for peaks at the same Raman shift. The first 3 significant clusters of Stokes peaks were integrated, and their areas were plotted as a function of Raman pump energy in Figure 9.3b-d. Peak area for all three clusters was found to be linear with pump intensity, which is the expected dependence for first order FSRS spectra, according to Equation 9.3. Prior to this work, no relationship between Raman Gain and pump intensity for second order Raman spectra has been derived.

The trends of the peak areas for the first 2 peak clusters show minor deviations from linearity. We attribute this to the shape of the background signal, which has a minimum near the fundamental. The integrated area for these peaks is defined as a straight line connecting the edges the peak. This method likely omits some of the contribution from the Raman Gain on top of the background signal. This is supported by the lack of linear deviation in Raman Gain of the third peak cluster, which sits on top of the background such that a straight line is more likely to describe the difference between the Raman Gain and the background. To further confirm the linearity of the Raman Gain, an additional data set was collected. One of the features explored within this additional data set was the relationship between the background signal and the alignment of the Raman pump and probe in the time domain. For the data set displayed in Figure 9.3, the temporal alignment of the Raman pump and probe was performed such that the minimum of the background signal was close to the fundamental. In the additional data set (Appendix G), the pump alignment was chosen for minimum interference with the stokes peaks of interest (0 – 1100 cm^{-1}) region. Data points corresponding to pump energies were also collected at more finely spaced points, and in random order to eliminate effects from long-term fluctuations in alignment. Analysis of the Raman Gain of the first 3 peak clusters within this data showed strong linearity with pump intensity.

9.4 Discussion

For a perovskite with a primitive unit cell consisting of 5 atoms, a total of 15 phonon modes, 3 acoustic and 12 optical are expected. The three acoustic modes are those of a triply degenerate F_{1u} mode, the remaining optical modes consist of three triply degenerate F_{1u} and one triply degenerate F_{2u} mode. All these transitions are Raman inactive in first-order. This is evident from group theory considerations; STO belongs to O_h point group, whose character table shows no Raman active species for F_{1u} and F_{2u} modes (often shown as T_{1u} and T_{2u}). One can also invoke the semi-classical polarizability model to see why first order phonon bands should be inactive in STO. This approach is also useful for understanding the coupling between the Raman fundamental and vibrational modes within the material, and how polarizability derivatives determine what modes are Raman active.

According to the polarizability model, the material response $\vec{P}$ to an external electric field $\vec{E}$ depends on the polarizability of the material α.

$$\vec{P} = \alpha\vec{E} \tag{9.4}$$

The polarizability is often expressed as a Taylor series as a function of the generalized molecular coordinate Q:

$$\alpha = \alpha_0 + (\frac{d\alpha}{dQ})_0 Q + \cdots \tag{9.5}$$

The 0^{th} term (α_0) in the expansion represents Rayliegh scattering, and the first order term represents first order Raman scattering. For phonon modes to be Raman active, the polarizability of the crystal must change with the generalized coordinate Q. Assuming harmonic vibrations (small oscillations about equilibrium) associated with the k^{th} mode, one can write

$$Q_k = Q_{k0}\cos\omega_k t. \tag{9.6}$$

Then, expressing the electric field to explicitly show time dependence

$$\vec{E} = \vec{E_0}\cos\omega_0 t. \tag{9.7}$$

allows us to re-write Equation 9.8 as

$$\vec{P} = \alpha_0\vec{E_0}\cos\omega_0 t + (\frac{d\alpha}{dQ_k})_0 Q_{k0}\cos\omega_k t\vec{E_0}\cos\omega_0 t + \cdots \tag{9.8}$$

or equivalently

$$\vec{P} = \alpha_0\vec{E_0}\cos\omega_0 t + (\frac{d\alpha}{dQ_k})_0 Q_{k0}\vec{E_0}[\cos((\omega_0 - \omega_k)t) + \cos((\omega_0 + \omega_k)t)] \tag{9.9}$$

which explicitly shows the frequency shifts of the stokes $\omega_0 - \omega_k$ and anti-stokes $\omega_0 + \omega_k$ Raman transitions [157].

Modes supported by cubic perovskites are those that do not change the polarizability of the crystal unit cell (rocking modes) or are those which do change the polarizability of an individual cell, but are canceled out by an opposite change in neighboring cells (breathing modes). For such cases, the first order term in the Taylor series vanishes ($(\frac{d\alpha}{dQ})_0 = 0$). To model the second-order Raman modes, the result of overtone and combination phonon modes, one must invoke a higher order term in the Taylor series for α, and consider contributions from multiple modes (k):

$$\alpha = \alpha_0 + (\frac{\partial\alpha}{\partial Q})_0 + \frac{1}{2}\sum_{k,l}(\frac{\partial^2\alpha}{\partial Q_k\partial Q_l})Q_K Q_l + \cdots . \tag{9.10}$$

Following the same procedure that led to Equation 9.9, Equation 9.10 leads to induced polarization described by terms such as $\omega \pm 2\omega_k$ and $\omega_0 \pm (\omega_k \pm \omega_l)$, whose intensities depend on second order derivatives of α [157].

Prior to this work, no FSRS spectra have been collected on STO, whose Raman active modes are entirely second order, and no models that predict the dependence of second order Raman gain on pump intensity have been reported. To motivate a possible approach to building such a model, we follow the work of Lee et. al. [155] and apply their methodology to the second-order term in α. For the case of first order FSRS spectra, the dependence of the Raman Gain on pump power has been derived using the semi-classical model of polarizability. Considering the first order dependence of α on Q, applying Lagrange's Equations and adding a phenomenological damping term $2\gamma dQ/dt$, the differential equation for the time dependence of Q can be written:

$$\frac{d^2Q}{dt^2} + 2\gamma\frac{dQ}{dt} + \omega_0^2 Q = (\frac{d\alpha}{dQ})_0|\vec{E}(\vec{r},t)|^2. \tag{9.11}$$

Using this model, along with Maxwell's equations, the Raman Gain can be shown to have a linear dependence on the pump intensity Equation 9.3. Invoking the same strategy for the second order term yields a set of coupled equations for two generalized coordinates Q_k, Q_l:

$$\frac{\partial^2 Q_k}{\partial t^2} + 2\gamma_k\frac{\partial Q_k}{\partial t} + (\omega_{0,k}^2) - |\vec{E}(\vec{r},t)|^2(\frac{\partial^2\alpha}{\partial Q_k^2})_0)Q_k = (\frac{\partial^2\alpha}{\partial Q_k \partial Q_l})_0 Q_l|\vec{E}(\vec{r},t)|^2 \tag{9.12}$$

$$\frac{\partial^2 Q_l}{\partial t^2} + 2\gamma_l\frac{\partial Q_l}{\partial t} + (\omega_{0,l}^2) - |\vec{E}(\vec{r},t)|^2(\frac{\partial^2\alpha}{\partial Q_k^2})_0)Q_l = (\frac{\partial^2\alpha}{\partial Q_k \partial Q_l})_0 Q_k|\vec{E}(\vec{r},t)|^2 \tag{9.13}$$

There is no exact solution for this set of DE's as written. However, we can consider the overtones and combination bands separately. This leads to a single equation for the overtone:

$$\frac{\partial^2 Q_k}{\partial t^2} + 2\gamma_k\frac{\partial Q_k}{\partial t} + (\omega_{0,k}^2) - |\vec{E}(\vec{r},t)|^2(\frac{\partial^2\alpha}{\partial Q_k^2})_0)Q_k = 0 \tag{9.14}$$

and, unsurprisingly, a set of coupled equations for the combination:

$$\frac{\partial^2 Q_k}{\partial t^2} + 2\gamma_k\frac{\partial Q_k}{\partial t} + \omega_{0,k}^2 Q_k = (\frac{\partial^2\alpha}{\partial Q_k \partial Q_l})_0 Q_l|\vec{E}(\vec{r},t)|^2 \tag{9.15}$$

$$\frac{\partial^2 Q_l}{\partial t^2} + 2\gamma_l\frac{\partial Q_l}{\partial t} + \omega_{0,l}^2 Q_l = (\frac{\partial^2\alpha}{\partial Q_k \partial Q_l})_0 Q_k|\vec{E}(\vec{r},t)|^2 \tag{9.16}$$

The overtone is a variation on a Mathieu differential equation, and the combination bands are described by a set of mutually driven harmonic oscillators that exchange energy through the electric field. Using the semi-classical approach to deriving an expressing for the second-order Raman gain in FSRS is an ongoing effort that will be explored in a future publication. However, given the linearity of the analyzed data with pump intensity, and the similar electric field dependence seen in the above differential equation, we have confidence that a linear relationship can be derived.

Given the fact that overtones and combinations are described differential equations of varying forms, there is no reason to assume that the Raman gain for both types of modes will carry the same pump dependence. However, the analysis from Figure 9.3 suggests a linear relationship for both types of modes. The analysis of the dependence of the Raman gain on pump intensity involves the integration of three spectral features, two of which are clusters of 3 overlapping peaks, and one is a single peak at 1033 cm^{-1}. The two clusters are made up of peaks which are due to both overtones and combinations, and the single peak is due to an overtone according to Nilsen et. al. [142]. The fact that linearity is observed for an individual overtone, and overlapping combinations and overtones suggests that the linear relationship holds for both types of peaks.

9.5 Conclusions

The first FSRS spectra on single-crystal bulk STO have been collected at standard conditions. The Raman shifts observed agree well with previous spectra collected using spontaneous Raman scattering. Previous work has assigned these peaks to second order overtone and combination phonon bands. We observe that the Raman Gain of the carries a linear dependence on the intensity of the Raman pump, as is the case for first order FSRS. Differential equations are presented which follow the strategy of using a semi-classical oscillator model to derive the relationship between Raman gain and pump energy for first order FSRS. Full development of a model for second order Raman gain with pump intensity is an ongoing effort. The observed peaks also come with a strong negative background, the origin of which is not known, that also depends on pump energy. The investigation of this background will be left for later work.

Bibliography

[1] Ibrahim Dincer, Marc A. Rosen, and Maan Al-Zareer. 3.11 chemical energy production. In Ibrahim Dincer, editor, Comprehensive Energy Systems, pages 470–520. Elsevier, Oxford, 2018.

[2] J. Rossmeisl. Electrolysis of water oxide surfaces. Journal of Electroanalytical Chemistry, 607:83–89, 2007.

[3] Michael Busch, Niels B. Halck, Ulrike I. Kramm, Samira Siahrostami, Petr Krtil, and Jan Rossmeisl. Beyond the top of the volcano? – a unified approach to electrocatalytic oxygen reduction and oxygen evolution. Nano Energy, 29:126–135, 2016. Electrocatalysis.

[4] B. Hammer and J. K. Norskov. Theoretical surface science and catalysis–calculations and concepts. Advances in Catalysis, 45:71–129, 2004.

[5] N. M. Markovic. Interfacing electrochemistry. Nature Materials, 12:101–102, 2013.

[6] Jan Kern, Ruchira Chatterjee, Iris D Young, Franklin D Fuller, Louise Lassalle, Mohamed Ibrahim, Sheraz Gul, Thomas Fransson, Aaron S Brewster, Roberto Alonso-Mori, et al. Structures of the intermediates of kok's photosynthetic water oxidation clock. Nature, 563(7731):421–425, 2018.

[7] Cassius Boyd, Shay McBride, Michael Paolino, Moritz Lang, Geoffroy Hautier, and Tanja Cuk. Assigning surface hole polaron configurations of titanium oxide materials to excited-state optical absorptions. Journal of the American Chemical Society, 147(13):10981–10991, 2025.

[8] Jun Cheng, Joost VandeVondele, and Michiel Sprik. Identifying trapped electronic holes at the aqueous tio2 interface. The Journal of Physical Chemistry C, 118(10):5437–5444, 2014.

[9] Dong Wang, Tian Sheng, Jianfu Chen, Hai-Feng Wang, and PJNC Hu. Identifying the key obstacle in photocatalytic oxygen evolution on rutile tio2. Nature Catalysis, 1(4):291–299, 2018.

[10] O. F. Schirmer. O-bound small polarons in oxide materials. J. Phys.: Condens. Matter, 18:R667–R704, 2006.

[11] I. N. Hulea, S. Fratini, H. Xie, C. L. Mulder, N. N. Iossad, G. Rastelli, S. Ciuchi, and A. F. Morpurgo. Tunable frolich polarons in organic single-crystal transistors. Nature Materials, 5:982–986, 2006.

[12] Christen Courter, James Stewart, and Tanja Cuk. Moderate electron doping assists in dissociating water on a transition metal oxide surface (n-srtio3). The Journal of Physical Chemistry C, 127(10):4905–4916, 2023.

[13] Michael Busch, Niels B Halck, Ulrike I Kramm, Samira Siahrostami, Petr Krtil, and Jan Rossmeisl. Beyond the top of the volcano?–a unified approach to electrocatalytic oxygen reduction and oxygen evolution. Nano Energy, 29:126–135, 2016.

[14] J. Cheng and M. Sprik. Acidity of the aqueous rutile tio2(110) surface from density functional theory based moleculaer dynamics. J. Chem. Theory Comput., 6:880–889, 2010.

[15] D Frank Ogletree, Hendrik Bluhm, Eleonore D Hebenstreit, and Miquel Salmeron. Photoelectron spectroscopy under ambient pressure and temperature conditions. Nuclear Instruments and Methods in Physics Research Section A: Accelerators, Spectrometers, Detectors and Associated Equipment, 601(1-2):151–160, 2009.

[16] John T Newberg, David E Starr, Susumu Yamamoto, Sarp Kaya, Tom Kendelewicz, Erin R Mysak, Soeren Porsgaard, Miquel B Salmeron, Gordon E Brown Jr, Anders Nilsson, et al. Formation of hydroxyl and water layers on mgo films studied with ambient pressure xps. Surface Science, 605(1-2):89–94, 2011.

[17] Susumu Yamamoto, Tom Kendelewicz, John T Newberg, Guido Ketteler, David E Starr, Erin R Mysak, Klas J Andersson, Hirohito Ogasawara, Hendrik Bluhm, Miquel Salmeron, et al. Water adsorption on α-fe2o3 (0001) at near ambient conditions. The Journal of Physical Chemistry C, 114(5):2256–2266, 2010.

[18] John T Newberg, David E Starr, Susumu Yamamoto, Sarp Kaya, Tom Kendelewicz, Erin R Mysak, Soeren Porsgaard, Miquel B Salmeron, Gordon E Brown Jr, Anders Nilsson, et al. Autocatalytic surface hydroxylation of mgo (100) terrace sites observed under ambient conditions. The Journal of Physical Chemistry C, 115(26):12864–12872, 2011.

[19] Guido Ketteler, Susumu Yamamoto, Hendrik Bluhm, Klas Andersson, David E Starr, D Frank Ogletree, Hirohito Ogasawara, Anders Nilsson, and Miquel Salmeron. The nature of water nucleation sites on tio2 (110) surfaces revealed by ambient pressure x-ray photoelectron spectroscopy. The Journal of Physical Chemistry C, 111(23):8278–8282, 2007.

[20] Xingyi Deng, Tirma Herranz, Christoph Weis, Hendrik Bluhm, and Miquel Salmeron. Adsorption of water on cu2o and al2o3 thin films. The Journal of Physical Chemistry C, 112(26):9668–9672, 2008.

[21] Daniel J Aschaffenburg, Seiji Kawasaki, Chaitanya Das Pemmaraju, and Tanja Cuk. Accuracy in resolving the first hydration layer on a transition-metal oxide surface: Experiment (ap-xps) and theory. The Journal of Physical Chemistry C, 124(39):21407–21417, 2020.

[22] Zhu Chen, Coleman X Kronawitter, Iradwikanari Waluyo, and Bruce E Koel. Investigation of water dissociation and surface hydroxyl stability on pure and ni-modified coooh by ambient pressure photoelectron spectroscopy. The Journal of Physical Chemistry B, 122(2):810–817, 2018.

[23] E Holmström, P Spijker, and AS Foster. The interface of srtio3 and h2o from density functional theory molecular dynamics. Proceedings of the Royal Society A: Mathematical, Physical and Engineering Sciences, 472(2193):20160293, 2016.

[24] Iulian N Hulea, Simone Fratini, H Xie, Cornelis L Mulder, Nikolai N Iossad, Gianluca Rastelli, Sergio Ciuchi, and Alberto F Morpurgo. Tunable fröhlich polarons in organic single-crystal transistors. Nature materials, 5(12):982–986, 2006.

[25] Beverly Brooks Hinojosa, Tim Van Cleve, and Aravind Asthagiri. A first-principles study of h2o adsorption and dissociation on the srtio3 (100) surface. Molecular Simulation, 36(7-8):604–617, 2010.

[26] Hieu H Pham, Mu-Jeng Cheng, Heinz Frei, and Lin-Wang Wang. Surface proton hopping and fast-kinetics pathway of water oxidation on co3o4 (001) surface. ACS Catalysis, 6(8):5610–5617, 2016.

[27] Yong Xu and Martin AA Schoonen. The absolute energy positions of conduction and valence bands of selected semiconducting minerals. American mineralogist, 85(3-4):543–556, 2000.

[28] Ilya Vinogradov, Suryansh Singh, Hanna Lyle, Michael Paolino, Aritra Mandal, Jan Rossmeisl, and Tanja Cuk. Free energy difference to create the m-oh* intermediate of the oxygen evolution reaction by time-resolved optical spectroscopy. Nature materials, 21(1):88–94, 2022.

[29] C Thomsen, Holger T Grahn, Humphrey J Maris, and Jan Tauc. Surface generation and detection of phonons by picosecond light pulses. Physical Review B, 34(6):4129, 1986.

[30] Emanuele Pontecorvo, Michele Ortolani, Dario Polli, Marco Ferretti, Giancarlo Ruocco, Giulio Cerullo, and Tullio Scopigno. Visualizing coherent phonon propagation in the 100 ghz range: A broadband picosecond acoustics approach. Applied Physics Letters, 98(1), 2011.

[31] Stefano Brivio, Dario Polli, Andrea Crespi, Roberto Osellame, G Cerullo, and Riccardo Bertacco. Observation of anomalous acoustic phonon dispersion in srtio3 by broadband stimulated brillouin scattering. Applied Physics Letters, 98(21), 2011.

[32] Stefano Brivio, Dario Polli, Andrea Crespi, R Osellame, G Cerullo, and Riccardo Bertacco. Response to "comment on 'observation of anomalous acoustic phonon dispersion in srtio3 by broadband stimulated brillouin scattering'" [appl. phys. lett. 100, 206101 (2012)]. Applied Physics Letters, 100(20), 2012.

[33] Arnaud Devos, Y-C Wen, P-A Mante, and C-K Sun. Comment on "observation of anomalous acoustic phonon dispersion in srtio3 by broadband stimulated brillouin scattering" [appl. phys. lett. 98, 211907 (2011)]. Applied Physics Letters, 100(20), 2012.

[34] Matthias M Waegele, Xihan Chen, David M Herlihy, and Tanja Cuk. How surface potential determines the kinetics of the first hole transfer of photocatalytic water oxidation. Journal of the American Chemical Society, 136(30):10632–10639, 2014.

[35] Philipp Kukura, David W McCamant, and Richard A Mathies. Femtosecond stimulated raman spectroscopy. Annu. Rev. Phys. Chem., 58(1):461–488, 2007.

[36] Yuan Feng, Ilya Vinogradov, and Nien-Hui Ge. General noise suppression scheme with reference detection in heterodyne nonlinear spectroscopy. Optics Express, 25(21):26262–26279, 2017.

[37] Yuan Feng, Ilya Vinogradov, and Nien-Hui Ge. Optimized noise reduction scheme for heterodyne spectroscopy using array detectors. Optics express, 27(15):20323–20346, 2019.

[38] Tanja Cuk, Michael Paolino, Suryansh Singh, James Stewart, Xihan Chen, and Ilya Vinogradov. Ultrafast electronic and vibrational spectroscopy of electrochemical transformations on a metal-oxide surface during oxygen evolution catalysis. ACS Catalysis, 14(13):9901–9926, 2024.

[39] Matthew SJ Marshall, David T Newell, David J Payne, Russell G Egdell, and Martin R Castell. Atomic and electronic surface structures of dopants in oxides: Stm and xps of nb- and la-doped srtio 3 (001). Physical Review B—Condensed Matter and Materials Physics, 83(3):035410, 2011.

[40] R De Gryse, WP Gomes, F_ Cardon, and J Vennik. On the interpretation of mott-schottky plots determined at semiconductor/electrolyte systems. Journal of the Electrochemical Society, 122(5):711, 1975.

[41] G Cooper, JA Turner, and AJ Nozik. Mott-schottky plots and flatband potentials for single crystal rutile electrodes. Journal of the Electrochemical Society, 129(9):1973, 1982.

[42] Hanna Lyle, Suryansh Singh, Elena Magnano, Silvia Nappini, Federica Bondino, Sadegh Yazdi, and Tanja Cuk. Assessing and quantifying thermodynamically concomitant degradation during oxygen evolution from water on srtio3. ACS Catalysis, 13(12):8206–8218, 2023.

[43] Zhi Wei Seh, Jakob Kibsgaard, Colin F Dickens, IB Chorkendorff, Jens K Nørskov, and Thomas F Jaramillo. Combining theory and experiment in electrocatalysis: Insights into materials design. Science, 355(6321):eaad4998, 2017.

[44] Bert M Weckhuysen. Chemical imaging of spatial heterogeneities in catalytic solids at different length and time scales. Angewandte Chemie International Edition, 48(27):4910–4943, 2009.

[45] Inge LC Buurmans and Bert M Weckhuysen. Heterogeneities of individual catalyst particles in space and time as monitored by spectroscopy. Nature chemistry, 4(11):873–886, 2012.

[46] Jens K Nørskov, Thomas Bligaard, Britt Hvolbæk, Frank Abild-Pedersen, Ib Chorkendorff, and Claus H Christensen. The nature of the active site in heterogeneous metal catalysis. Chemical Society Reviews, 37(10):2163–2171, 2008.

[47] Miao Zhang and Heinz Frei. Towards a molecular level understanding of the multi-electron catalysis of water oxidation on metal oxide surfaces. Catalysis Letters, 145:420–435, 2015.

[48] Isabela C Man, Hai-Yan Su, Federico Calle-Vallejo, Heine A Hansen, José I Martínez, Nilay G Inoglu, John Kitchin, Thomas F Jaramillo, Jens K Nørskov, and Jan Rossmeisl. Universality in oxygen evolution electrocatalysis on oxide surfaces. ChemCatChem, 3(7):1159–1165, 2011.

[49] Xihan Chen, Stephanie N Choing, Daniel J Aschaffenburg, C Das Pemmaraju, David Prendergast, and Tanja Cuk. The formation time of ti–o• and ti–o•–ti radicals at the n-srtio3/aqueous interface during photocatalytic water oxidation. Journal of the American Chemical Society, 139(5):1830–1841, 2017.

[50] David M Herlihy, Matthias M Waegele, Xihan Chen, CD Pemmaraju, David Prendergast, and Tanja Cuk. Detecting the oxyl radical of photocatalytic water oxidation at an n-srtio3/aqueous interface through its subsurface vibration. Nature chemistry, 8(6):549–555, 2016.

[51] Miao Zhang, Moreno De Respinis, and Heinz Frei. Time-resolved observations of water oxidation intermediates on a cobalt oxide nanoparticle catalyst. Nature chemistry, 6(4):362–367, 2014.

[52] Omid Zandi and Thomas W Hamann. Determination of photoelectrochemical water oxidation intermediates on haematite electrode surfaces using operando infrared spectroscopy. Nature chemistry, 8(8):778–783, 2016.

[53] Jia Chen, Ye-Fei Li, Patrick Sit, and Annabella Selloni. Chemical dynamics of the first proton-coupled electron transfer of water oxidation on tio2 anatase. Journal of the American Chemical Society, 135(50):18774–18777, 2013.

[54] Jan Philip Kraack and Peter Hamm. Surface-sensitive and surface-specific ultrafast two-dimensional vibrational spectroscopy. Chemical Reviews, 117(16):10623–10664, 2017.

[55] Jan Philip Kraack, Andres Kaech, and Peter Hamm. Surface enhancement in ultrafast 2d atr ir spectroscopy at the metal-liquid interface. The Journal of Physical Chemistry C, 120(6):3350–3359, 2016.

[56] Benjamin Klahr, Sixto Gimenez, Francisco Fabregat-Santiago, Juan Bisquert, and Thomas W Hamann. Photoelectrochemical and impedance spectroscopic investigation of water oxidation with "co–pi"-coated hematite electrodes. Journal of the American chemical society, 134(40):16693–16700, 2012.

[57] Xihan Chen, Daniel J Aschaffenburg, and Tanja Cuk. Selecting between two transition states by which water oxidation intermediates decay on an oxide surface. Nature Catalysis, 2(9):820–827, 2019.

[58] Jörg Libuda, Ingo Meusel, Jens Hartmann, and H-J Freund. A molecular beam/surface spectroscopy apparatus for the study of reactions on complex model catalysts. Review of Scientific Instruments, 71(12):4395–4408, 2000.

[59] Roger Parsons. The rate of electrolytic hydrogen evolution and the heat of adsorption of hydrogen. Transactions of the Faraday Society, 54:1053–1063, 1958.

[60] Yi Zhang, Xuguang Jia, Shuang Liu, Bo Zhang, Keman Lin, Jiayu Zhang, and Gavin Conibeer. A review on thermalization mechanisms and prospect absorber materials for the hot carrier solar cells. Solar Energy Materials and Solar Cells, 225:111073, 2021.

[61] Chirasmita Bhattacharya, Sandra Elizabeth Saji, Akhil Mohan, Vasudeva Madav, Guohua Jia, and Zongyou Yin. Sustainable nanoplasmon-enhanced photoredox reactions: Synthesis, characterization, and applications. Advanced Energy Materials, 10(40):2002402, 2020.

[62] Anderson Janotti, Joel B Varley, Minseok Choi, and Chris G Van de Walle. Vacancies and small polarons in srtio 3. Physical Review B, 90(8):085202, 2014.

[63] Hungru Chen and Naoto Umezawa. Hole localization, migration, and the formation of peroxide anion in perovskite sr ti o 3. Physical Review B, 90(3):035202, 2014.

[64] Andrea Rubano, D Paparo, F Miletto Granozio, Umberto Scotti di Uccio, and Lorenzo Marrucci. Blue luminescence of srtio3 under intense optical excitation. Journal of Applied Physics, 106(10), 2009.

[65] Shosuke Mochizuki, Fumito Fujishiro, and Seiko Minami. Photoluminescence and reversible photo-induced spectral change ofsrtio3. Journal of Physics: Condensed Matter, 17(6):923, 2005.

[66] N Aaron Deskins and Michel Dupuis. Intrinsic hole migration rates in tio2 from density functional theory. The Journal of Physical Chemistry C, 113(1):346–358, 2009.

[67] Florian Le Formal, Ernest Pastor, S David Tilley, Camilo A Mesa, Stephanie R Pendlebury, Michael Gratzel, and James R Durrant. Rate law analysis of water oxidation on a hematite surface. Journal of the American Chemical Society, 137(20):6629–6637, 2015.

[68] Andreas Kafizas, Yimeng Ma, Ernest Pastor, Stephanie R Pendlebury, Camilo Mesa, Laia Francàs, Florian Le Formal, Nuruzzaman Noor, Min Ling, Carlos Sotelo-Vazquez, et al. Water oxidation kinetics of accumulated holes on the surface of a tio2 photoanode: a rate law analysis. ACS catalysis, 7(7):4896–4903, 2017.

[69] Aritra Mandal, Krupa Ramasesha, Luigi De Marco, and Andrei Tokmakoff. Collective vibrations of water-solvated hydroxide ions investigated with broadband 2dir spectroscopy. The Journal of chemical physics, 140(20), 2014.

[70] Carlos R Baiz, Chunte Sam Peng, Mike E Reppert, Kevin C Jones, and Andrei Tokmakoff. Coherent two-dimensional infrared spectroscopy: Quantitative analysis of protein secondary structure in solution. Analyst, 137(8):1793–1799, 2012.

[71] Gilbert W Stewart. On the early history of the singular value decomposition. SIAM review, 35(4):551–566, 1993.

[72] Hannes Guhl, Wolfram Miller, and Karsten Reuter. Water adsorption and dissociation on srtio 3 (001) revisited: A density functional theory study. Physical Review B—Condensed Matter and Materials Physics, 81(15):155455, 2010.

[73] Sean T Roberts, Krupa Ramasesha, Poul B Petersen, Aritra Mandal, and Andrei Tokmakoff. Proton transfer in concentrated aqueous hydroxide visualized using ultrafast infrared spectroscopy. The Journal of Physical Chemistry A, 115(16):3957–3972, 2011.

[74] Dominik Marx, Amalendu Chandra, and Mark E Tuckerman. Aqueous basic solutions: hydroxide solvation, structural diffusion, and comparison to the hydrated proton. Chemical reviews, 110(4):2174–2216, 2010.

[75] Fivos Perakis, Susanne Widmer, and Peter Hamm. Two-dimensional infrared spectroscopy of isotope-diluted ice ih. The Journal of chemical physics, 134(20), 2011.

[76] Luigi De Marco, William Carpenter, Hanchao Liu, Rajib Biswas, Joel M Bowman, and Andrei Tokmakoff. Differences in the vibrational dynamics of h2o and d2o: observation of symmetric and antisymmetric stretching vibrations in heavy water. The Journal of Physical Chemistry Letters, 7(10):1769–1774, 2016.

[77] Sencer Selcuk and Annabella Selloni. Facet-dependent trapping and dynamics of excess electrons at anatase tio2 surfaces and aqueous interfaces. Nature materials, 15(10):1107–1112, 2016.

[78] Hans Swenson and Nicholas P Stadie. Langmuir's theory of adsorption: A centennial review. Langmuir, 35(16):5409–5426, 2019.

[79] Jun Cheng and Michiel Sprik. Acidity of the aqueous rutile tio2 (110) surface from density functional theory based molecular dynamics. Journal of chemical theory and computation, 6(3):880–889, 2010.

[80] Sharon Hammes-Schiffer and Alexei A Stuchebrukhov. Theory of coupled electron and proton transfer reactions. Chemical reviews, 110(12):6939–6960, 2010.

[81] Dmitry E Polyansky, James T Muckerman, Jonathan Rochford, Ruifa Zong, Randolph P Thummel, and Etsuko Fujita. Water oxidation by a mononuclear ruthenium catalyst: Characterization of the intermediates. Journal of the American Chemical Society, 133(37):14649–14665, 2011.

[82] Javier J Concepcion, Ming-Kang Tsai, James T Muckerman, and Thomas J Meyer. Mechanism of water oxidation by single-site ruthenium complex catalysts. Journal of the American Chemical Society, 132(5):1545–1557, 2010.

[83] Kai Cui, Alexander V Soudackov, Matthew C Kessinger, Jeremiah Xu, Gerald J Meyer, and Sharon Hammes-Schiffer. General kinetic model for ph dependence of proton-coupled electron transfer: Application to an electrochemical water oxidation system. Journal of the American Chemical Society, 145(35):19321–19332, 2023.

[84] Matthew Kessinger, Alexander V Soudackov, Jenny Schneider, Rachel E Bangle, Sharon Hammes-Schiffer, and Gerald J Meyer. Reorganization energies for interfacial proton-coupled electron transfer to a water oxidation catalyst. Journal of the American Chemical Society, 144(44):20514–20524, 2022.

[85] Ding-Yuan Kuo, Hanjong Paik, Jan Kloppenburg, Brendan Faeth, Kyle M Shen, Darrell G Schlom, Geoffroy Hautier, and Jin Suntivich. Measurements of oxygen electroadsorption energies and oxygen evolution reaction on ruo2 (110): a discussion of the sabatier principle and its role in electrocatalysis. Journal of the American Chemical Society, 140(50):17597–17605, 2018.

[86] Akihito Imanishi, Tomoaki Okamura, Naomichi Ohashi, Ryuhei Nakamura, and Yoshihiro Nakato. Mechanism of water photooxidation reaction at atomically flat tio2 (rutile)(110) and (100) surfaces: dependence on solution ph. Journal of the American Chemical Society, 129(37):11569–11578, 2007.

[87] Cristiana Di Valentin and Annabella Selloni. Bulk and surface polarons in photoexcited anatase tio2. The Journal of Physical Chemistry Letters, 2(17):2223–2228, 2011.

[88] Robert E Warburton, James M Mayer, and Sharon Hammes-Schiffer. Proton-coupled defects impact o–h bond dissociation free energies on metal oxide surfaces. The Journal of Physical Chemistry Letters, 12(40):9761–9767, 2021.

[89] Robert E Warburton, Alexander V Soudackov, and Sharon Hammes-Schiffer. Interfacial proton-coupled electron transfer via localized trap states on metal oxide surfaces. The Journal of Physical Chemistry C, 128(19):7903–7912, 2024.

[90] Yongpeng Liu, Florian Le Formal, Florent Boudoire, and Néstor Guijarro. Hematite photoanodes for solar water splitting: a detailed spectroelectrochemical analysis on the ph-dependent performance. ACS Applied Energy Materials, 2(9):6825–6833, 2019.

[91] Grazia Gonella, Ellen HG Backus, Yuki Nagata, Douwe J Bonthuis, Philip Loche, Alexander Schlaich, Roland R Netz, Angelika Kühnle, Ian T McCrum, Marc TM Koper, et al. Water at charged interfaces. Nature Reviews Chemistry, 5(7):466–485, 2021.

[92] AJ Sabbah and D Mark Riffe. Femtosecond pump-probe reflectivity study of silicon carrier dynamics. Physical Review B, 66(16):165217, 2002.

[93] Jorge Osorio-Guillén, Stephan Lany, and Alex Zunger. Atomic control of conductivity versus ferromagnetism in wide-gap oxides¡? format?¿ via selective doping: V, nb, ta in anatase tio 2. Physical review letters, 100(3):036601, 2008.

[94] Scott A Chambers, Timothy C Droubay, Cigdem Capan, and GY Sun. Unintentional f doping of srtio3 (001) etched in hf acid-structure and electronic properties. Surface science, 606(3-4):554–558, 2012.

[95] Yasuhiro Yamada and Yoshihiko Kanemitsu. Band-to-band photoluminescence in srtio 3. Physical Review B—Condensed Matter and Materials Physics, 82(12):121103, 2010.

[96] Yasuhiro Yamada, Hideki Yasuda, Takeshi Tayagaki, and Yoshihiko Kanemitsu. Photocarrier recombination dynamics in highly excited srtio3 studied by transient absorption and photoluminescence spectroscopy. Applied Physics Letters, 95(12), 2009.

[97] Tanja Cuk. Phenomenology of intermediate molecular dynamics at metal-oxide interfaces. Annual Review of Physical Chemistry, 75(1):457–481, 2024.

[98] Joseph Rabani and Max S Matheson. Pulse radiolytic determination of p k for hydroxyl ionic dissociation in water. Journal of the American Chemical Society, 86(15):3175–3176, 1964.

[99] Joseph Rabani, William A Mulac, and Max S Matheson. The pulse radiolysis of aqueous tetranitromethane. 1 i. rate constants and the extinction coefficient of eaq-. ii. oxygenated solutions. The Journal of Physical Chemistry, 69(1):53–70, 1965.

[100] James L Weeks and Joseph Rabani. The pulse radiolysis of deaerated aqueous carbonate solutions. i. transient optical spectrum and mechanism. ii. pk for oh radicals1. The Journal of Physical Chemistry, 70(7):2100–2106, 1966.

[101] David C Grills, Dmitry E Polyansky, and Etsuko Fujita. Application of pulse radiolysis to mechanistic investigations of catalysis relevant to artificial photosynthesis. ChemSusChem, 10(22):4359–4373, 2017.

[102] Suryansh Singh, Hanna Lyle, Luca D'Amario, Elena Magnano, Ilya Vinogradov, and Tanja Cuk. Coherent acoustic interferometry during the photodriven oxygen evolution reaction associates strain fields with the reactive oxygen intermediate (ti–oh*). Journal of the American Chemical Society, 143(39):15984–15997, 2021.

[103] cI G Austin and N Fr Mott. Polarons in crystalline and non-crystalline materials. Advances in physics, 18(71):41–102, 1969.

[104] Hanna Lyle, Suryansh Singh, Michael Paolino, Ilya Vinogradov, and Tanja Cuk. The electron-transfer intermediates of the oxygen evolution reaction (oer) as polarons by in situ spectroscopy. Physical Chemistry Chemical Physics, 23(44):24984–25002, 2021.

[105] Leonardo RV Buizza and Laura M Herz. Polarons and charge localization in metal-halide semiconductors for photovoltaic and light-emitting devices. Advanced Materials, 33(24):2007057, 2021.

[106] Jasleen Kaur, Manas Likhit Holekevi Chandrappa, Chi Chen, and Shyue Ping Ong. Polaron-induced metal-to-insulator transition in vanadium oxides from density functional theory calculations. Physical Review B, 107(12):125162, 2023.

[107] Kelvin HL Zhang, Yingge Du, Alexandra Papadogianni, Oliver Bierwagen, Shawn Sallis, Louis FJ Piper, Mark E Bowden, Vaithiyalingam Shutthanandan, Peter V Sushko, and Scott A Chambers. Perovskite sr-doped lacro3 as a new p-type transparent conducting oxide. Advanced Materials, 27(35):5191–5195, 2015.

[108] Michele Reticcioli, Ulrike Diebold, and Cesare Franchini. Modeling polarons in density functional theory: lessons learned from tio2. Journal of Physics: Condensed Matter, 34(20):204006, 2022.

[109] Jeffrey Roshan De Lile, Ashkan Bahadoran, Su Zhou, and Jiujun Zhang. Polaron in tio2 from first-principles: A review. Advanced Theory and Simulations, 5(2):2100244, 2022.

[110] N Aaron Deskins and Michel Dupuis. Electron transport via polaron hopping in bulk ti o 2: A density functional theory characterization. Physical Review B—Condensed Matter and Materials Physics, 75(19):195212, 2007.

[111] Jie-Qiong Li, Lingyi Meng, Michiel Sprik, and Jun Cheng. Thermodynamic investigation of proton/electron interplay on the pourbaix diagram at the tio2/electrolyte interface. The Journal of Physical Chemistry C, 124(35):19003–19014, 2020.

[112] Michele Reticcioli, Martin Setvin, Michael Schmid, Ulrike Diebold, and Cesare Franchini. Formation and dynamics of small polarons on the rutile tio 2 (110) surface. Physical Review B, 98(4):045306, 2018.

[113] Ye-Fei Li and Annabella Selloni. Pathway of photocatalytic oxygen evolution on aqueous tio2 anatase and insights into the different activities of anatase and rutile. ACS Catalysis, 6(7):4769–4774, 2016.

[114] Camilo A Mesa, Laia Francas, Ke R Yang, Pablo Garrido-Barros, Ernest Pastor, Yimeng Ma, Andreas Kafizas, Timothy E Rosser, Matthew T Mayer, Erwin Reisner, et al. Multihole water oxidation catalysis on haematite photoanodes revealed by operando spectroelectrochemistry and dft. Nature chemistry, 12(1):82–89, 2020.

[115] Giulia Righi, Julius Plescher, Franz-Philipp Schmidt, R Kramer Campen, Stefano Fabris, Axel Knop-Gericke, Robert Schlögl, Travis E Jones, Detre Teschner, and Simone Piccinin. On the origin of multihole oxygen evolution in haematite photoanodes. Nature Catalysis, 5(10):888–899, 2022.

[116] Kevin M Rosso and Michel Dupuis. Reorganization energy associated with small polaron mobility in iron oxide. The Journal of chemical physics, 120(15):7050–7054, 2004.

[117] Marcel Risch, Franziska Ringleb, Mike Kohlhoff, Peter Bogdanoff, Petko Chernev, Ivelina Zaharieva, and Holger Dau. Water oxidation by amorphous cobalt-based oxides: in situ tracking of redox transitions and mode of catalysis. Energy & Environmental Science, 8(2):661–674, 2015.

[118] Isabel M Klein, Hanzhe Liu, Danika Nimlos, Alex Krotz, and Scott Kevin Cushing. Ab initio prediction of excited-state and polaron effects in transient xuv measurements of α-fe2o3. Journal of the American Chemical Society, 144(28):12834–12841, 2022.

[119] Lucas M Carneiro, Scott K Cushing, Chong Liu, Yude Su, Peidong Yang, A Paul Alivisatos, and Stephen R Leone. Excitation-wavelength-dependent small polaron trapping of photoexcited carriers in α-fe2o3. Nature materials, 16(8):819–825, 2017.

[120] Somnath Biswas, Spencer Wallentine, Savini Bandaranayake, and L Robert Baker. Controlling polaron formation at hematite surfaces by molecular functionalization probed by xuv reflection-absorption spectroscopy. The Journal of chemical physics, 151(10), 2019.

[121] Jakub Husek, Anthony Cirri, Somnath Biswas, and L Robert Baker. Surface electron dynamics in hematite (α-fe 2 o 3): correlation between ultrafast surface electron trapping and small polaron formation. Chemical science, 8(12):8170–8178, 2017.

[122] Tadashi Watanabe, Akira Fujishima, and Ken-ichi Honda. Photoelectrochemical reactions at srtio3 single crystal electrode. Bulletin of the Chemical Society of Japan, 49(2):355–358, 1976.

[123] Thomas D Kühne, Marcella Iannuzzi, Mauro Del Ben, Vladimir V Rybkin, Patrick Seewald, Frederick Stein, Teodoro Laino, Rustam Z Khaliullin, Ole Schütt, Florian Schiffmann, et al. Cp2k: An electronic structure and molecular dynamics software package-quickstep: Efficient and accurate electronic structure calculations. The Journal of Chemical Physics, 152(19), 2020.

[124] Joost VandeVondele, Matthias Krack, Fawzi Mohamed, Michele Parrinello, Thomas Chassaing, and Jürg Hutter. Quickstep: Fast and accurate density functional calculations using a mixed gaussian and plane waves approach. Computer Physics Communications, 167(2):103–128, 2005.

[125] Manuel Guidon, Jurg Hutter, and Joost VandeVondele. Robust periodic hartree- fock exchange for large-scale simulations using gaussian basis sets. Journal of chemical theory and computation, 5(11):3010–3021, 2009.

[126] Wei Chen, Sinéad M Griffin, Gian-Marco Rignanese, and Geoffroy Hautier. Nonunique fraction of fock exchange for defects in two-dimensional materials. Physical Review B, 106(16):L161107, 2022.

[127] Matthias Krack. Pseudopotentials for h to kr optimized for gradient-corrected exchange-correlation functionals. Theoretical Chemistry Accounts, 114(1):145–152, 2005.

[128] Joost VandeVondele and Jürg Hutter. Gaussian basis sets for accurate calculations on molecular systems in gas and condensed phases. The Journal of chemical physics, 127(11), 2007.

[129] Manuel Guidon, Jurg Hutter, and Joost VandeVondele. Auxiliary density matrix methods for hartree- fock exchange calculations. Journal of chemical theory and computation, 6(8):2348–2364, 2010.

[130] Stefano Falletta, Julia Wiktor, and Alfredo Pasquarello. Finite-size corrections of defect energy levels involving ionic polarization. Physical Review B, 102(4):041115, 2020.

[131] Jack Strand, Sergey K Chulkov, Matthew B Watkins, and Alexander L Shluger. First principles calculations of optical properties for oxygen vacancies in binary metal oxides. The Journal of Chemical Physics, 150(4), 2019.

[132] Marcella Iannuzzi, Thomas Chassaing, Thomas Wallman, and Jürg Hutter. Ground and excited state density functional calculations with the gaussian and augmented-plane-wave method. Chimia, 59(7-8):499–499, 2005.

[133] Igor Sokolović, Giada Franceschi, Zhichang Wang, Jian Xu, Jiří Pavelec, Michele Riva, Michael Schmid, Ulrike Diebold, and Martin Setvín. Quest for a pristine unreconstructed srtio 3 (001) surface: An atomically resolved study via noncontact atomic force microscopy. Physical Review B, 103(24):L241406, 2021.

[134] Manuel Plaza, Xin Huang, JY Peter Ko, Mei Shen, Burton H Simpson, Joaquín Rodríguez-López, Nicole L Ritzert, Kendra Letchworth-Weaver, Deniz Gunceler, Darrell G Schlom, et al. Structure of the photo-catalytically active surface of srtio3. Journal of the American Chemical Society, 138(25):7816–7819, 2016.

[135] Marius Schmidt, Sudarshan Rajagopal, Zhong Ren, and Keith Moffat. Application of singular value decomposition to the analysis of time-resolved macromolecular x-ray data. Biophysical journal, 84(3):2112–2129, 2003.

[136] Christopher C Paige and Michael A Saunders. Towards a generalized singular value decomposition. SIAM Journal on Numerical Analysis, 18(3):398–405, 1981.

[137] Charles F Van Loan. Generalizing the singular value decomposition. SIAM Journal on numerical Analysis, 13(1):76–83, 1976.

[138] Shay McBride, Wei Chen, Tanja Cuk, and Geoffroy Hautier. Do small hole polarons form in bulk rutile tio2? The Journal of Physical Chemistry Letters, 16(9):2333–2339, 2025.

[139] Michael A Henderson. The interaction of water with solid surfaces: fundamental aspects revisited. Surface Science Reports, 46(1-8):1–308, 2002.

[140] Peiwei You, Daqiang Chen, Xinbao Liu, Cui Zhang, Annabella Selloni, and Sheng Meng. Correlated electron–nuclear dynamics of photoinduced water dissociation on rutile tio2. Nature Materials, 23(8):1100–1106, 2024.

[141] George B Kauffman. Inorganic chemistry, (miessler, gary l.; tarr, donald a.), 2000.

[142] WG Nilsen and JG Skinner. Raman spectrum of strontium titanate. the Journal of chemical physics, 48(5):2240–2248, 1968.

[143] PA Fleury and JM Worlock. Electric-field-induced raman effect in paraelectric crystals. Physical Review Letters, 18(16):665, 1967.

[144] V Dvořák. First-order raman effect induced by the static electric field in cubic perovskite-type ferroelectrics. Physical Review, 159(3):652, 1967.

[145] AA Sirenko, IA Akimov, JR Fox, AM Clark, Hong-Cheng Li, Weidong Si, and XX Xi. Observation of the first-order raman scattering in srtio 3 thin films. Physical review letters, 82(22):4500, 1999.

[146] VN Denisov, BN Mavrin, VB Podobedov, and JF Scott. Hyper-raman spectra and frequency dependence of soft mode damping in srtio3. Journal of Raman spectroscopy, 14(4):276–283, 1983.

[147] H Vogt. Hyper-raman tensors of the zone-center optical phonons in srtio 3 and ktao 3. Physical Review B, 38(8):5699, 1988.

[148] MP Fontana and M Lambert. Linear disorder and temperature dependence of raman scattering in batio3. Solid State Communications, 10(1):1–4, 1972.

[149] RA Cowley. Lattice dynamics and phase transitions of strontium titanate. Physical Review, 134(4A):A981, 1964.

[150] RF Schaufele and MJ Weber. First-and second-order raman scattering of srtio3. The Journal of Chemical Physics, 46(7):2859–2861, 1967.

[151] U Balachandran and NG Eror. Raman spectra of strontium titanate. Journal of the American Ceramic Society, 65(4):c54–c56, 1982.

[152] H Trabelsi, M Bejar, E Dhahri, MPF Graça, MA Valente, and K Khirouni. Structure, raman, dielectric behavior and electrical conduction mechanism of strontium titanate. Physica E: Low-dimensional Systems and Nanostructures, 99:75–81, 2018.

[153] David W McCamant, Philipp Kukura, and Richard A Mathies. Femtosecond broadband stimulated raman: A new approach for high-performance vibrational spectroscopy. Applied spectroscopy, 57(11):1317–1323, 2003.

[154] Renee R Frontiera and Richard A Mathies. Femtosecond stimulated raman spectroscopy. Laser & Photonics Reviews, 5(1):102–113, 2011.

[155] Soo-Y Lee, Donghui Zhang, David W McCamant, Philipp Kukura, and Richard A Mathies. Theory of femtosecond stimulated raman spectroscopy. The Journal of chemical physics, 121(8):3632–3642, 2004.

[156] Rorbert L Carman, F Shimizu, CS Wang, and N Bloembergen. Theory of stokes pulse shapes in transient stimulated raman scattering. Physical Review A, 2(1):60, 1970.

[157] Gábor Keresztury, JM Chalmers, and PR Griffith. Raman spectroscopy: theory. Handbook of vibrational spectroscopy, 1:71–87, 2002.

[158] David W McCamant, Philipp Kukura, Sangwoon Yoon, and Richard A Mathies. Femtosecond broadband stimulated raman spectroscopy: Apparatus and methods. Review of scientific instruments, 75(11):4971–4980, 2004.

[159] David P Hoffman, David Valley, Scott R Ellis, Mark Creelman, and Richard A Mathies. Optimally shaped narrowband picosecond pulses for femtosecond stimulated raman spectroscopy. Optics Express, 21(18):21685–21692, 2013.

[160] Iciar Arnay, Juan Rubio-Zuazo, and German R Castro. Impact of cleaning methods on the structural properties and morphology of srtio3 surface. Applied Surface Science, 427:561–565, 2018.

[161] Hendrik Bluhm. Photoelectron spectroscopy of surfaces under humid conditions. Journal of Electron Spectroscopy and Related Phenomena, 177(2-3):71–84, 2010.

[162] Stephanie N Choing Choing. Spectroscopic Studies of Physical and Electronic Structure in Transition Metal Oxide Photocatalysts. PhD thesis, UC Berkeley, 2016.

[163] John T Newberg, David E Starr, Susumu Yamamoto, Sarp Kaya, Tom Kendelewicz, Erin R Mysak, Soeren Porsgaard, Miquel B Salmeron, Gordon E Brown Jr, Anders Nilsson, et al. Formation of hydroxyl and water layers on mgo films studied with ambient pressure xps. Surface Science, 605(1-2):89–94, 2011.

[164] EK Sanchez, S Ha, J Grim, M Skowronski, WM Vetter, M Dudley, R Bertke, and WC Mitchel. Assessment of polishing-related surface damage in silicon carbide. Journal of The Electrochemical Society, 149(2):G131, 2002.

[165] Kelsey A Stoerzinger, Wesley T Hong, Ethan J Crumlin, Hendrik Bluhm, Michael D Biegalski, and Yang Shao-Horn. Water reactivity on the lacoo3 (001) surface: an ambient pressure x-ray photoelectron spectroscopy study. The Journal of Physical Chemistry C, 118(34):19733–19741, 2014.

Appendix A

Gating for Data Collection Camera

A.1 Description and Pseudo-code

Table A.1: Inputs and Outputs for the Arduino that serves the gate the trigger for the referencing and acquisition cameras. The gating serves to establish a consistent 'shot # 1' with respect to the different possible pulse combinations.

Inputs			
Arduino pgm	**Label on Cable**	**ns lable**	**fs laser**
2 CHOPPER	Chopper	CD output from SRS # 2	OUT1 from chopper (250 Hz for Raman, 500 Hz for TR)
4 TRIGGER	Cam Sync SDG	AB output from SRS # 1 (1 kHz laser trigger)	
7 GATE	Shutter on/off	Shutter Arduino Output, 1 = shutter open, 0 = closed	
6 CAMERAOUT	Can Out	Logic Out from acquisition camera	
Output			
11 CAMERAIN	Cam In	Trigger for referencing and acquisition camera	

The purpose of this program is to ensure that data is collected beginning with the appropriate 'shot # 1' with respect to the on/off status of the UV and Raman pump pulses. Each configuration of the lasers pulse is unique and will occur in cyclical order. Therefore, data analysis can be designed to accommodate these pulse combinations regardless of which comes first, as long the same pulse combination arrives first. This is achieved by monitoring several digital TTL signals, and using the output of an optical chopper to define 'shot # 1'. This chopper signal corresponds to the UV chopper in TR experiments and to the Raman pulse chopper in FSRS experiments. This signals are inputs to an Arduino which is programmed to gate the trigger pulse to the acquisition and reference cameras. The inputs and outputs for the Arduino program are described in Table A.1:

The pseudo-code for this program is shown below:

- when the camera busy (CAMERA OUT) is low, the shutter is open (GATE is high), flag = 0 (variable defined in program), and rising edge detected from chopper output: wait 3.7 ms, and set flag to 1
- when camera busy (CAMERA OUT) is high: set flag to 0, and set camera sync (CAMERA IN) to 0
- when flag = 1, and laser (TRIGGER) is high, CAMERA IN is high
- when flag = 1, and TRIGGER is high, CAMERA IN is low

The first item prepares a variable within the code (flag), after waiting a prescribed amount of time once a rising edge is detected on the chopper signal. This Arduino then acts an AND gate for the main laser trigger and the flag variable.

A.2 Arduino Code

```
//use digital pins 0-7 as inputs for PIND function to work
#define CHOPPER 2
#define TRIGGER 4
#define CAMERAOUT 6
#define GATE 7
#define CAMERAIN 11


int flag = 0;
byte edge = 0;
byte chopsig = 0;
```

```
void setup() {
pinMode(CAMERAIN, OUTPUT);      //output to camera
pinMode(CHOPPER, INPUT_PULLUP); //500 HZ chopper signal (TR) 250 Hz chopper (FSRS)
pinMode(TRIGGER, INPUT_PULLUP); //trigger from laser
pinMode(GATE, INPUT_PULLUP);    //trigger from shutter
CAMERAOUT, INPUT_PULLUP);       //output from camera
}


void loop () {
chopsig = (PIND & (1 << CHOPPER)); //read 250 Hz chopper state and store in chopsig
chopsig = chopsig >> CHOPPER;      //chopsig is 0 or 1 if chopper is lo or hi
edge = edge << 1;                  //bitshift chop sig into edge variable
edge = edge | chopsig;             //change LSB to 0 or 1 for chopper lo or hi
edge = edge & 0b00000011;          //clear all but 2 least significant bits


//when cameraout is low, gate is high, flag is 0, rising edge on chopper 2, set flag
//high
if (!(PIND & (1 << CAMERAOUT)) && (PIND & (1 << GATE) && flag == 0) && edge == 1) {
     flag = 1;
     delayMicroseconds(3700) //wait ~ 3/4 of a 250 Hz cycle to ensure first trigger
                             //pulse is on a rising edge
     }
```

```
//camera is busy (high)

else if (PIND & (1 << CAMERAOUT)) {

     flag = 0;

     PORTB = PORTB & 0b11110111; //reset all flags and set camera output to 0

     }



//laser trigger is high and flag is set to 1

else if (PIND & (1 << TRIGGER) && flag == 1) {

     PORTB = PORTB | 0b00001000; //set camera output high (collect)

     }



//laser trigger is low and flag is set to 1

else if ( !(PIND & (1 << TRIGGER) && flag == 1)) {

     PORTB = PORTB & 0b11110111; //set camera output low (don't collect)

     }

}
```

Appendix B

Supplemental Transient Reflectance Data at the Short Time Scale for $SrTiO_3$

B.1 Full Spectra from varying Na^+ concentration at pH 7 and 13

In all TR experiments, Na^+ is present as the only counter-cation. TR was also measured with varying Na^+ concentration while maintaining constant pH. Na_2SO_4 was used to control Na^+ concentration at two unbuffered pH conditions, pH 7 and pH 13. Figure B.1 shows the transient optical spectra for varying Na^+ concentration. Both absorptive and emissive signals are present, but there is no discernible trend with Na^+ concentration and therefore ionic strength at either pH condition (A,B).

B.2 Transient Reflectance and SVD for 0.5% and 0.7% n-$SrTiO_3$

The spectra in Figure B.2 show that a pH dependence exists for the 0.1% n-doped $SrTiO_3$, there is no observable dependence at 0.5% or 0.7% doping. Additionally, higher doped samples show less emission in general (note the change in mOD scale in b) and c)). The above is a representative set of data, with spectra selected to show the pH dynamics and lack thereof. Complete data sets were collected for each doping density and were used to perform an SVD analysis.

Figure B.3 shows the singular value decomposition of the data represented in Figure B.2, confirming that the 2 significant components carry a pH dependence, while the higher doped n-$SrTiO_3$ does not. The SVD analysis utilized by comparing kinetic traces, which contain the information on the time-dependent populations. Since this is a raw (unconstrained) SVD analysis, the spectra assigned to the populations will differ based on the range of data collected in both time and energy.

Figure B.1: Transient optical spectra of varying Na^+ concentration in (A) pH 7 conditions and (B) pH 13 conditions. Both pH conditions were unbuffered in closed-circuit (0 V). Note the change in mOD scale between pH 7 and 13.

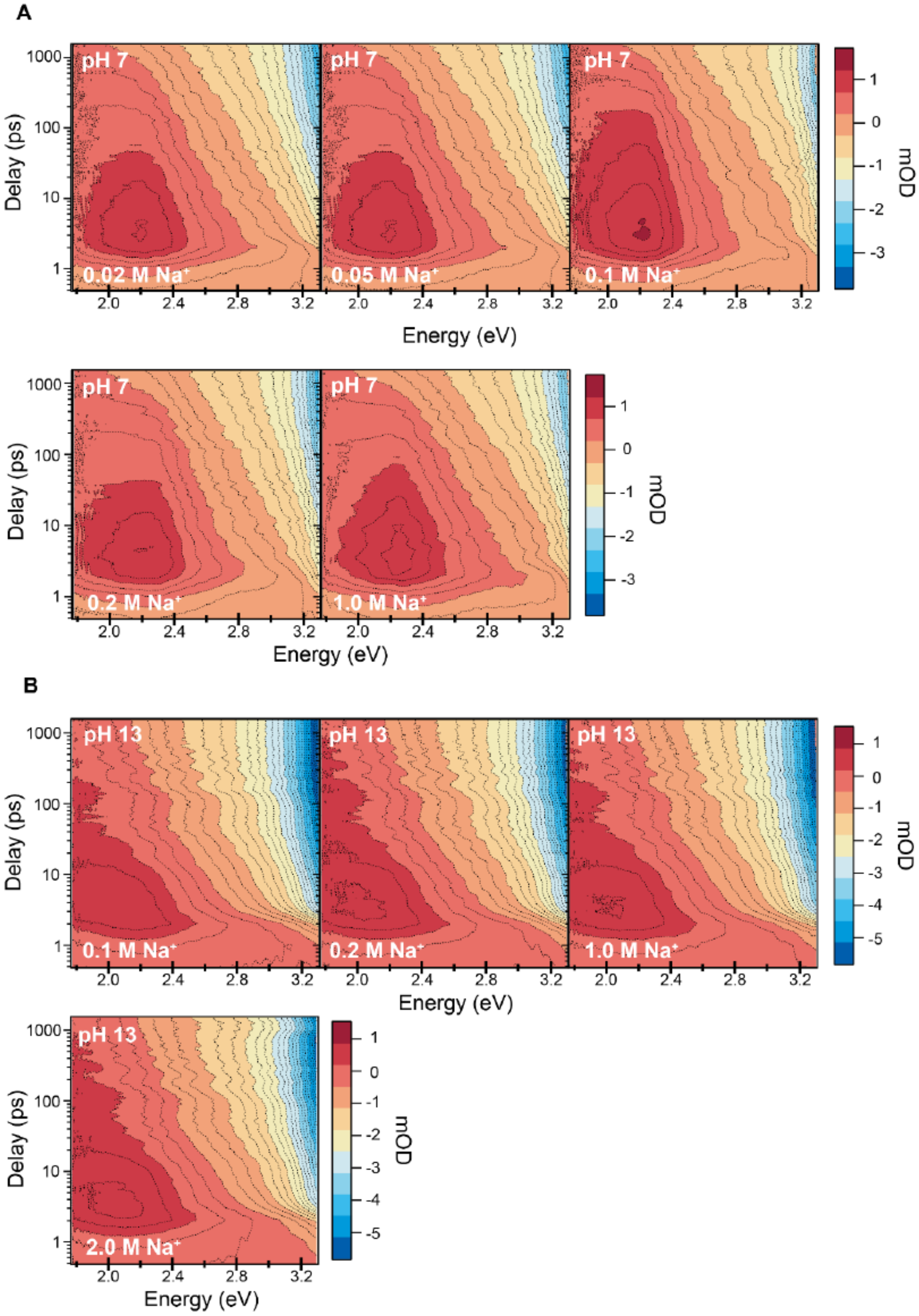

Figure B.2: pH dependence of different n-doping densities shown for a) 0.1% n-$SrTiO_3$, b) 0.5% n-$SrTiO_3$, and c) 0.7% n-$SrTiO_3$. All data are collected at 0 V and solutions are phosphate buffered.

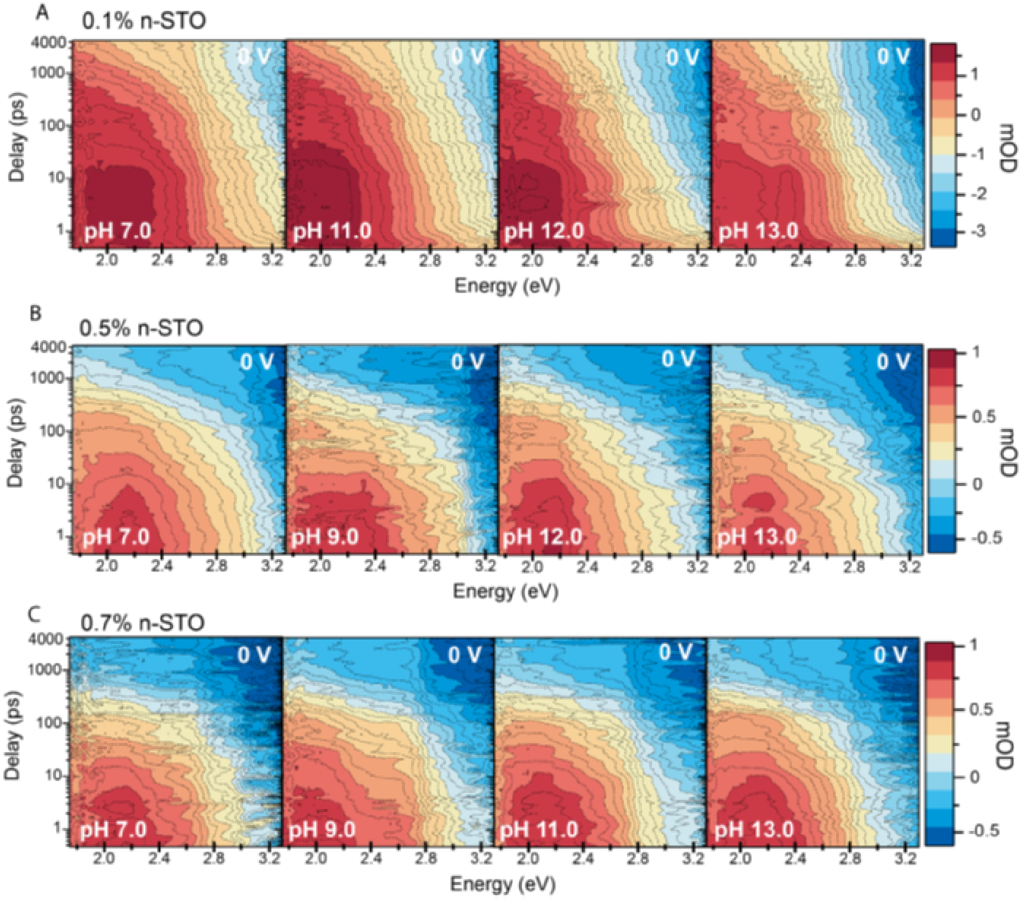

Figure B.4 shows that the rotation and constrained SVD analysis reproduces a nearly sigmoidal pH dependence in the newly acquired data on 0.1% n-$SrTiO_3$, while the $A_1 \sim 2$ ps component in the 0.5%, and 0.7% doped smaples show little to no observable pH dependence. This confirms observations based on the raw data (Figure B.2) and unconstrained SVD analysis (Figure B.3). A lack of observable pH dependence in TR reflects a change in the hydroxylation of the highly doped $SrTiO_3$ surfaces as shown by AP-XPS (Section 2.1). The hydroxylation increase by a factor of $\sim$2 suggests that the equilibrium (Equation 6.1) with the electrolyte cannot bu pushed in the accessible pH range. AP-XPS data for 0.5% doped $SrTiO_3$ is not available, but the similarity in optical data to 0.5% doped $SrTiO_3$ suggests a high level of surface hydroxylation.

A fully hydroxylated surface changes the way one would think about hole-trapping, in that

Figure B.3: Raw SVD analysis of pH dependence of different n-doping densities shown for a) 0.1% n-$SrTiO_3$, b) 0.5% n-$SrTiO_3$, and c) 0.7% n-$SrTiO_3$. Spectra and kinetics for the first 2 SVD components are shown.

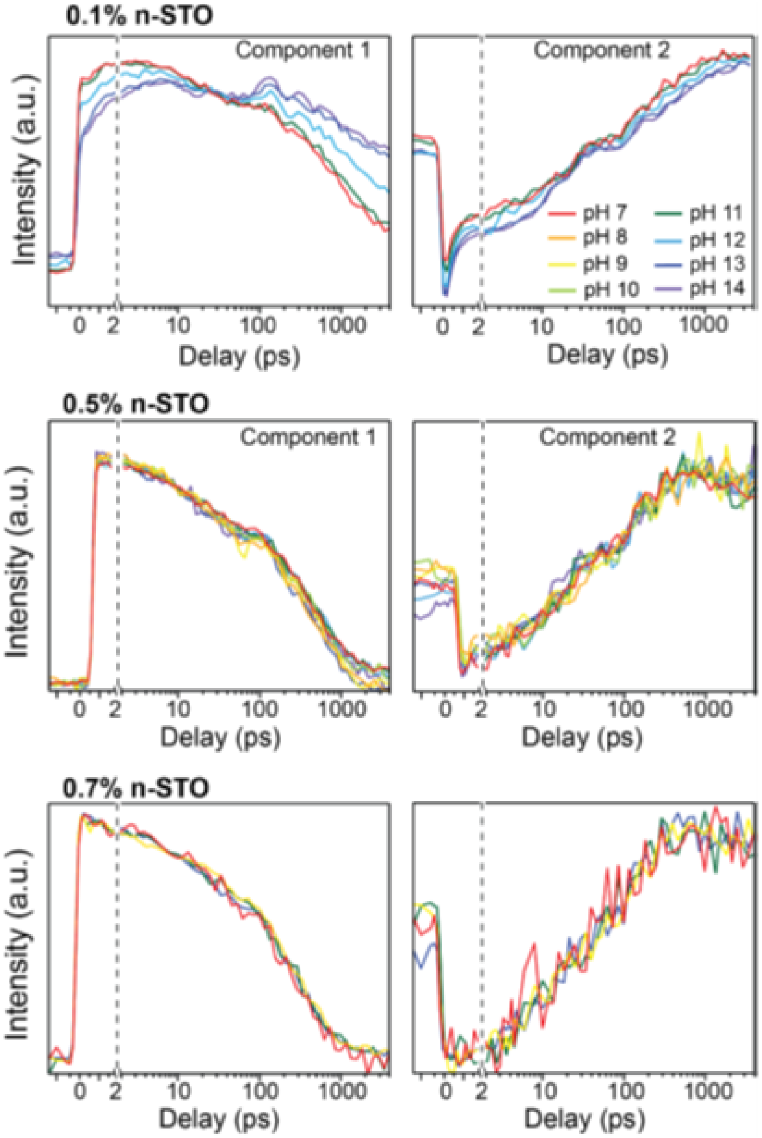

the hole could delocalize among the sites on the now 2D network of hydroxyl groups. The could lead to a lower $\Delta G_{OH^*}(U_{VB})$ for reaction 6.2 associated with more delocalized hole-polaron orbitals. The lower $\Delta G_{OH^*}(U_{VB})$ implies less trapping, while the delocalization of the hole-polaron orbital implies a weaker optical transition dipole for emission. Both effects imply less overall emission in the TR as observed in Figure B.2. Therefore, we have a dichotomy between a fully hydroxylated surface (0.7% n-$SrTiO_3$) in which both little pH dependence and less emission are anticipated and

Figure B.4: a) Rotational Analysis and b) Contrained SVD of different n-doping densities shown for 0.1% n-$SrTiO_3$, 0.5% n-$SrTiO_3$, and 0.7% n-$SrTiO_3$.

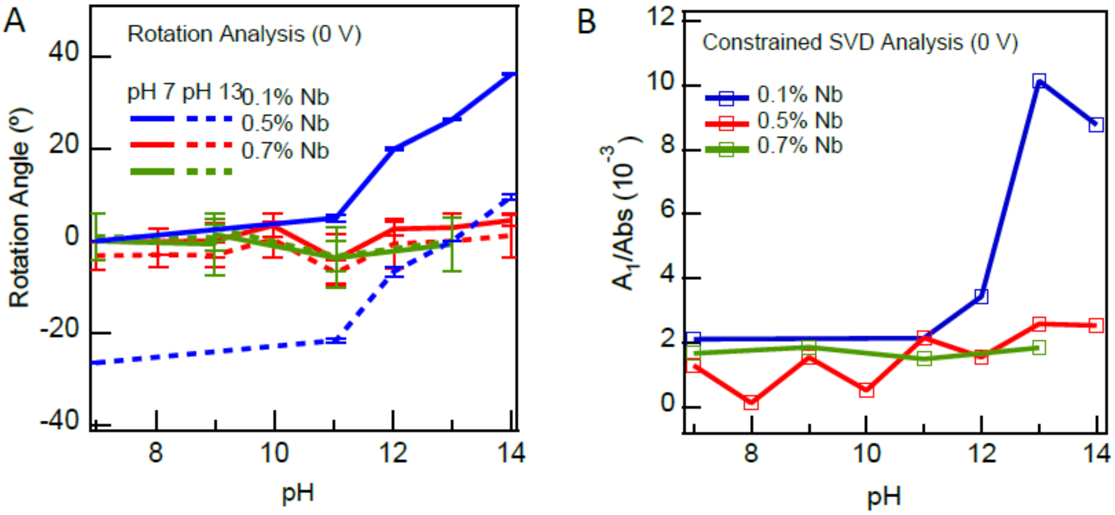

a surface with isolated hydroxyls among water absorbed and bare oxygen sites (undoped, 0.1 % n-$SrTiO_3$), where the equilibrium can be pushed by pH and localized hole traps lead to more emission. In a range of n-doping in between 0.1% and 0.5%, one might expect a pH dependence but with less emissive signal overall. These considerations do have significant implications on the nature of the first electron transfer intermediates (M-OH^*) that lead to different oxides and we leave this for future work.

B.3 Other Reaction Conditions, Unbuffered Sulfate Solutions, OC

The constrained SVD analysis was performed on closed-circuit TR data taken in unbuffered electrolyte conditions where Na_2SO_4 was used as the counter ion to maintain a constant sodium ion concentration of 100 mM (excluding pH 14, which is necessarily 1 M NaOH). The constrained kinetic components are shown in Figure B.5a and b. The two pH-independent time constants (Figure B.5c) from the emissive growth are consistent with those of phosphate-buffered data. The emissive kinetics of sulfate-unbuffered data exhibit sigmoidal behavior at the same pH (11.7) as the phosphate buffered data, albeit with a stronger pH dependence. Between pH 7 and pH 13, the A_1/Abs component of emission increases by a multiplicative factor of ~3 (Figure B.6d)rather than

Figure B.5: Doping Comparison for n-$SrTiO_3$ at 0 V with Constrained SVD Analysis of TR Spectra in Unbuffered Solution with Na^+ as the Counter Ion. Constrained kinetics are show as a) emissive and b) absorptive components. c) Time constants from the biexponential fit of the constrained kinetics as a function of pH. d) Amplitudes associated with the emissive time constants normalized by the integrated absorption as a function of pH.

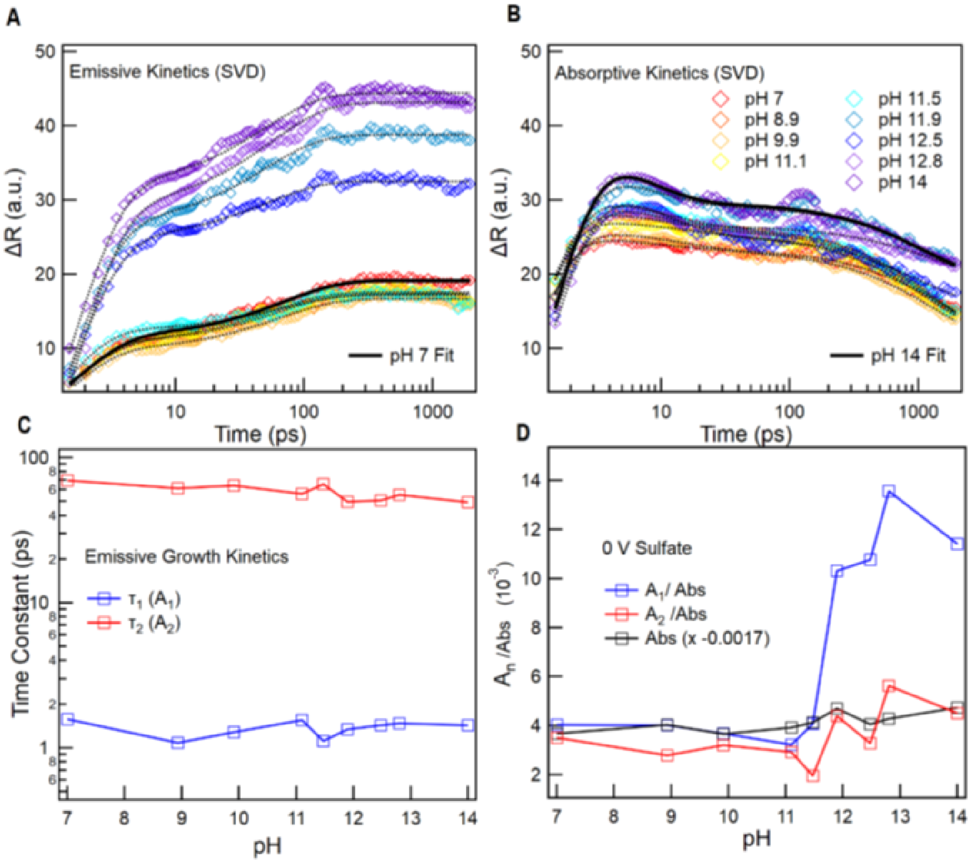

∼2. Absorptive kinetics also exhibit a small pH dependence not observed in phosphate-buffered conditions.

The constrained SVD analysis was performed on open-circuit TR data taken in unbuffered electrolyte conditions where Na_2SO_4 was used as the counter ion to maintain a constant sodium ion concentration of 100 mM (excluding pH 14, which is necessarily 1 M NaOH) and the constrained kinetic components are shown in Figure B.6a and b. The time constants (Figure B.6c exhibits relatively time independent behavior, just like the closed circuit condition counterpart. The A_1/abs (Figure B.6d) emissive kinetics of open-circuit data exhibit sigmoidal behavior at a similar pH (11.7) as the phosphate buffered data and with a factor of ∼ 4 increase between pH 7 and pH 13.

Figure B.6: Doping Comparison for n-$SrTiO_3$ in OC with Constrained SVD Analysis of TR Spectra in Unbuffered Solution with Na^+ as the Counter Ion. Constrained kinetics are show as a) emissive and b) absorptive components. c) Time constants from the biexponential fit of the constrained kinetics as a function of pH. d) Amplitudes associated with the emissive time constants normalized by the integrated absorption as a function of pH.

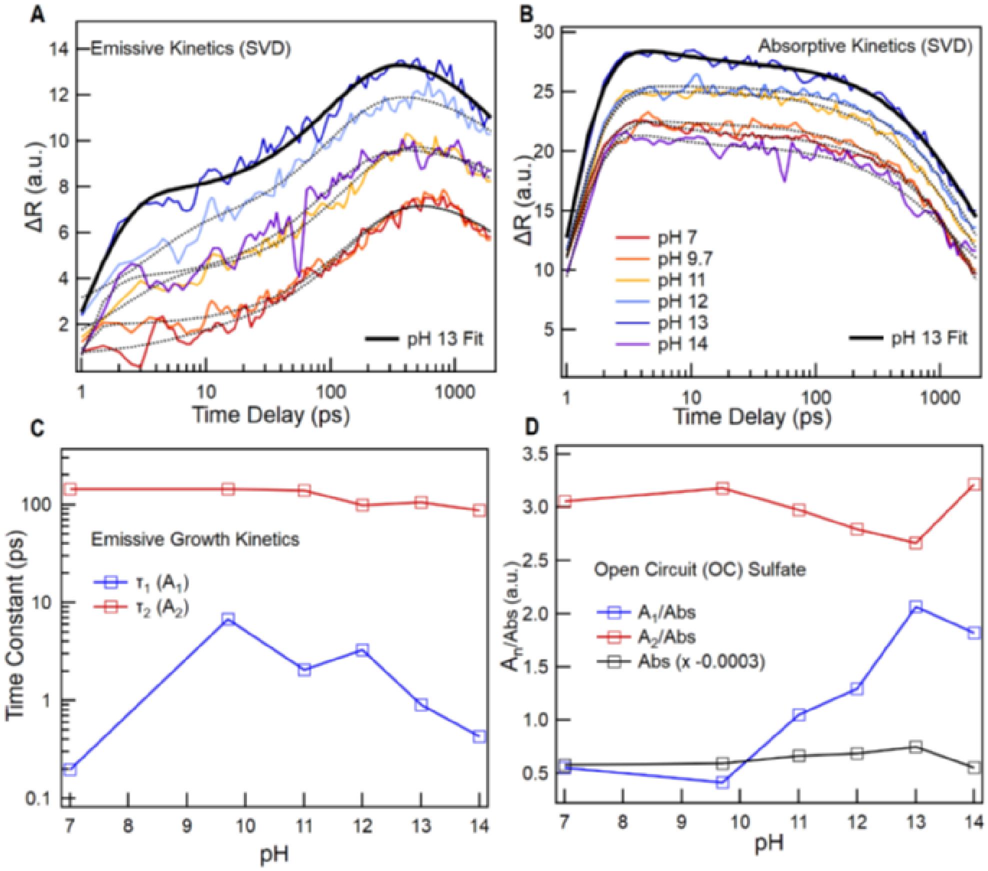

The broader curve could be due to not disentangling the absorptive or A_2 (the second emissive component) contribution in the SVD analysis due to the low number of surface polarons.

B.4 Kinetic Isotope Effect

The kinetic isotope effect was tested in pH 7 and pH 13 conditions using dueterated water and sodium hydroxide. The kinteic traces taken at 400 nm (Figure B.7a) corresponding to various reaction conditions show little difference when directly compared to each other, signaling that a deeper analysis is required. Thus, constrained SVD analysis was performed on the data sets to get

Figure B.7: H_2O/D_2O Kinetic Isotope Effect. a) Raw kinetic traces. b) and c) Constrained Kinetic and absorptive components respectively.

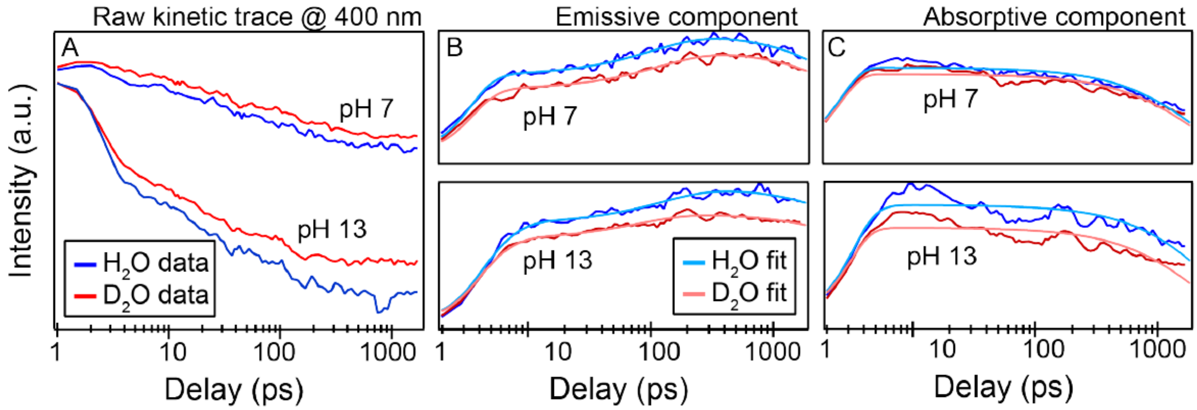

Table B.1: H_2O/D_2O Kinetic Isotope Effect. Column 3 shows the extracted time constants for the $\sim$ 2 ps A_1 emissive component and the resulting KIE ratio. teo different trials are shown (KIE 1 and KIE 2).

KIE 1	**Isotope**	τ_1	$\mathbf{K_{1H}/K_{1D}}$
pH 7	D_2O	1.49 ± 0.12	1.40 ± 0.13
pH 7	H_2O	2.09 ± 0.11	
pH 13	D_2O	2.39 ± 0.13	0.96 ± 0.07
pH 13	H_2O	2.31 ± 0.13	
KIE 2	**Isotope**	τ_1	$\mathbf{K_{1H}/K_{1D}}$
pH 7	D_2O	2.68 ± 0.20	0.73 ± 0.08
pH 7	H_2O	1.97 ± 0.16	
pH 13	D_2O	2.56 ± 0.12	1.09 ± 0.08
pH 13	H_2O	2.81 ± 0.16	

the emission only and absorption only spectra. The corresponding kinetic traces (Figure B.7b and c respectively) were then fit to biexponentials for the A_1 and A_2 populations. The time constants extracted represent the reaction rate assuming a first order reaction and thus can used to determine the presence of a KIE or lack thereof. The time constants associated with the emissive, $\sim$ 2 ps A_1 population for both pH 7 and pH 13, with for two trials each, are given in Table 1.

The ratio of rate constants of hydrogenated vs deuterated runs under similar conditions is in the range of 0.73 to 1.4 and the lack of any observable trend leads us to believe that there is no apparent KIE and thus there are no free protons as products. This result suggests that the hole-transfer reaction does not involve a full proton transfer to the solution.

B.5 Langmuir Isotherm through pH 14

Figure B.8: Langmuir Isotherm. (A) Isotherm with pH 14 data point included. (B) Comparison of fits through pH 13 and through pH 14 which shows that the equilibrium constant is defined in both cases within the error (± 30).

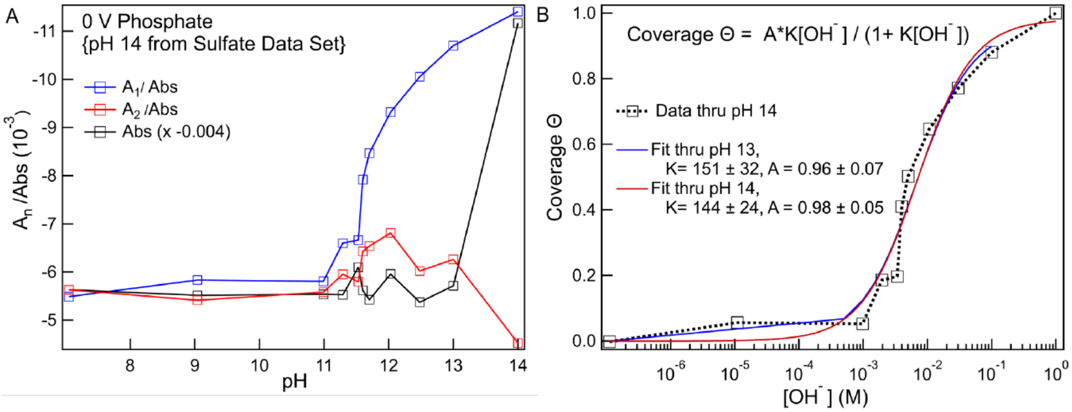

Since the two data sets (sulfate and phosphate), while taken on the same optical system, were taken at different times, the integrated absorption (black) is different due to changes in pump-probe overlap and laser fluctuations. It is nice that if we do use this integrated absorption as a normalization, the data set is continuous. To what extent it affects the value of K between pH 13 and pH 14 is also shown, $K = 151$ vs. $K = 144$, which is within the fitting error of ± 30. We note that the coverage may not be fully saturated by pH 14, but the difference between pH 13 and pH 14 indicates that the extracted K value would not change significantly.

Appendix C

Concatenation of data

Figure C.1: Short-time scale transient reflectance data collected for the purpose of concatenating with longtime data. These datasets serve as the benchmark for the magnitude of the emissive signature on the high-energy end of our time-resolved spectrum.

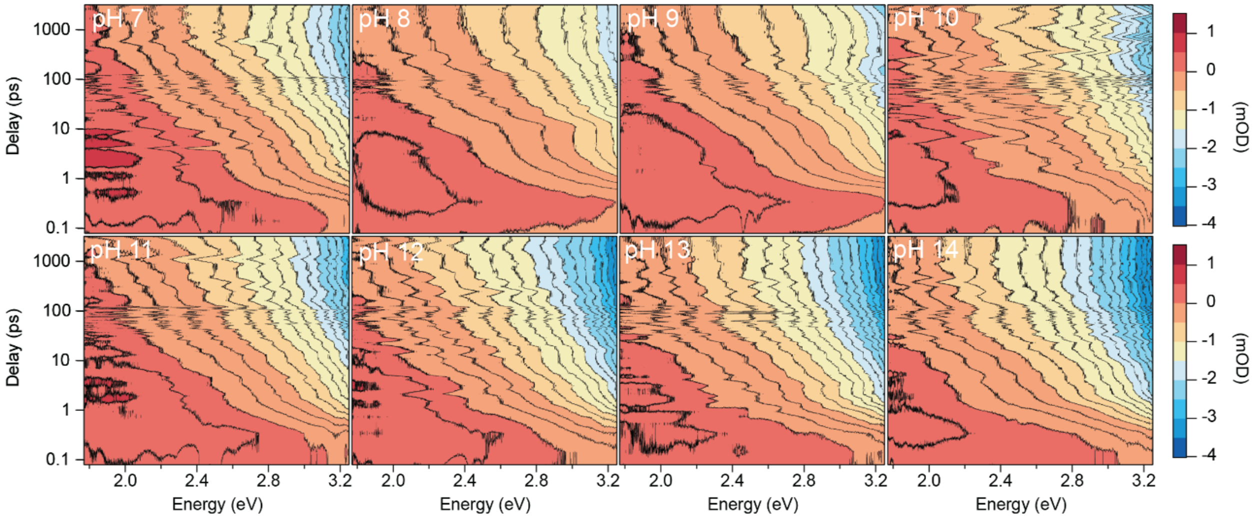

The time dynamics of the measured emissive transient signal can be thought of as having three sections: growth, metastability, and decay. The growth of the absorptive and emissive portions of this signal hap-pens on a scale of ∼2 ps and ∼60 ps respectively. To resolve these fast time scale growth dynamics, a ∼150 fs laser pulse is used as a pump. The short time scale of this laser pulse allows us to probe growth kinetics at sub-ps resolution. A moveable SMC100 stage with a pair of retroreflectors is utilized to generate a pump-probe delay from -2 to 4000 ps. This is referred to as the "short-timescale" data and is shown above in Figure C.1.

Figure C.2: Concatenated data. These datasets show the complete growth, metastability, and decay of our signal of interest. The long-timescale data is scaled such that it agrees with the short-timescale data at the point of concatenation.

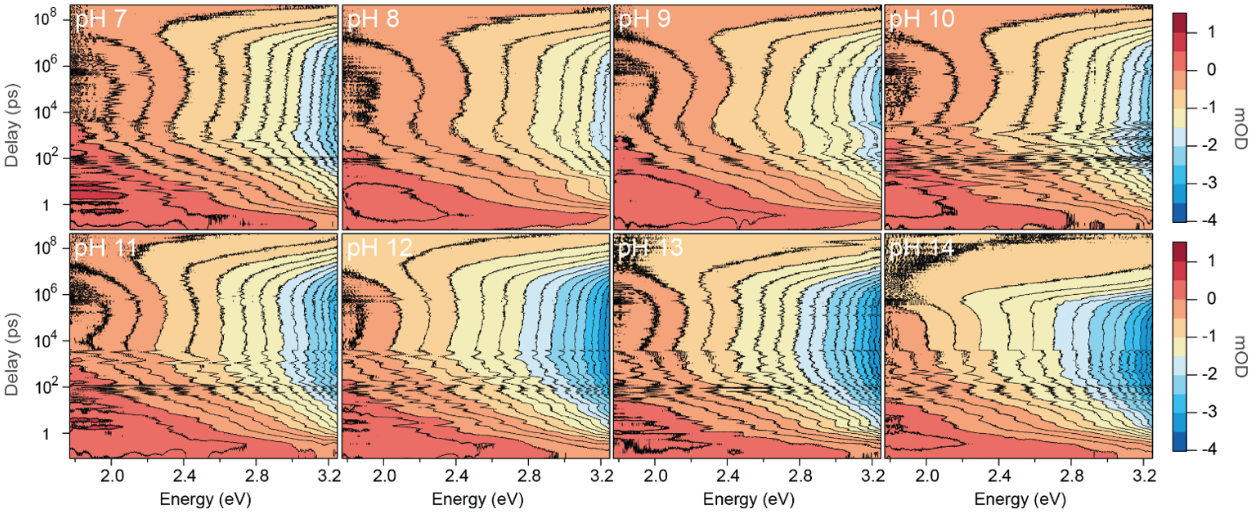

To capture the longtime dynamics of the transient signal (metastability and decay), an electronically triggered ns laser is used as a pump (instead of the fs laser pulse). This allows for delays into the 100 μs region and beyond, enabling us to fully probe the decay dynamics of the system. However, the pulse width of this laser is ∼1 ns, and therefore unable to resolve fast growth dynamics. To capture the dynamics of this system from start to finish, it is thus necessary to collect transient spectra in two separate timescales. Transient spectra in the separate timescales are then concatenated to produce a data set spanning the entire time range, as shown in Figure C.2.

The process of concatenation involves scaling the long-timescale data to match the short-timescale data in the region where the spectra share common time points. Both long- and short-time data collection schemes are identical except for the pump laser. The fs scale pump is created by third harmonic generation of pulses from a highly stable laser source. Additionally, already established trends reported in previous work (2) on short-timescale kinetics were recreated using the fs pump. The short-timescale data is thus considered the benchmark for populations within this system, and long-timescale data is scaled to match the populations shown in the short-timescale data.

Figure C.3: Spectra from short- and long-time data at the point of concatenation from pH 7 and 13. The long-timescale data is scaled to match the short-timescale data, which is considered a benchmark for populations. The left panels show the raw spectra. The center panels show the spectra after shifting the long-time data to match the common zero cross point of the short-time data. The zero-crossing point (defined by a wavelength) is highlighted by the vertical line. The panels on the right show the spectra after fully scaling to minimize the difference between the two spectra.

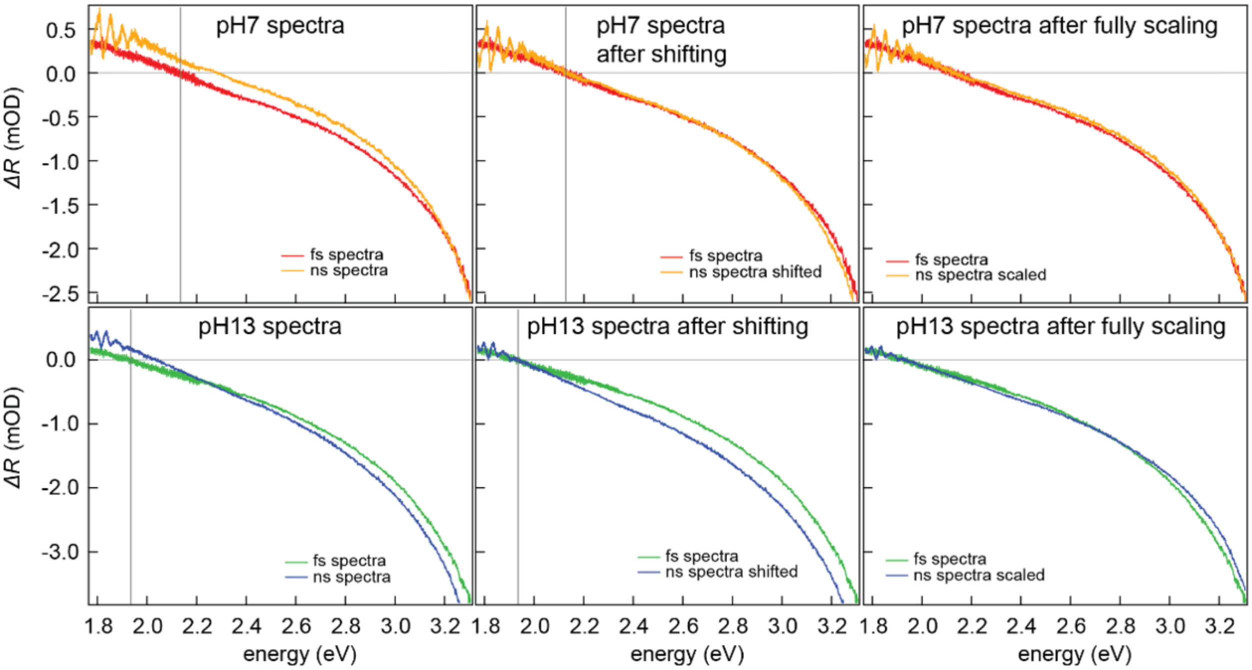

To scale the data, first the ns (long-time) data is shifted vertically such that the spectra at the point of concatenation from both timescales share a common zero-crossing point. The point of concatenation is defined as the final delay point on the fs timescale. To shift the ns data, a linear fit is done on a bracketed region (defined by a wavelength range) of the fs spectra in the neighborhood where the spectra cross zero. Similarly, a linear fit is done on the same region of the ns spectra. The entire ns dataset is then shifted by a constant such that the zero points on both linear fits are the same. Figure C.3 shows the spectra at the point of concatenation from pH 7 and 13 before and after shifting in the left and center panels respectively.

After shifting, the long-time data is multiplied by a factor designed to minimize the difference between long- and short-time data. The right most column of Figure C.3 show long- and short-

Figure C.4: Kinetics of pH 7 and 13 data at 400 nm. The kinetics are shown, from left to right, prior to scaling, after scaling, and finally after full concatenation. Once long-time data has been scaled to match the short-time scale data, all delays from the long-time scale data which overlap with the short-timescale data are dropped. The remaining long-time data is concatenated onto the short-timescale data.

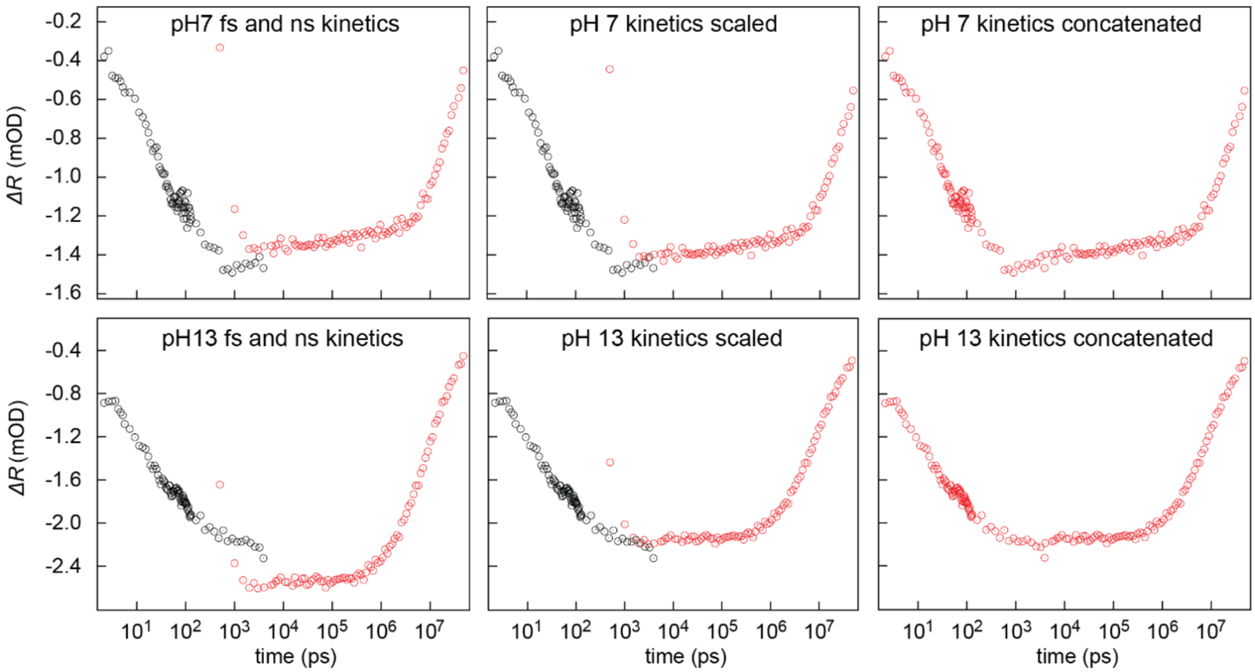

timescale spectra that have been fully scaled. Factors used to fully scale each dataset are an average of individual scaling factors computed from the spectra at each common delay point. That is, for each spectrum at the n^{th} common time delay, a scaling factor λ_n is calculated that minimizes the difference between the long- and short- time data. Common delay points prior to 1500 ps are ignored to ensure that the long-time data has reached the point of metastability. Scaling factors at the n^th common time delay are determined as follows: let $\vec{A}$ and $\vec{B}$ be vectors of different length. Suppose we want to scale $\vec{B}$ to minimize the magnitude of the difference between $\vec{A}$ and $\vec{B}$. That is, we want to minimize the norm $f(\lambda)$ of $\vec{A} - \lambda\vec{B}$:

$$f(\lambda) = \sqrt{\vec{A} - \lambda\vec{B}} \tag{C.1}$$

Setting the first derivative of Equation 4 equal to 0 we get

$$\frac{df(\lambda)}{d\lambda} = \frac{1}{2}\frac{-\vec{A}^T\vec{B} - \vec{B}^T\vec{A} + 2\lambda\vec{B}^T\vec{B}}{\sqrt{(\vec{A}-\lambda\vec{B})^T(\vec{A}-\lambda\vec{B})}} = 0 \tag{C.2}$$

$$2\lambda\vec{B}^T\vec{B} = \vec{A}^T\vec{B} + \vec{B}^T\vec{A}$$

$$\lambda = \frac{\vec{A}^T\vec{B}}{\vec{B}^T\vec{B}}$$

since $\vec{B}^T\vec{A} = \vec{A}^T\vec{B}$. The factor used to scale the long-time data is thus,

$$\lambda_n = \frac{\vec{short_n}^T\vec{long_n}}{\vec{long_n}^T\vec{long_n}} \tag{C.3}$$

where $\vec{short_n}$ and $\vec{long_n}$ are the short-time and long-time spectra at the n^{th} common delay. Kinetic traces at 400 nm from pH 7 and 13 during the concatenation process are shown in Figure C.4.

Appendix D

SVD Analysis of Data from Chapter 7 and 8

This appendix contains details regarding the SVD analysis on data from Chapters 7 and 6. SVD analysis is explained in Section 5.1 along with data from the study in Chapter 6.

D.1 Concatenated and Longtime Data SVD

Raw SVD components of concatenated data (Appendix C) on the $ps - \mu s$ timescale that is the subject of of the study in Chapter 7 is shown in Figure D.1. SVD analysis of the concatenated data reveals two significant singular values (Figure D.1A). This indicates that the first two spectral (Figure D.1B) and kinetic components (Figure D.1C) (the first two columns in $U^{(pH)}$ and $V^{(pH)}$)are sufficient to re-construct the data. Figure D.2 shows examples of longtime data reconstruction using the first 2 SVD components. Constrained SVD spectra (Figure D.2a),c)) and associated kinetics (Figure D.2b),d)) can be used to re-construct (Figure D.2e),g) the original data set, confirming that they are a thorough representation of the raw data (Figure D.2f),h)). Constrained SVD results for this data set are shown in Figure D.3. Finally, SVD from ns scale data is shown in Figure D.4. In this case, constraining is not done since there is only 1 significant SVD component.

Figure D.1: Unconstrained SVD results from concatenated data. Panel (A) shows singular values from the raw SVD analysis. Panels (B) and (C) shows the spectra and kinetics of the significant SVD components. The concatenated data has two significant SVD components.

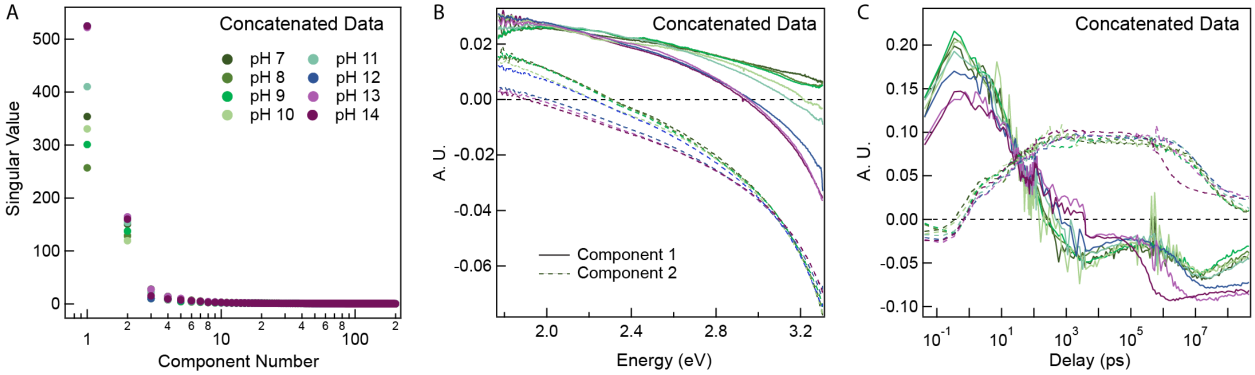

Figure D.2: Examples of longtime dataset reconstruction using the first two SVD components. The first two components from constrained SVD spectra ($U^{(t)}$) and kinetics ($V^{(t)}$) from pH 7 and 13 data are shown in A, B, C, and D. The corresponding data sets reconstructed from the first two constrained SVD components, as defined by $U^{(t)} \cdot (V^{(t)})^T$ in Equation 9, are shown in E and G for pH 7 and 13 respectively. The raw pH 7 and 13 datasets are presented in F and H for comparison.

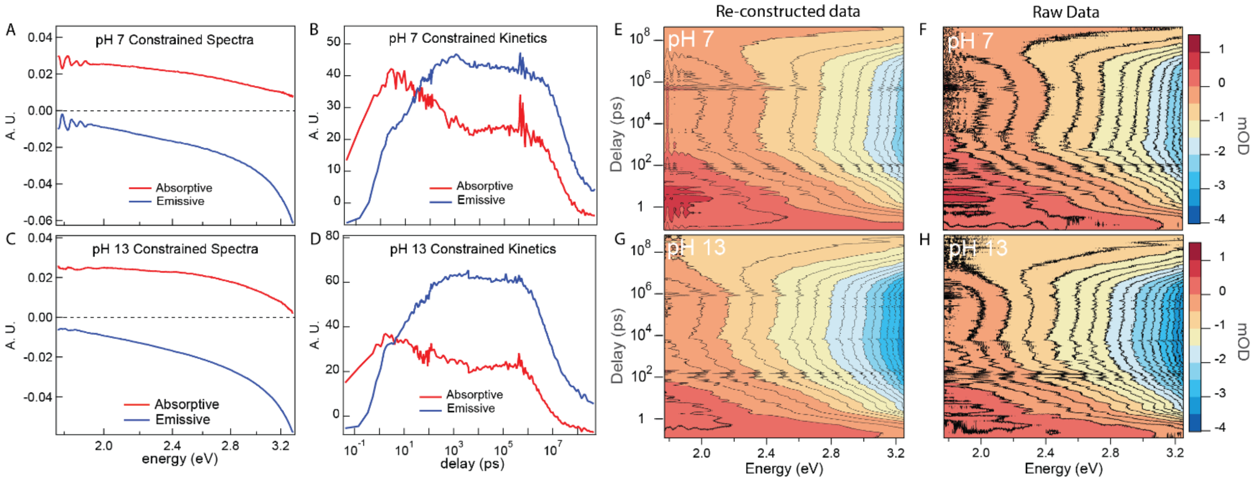

Figure D.3: Constrained SVD spectra ($U^{(t)}$) and kinetics ($V^{(t)}$) at a variety of pH points. Constrained absorptive A) and emissive B) spectra are obtained using a constrained basis shown in Figure 7.1C. Constrained absorptive C) and emissive D) kinetics are obtained in the same way. The emissive, constrained SVD kinetics track the pH dependence of our surface, which is quantified through a 4-exponential fit.

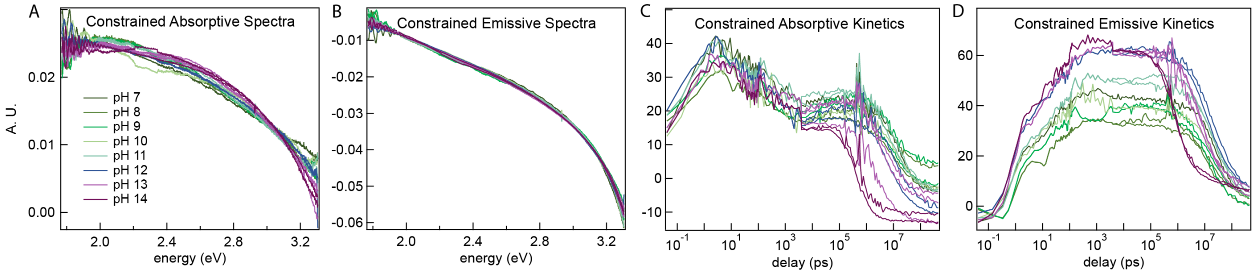

Figure D.4: Unconstrained SVD results from long-time data. Singular values from the raw SVD analysis are shown in A). Spectra and kinetics of the most significant SVD components are shown in B) and C). The long-time data has one significant SVD component since emission is the only dominant signal at this timescale.

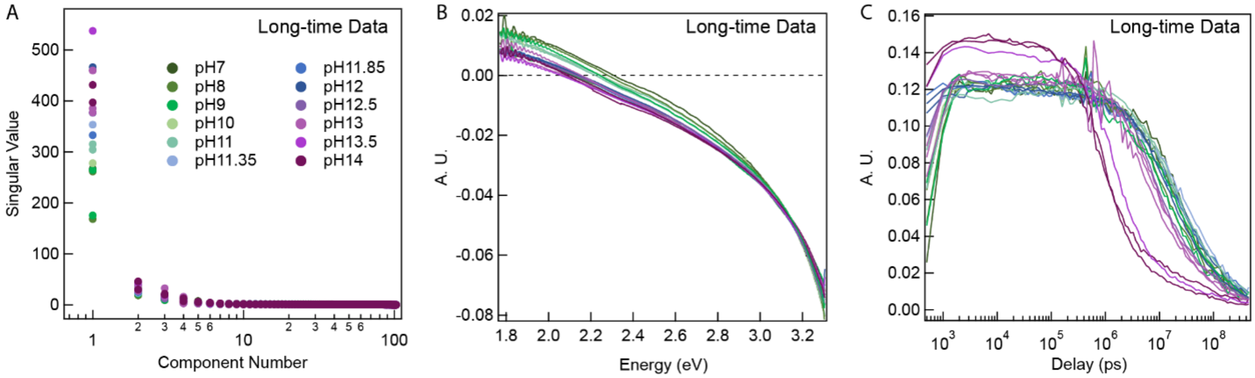

D.2 SVD from TiO_2 with varied doping density

Figure D.5: Reference timeslices of TiO_2: (a) Time slices taken between 1-5 ps and (b) between 60-100 ps for 0.5% doped samples and 150-600 ps for 0.05% and 0% samples, respectively. The black lines represent the averaged spectrum which was used as a reference spectrum for the first and second component, respectively.

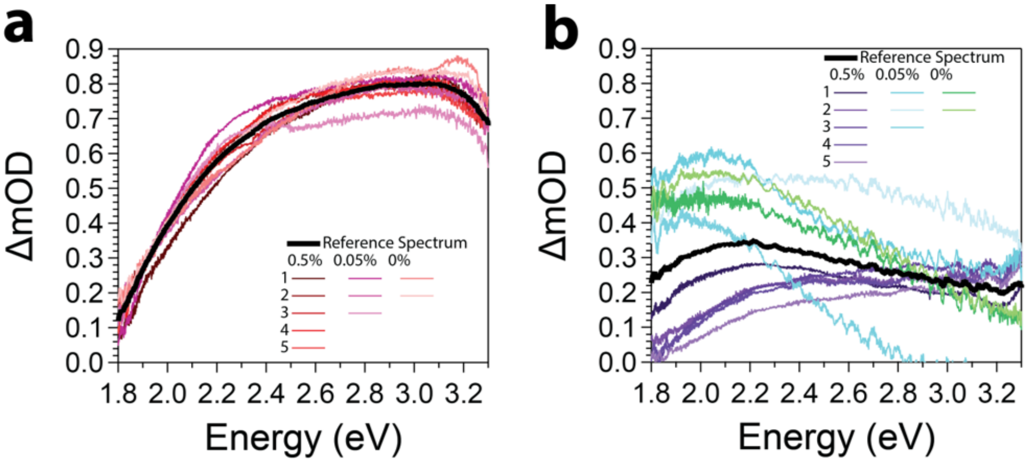

Since both relevant components in TiO_2 are of absorptive nature, it is difficult to separate them and extract their singular components. Looking at the raw data, two distinct absorptive peaks with different dynamics were observed. Together, with the fact that only the first two singular values are of significance, the assumption was made that two absorptive spectra are the main contributors to the signal. Reference spectra were extracted to serve as initial targets in our constrained SVD procedure. First component reference spectra were obtained by averaging spectra collected between time delays of 1 and 5 ps. Second component reference spectra were collected from spectra averaged between 60 and 100 ps for 0.5% doped samples and 150 and 600 ps for 0.05% and 0% samples, respectively. Those first and second component reference spectra are shown in Figure D.5a-b. The shape of the second component is far less consistent than that of the first one. This could be due to the lower amplitude and the variability across different external conditions. The 0.05% and 0% second component reference spectra also contain more noise, because we took fewer data points in the 150-600 ps time range. Note that all extracted reference spectra are averaged to obtain standard references for all datasets (thick black line in Figure D.5 a-b).

Figure D.6: Variation of parameters: The parameters for creating the constrained basis spectra are varied. a) First component spectrum constrained with various values of βa. The dotted spectrum is the optimal solution. b) Second component spectrum constrained with multiple values of α. Constrained first (c) and second (d) kinetics at various values of β and constant, optimal value of α. First (e) and second (f) constrained kinetics with constant, optimal β and varying α.

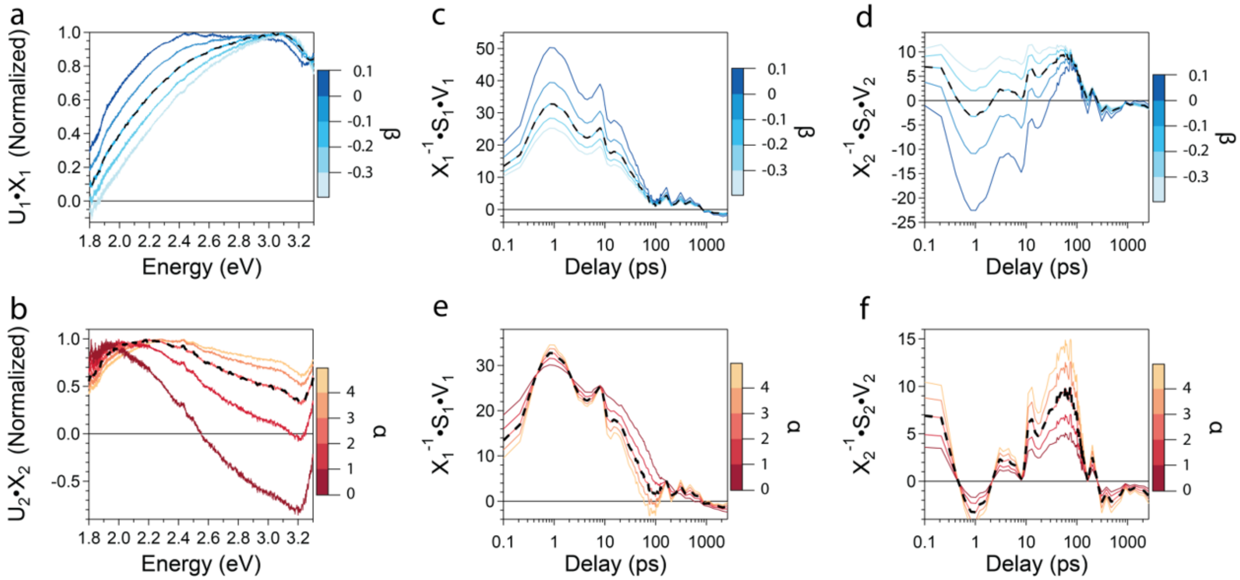

After constraining the spectral components to the reference spectra, they are refined by examining the constrained kinetics using different values for α and β. This process is illustrated by Figure D.6. Figure D.6a shows constrained first component spectra with various values of β. Constrained second component spectra at various values of α are shown in Figure D.6b. The dashed line is the optimal solution. The constrained kinetics are influenced by both α and β. To explore the influence of one parameter on the kinetics, one parameter is held constant while the other one is optimized. First and second component kinetics at varying β, and a constant, optimized value of α are shown in Figure D.6c-d. Figure D.6c shows that the main effect of β on the first component kinetics is to increase the intensity of the time traces with increasing β. The influence of β on the second component kinetics is more pronounced, as shown in Figure D.6d. At values of β lower than -0.2, the kinetics become increasingly meta-stable at early time ranges. This is not reflected in the data, as the second absorptive component does not appear until 60 to 100 ps. On the other hand, positive values of β make the early time kinetics significantly negative. Consequently, a β of roughly -0.1 provides a kinetic trace that reflects the data and is physically meaningful. The influence of α on the kinetics can also be examined at the optimal β, as shown in Figures D.6e-f. The kinetics become negative around 100 ps if the value of α is too large. Figure D.6f demonstrates that the main influence of α on the second component kinetics is the intensity of the kinetic traces. The intensity specifically increases with increasing α. Now, when α is 2.2, the first kinetic trace is positive and the second spectral component's shape is close to the reference spectrum. Thus, the optimal solution for the second component is obtained when α=2.2.

Figure D.7: Constrained SVD results of all TiO_2 datasets: a) First component SVD spectra constrained to first, dominant excited state absorption. Solid black line shows averaged constrained spectrum. b) Second component SVD spectra constrained to second excited state absorption. Averaged spectrum shown by solid black line. c) Constrained first component SVD kinetics. d) Constrained second component SVD kinetics.

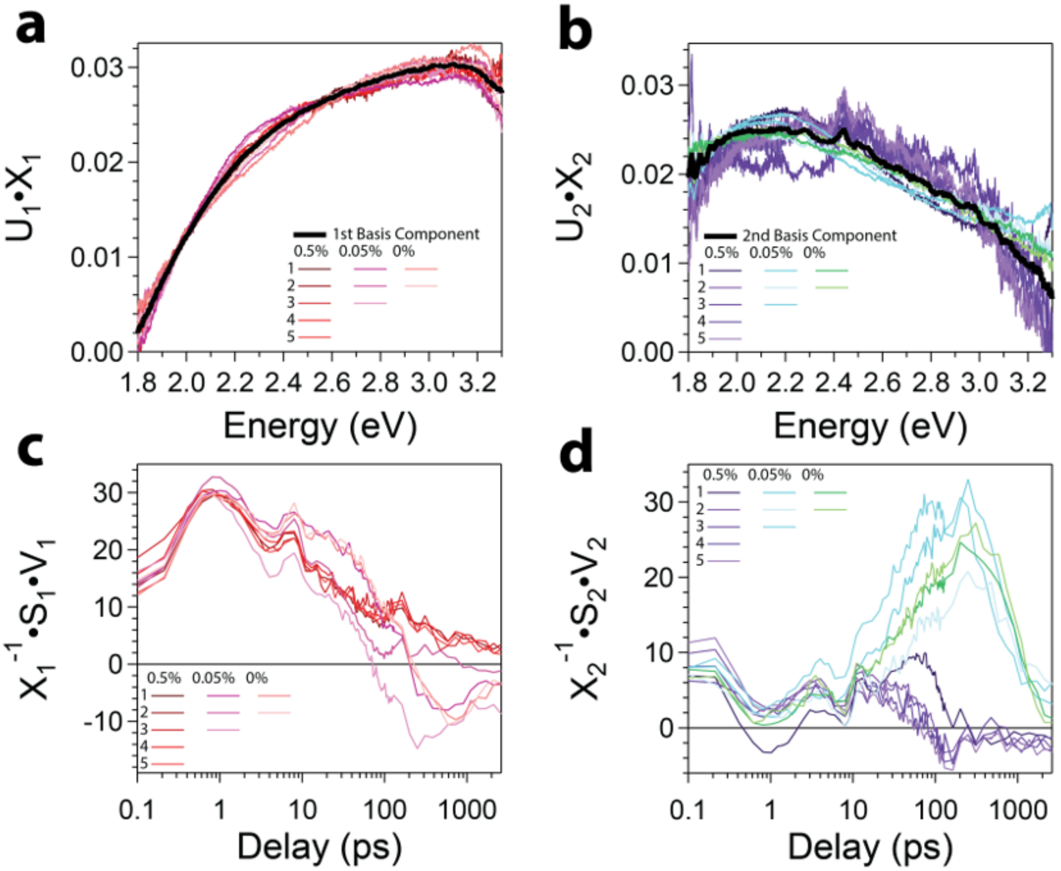

The constrained spectra and kinetics of a large TiO_2 dataset (contours shown in Figure 3.6) are shown in Figure D.7. Figures D.7a-b show the constrained first and second component spectra of the large TiO_2 dataset (with the averaged spectrum in black). The shape of the first and second component constrained spectra are quite consistent across all the datasets. Note that this was not the case in Figure D.5b, as there was considerable variation in the second component reference spectra.

First and second component constrained kinetics for the larger TiO_2 dataset are shown in Figure D.7c-d. The lifetime of the first and second component kinetics is longer for the 0.05% and 0% doped samples than in the 0.5% ones. Furthermore, the intensity of the second component increases three to four-fold for samples with doping levels lower than 0.5%. Negative kinetics are also observed at later times in some of the kinetic traces. A very small emissive signal toward the end of our delay range is responsible for these negative kinetics. This emissive signal could potentially be represented by one of the negligible SVD components, incorporated into our analysis, and remove the negative kinetics observed in Figures D.7c-d. Unfortunately, our SVD analysis becomes significantly more complex with three or more components, and the potential ability to remove the negative kinetics did not justify the added complexity. Thus, we leave the miniscule, late emission as a future area of investigation.

D.3 SVD from $SrTiO_3$ with varied doping density

For the $SrTiO_3$ SVD analysis, we constrain the first and second component spectra to be completely absorptive and emissive. Figure D.8a-b shows the constrained first and second component spectra at several values of α and β. At increasingly negative values of β, the spectrum becomes flat, and the absorptive peak starts to disappear. On the other hand, β values higher than 0.1 force the absorptive peak toward lower energies than are observed in the data. Consequently, the optimal spectrum lies in between these two extremes, and is highlighted by the dotted line. From Figure D.8b, it is clear that values of α above -1 will lead to a spectrum with both emission and absorption. Conversely, α values below -2.5 diminishes the emissive maximum observed around 2.9-3.3 eV. Thus, an emissive spectrum that retains this peak without becoming partially absorptive is the optimal solution for the second component.

Figure D.8: Variation of parameters: The parameters for creating the constrained basis spectra are varied. a) First component spectrum constrained with various values of β. The dotted spectrum is the optimal solution. b) Second component spectrum constrained with multiple values of α. Constrained first (c) and second (d) kinetics at various values of β and constant, optimal value of α. First (e) and second (f) constrained kinetics with constant, optimal β and varying α.

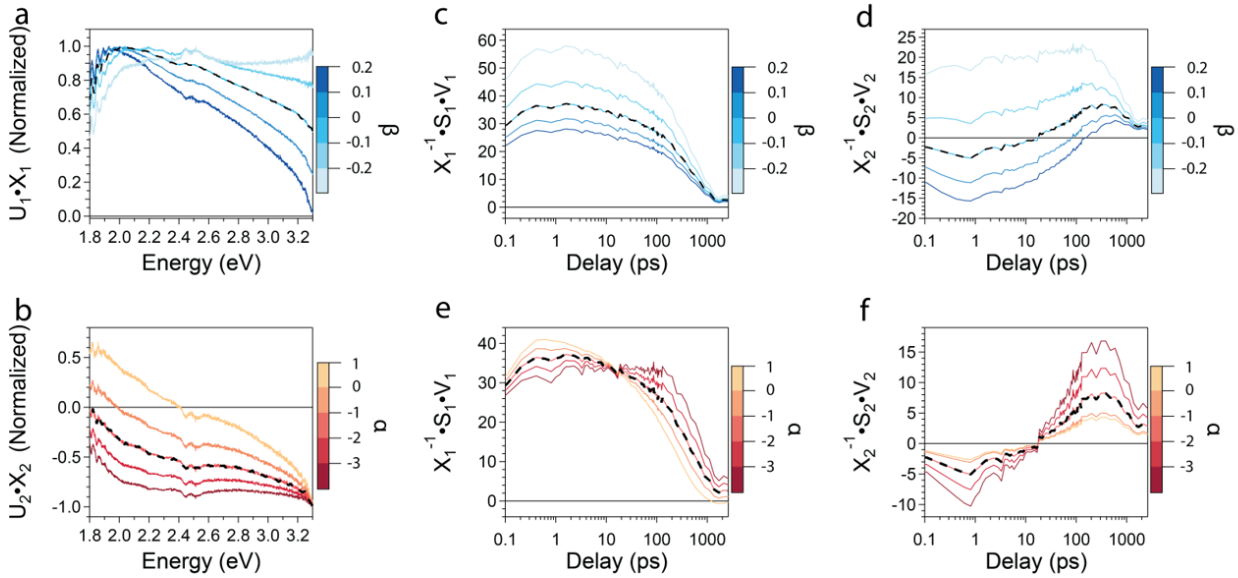

Figure D.8c-d shows the first and second component kinetics at varying β and a constant, optimal value of α. The intensity of the first component kinetics appears to increase as the value of β decreases. De-creasing the value of β also seems to increase the intensity of the second component kinetics. However, the exponential growth-like behavior of the second component kinetics is lost when β becomes smaller than -0.1. Negative kinetics are encountered for β values of zero or higher, and the time traces are more negative for higher β. Note that the absence of a clear emissive signal at early times in the STO datasets forces our optimal solution to have negative second component kinetics before 20-30 ps.

The first and second component constrained kinetics at a constant, optimal β and varying α are shown in Figure D.8e-f. Varying α appears to modify the intensity and lifetime of the first constrained component kinetics. The ultrafast rise in the first component kinetics also seems to disappear at α more negative than -2.7. All of the second component constrained kinetics are negative prior to a time delay around 20-30 ps, and then become positive. The intensity of second component kinetics also increases with decreasing α. Consequently, the optimal solution would ensure the spectral component is completely negative, and that the ultrafast rise in the first component kinetics is maintained. Our optimal solution (given by the dotted line), obtained with α = -1.7, fulfills those conditions.

Figure D.9: $SrTiO_3$ constrained SVD Results of OC, pH 7 larger dataset: a) First component SVD spectra con-strained to be completely absorptive. b) Second component SVD spectra constrained to be completely emissive. c) Constrained first component SVD kinetics. d) Constrained second component SVD kinetics.

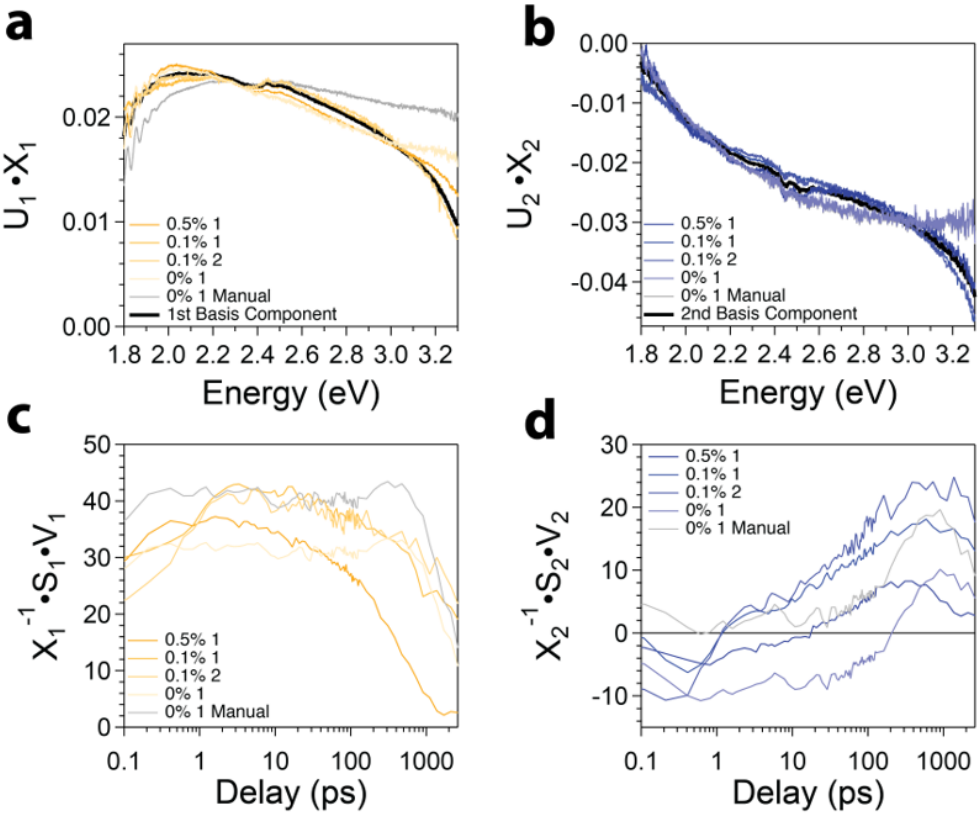

Figure D.9 shows the constrained SVD spectra and kinetics for the OC, pH 7 Nb-$SrTiO_3$ datasets discussed in this manuscript. Constrained first component kinetics in Figure D.9a show that the absorptive component in all three dopings can be constrained to the same basis (solid black line), and that basis has a peak in the 1.9-2.3 eV energy range. This is consistent with the absorptive maximum observed in the $SrTiO_3$ contour plots (Figure 3.8). The 0.5%, and 0.1% constrained, emissive second component spectrum are quite consistent with each other, but not with the 0% spectrum. This is shown in Figure D.9b. Constrained first and second component kinetics are shown in Figures D.9c-d. All constrained first component absorptive kinetics show an ultrafast rise and an exponential decay toward the end of our time range. Conversely, the emissive kinetics take tens of ps to exponentially rise toward a maximum and are negative in early time ranges to varying degrees.

Figure D.10: Nb-Doping dependence of $SrTiO_3$ and Constrained SVD analysis: a) Contours of 0.5%, 0.1% and 0% Nb-$SrTiO_3$ reconstructed from first two SVD spectral and kinetic components. Maximum normalized to one. b) Constrained first ($U_1 \cdot X_1$, orange) and second ($U_2 \cdot X_2$ blue) spectral SVD components for 0.5 %, 0.1%, 0% Nb-$SrTiO_3$ c) Constrained SVD Kinetics associated with the spectra shown in b).

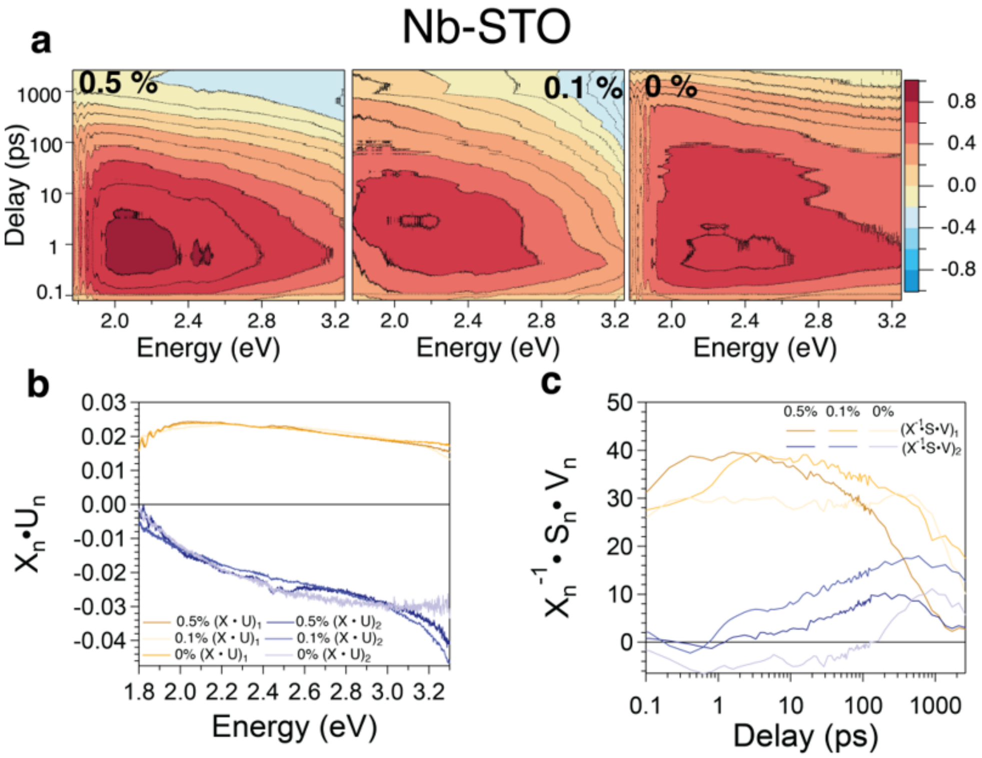

Also, for n-$SrTiO_3$ a doping dependent study was conducted. Data was recorded for 0.5% Nb 0.1% Nb and undoped $SrTiO_3$ (Figure D.10a). Constrained 1st (orange) and 2nd (blue) spectra and timetraces are shown in Figure D.10b and c, respectively. Like in TiO_2 the same first component can be found in every dataset with only varying population dynamics. The lifetime is extended for lower dopings. Similar spectra and timetraces were extracted for the second component. In the dataset of the lowest doped sample the second component deviates slightly from the higher dopings. This could be due to the very weak emissive signal in this material in our experimental time range.

D.4 Second SVD Component

Figure D.11 shows contours reconstructed from the second constrained component spectra and kinetics derived from the raw datasets shown in Figures 8.2-8.3. The constrained second component contour for TiO_2 (Figure D.11a) depicts a second component contour for $SrTiO_3$. The second component in $SrTiO_3$ is a high energy emission observed after roughly 10 ps in Figure D.11b. The sign change observed in the $SrTiO_3$ data is a result of sub-optimal optimization as is discussed in Section 3.2.4.

Figure D.11: Reconstructed Second Constrained Component Contours: Contours of the second constrained spectral and kinetic component $(U^t \cdot V^t)_2$ for a) TiO_2 abd b) $SrTiO_3$ datasets shown in Figures 8.2-8.3.

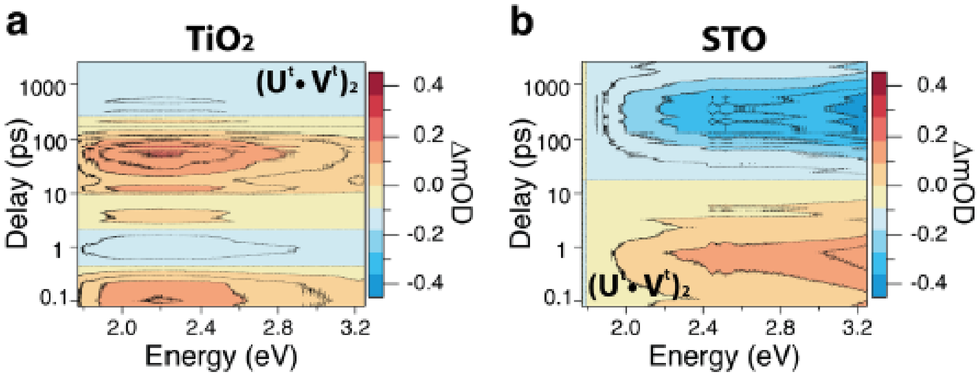

Appendix E

Fitting of data from Chapter 7

E.1 Alternative Fitting Function

Figure E.1: Fit with alternative function. A) Time constants for fit with four amplitudes (circle) and two amplitudes (cross). B) Rising amplitudes A_1 and A_2 of f_1 (Equation 7.1) compared to amplitudes of f_2. C) Decaying amplitudes A_3 and A_4 of f_1 compared to amplitudes of f_2. (D) Fit error as χ^2.

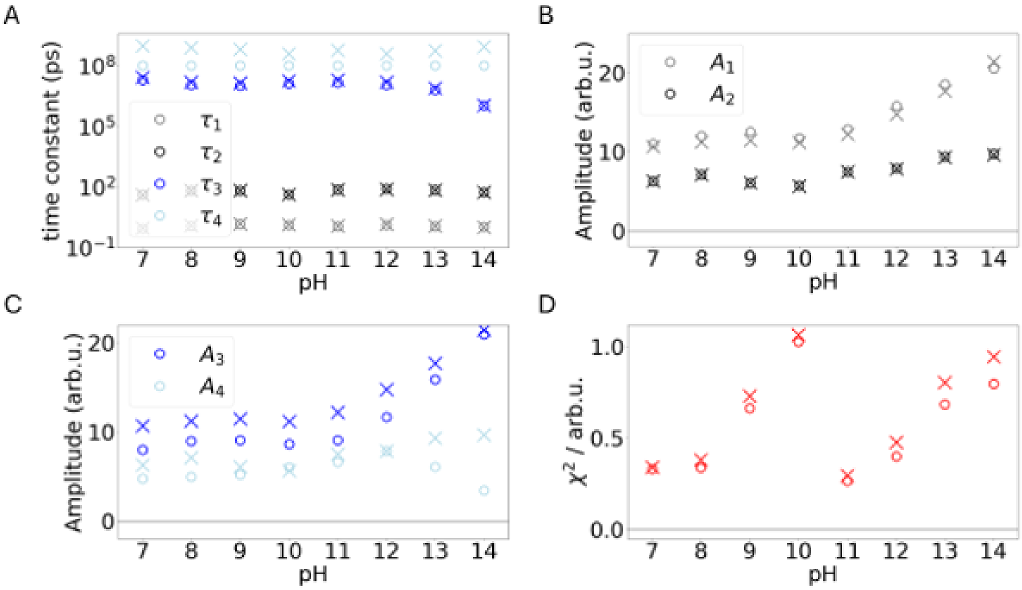

In fitting the emission populations in Chapter 6, the amplitudes for the rising and decaying populations are treated as separate. One could also assume that there are only two populations, $A_1$and A_2, that each show an exponential growth and decay:

$$f_2(t) = A_1(1 - \exp -t/\tau_1) \cdot \exp -t/\tau_3 + A_2(1 - \exp -t/\tau_2) \cdot \exp -t/\tau_4 \tag{E.1}$$

The results for the amplitudes and time constants are similar to the fit with four separate amplitudes as seen in Figure E.1. In addition, the general trends are preserved. The error of the fit is slightly lower when four amplitudes are used, especially for higher pH.

E.2 Long time data: Fitting Single Repeats vs. Averages

Figure E.2: Graphs of the averaged time traces for each pH (circles). The grey area around it represents the standard deviation for each delay point obtained from averaging the traces of each trial. The best fits are shown as a red line. The residuum is shown as red circles in the lower graph. The blue and orange dotted lines represent the two different exponential decay components.

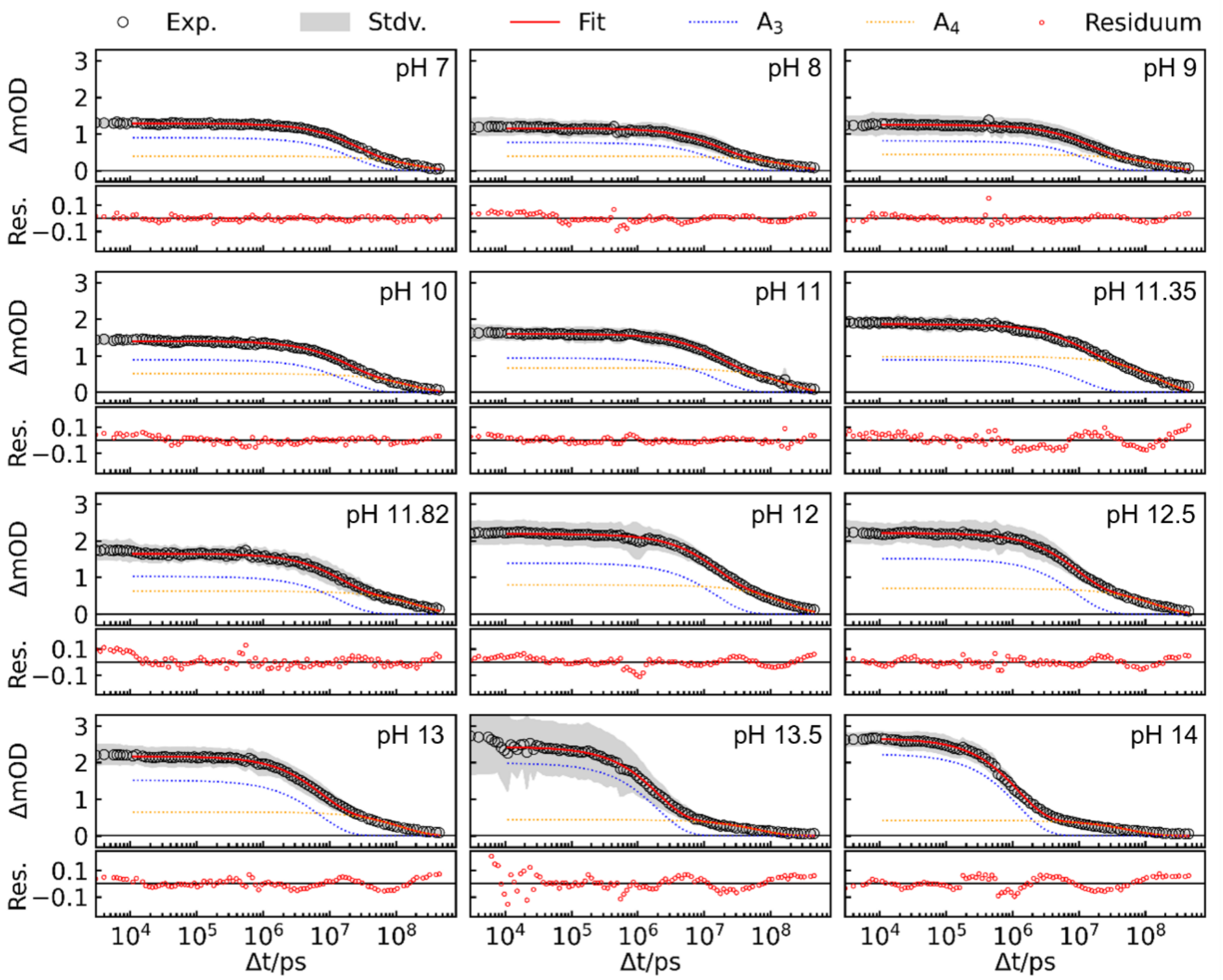

The observed signal intensity is influenced by a manifold of different factors. Surface imperfections and fluctuations in laser intensity are the main sources of signal disturbance. Surface imperfections can be detected by analyzing the raw reflected white light spectrum. Fluctuations in pump laser intensity can be detected by studying the photocurrent in dependence of time. For each pH, multiple repeats were recorded. After carefully sorting out repeats heavily influenced by significant variations in laser power or surface properties, single repeats of each pH were averaged to get reliable time traces. The fits of each pH are shown in Fig. E.2. The dotted purple and yellow lines represent the time traces associated with the two different decay components. The red circles in the lower graphs show the residuum (signal-fit). The grey shaded area depicts the standard deviation obtained from averaging the different traces. Time traces are observed at a center wavelength of 400 nm and averaged over a range of ±2.5 nm to improve the signal to noise ratio. The time traces are fitted with the biexponential decay function

$$S(t) = [A_3 \exp -t/\tau_3 + A_4 \exp -t/\tau_4] \cdot \theta(t - t_0) \tag{E.2}$$

with A_1 and A_2 being the amplitudes of the two components, τ_1 and τ_2 being the time constants of the components and θ being the Heaviside function.

Figure E.3: Amplitude of faster decay constants obtained from single measurement fits (+), averages of those fit results (blue circles) and averaged time traces of each pH (red circles). The blue solid line represents the fit of the averaged fit results for the single time traces, and the red solid line represents the fit of the fit results from the averaged time traces. The estimated uncertainty of determining A_3 was computed by calculating the standard deviation of the different trials for each pH point. All obtained standard deviations were averaged to get an estimated value.

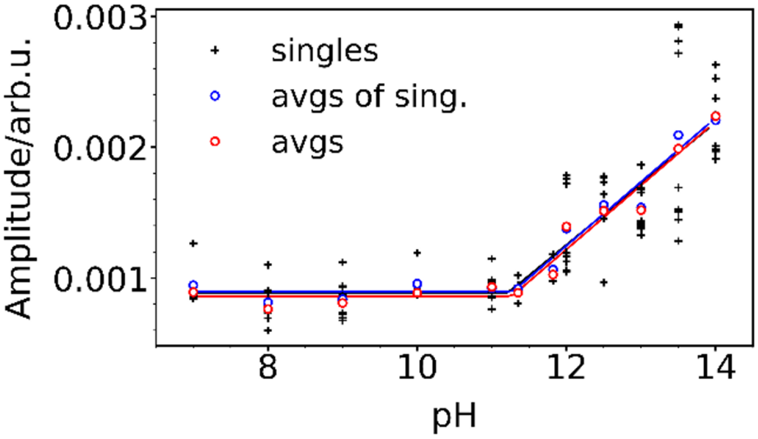

To show that the averaging process has no influence on the qualitative outcome of the analysis,

Table E.1: Obtained A_3 values for each pH with corresponding standard deviation (Std), number of trials (#Trials), standard error of the mean (SEM) and amplitudes obtained by fitting every single trace and then averaging the fit results for A_3. Fit results shown in the main manuscript are represented by A_3 (Avg. traces).

pH	$A_3/\Delta mOD$	$Std/\Delta mOD$	**# trials**	**SEM**/ΔmOD	A_3 **(Avg. traces)**/ΔmOD
7	0.95	0.15	6	0.06	0.89
8	0.82	0.13	9	0.04	0.76
9	0.84	0.13	10	0.04	0.81
10	0.96	0.11	6	0.04	0.89
11	0.92	0.10	9	0.03	0.93
11.35	0.92	0.08	4	0.04	0.89
11.82	1.07	0.07	4	0.04	1.03
12	1.38	0.31	10	0.10	1.39
12.5	1.56	0.29	6	0.12	1.51
13	1.54	0.17	14	0.05	1.5
13.5	2.09	0.68	9	0.23	1.99
14	2.21	2.61E-4	8	9.22E-5	2.24

the fit results of each individual repeat are shown in Figure E.3. After averaging the A_3 results for each individual trial, the trend is very similar to the values resulting from averaging the time traces first (as used in Chapter 7). The resulting pH onset from the constant/linear fit are the same within the experimental uncertainty for all three approaches.

Table E.2: Obtained parameters from fits on averaged time traces.

pH	$A_3/\Delta mOD$	$A_4/\Delta mOD$	$\tau_3/\mu s$	$\tau_4/\mu s$	**C**/ΔmOD
7	0.89	0.39	24.49	192.68	9.54E-4
8	0.76	0.39	16.69	203.23	9.54E-4
9	0.81	0.44	14.13	167.31	9.54E-4
10	0.89	0.51	18.04	166.58	9.54E-4
11	0.93	0.66	16.44	174.60	9.54E-4
11.35	0.89	0.98	10.71	159.83	9.54E-4
11.82	1.03	0.62	14.45	227.95	9.54E-4
12	1.39	0.79	15.26	178.84	9.54E-4
12.5	1.51	0.70	9.22	147.14	9.54E-4
13	1.52	0.65	7.26	124.76	9.54E-4
13.5	1.99	0.44	2.00	67.21	9.54E-4
14	2.24	0.42	1.23	60.42	9.54E-4

Appendix F

Theoretical and Computational Considerations for Hole Polaron Calculations for Chapter 8

F.1 Parametrization of the Hybrid Functional

Figure F.1: Single particle defect levels as a function of mixing parameter α for (a) the electron polaron in rutile TiO_2 and (b) the hole polaron in STO. We find that at an exact exchange of 15% Koopmans' condition is satisfied in TiO_2. In STO, Koopmans' condition is satisfied at 16% exchange rate.

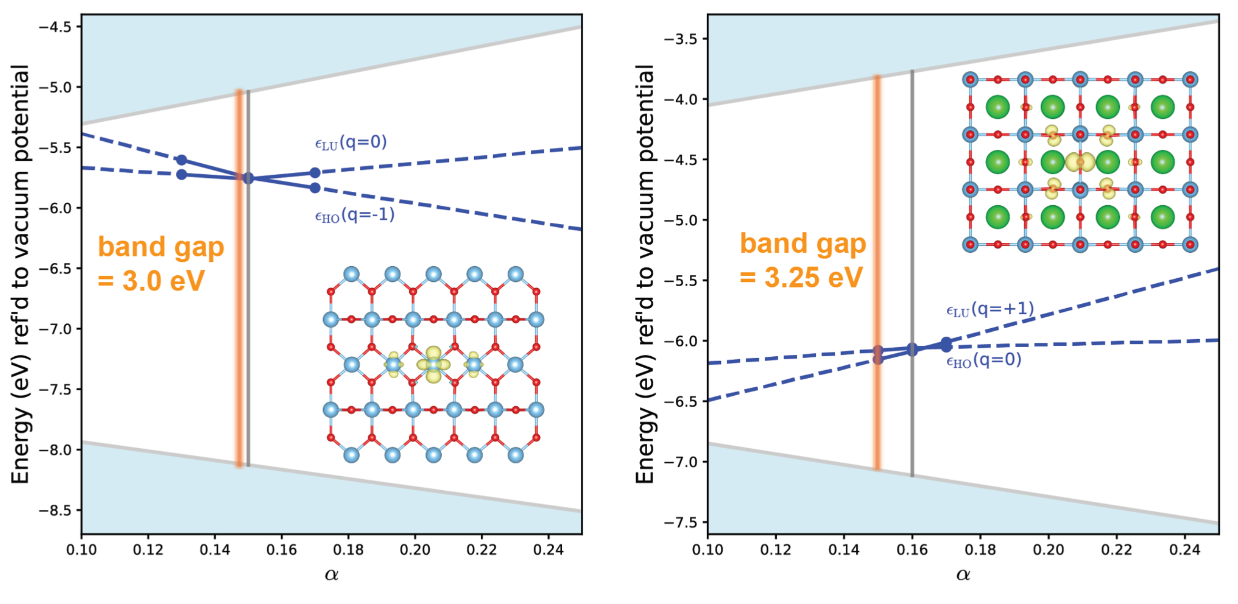

We choose exchange fraction from first principles to reproduce the piecewise linearity of total energy of the known stable bulk polarons (electron polaron in TiO_2, hole polaron in STO). This method has been shown to accurately reproduce band gaps and correctly predict polaron formation.

We find that the mixing parameter α=0.15 satisfies Koopmans' condition in TiO_2, and α=0.16 satisfies Koopmans' condition in STO. Rather than use a different exchange fraction for the two materials, we chose to use α=0.15 for both, as this exchange fraction still satisfies the condition within 0.05 eV in STO and more accurately reproduces the experimental band gap of both TiO_2 and STO.

The exchange fraction needed to satisfy Koopmans' condition for surface polarons (α_K) was different from the exchange fraction that reproduced the band gap and accurately modeled bulk polarons (α_G). This difference between 2D and 3D exchange fraction has been previously described for point defects in WS_2 (Chen 2022), and stems from the difference in screening behavior between delocalized band edges and localized defects in 2D systems. As suggested in that work, we report polaron defect levels at α_K, with the band gap from α_G, aligning the two computations via their vacuum level.

Figure F.2: Single particle defect levels as a function of mixing parameter α for (a) surface hole polarons in rutile TiO_2 (100) and (b) surface hole polarons in STO (001). The α that satisfies Koopmans' condition for bulk polarons and reproduces the band gap is highlighted in gray. The range of α that satisfies Koopmans' condition for the surface polarons is highlighted in orange. The exchange fraction needed to satisfy Koopmans' condition on the surface is higher than in the bulk.

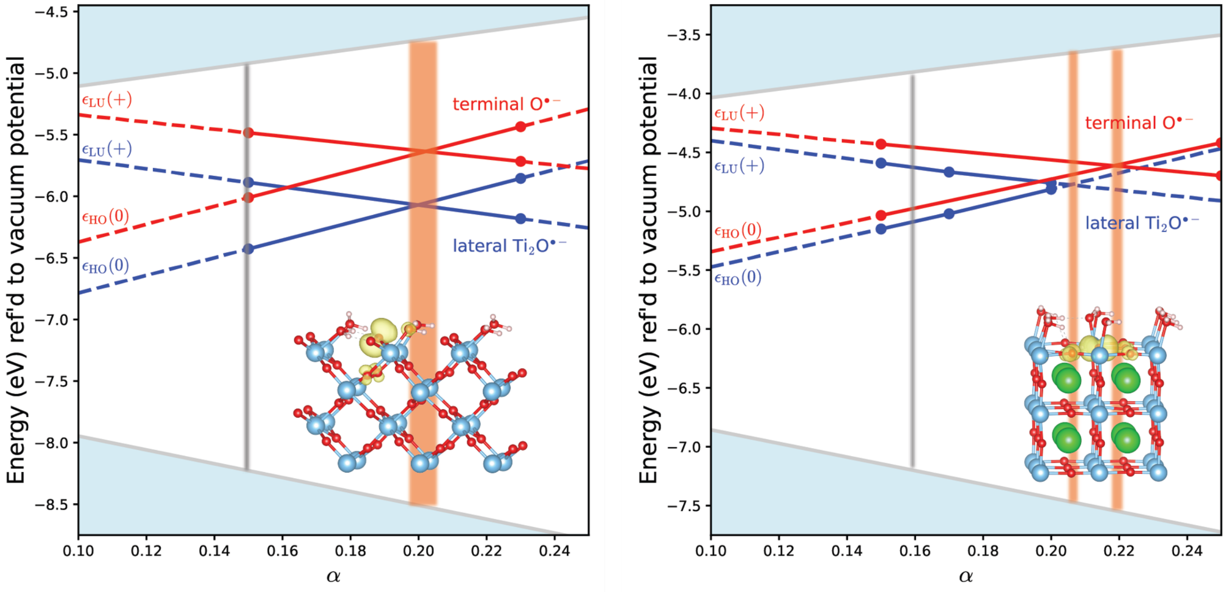

F.2 Optical Dipole of Other Surface Polarons

The less stable polarons TiO_2 bridge $Ti_2O^{\bullet-}$ and STO terminal $O^{\bullet-}$ have oscillator strengths almost a full order of magnitude lower than the more stable polarons, with peaks at 2.6 eV and 2.3 eV, respectively. Without further experimental work, it is impossible to determine in STO whether the 2.2 eV experimental peak corresponds to the terminal or lateral polaron, but the larger optical dipole and lower formation energy of the lateral polaron led us to assign the peak mainly to the lateral polaron. The bridge polaron peak at 2.6 eV does not match what is observed experimentally, leading us to assign the ESA in TiO_2 to the stable terminal polaron. However, this polaron could be contributing to the broadness of the spectra.

Figure F.3: Computed optical dipole of surface trapped holes (a-d) Optical dipole of first 10 vertical excitations (black) from the valence band to trapped hole states at, respectively, TiO_2 (100) bridge $Ti_2O^{\bullet-}$, STO (001) bridge $Ti_2O^{\bullet-}$, TiO_2 (100) terminal $O^{\bullet-}$, and STO (001) terminal $O^{\bullet-}$. Spectral line shape (red) is approximated with Gaussian broadening with FWHM=0.4. Dipole is reported for probe electric field parallel to the extraordinary axis in TiO_2 and averaged in the plane of the surface for STO.

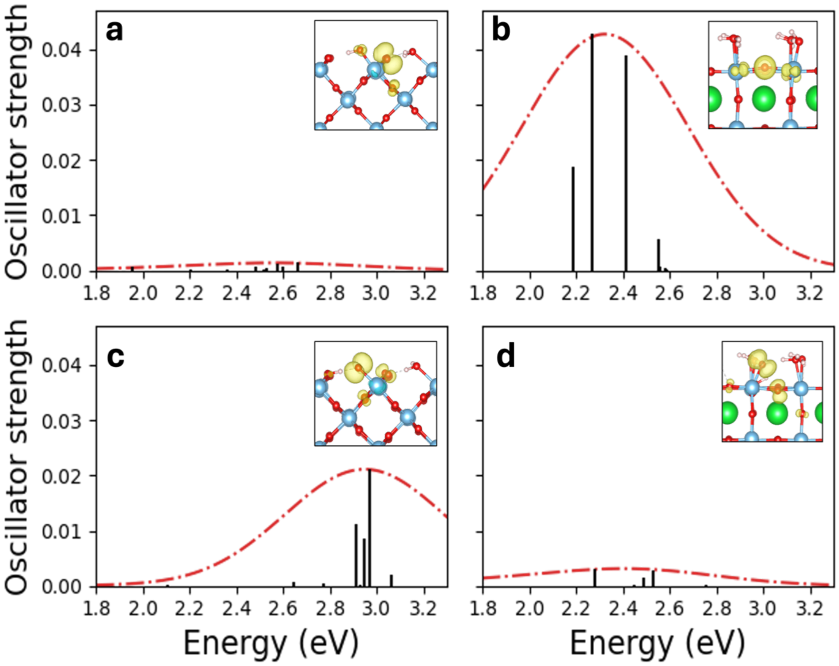

F.3 Polaron Binding Energy and Vertical Transition Levels from DFT

Table F.1: Computed polaron formation energy and vertical transition levels from hybrid DFT. HOMO refers to the highest occupied molecular orbital and LUMO is lowest unoccupied molecular orbital.

		formation energy (eV)	HOMO-LUMO (eV)
TiO_2 (100)	Terminal	-0.71	2.70
	Bridge	-0.33	2.30
	Bulk Electron	-0.07	0.69
STO (001)	Terminal	-0.67	2.68
	Lateral	-0.88	2.49
	Bulk Electron	-0.05	0.99

F.4 Valence Band States contributing to Vertical Transitions

Figure F.4: Shift of optical dipole peak (red) relative to electronic level (blue) overlaid on normalized spectra: (a-c) TiO_2 shows a peak blueshift relative to the electronic level of around 200 meV across all polarons. The TiO_2 bulk hole polaron is shown for reference only – this polaron is not thermodynamically stable. (d-f) STO optical dipole peak is lower in energy than the electronic lev-el by ~250 meV across all polarons.

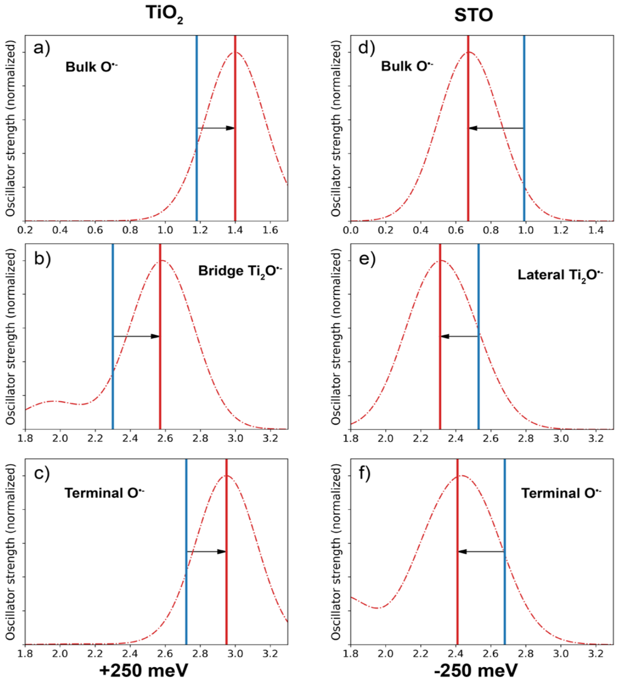

Figure F.4 shows the shift from electronic vertical transition (blue) to peak absorption calculated from TD-DFT (red). The shift is consistent across polarons in the same material, suggesting that the shift is due to material-specific properties such as the valence band character and exciton binding energy, rather than differences between the polarons.

We find that across polarons, the strongest vertical transition in TiO_2 originates from below the valence band maximum, while STO has states near the VBM that have a strong transition to the polaron. Figure F.5 illustrates this with the stable polarons at TiO_2 terminal and STO lateral. We can also explain some of the intensity difference and shift between the two oxides by the density of states near the valence band. STO has high density of states near the valence band, while TiO_2 has higher density of states deeper in the valence band. This can be illustrated by a joint density of states as shown in Figure F.6. Even ignoring wavefunction overlap, STO has a much brighter initial peak, while TiO_2 becomes brighter at energies higher than the charge transition level.

Figure F.5: Joint density of states: Joint density of states gives us an understanding of the absorption spectra ignoring wavefunction overlap, considering only density of states. STO has much higher density of states at the valence band, leading to a stronger transition from the VB to the polaron than in TiO_2. The charge transition level of the polaron is shown with a blue line.

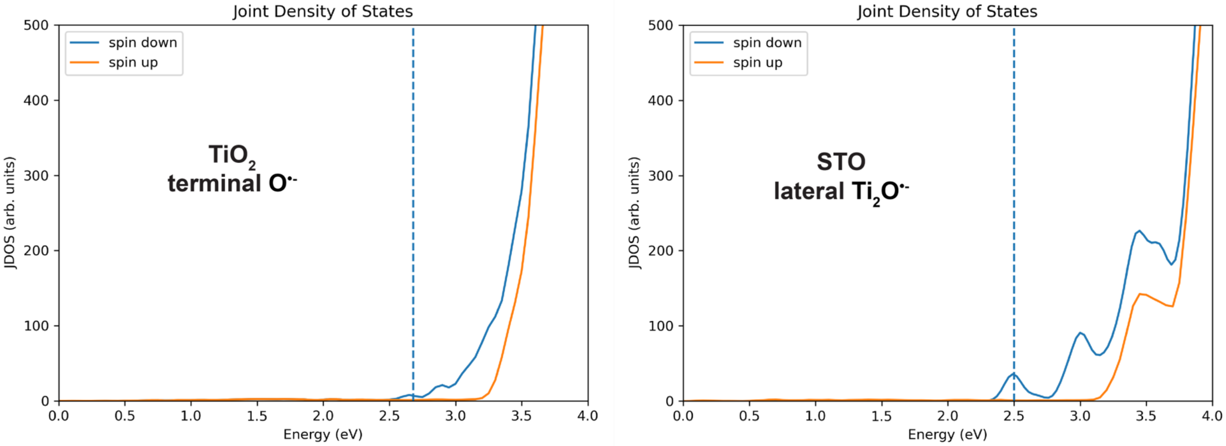

Figure F.6: Occupied states (blue) and unoccupied states (orange) contributing to the "brightest" optical peak for hole polarons at a) TiO_2 terminal $O^{\bullet -}$ and b) STO lateral $Ti_2O^{\bullet -}$. Circles indicate states involved in the transition, with the size of the circle corresponding to the strength of the contribution. Both excita-tions involve a transition from the valence band to the mid-gap polaron state. The occupied states involved in TiO_2 are below the valence band maximum, while in STO they are close to the VBM.

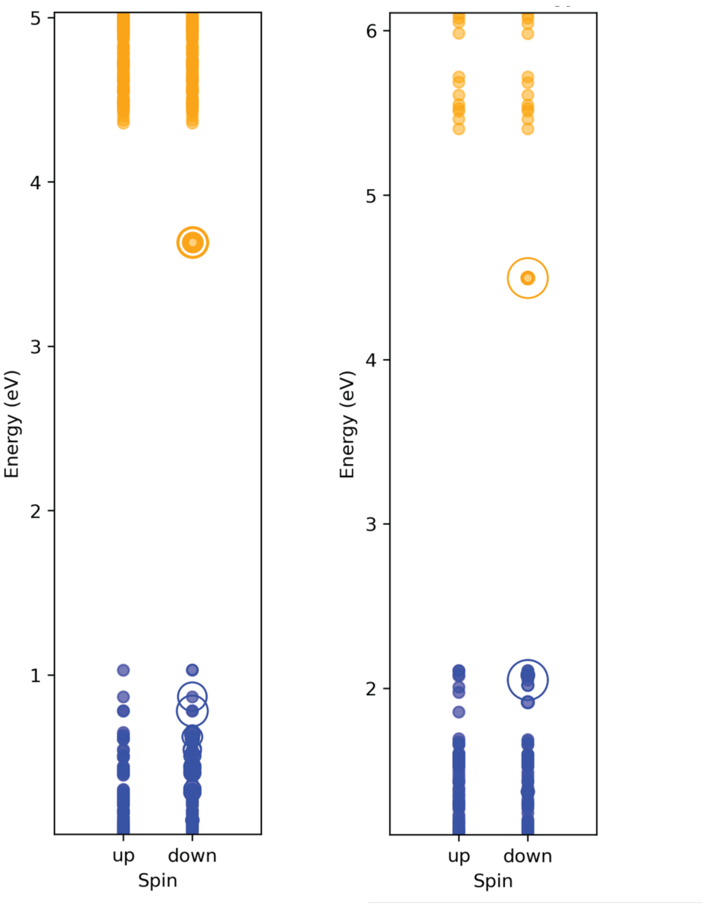

F.5 Less Probable Transitions

Figure F.7 shows the experimentally determined spectra of STO and TiO_2 compared to the calculated spectra of the less probable hole polarons in STO (terminal) and TiO_2 (bridge).

Figure F.7: Theory compared to less probable transitions: Solid lines are the experimental spectra. Stick spectra correspond to probabilities for an optical transition, normalized to one with respect to the maximum probability in STO and TiO_2, respectively. Dashed lines represent stick spectra after gaussian broadening with a width of 800 meV. The theoretical spectra correspond to transitions associated with the STO terminal $O^{•-}$ and the TiO_2 bridge $i_2O^{•-}$ hole polaron.

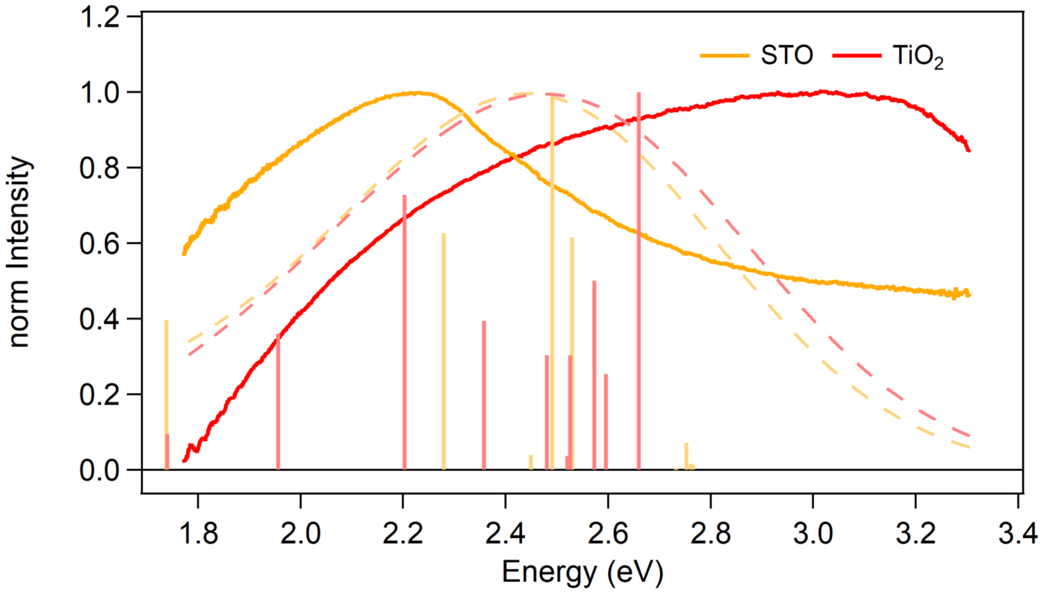

F.6 Determination of Spectral Maxima for $SrTiO_3$ and TiO_2

Figure F.8 provides a summary of our methodology for determining the different ESA maxima in TiO_2 and $SrTiO_3$. First component constrained SVD spectra, and their derivatives, for the 0.5% STO and TiO_2 data shown in Figure 8.3c are plotted in Figure 3.3. The derivatives of the $SrTiO_3$ and TiO_2 spectra are 0, and match up with the observed spectral maxima, at 2.03 eV and 3.06 eV, respectively. This corresponds to an energy shift of 1.03 eV. Note that these spectral maxima and energy shift are only calculated from one dataset. A more accurate energy shift could be determined from the averaged constrained SVD components. Figure F.8b shows the averaged

Figure F.8: Determination of spectral maxima: a) Constrained first component spectra, and their derivatives, of OC, pH 7 0.5% Nb-$SrTiO_3$ and 0.5% Nb-TiO_2 shown in Figure 8.3. b) Averaged constrained first component spectra, and their derivatives, from closed circuit, pH dependent $SrTiO_3$ and doping dependent TiO_2 datasets.

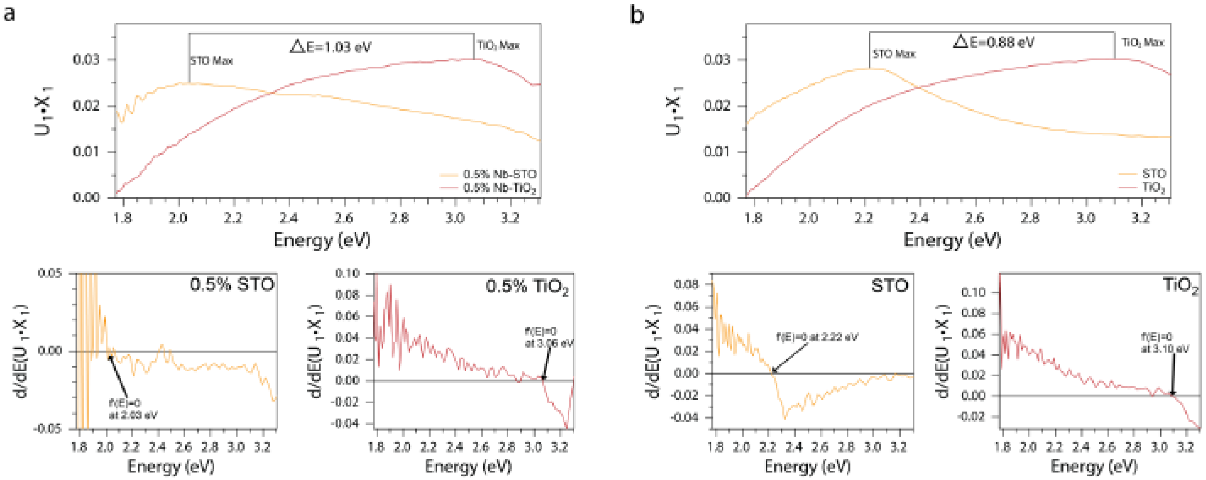

constrained first component spectra, and their derivatives, from the 0V, pH dependent $SrTiO_3$ and doping dependent TiO_2 datasets. The derivative of the averaged constrained first component $SrTiO_3$ and TiO_2 spectrum is 0 at 2.22 eV and 3.10 eV, respectively. Consequently, the difference between the absorptive maxima in TiO_2 and $SrTiO_3$ is 0.88 eV.

Appendix G

A Second Data Set Collected for Raman Gain Dependence on Pump Energy

Figure G.1: Secondary analysis of Raman Gain dependence on Raman Pump Energy. a) FSRS spectra of STO collected at more finely space Raman pump energies, with a slightly different pump and probe overlap in time. Changing this temporal overlap results in a shift in the background, allowing for more accurate manual integration or Stokes peaks. b),c),d) Integrated area of Raman peaks for the the first three Stokes peak clusters, along with a linear fit. The trend with pump energy is clearly linear.

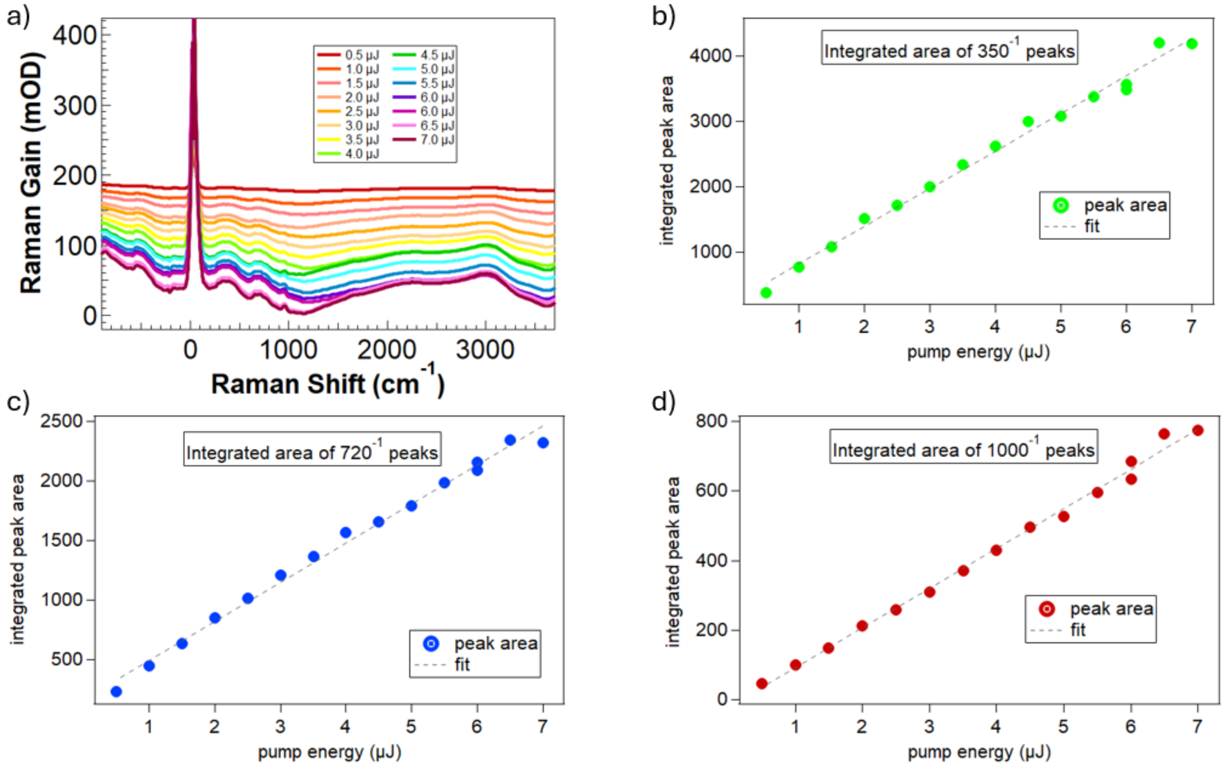

To confirm the conclusions drawn from FSRS data at different pump energies, a second data set was collected. The goals of this data set were several fold: to repeat the data and confirm the trend, collect more finely spaced data points in random order to eliminate artifacts from long-term spatial overlap changes, to shift the background to allow for more accurate peak integration. The source of the background is not understood, and will not be discussed in this work. The background does however seem to have a minimum that shifts as the time-domain pump/probe overlap changes. Previous data (Figure 9.3) was collected with the alignment performed such that this minimum was as close as possible to the fundamental. This resulted in slight deviations from linearity for higher pump energies. The data displayed in Figure G.1a was collected with time domain pump alignment conducted such that the background minimally interfered with the peaks of interest (first 3 clusters of Stokes peaks). Integration of these peaks, using the same method as for the previous data showed very nice linearity, confirming the conclusion drawn in Chapter 9.